Strength of Tantalum at High Pressures through Richtmyer-Meshkov Laser Compression Experiments and Simulations

Thesis by
Kristen Kathleen John

In Partial Fulfillment of the Requirements
For the Degree of
Doctor of Philosophy

California Institute of Technology
Pasadena, California

2014
(Defended August 30, 2013)

"Whatever you are, be a good one." – Abraham Lincoln

To Mom, Dad, Susie, Terrie, and Ryan, for leading by example.

Acknowledgements

I am extremely grateful for my advisor, Professor G. "Ravi" Ravichandran. I could not have asked for a more supportive, encouraging, and patient mentor. Over the years, Ravi has provided me with a unique research experience that helped me grow in more ways than I imagined.

I would like to thank the members of my thesis committee: Professors Kaushik Bhattacharya, Dennis Kochmann, and Michael Ortiz for providing their support and enthusiasm for my research.

I am especially thankful for the two very talented post-docs that I had the pleasure to work with: Dr. Bo Li and Dr. Aaron Stebner. Bo was my modeling sage and made the simulations aspect of my research possible. Aaron became my mentor and "go-to" guy for several of the experiments.

I was very fortunate to have the chance to work with physicists and scientists from Lawrence Livermore National Laboratory (LLNL) throughout my time at Caltech. I am especially grateful for my mentors, Dr. Hye-Sook Park and Dr. Bruce Remington. I am also very grateful for the guidance I received from Dr. Jon Belof, Dr. Brian Maddox, Dr. Chris Plechaty, and Dr. Chris Wehrenberg. I am also thankful for the collaboration with General Atomics for our targets, particularly Dr. Greg Randall. I am grateful for the opportunity to have spent a summer at LLNL learning from some amazing people. I am also thankful for the several trips I was able to make to the Omega Laser Facility at the University of Rochester's Laboratory for Laser Energetics (LLE). I would like to thank all the wonderful people at these locations that made my visits possible and productive.

My days at Caltech were always more enjoyable when I had the chance to interact with the amazing folks of GALCIT and MCE. I am very thankful for the support I received from Cheryl Gause, Jackie Gish, Petros Arakelian, Christine Ramirez, Dimity Nelson, Lydia Suarez, Denise Ruiz, and Leslie Rico.

I would like to thank Brandon Runnels, Laurence Bodelot, Sagar Vaidyanathan, Nick Mai, Stan Wojnar, Aaron Albrecht, and Andy Richards. I would also like to thank all the mentors I have had along the way including Hans Mark, Ron Pechacek, David Hash, Rui Huang, Sean Buckley, Wallace Fowler, Lisa Guerra, Greg Davis, Yunjin Kim, and Therese Larson.

My experience at Caltech was made special by the presence of some wonderful friends I made along the way. To my fellow first-years, thank you for the good times and late nights in the first-year office: Victoria Stolyar, Andy Galvin, Stephanie Coronel, Jomela Meng, Terry Gdoutos, Namiko Saito, Jocelyn Escourrou, Philipp Oettershagen, Adrián Sánchez Menguiano, Juan Pedro Méndez Granado, Ignacio Maqueda, Xin Ning, Landry Fokoua Djodom, Brad Lyon, and Siddhartha Verma. I am also thankful for the wonderful friendships I made with Melissa Tanner, Mike Rauls, and Cindy Wang.

I am tremendously grateful for my fellowship, the Department of Energy National Nuclear Security Administration Stewardship Science Graduate Fellowship (DOE NNSA SSGF). The four years of this fellowship guided my research and provided me with the unique opportunity to collaborate with a national lab (LLNL) during my graduate research. It gave me the chance to explore properties of materials under extreme conditions and to broaden my horizon beyond the aerospace industry and into the energy industry and stewardship science. I am very grateful to the Krell Institute for making this all possible, particularly to Lucille Kilmer, John Ziebarth, Michelle King, and Jim Corones. I am also thankful for the summers I had in

D.C. with the other fellows, getting the chance to learn about the remarkable research going on in stewardship science across the country. I am also appreciative for the funding I received from Caltech's NNSA Predictive Science Academic Alliance Program (PSAAP) program.

Universally, I would like to thank every teacher I had along the way who encouraged me to pursue my dreams. From kindergarten through high school, from undergrad through grad school, I have been exceptionally fortunate to have such inspiring educators in my life. And a special thank you to the ones who said I could do anything I put my mind to.

I am so thankful for the incredible support team I have always had in my personal life. I am grateful to have the most amazing friends, grandparents, aunts, uncles, cousins, brothers-in-law, parents-in-law, and of course, niece and nephews! And thank you to Pluto for being by my side while I wrote my thesis, literally!

Most importantly, thank you to my family for being there for me since forever! My amazing parents and sisters have always been my best supporters, and I am grateful for every moment I have with them. Thank you to my husband, Ryan, for your love, support, patience, and frequent-flying over the last few years. In order of appearance, to Mom, Dad, Susie, Terrie, and Ryan, I owe you everything. Thank you!

Abstract

Strength at extreme pressures (>1 Mbar or 100 GPa) and high strain rates (10^6-10^8 s^{-1}) of materials is not well characterized. The goal of the research outlined in this thesis is to study the strength of tantalum (Ta) at these conditions. The Omega Laser in the Laboratory for Laser Energetics in Rochester, New York is used to create such extreme conditions. Targets are designed with ripples or waves on the surface, and these samples are subjected to high pressures using Omega's high energy laser beams. In these experiments, the observational parameter is the Richtmyer-Meshkov (RM) instability in the form of ripple growth on single-mode ripples. The experimental platform used for these experiments is the "ride-along" laser compression recovery experiments, which provide a way to recover the specimens having been subjected to high pressures. Six different experiments are performed on the Omega laser using single-mode tantalum targets at different laser energies. The energy indicates the amount of laser energy that impinges the target. For each target, values for growth factor are obtained by comparing the profile of ripples before and after the experiment. With increasing energy, the growth factor increased.

Engineering simulations are used to interpret and correlate the measurements of growth factor to a measure of strength. In order to validate the engineering constitutive model for tantalum, a series of simulations are performed using the code Eureka, based on the Optimal Transportation Meshfree (OTM) method. Two different configurations are studied in the simulations: RM instabilities in single and multimode ripples. Six different simulations are performed for the single ripple configuration of the RM instability experiment, with drives corresponding to laser energies used in the experiments. Each successive simulation is performed at higher drive energy, and it is observed that with increasing energy, the growth factor increases. Overall, there is favorable agreement between the data from the simulations and the experiments. The peak growth factors from the simulations and the experiments are within 10% agreement. For the multimode simulations, the goal is to assist in the design of the laser driven experiments using the Omega laser. A series of three-mode and four-mode patterns are simulated at various energies and the resulting growth of the RM instability is computed. Based on the results of the simulations, a configuration is selected for the multimode experiments. These simulations also serve as validation for the constitutive model and the material parameters for tantalum that are used in the simulations.

By designing samples with initial perturbations in the form of single-mode and multimode ripples and subjecting these samples to high pressures, the Richtmyer-Meshkov instability is investigated in both laser compression experiments and simulations. By correlating the growth of these ripples to measures of strength, a better understanding of the strength of tantalum at high pressures is achieved.

Table of Contents

List of Figures

List of Tables

Chapter 1

Introduction

1.1 Background

Engineering aims to find solutions to problems that exist in the world. By integrating experiments, theory, and simulations, engineers can apply a variety of techniques to understand and solve complex problems. Within Aerospace Engineering, an interdisciplinary approach is employed, combining the fields of solid mechanics, fluid dynamics, and materials science. Solid mechanics studies the behavior of materials in response to external forces. In particular, the study of dynamic behavior of materials deals with understanding the motion and deformation that occurs when materials are subjected to events that impart high energy density in the materials, such as hypervelocity impact and blast. The response of materials undergoing dynamic loads is considerably different from materials that are under static or quasi-static conditions [1, 2]. To predict the response of materials under loading, it is essential to understand properties of the material, such as strength and plastic flow. At low velocity impacts where the rate of deformation, or strain rate, is around 10-10^2 s^{-1}, the pressures are low and the materials do not exhibit rate dependent behavior in their strength (yield stress). For dynamic events with strain rates of 10^3-10^4 s^{-1}, metals begin to exhibit a rate dependent behavior in their strength and plastic flow. At much higher strain rates of 10^5-10^8 s^{-1}, the material behavior is not as well understood in terms of their strength and flow behavior. At very high stresses as those encountered in shock experiments, the state of stress is essentially hydrodynamic and the solid material is assumed to exhibit fluid-like behavior. Strength at extreme pressures (>1 Mbar (100 GPa)) and strain rates (>10^7 s^{-1}) is not well characterized, and the means to create these conditions in a laboratory setting are not simple.

1.2 Motivation

Material strength is the resistance of a material to permanent or plastic deformation. Solid state dynamics at extreme pressures (0.1 – 1 Mbar) and strain rates (10^6-10^8 s^{-1}) pushes the current limit of materials science to orders of magnitude higher pressures [3]. This brings about the challenge of quantifying strength in this new regime. By comparing simulations with experiments at these conditions, the constitutive models for strength can be validated and/or improved. To measure strength at extreme conditions of pressures and strain rates, a new experimental platform has been

proposed by Remington and his coworkers at Lawrence Livermore National Laboratory (LLNL), which is based on measuring perturbation growth of instabilities in solid state samples of metals by creating a well characterized ripple on the material [3]. When subjected to high pressures by generating drives using high energy lasers, the amplitude of the ripple will grow. If the material had no strength, it would act as a fluid and the ripple would grow rapidly due to instabilities. At these conditions, however, the material strength acts as a strong stabilizing force which results in a reduced rate and magnitude of amplitude growth [3]. The amount by which the growth is reduced is a measure of the material's strength [4]. Higher strength results in less growth, just as no material strength would result in large amounts of growth.

1.3 Applications

The motivation of the research presented in this thesis is to advance the understanding of material strength at extremely high pressures (>1 Mbar). Additionally, understanding of strength at high pressures has applications in fusion energy, hypervelocity impacts, astrophysics, aerospace engineering, and the military.

In astrophysics, applications include studying planetary impacts and understanding the planetary bodies. The facilities used to create these high pressure and high strain rate environments are some of the few in the world that come close to emulating conditions (3.6 Mbar) at the core of the Earth and other planetary bodies. Matter at extreme densities, pressures, and temperatures is common in our universe; for instance, the metallic core of Jupiter is around 77 Mbar [5]. To understand planetary evolution, astrophysicists must know the material properties at extreme conditions, and the way to explore the deep interior of giant planets and stars is to use lasers to recreate these conditions in the laboratory [5]. The equation of state (EOS) of data gained from such studies can lead to answers about the start of our solar system. For instance, using luminosity data, evolutionary data, and EOS models, the age of Jupiter was estimated to be 4.7 billion years, compared to the age of our solar system, which is 4.6 billion years [5].

The study of high strain rate phenomena for military applications is abundant, including explosives and ballistic impact, as well as oil well perforation, seismological studies, fragmentation, and nuclear technology [1]. In aerospace engineering, an application of this research relates to hypervelocity impacts, which involves space shielding. Every spacecraft must have some form of space shielding to protect itself from millimeter sized particles, such as micrometeorites, that are traveling at 10-100 km/s. Through the use of whipple shields, modern day spacecraft are protected.

By correlating instability growth to strength of metals, a unique technique for quantifying strength is employed. Another byproduct of this research is further insight into the Richtmyer-Meshkov (RM) and Rayleigh-Taylor (RT) instabilities in matter that is in solid state. These instabilities are the observational parameter used in the experiments and simulations; however, by

creating these instabilities, more knowledge is gained into the physics behind them and how they evolve in metals.

The most extreme application of this research is fusion energy. The facilities used to create the conditions to study strength at such high strain rates and pressures are the same facilities that are performing experiments to create the conditions necessary to reach ignition. The concept of fusion (the process that powers our Sun and stars) involves fusing together light atoms such as hydrogen to form heavier elements such as helium. The concept basically suggests that if possible, more energy could essentially be created in the system than what was put in. If this could be a viable source of energy, this would provide abundant energy. One issue that is keeping fusion energy from occurring is a process called ignition. Ignition has several requirements, one being that the fusion target must compress symmetrically. However, instabilities can occur during the compression and release that can prevent ignition. The present research involves studying material strength by examining these instabilities. If sufficient understanding can be gained, this could potentially impact the way fusion targets are designed and what materials are used in ignition experiments.

Tantalum (Ta) is the metal studied in the experiments and simulations discussed in the subsequent chapters. Tantalum is interesting because of its high density, high melting point, and relatively high ductility. Tantalum has body-centered cubic structure and does not undergo phase transition of interest in the present study (1-3 Mbar).

In general, the research presented in this thesis is relevant to impact dynamics, high energy density physics, materials science, and in understanding the strength of materials at these extreme conditions.

1.4 Strength Models

As higher pressures and strain rates are achieved in the laboratory, more accurate descriptions of materials can be created in constitutive models. Such strength and material models are critical to developing simulations that can predict what will happen in these materials in applications. The phenomenological engineering constitutive model used in the simulations in this thesis is discussed in great detail in Chapter 3, along with the material model for tantalum. This section briefly discusses some of the other strength models that have been commonly used to predict material behavior over the last several decades.

To infer material strength using the RM or RT instability experiments, simulations must utilize an appropriate strength model. The observational parameter in the experiments is the growth factor. The following phenomenological models have been used to predict the growth factor in an effort to improve the models for strength.

1.4.1 Steinberg-Guinan

The Steinberg-Guinan (SG) model assumes the yield stress increases with strain rate; however, at high strain rates (>10^5 s^{-1}), the strength becomes rate independent [6]. Therefore, the yield stress reaches a peak value that is essentially strain rate independent. Steinberg and Guinan also suggest that the shear modulus increases as pressure increases, and it decreases as temperature increases. Therefore, the model incorporates the Bauschinger effect. Essentially, the model presents equations for yield strength and shear modulus that are functions of effective plastic strain, pressure, and temperature. Melting is based on the Lindemann law, so if temperature in the material exceeds the specified melting temperature, the yield strength and shear modulus will be set to zero. The EOS is energy based. The key SG equations for yield stress at high strain rate are below [6].

$$\sigma = \sigma_0 f(\varepsilon_p) G(P,T)/G_0 \tag{1.1}$$

$$\sigma_0 f(\varepsilon_p) = \sigma_0 \{1 + \beta(\varepsilon_p + \varepsilon_i)\}^n \leq \sigma_{max} \tag{1.2}$$

$$G(P,T) = G_0 \left\{1 + AP/\eta^{\frac{1}{3}} - B(T-300)\right\} \tag{1.3}$$

$$A = \frac{1}{G_0}\frac{dG}{dP} \tag{1.4}$$

$$B = \frac{1}{G_0}\frac{dG}{dT} \tag{1.5}$$

Table 1.1: Material Properties for Tantalum Used in the Steinberg-Guinan Engineering Model

Symbol	Parameter	Units	Tantalum
σ	yield strength	Mbar	-
σ_0	yield strength at the Hugoniot elastic limit	Mbar	7.7e-03
ε_p	equivalent plastic strain	-	-
G	shear modulus	Mbar	-
P	pressure	Mbar	-
T	Temperature	K	-
G_0	initial shear modulus	Mbar	0.690
B	temperature dependence of shear modulus	K^{-1}	1.3e-04
ε_i	initial plastic strain	-	0
β, n	work hardening parameters	-	22, 0.283
σ_{max}	work hardening maximum	Mbar	1.1e-02
A	pressure dependence of the shear modulus	$Mbar^{-1}$	1.45
ϱ_0	initial density	g/cm^3	16.69
η	compression	-	-

1.4.2 Preston-Tonks-Wallace

The Preston-Tonks-Wallace (PTW) is a dislocations-based model that uses Orowan's equation from dislocation mechanics for the strain rate [7].

$$\frac{d\varepsilon}{dt} = \rho_{disloc} b \langle v_{disloc} \rangle \tag{1.6}$$

The strain rate depends on the dislocation density and velocity, as well as the Burgers vector modulus. Dislocation velocity depends on stress, temperature, and the presence of dislocation obstacles [8]. In the PTW model, the average of the dislocation velocity is viewed as two distinct regimes. The first is the thermal activation region and the second is the phonon drag region. The equations below represent the PTW model for high strain rate. PTW takes into account normalized work hardening, saturation stress, yield stress, a Voce hardening law, and certain dimensionless parameters. The saturation stress is shown below, where κ and γ are material constants.

$$\sigma_s = 2G \max\left\{ \begin{matrix} s_0 - (s_0 - s_\infty)\ \mathrm{erf}\left[\kappa \hat{T} \ln\left(\frac{\gamma \dot{\varepsilon}}{\dot{\varepsilon}}\right)\right] \\ s_0 \left(\frac{\dot{\varepsilon}}{\gamma}\right)^{\beta} \end{matrix} \right\} \tag{1.7}$$

$$\gamma \sim \rho_{disloc} b^2 \tag{1.8}$$

$$\kappa \sim \frac{1}{U_k} \tag{1.9}$$

1.4.3 Johnson-Cook

Another model is the Johnson-Cook (JC) model. This model is empirical and depends on equivalent plastic strain (ε_p), plastic strain rate ($\dot{\varepsilon_p}$), and several material constants (*A, B, C, n, m*).

$$\sigma_y\left(\varepsilon_p \dot{\varepsilon}_p, T\right) = \left[A + B(\varepsilon_p)^n\right]\left[1 + C \ln(\dot{\varepsilon_p}^*)\right]\left[1 - (T^*)^m\right] \tag{1.10}$$

1.4.4 Multiscale Strength Model and Tantalum Material Model

A multiscale strength model for extreme loading conditions has been created at LLNL, as well as a material model for tantalum using this multiscale approach [9, 10]. The multiscale model, led by Nathan Barton, is designed such that strength depends on pressure, temperature, strain rate, and dislocation density [9]. The multiscale ranges from the atomistic level to the continuum level, and the simulation methods include density functional theory, molecular statics and dynamics, dislocation dynamics, and continuum approaches [9]. The strength model is applicable to strain

rates greater than 10^4 s^{-1}, and predictions from the model have agreed well with material strength experiments. The continuum strength model for tantalum, led by Richard Becker, is a simplified version of a previous model that has fewer parameters, and the material strength depends on plastic strain rate, temperature, pressure, and dislocation density [10].

There are no explicit relations that couple the conditions of instabilities to material strength [11]. Until such a mathematical model exists, we rely on empirical strength models to understand the relationship between strength and instabilities. These models are primarily concerned with describing the stress as a function of strain-rate, as shown below [11].

$$\text{Preston-Tonks-Wallace (PTW) model} \rightarrow \sigma \propto \mu(\dot{\varepsilon})^{1/4} \tag{1.11}$$

$$\text{Steinberg-Guinan (SG) model} \rightarrow \sigma \propto \dot{\varepsilon} \tag{1.12}$$

$$\text{Steinberg-Lund (SL) model} \rightarrow \sigma \propto \dot{\varepsilon} \tag{1.13}$$

$$\text{Multiscale model (LLNL)} \rightarrow \sigma \propto \mu < \dot{\varepsilon} > \sqrt{6} \tag{1.14}$$

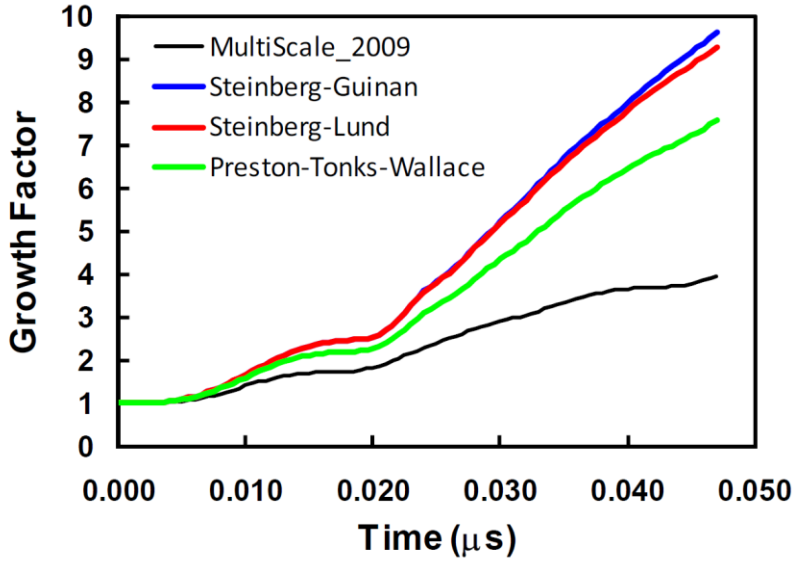

Figure 1.1: Evolution of predicted growth factors in time for the Steinberg-Guinan, Steinberg-Lund, and Preston-Tonks-Wallace strength models, along with the LLNL multiscale model [10].

In Figure 1.1, the results are shown for predictions from Rayleigh-Taylor growth factors. The following section discusses the different types of instabilities studied in these types of experiments and simulations.

1.5 Instabilities

The observational parameter in the experiments and simulations used in this research is the Richtmyer-Meshkov instability. Both the simulations and experiments are modeled after a platform that studies Rayleigh-Taylor instabilities.

1.5.1 Rayleigh-Taylor Instability

A Rayleigh-Taylor (RT) instability occurs when a lighter fluid pushes a heavier fluid. The instability was named for Lord Rayleigh and G.I. Taylor, and it occurs at the interface of the two fluids of different density when the lighter one is accelerated into the heavier one. Similarly, a RT instability will result if a heavier fluid is sitting on top of a lighter fluid in the presence of gravity. Examples of RT instabilities are found in astrophysics (supernova explosions), the atmosphere and ocean, in geological flows (oil trapped in salt domes and underwater), and in inertial confinement fusion [12]. The equations for RT instabilities are below.

$$h \approx h_0 e^{\gamma t} \tag{1.15}$$

$$\gamma = \sqrt{Ag\lambda} \tag{1.16}$$

$$A = \frac{\rho_h - \rho_l}{\rho_h + \rho_l} \tag{1.17}$$

In these equations, h is the height of the disturbance, λ is a measure of the wavelength, ρ_l is the density of the light fluid, and ρ_h is the density of the heavy fluid. A is called the Atwood number, which is bounded between 0 and 1, and g is gravity or the acceleration. Growth factor is represented by γ. Figure 1.2 shows what a RT instability looks like over time.

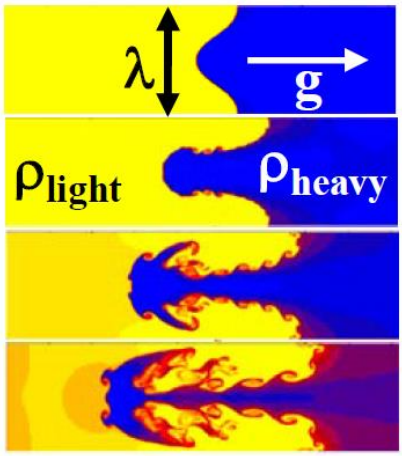

Figure 1.2: Classical depiction of the RT instability with a light fluid pushing a heavy fluid, and the resulting formation of Kelvin-Helmholtz instabilities and mushrooms [13].

The Kelvin-Helmholtz (KH) instabilities depicted in the later images of the RT instability in Figure 1.2 occur when a velocity shear is present in a fluid, or if a velocity difference exists across the interface of two fluids [13]. The typical example of this in nature is wind blowing across water, creating waves. This is also evident in clouds, as well in astrophysics, such as in Saturn's bands, Jupiter's Red Spot, and the sun's corona [14].

1.5.2 Richtmyer-Meshkov Instability

The Richtmyer-Meshkov (RM) instability is similar to the RT instability in that it occurs when a lighter medium is accelerated into a heavier one. The difference is that the interface is accelerated by the passage of a shock wave. Figure 1.3 shows what the setup of the RM instability interface may look like. The instability starts as a small amplitude perturbation that grows linearly with time, evolves to a nonlinear regime which may result in bubbles or spikes, and progresses to a regime in which the two mediums mix [15, 16, 17]. The RM instability has been described as the impulsive-acceleration limit of the RT instability [15]. In the experiments and simulations in this research, the ripples can grow via the RM instability, where a shock propagates from a plastic ablator (ρ_l) to the metal (ρ_h), and refraction at the rippled interface leads to growth in the ripple peak-to-valley (PV) amplitude.

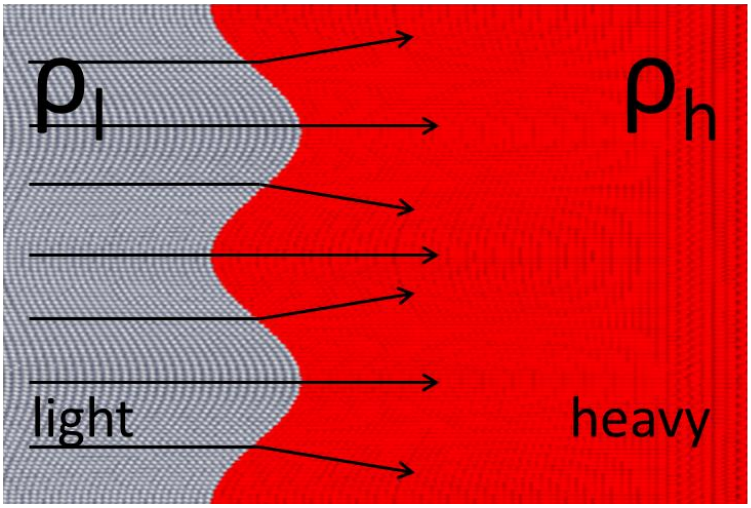

Figure 1.3: Richtmyer-Meshkov (RM) instability at the interface of a lighter medium pushing into a heavier medium.

Below are the equations that define growth via the RM instability, where η represents the peak to valley amplitude, γ represents growth factor, λ is the wavelength, ρ_l is the density of the light medium (ablator), and ρ_h is the density of the heavy medium (metal).

$$\gamma = \frac{\eta(t)}{\eta(t=0)} \sim 1 + \left(\frac{2\pi}{\lambda} uA\right) t \tag{1.18}$$

$$A = \frac{\rho_l - \rho_h}{\rho_l + \rho_h} \tag{1.19}$$

Applications of RM instabilities can be found in astrophysics (i.e. supernovae), supersonic combustion (fuel oxidants interface is improved with the breakup of fuel into droplets), detonation combustion (in ignitable mixtures of flammable gases along with oxygen), and inertial confinement fusion [16]. The targets for inertial confinement fusion (ICF) consist of an inner fuel layer of Deuterium-Tritium (DT), which are isotopes of hydrogen surrounded by a shell. During the implosion, the hot shell material around the cold DT fuel layer becomes shock-accelerated. To achieve ignition, the mixing of the shell and fuel cannot occur [18]. Therefore, the manufacturing of targets is critical such that the surface is smooth, because any imperfections in the surface will act as initial perturbations that may instigate the propagation of the RM instability.

1.5.3 Shock-induced Interface Instability in Viscous Fluids and Metals

In a study by Karnig Mikaelian of Lawrence Livermore National Laboratory (LLNL), there is interest in the shock-induced interface instability in viscous fluids and metals [19]. Analytic expressions for the amplitudes of the perturbations at the interface of the viscous materials subjected to a shock are presented. This research addresses questions of scaling (what parameters affect growth factor), viscosity, strength, compressibility, and nonlinearity. They relate viscosity and strength, as well as a new method that measures viscosity at high pressures and temperatures. When a low-density fluid (ρ_l) accelerates a high-density fluid (ρ_h), the perturbations at the interface will grow exponentially with time as $\eta(t) \sim e^{\gamma t}$. This growth, however, is much slower in fluids with viscosities, as would be expected. Studies of RT instabilities have found applications in geophysical experiments [19]. Likewise, plasticity of metals with strength will exhibit the same stabilizing properties. Metals will not flow unless they are subjected to large pressures, and when they do flow, the growth is much slower than in fluids. Given large pressures and/or a shear modulus for a metal, there exists a critical amplitude η and wavelength λ below which the perturbations will not grow [19]. Similarly, in the RM instability, given a viscous fluid or metal with strength, this suppression of growth will occur. Mikaelian's work discusses the work done in these areas and how viscosity or strength can be used to damp perturbed surfaces. The research concludes that the viscous RM instability in the linear and incompressible regime is well described and that μ has a weaker effect in nonlinear problems. In general, RM experiments that have viscosity will be useful with a smaller amplitude.

1.5.4 Instabilities in Experiments

In ICF, any initial irregularities in the surface of the target may lead to RT or RM instabilities. However, in this research, the goal is to create RT and RM instabilities because they are the observational parameter. The growth of the instabilities is used to correlate to a measure of strength. Therefore, in the experiments and simulations discussed in the succeeding chapters, the idea is to start with a sample that has an initial imperfection in the form of a ripple or wave. These small amplitude perturbations, once impacted, help to initiate growth of the instabilities. The relationship between strength and instability growth is twofold; the growth can be used to quantify the strength, but strength of a material can stabilize or reduce the instability growth. Therefore, while the goal is to further understand strength of materials using the growth as the observational parameter, the resulting knowledge of strength can help lead to advances in ICF target design that use increased strength to avoid the unwanted instabilities.

In simulations, experiments, and theory, instabilities are studied as single-mode perturbations and multimode perturbations. Single-mode means only one initial wavelength is designed into the surface of the sample. Multimode implies that a number of different wavelength modes are present in the initial amplitudes. The RM single-mode case is simpler to model and may provide insight into the interaction of the shock and the interface of the two mediums, along with the resulting perturbations of the initial amplitudes [20]. The RM multimode case provides insight into the nonlinearity of the growth, and serves to represent a more random, realistic model of the types of imperfections and irregularities that may be found at the interfaces of two interacting materials [20].

1.6 High Pressure and Materials Testing Facilities

A range of facilities are available to create conditions of high pressure to perform compression of materials at a range of velocities and pressures. Figure 1.4 shows some of the types of facilities available for impact dynamics.

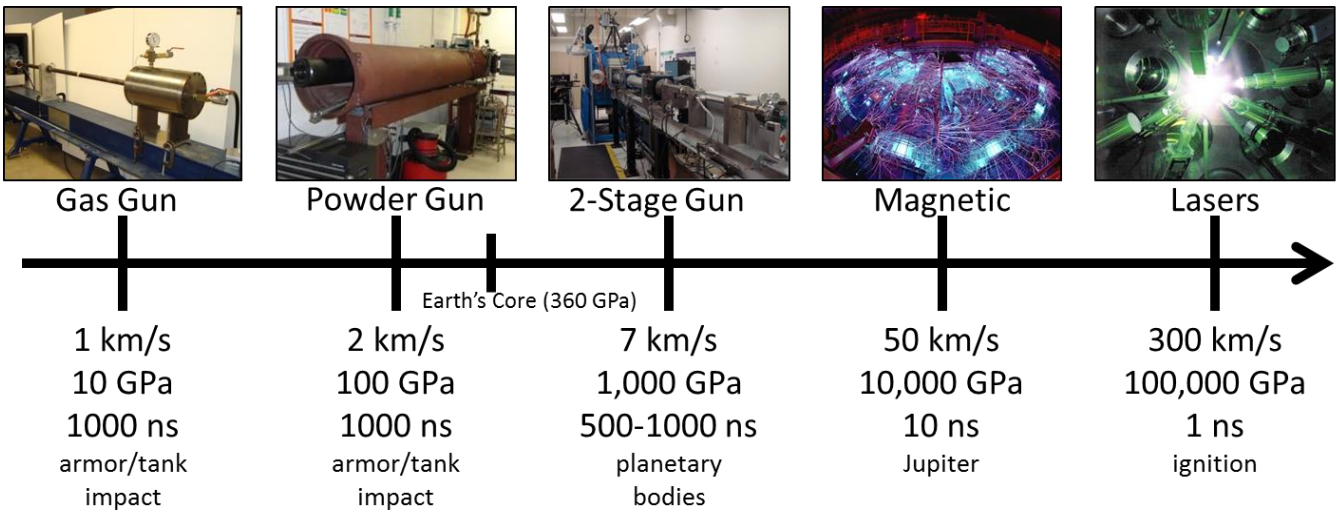

Figure 1.4: Types of facilities used to create high pressure and compression conditions, with velocity, pressure, duration of pulse, and applications.

At one end of the spectrum, gas guns and powder guns are used to study ballistic impacts that have applications in armor and tank impact, as well as the ability to study material behavior for a variety of materials over a range of impact conditions. These types of instruments are far less expensive than higher impact facilities, more accessible, less complex to use, and have relatively fast turnaround times. Gas guns and powder guns, along with 2-stage guns, are more common in a university setting, whereas magnetic and laser facilities are often part of government-funded facilities. At the Graduate Aerospace Laboratories of the California Institute of Technology (GALCIT), a gas gun, powder gun, and 2-stage light gas gun (SPHIR) are all available to study hypervelocity impacts. As a part of this research, the gas gun was used to demonstrate the correlation between strength and ripple growth of instabilities, using ballistic gelatin as the material.

Other types of facilities are available for materials testing, such as Sandia National Laboratory's Z-machine, which is the largest x-ray generator in the world. Its goal is to advance nuclear fusion and it has produced nearly 2 MJ of energy, used to create a magnetic field that implodes a plasma in a target [21]. A new concept called Magnetized Liner Inertial Fusion (MagLIF) is being developed by physicists to perform dynamic materials properties experiments on the Z-machine [22]. The potential for this concept (i.e. magnetic ICF) would be remarkable; however, the concept is struggling because of the presence of instabilities, leading physicists to perform several experiments studying rippled samples and the formation of instabilities [22]. The LANSCE facility at Los Alamos National Laboratory is one of the world's most powerful linear accelerators, capable of accelerating protons to nearly a billion electron volts for a variety of materials testing experiments [23]. For instance, a group of scientists at LANSCE's proton radiography (pRad) facility performed experiments measuring Rayleigh-Taylor growth in metals by driving high explosives into the samples and studying the growth side-on [24].

On the high end of the spectrum, some of the most advanced laser facilities are used to produce 100 Mbar pressures on mm^2 to cm^2 areas. The Omega laser facility, located at the University of Rochester's Laboratory for Laser Energetics (LLE), is used in this research and discussed in Chapter 2. It is one of the most powerful and highest energy lasers in the world, uses a 60-beam ultraviolet frequency-tripled neodymium glass laser, and is capable of delivering 30 kilojoules at up to 60 terawatts onto a target less than 1 millimeter in diameter [25]. LLNL is home to several laser facilities including Janus and Jupiter. LLNL's National Ignition Facility (NIF) is the world's largest laser, uses 192 beams, and is capable of delivering Megajoules of energy to the targets, which is 60 times more than any other facility [26]. The goal of NIF is to achieve inertial confinement fusion in a laboratory setting, but it is also used to perform materials testing at extreme conditions [27].

1.7 Outline

Through both experiments and simulations, this thesis examines the role of Richtmyer-Meshkov instabilities in determining strength of tantalum at high pressures. Chapter 2 discusses the experiments performed at Omega. Within this chapter, the Omega laser facility and its diagnostics are described, followed by a description of the two different types of experimental platforms used in this research (isentropic compression experiments and laser compression recovery experiments). Both single-mode and multimode ripple experiments are covered along with a discussion of the experimental design decisions and expectations. The processes for target fabrication and characterization are described. The last section of the chapter presents the results of the first experiments performed at Omega using the laser compression recovery platform for single-mode ripples. Chapter 3 provides the background for the simulations performed in this research. The optimal transportation meshfree method used in the code is described, along with the engineering model used in the simulations. The components and tools needed to use the code for pre- and post-processing are described in detail, followed by a section on using the code. This section discusses the computational environment used, along with the configuration and parameters used in these simulations, as well as the material and model validation for tantalum. The chapter concludes with the definition and derivation of growth factor. Chapters 4 and 5 present the results of the simulations. Chapter 4 focuses on the results of the RM single-mode simulations and the six tests that were conducted in conjunction with Omega experiments. The chapter concludes with a comparison of the simulations to the experimental data from Omega. Chapter 5 focuses on the results of the RM multimode simulations and the various patterns, configurations, and energies tested. Chapter 5 concludes with a discussion of how the results influenced design decisions for upcoming Omega experiments, and how they will help to predict the results of these experiments. Chapter 6 provides conclusions for the current research, as well as recommendations for how this research can be expanded upon in the future.

Chapter 2

Richtmyer-Meshkov Laser Experiments

The goal of the research outlined in this thesis is to study the strength of tantalum (Ta) at high pressures (> 1 Mbar or 100 GPa) and high strain rates (10^6-10^8 s^{-1}). The strength measurements are made by studying instabilities (Rayleigh-Taylor, Richtmyer-Meshkov) at extreme conditions by using lasers to create such conditions. To create these extreme conditions in a laboratory setting, a high energy laser is used – the Omega Laser at the Laboratory for Laser Energetics (LLE) in Rochester, NY. This section describes the Omega laser, its diagnostics, the experimental platforms utilized, and the different types of experiments and science that can emerge from laser experiments in regards to studying strength of tantalum.

2.1 The Omega Laser

2.1.1 The Omega Facility & High Energy Density Physics

The Omega Laser is located in Rochester, New York at the University of Rochester's Laboratory for Laser Energetics (LLE). LLE was started in 1970 with the objective of investigating the interaction of high-power lasers with matter. The laser facilities at LLE actually consist of two lasers, Omega and Omega EP. Since both are used in experiments and referenced in this research, the facility and lasers will be referred to as Omega or the Omega laser unless a specific laser is mentioned. Research at Omega is ideal for experiments that require high-intensity laser beams. Several of the fundamental studies at Omega involve applications in the field of high energy density physics. These types of experiments use an intense pulse of laser light that focuses to diameters as small as tens of wavelengths of laser light with intensities that can reach 10^{16} W/cm^2 [28]. When a laser pulse with this magnitude of intensity irradiates a solid material, the material quickly becomes a plasma, reaching temperatures of 10^7 K and densities of 10 g/cm^3. The environment created by this plasma provides the ideal setting to study thermonuclear fusion, shock waves, materials science, laboratory astrophysics, spectroscopy of highly ionized atoms, and the fundamental physics of matter under high intensities [28].

To meet the needs of high energy density physics experiments, Omega provides this high-energy irradiation capability. Omega is a 60-beam, 300 KJ laser system which operates at a wavelength of 351 nm. The target chamber is complete with numerous diagnostics that users can take advantage of when performing experiments. High-energy density science research at Omega includes inertial

fusion, plasma physics, laboratory astrophysics, fundamental physics, materials science, chemistry, and biology [28].

In addition to the lasers and diagnostics, users of the Omega facility are able to use supporting labs, computer resources, shop facilities, and other engineering facilities. When using Omega, a team of over a dozen LLE employees operate the facilities and experiments. The scientists and principal investigators involved in the experiments are stationed in a control room where they can direct experimental parameters and specifications to the Omega operators. Users of the Omega facility include the following: Department of Energy (DOE) National Labs: Lawrence Livermore National Laboratory (LLNL), Los Alamos National Laboratory (LANL), and Sandia National Laboratory (SNL). Additionally, other users such as universities can be granted laser time through the National Laser Users' Facility (NLUF) and call-for-proposal opportunities. Users are typically granted one day at the facility to perform "shots" for their experiment. The Omega facility is capable of operating at approximately one shot per hour, making it possible for users to perform several experiments in one day.

2.1.2 System Specifications and Laser Energy Performance

Omega, which operates as a 60 beam system, produces 30 kJ with temporally shaped pulses and peak powers up to 45 TW. The specifications for Omega are shown in Table 2.1. The on-target energy goal is "dictated by the requirement to conduct hydrodynamically equivalent capsule implosions that produce diagnostic signatures sufficient to adequately diagnose the fuel-core performance" [28]. The choice of using short wavelength ultraviolet laser light (351 nm) was because of its historical use a laser-fusion driver. This is because it has enhanced absorption and a low production of hot-electrons. Neodymium (Nd) is a soft metal often used for lasers. Nd:glass was selected as the master oscillator/power amplifier and produces 60 beams of infrared energy (1054 nm). This optical system of converting the beams to UV, which occurs at the end of the amplifier before it is delivered to the target, is called the frequency-conversion crystal (FCC) subsystem [28]. To ensure uniformity of the laser, the system must balance the beam-to-beam energy and each beam must produce a uniform spot on the target. Smoothing techniques are used to optimize this instantaneous uniformity. To minimize the hydrodynamic instabilities in the implosions, which is an important feature of these research interests, the system is capable of producing temporally shaped pulses.

Table 2.1: Omega Specifications [28]

Energy on target	Up to 30 kJ in a 1-ns square pulse
Wavelength	351 nm (third harmonic of Nd:glass)
Lasing medium	Nd-doped phosphate glass
Number of beams	60
Irradiation nonuniformity	1%–2%
Beam-to-beam energy balance	Less than 4% rms on target
Beam-to-beam power balance	<1% @ peak
Beam smoothing	spectral dispersion, polarization & phase smoothing
Pulse shaping	0.1- to 4-ns arbitrary shapes with 40:1 contrast
Repetition rate	One shot/h
Laser and diagnostic pointing	Any location within 1 cm of chamber center

Laser-energy performance is critical to experiments. Table 2.2 summarizes the energy performance of Omega assuming a 1.0 ns square pulse. Other UV pulse shapes are available for experiments. However, UV power is very dependent on shape because the conversion to UV is a nonlinear, intensity dependent process. Therefore, Omega laser performance is optimized using a 1 ns square pulse, meaning that the maximum UV energy will be delivered to the target with a 1 ns square pulse. In the Table 2.2, the performance is given for two cases: the first is for no SSB bandwidth and the second is for a 1.0 THz SSD bandwidth, assuming nominal peak power for the system and optimal IR to UV conversion. SSD or smoothing by spectral dispersion is one of the smoothing techniques used to ensure uniformity of the energy by modulating the wavelength of the master-oscillator pulse [28].

Table 2.2: Energy Performance of Omega with a 1.0 ns Square Pulse [28]

	No SSD bandwidth	1.0-THz SSD
Peak power of main pulse	31.2 TW	23.8 TW
UV energy on target (kJ)	31.2	23.8
UV energy after FCC (kJ)	35.2	27
Average fluence after FCC (J/cm2)	1.13	0.87
Peak fluence after FCC (J/cm2)	2.02	1.55
Conversion efficiency	70%	55%
IR energy before FCC (kJ)	50.4	50.4
IR avg. fluence before FCC (J/cm2)	1.59	1.59
IR peak fluence before FCC (J/cm2)	2.84	2.84

2.1.3 Diagnostics

Omega contains a large suite of diagnostics. Below is a list of the diagnostics that are available in the facility [28, 29].

- Charged-Particle Diagnostics
    - Magnet-based charged-particle spectrometers
    - Wedge-range-filter proton spectrometers
    - High-areal-density wedge-range-filter spectrometers
    - Proton temporal diagnostic
- X-Ray Imaging
    - X-ray pinhole cameras
    - X-ray framing cameras
    - Kirkpatrick–Baez microscopes
    - Gated monochromatic x-ray imager (GMXI)
    - CID-camera readout system
- Optical Streak Cameras
- X-Ray Streak Cameras
- Time-Resolved Hard-X-Ray Detector
- Hard-X-Ray Spectrometer
- Pinhole-Array X-Ray Spectrometer
- Neutron Diagnostics
    - Activation detectors
    - Neutron time-of-flight detectors
    - Neutron temporal diagnostic
    - Neutron bang-time detectors
    - Neutron magnetic recoil spectrometer
- Full-Aperture Backscatter Stations
- Near-Backscatter Imaging
- X-Ray Backlighter Capabilities
- Short-Pulse Backlighter Development
- Velocity Interferometry System for Any Reflector (VISAR)
- Streaked Optical Pyrometer
- Cryogenic-Target Characterization Diagnostic

In addition to Omega's target diagnostics, there are a number of diagnostics that were developed by external users. Many of these are available for all users. In the isentropic compression experiments, a diagnostic called Dante is used which is a time-resolved x-ray spectrometer. This was developed by LLNL but is used on nearly all the experiments to measure x-rays through filters. For a more complete list, along with details on the capabilities of the target diagnostics, the National Laser Users' Facility (NLUF) Users' Guide is a good resource.

2.2 Experimental Setup

Two types of experimental setups exist for performing strength experiments in laser facilities based on the loading of the sample: (i) indirect drive and (ii) direct drive. The goal of these experiments is to study the strength of metals at high pressures (>1 Mbar) and high strain rates ($>10^6$ s^{-1}). In the current experiments, the focus is on studying tantalum, though the technique itself is applicable to the study of any solid. The experimental platforms for studying strength using instabilities were developed over the last few years by the team at LLNL and have been used to study a wide range of metals [30, 31, 32, 33]. To study the strength of metals at high pressures, a quasi-isentropic ramped drive is used, consisting of a reservoir-gap-sample configuration (see Figure 2.1) which is referred to as indirect drive [34]. These experiments can be performed at high energy laser facilities such as Omega and NIF. The objective of such experiments is to gain a better understanding of the strength of the metals being studied, to learn about the growth related to the Rayleigh-Taylor instabilities (RTI), and to potentially stabilize or reduce the RTI growth via the material strength [35, 36]. This is done by measuring the growth of the Rayleigh Taylor instabilities, which is accomplished by putting a well characterized ripple in the material and measuring the growth of the ripple using either face-on radiography or post-mortem characterization of the ripples [30, 32]. In the direct drive configuration, the laser directly impinges on the ablator which launches a ramped shock into the material of interest [37]. The specimens can be recovered for microstructural and other post-mortem characterization by catching the sample in a soft capture media in a recovery tube.

By performing such experiments that study deformation under compression, one can learn about macroscopic and microscopic properties of materials subjected to very high pressures and strain rates [36, 38]. The macroscopic properties of the material that are of interest include strength, spall strength, ductility, and work hardening. The microscopic characteristics that are of interest include crystal structure at high pressures, phase transformations, deformation, and failure mechanisms including dislocations, twinning, and void formation among others.

2.2.1 Indirect Drive

The indirect drive technique is based on a laser-driven high pressure platform used to compress materials under near isentropic conditions by using ramp compression [34]. The ripple sample is driven by a ramped drive from a reservoir-gap-sample configuration [39]. The ripple growth from the Rayleigh-Taylor instability (RTI) is measured using face-on radiography. The observational parameter is the RTI. Following the experiments, the growth measurements are compared with constitutive strength models. Figure 2.1 shows the experimental setup:

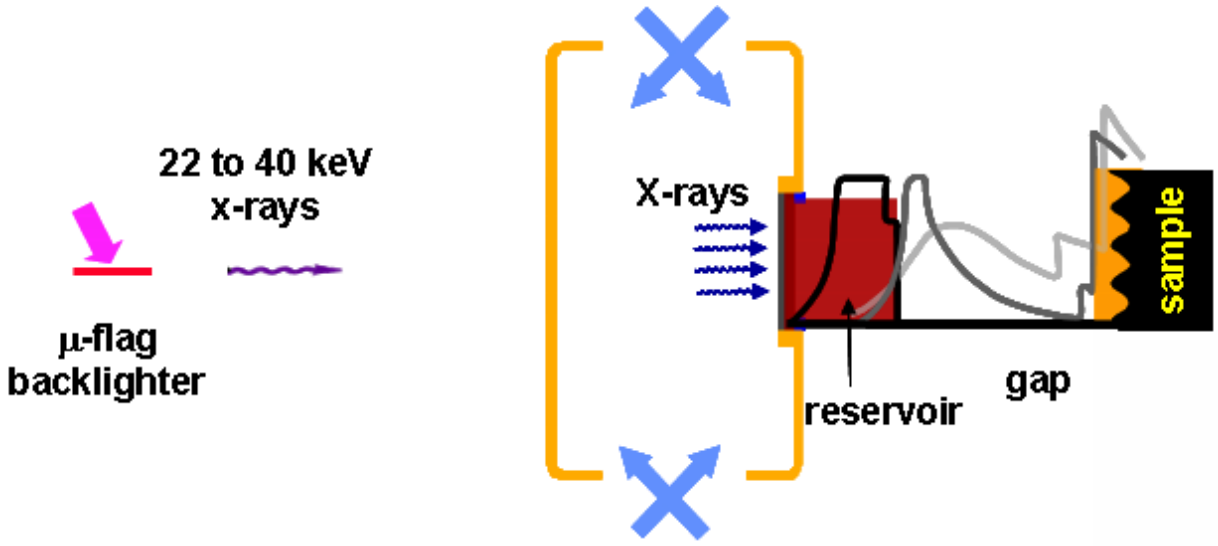

Figure 2.1: Experimental Platform to test materials at high pressures; up to 20 kJ of laser energy creates a ramp drive in a reservoir-gap configuration that is mounted on the side of a hohlraum [30].

In the above illustration, the laser energy (represented by the blue arrows) is directed into a hohlraum. Upon exiting the hohlraum, the laser (up to 20 KJ of laser energy) drives a strong shock through a low-Z reservoir, which unloads across a vacuum gap and stagnates on the sample [39]. This generates a nearly isentropic pressure profile in the sample.

The parameters of the reservoir-gap-sample configuration can be adjusted based on the needs of the experiments and the materials being used. However, after several successful sets of experiments, certain parameters are kept the same because they work efficiently. The following is an example of the materials, spacing, and other parameters used for the reservoir, gap, sample, and backlighter [30, 31, 32, 33].

- Reservoir
  - 25 μm thick beryllium ablator
  - 200 μm thick 12.5% bromine-doped polystyrene
- Gap
  - 400 μm gap
- Ta sample
  - 50 μm mean substrate thickness
  - preimposed sinusoidal ripple on the driven side
  - wavelengths of 50 to 100 μm and 2 μm amplitudes
  - sample backed by a 100 μm thick LiF tamper
- Backlighter
  - ripple growth measured by face-on radiography
  - to probe thickness of sample, a high energy backlighter was developed using high-intensity short pulse lasers

- for Omega experiment, 22 keV energy was optimal to produce best contrast from the ripples
- since ripples are 1-D features, a micro-flag edge-on a 1-D x-ray source aligned to ripple orientation is used to generate a bright x-ray source

Omega Experiments Using this Platform

Figure 2.2 contains two plots that show the types of results that can come from these Omega experiments. The first plot shows how the growth of the ripple is measured, and that the growth is substantial. The other plot has Omega data points alongside various strength models to show how they compare [30].

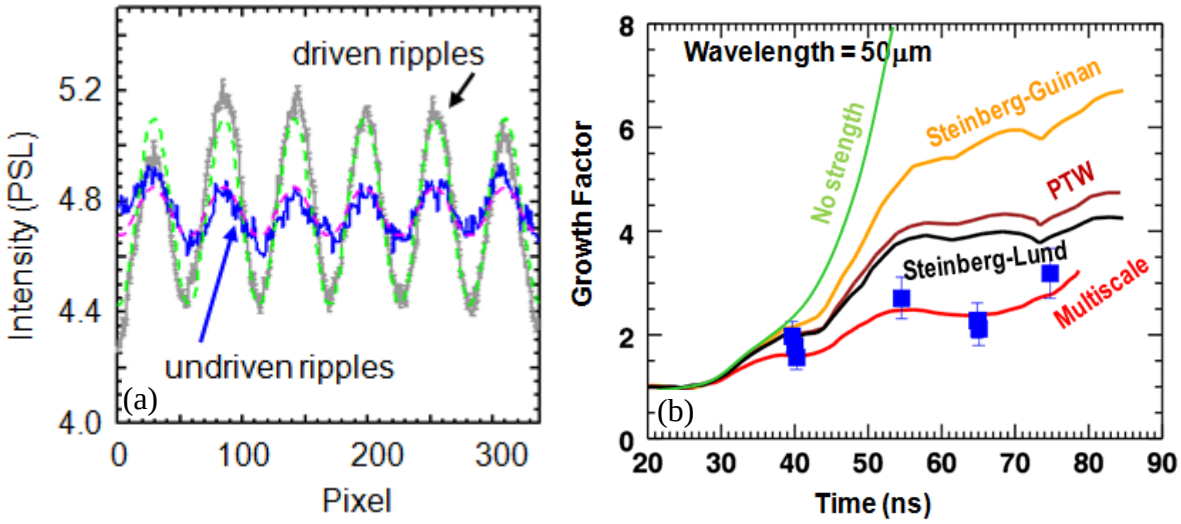

Figure 2.2: (a) Lineouts of the driven and undriven ripples from λ=50μm ripple region. The driven ripple growth is evident; (b) Ta Rayleigh-Taylor growth factors as a function of time. Omega data points are the blue squares. Various material strength models are plotted for comparison [30].

The goal of this section has been to illustrate the experimental platform typically used at Omega to test material strength. Different groups may test strength in other ways, and as seen in the following section, a new method has been developed that makes performing experiments more accessible to universities such as Caltech by riding alongside existing experiments.

2.2.2 Laser Compression Recovery Experiments (Ride-along)

This section discusses the "ride-along" setup used in this study. This serves as the experimental platform for Omega experiments that can study strength of metals at high pressures via the Rayleigh-Taylor or the Richtmyer-Meshkov instabilities. These ride-along experiments are also referred to as laser compression recovery experiments. At Caltech, these efforts were led by Dr. Aaron Stebner. The design and development of the ride-along setup is a joint collaboration between LLNL, Caltech, and General Atomics (GA). The idea of the "ride-along" is to be able to perform

experiments as a secondary experiment alongside an existing primary experiment by diverting one of the primary experiment's unused beams to a separate target.

The objective of the ride-along setup is to create an experimental platform to characterize the strength of metals at pressures greater than 1 Mbar. This is a new platform that can study both RM and RT instabilities. The purpose of these laser compression recovery experiments is to characterize instabilities, yield strength, and phase transformations at high pressures. This new platform has been and will continue to be used on experiments on Ta, and eventually Fe. To design future experiments and to analyze or predict the results of these experiments, two different codes are utilized: the Eureka code of the Michael Ortiz group, and the 1D hydrodynamic software (Hyades), both of which are discussed in Chapter 3. Through combined analysis of the numerical and empirical data, fundamental understanding of Ta & Fe strength at high pressures as it correlates to the development of RT and RM instabilities, yield strength, and phase transformations will be advanced. In this research, only Ta strength is studied. However, it is important to note that this setup can be used in the future for studying a variety of metals at high pressures, including Fe.

Experimental Platform – The "Ride-Along" Recovery Tube

To perform these ride-along experiments, the platform had to be designed. The basis of the new experimental platforms is a universal "ride-along" recovery tube. The reusable recovery tubes accommodate both RM and RT target stack configurations developed by the LLNL team for studying strength of materials at high pressure. The tubes are designed to allow these experiments to "ride-along" next to a primary experiment that does not require all 60 of Omega's beams. The tube geometries do not interfere with the primary experiment, and one of the unused beams is used to drive a shock wave through the target. Aerogel catchers enable post-shot target recovery and analysis.

Figure 2.3 is a cross section of the recovery tube followed by 3D CAD models of the recovery tube. The recovery tube itself has a retainer ring at the end where the target stack is held. Inside the recovery tube is the catcher. The catcher material is aerogel with a density of 50 mg/cc. The catcher has to be just the right density such that it catches and recovers the target upon impact without letting it fly through it, but not so hard that it breaks the target. The other end of the recovery tube is fitted with an adaptor that connects to the Nova Mount such that the tube can be used on Omega. The recovery tube, adaptor, and retaining ring were all modeled at Caltech using the 3D CAD program SolidWorks, and machined and assembled at Caltech. The Nova Mount was designed and constructed by LLNL. The targets were constructed at GA.

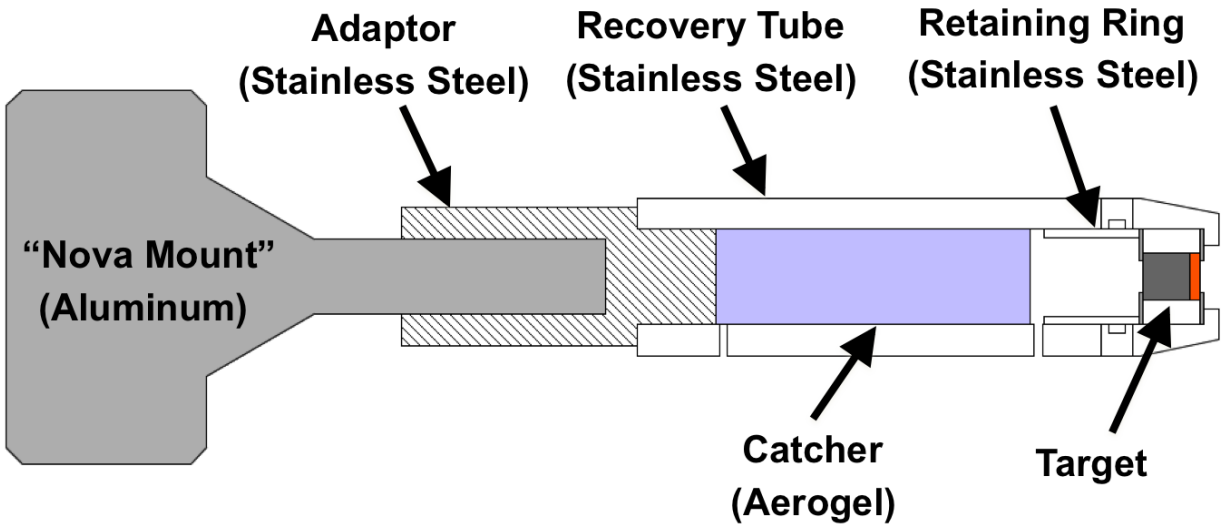

Figure 2.3: Cross-section of the recovery tube used in the ride-along experiments. These tubes allow the experiment to "ride-along" next to a primary experiment, in which one of the unused beams is used to drive a shock wave through the target. The aerogel catcher is used to recover the target for post-shot analysis.

Figure 2.4: 3D CAD models of the recovery tube parts, including the nova mount adaptor, the recovery tube, the target retainer ring, and the washers. These parts were modeled, machined, and assembled at Caltech.

The targets are secured within a target stack that is mounted on the end of the retainer ring. The target stacks can be constructed such that either RT or RM instabilities can be studied. See the two illustrations in Figure 2.5 for the RT and RM target stacks.

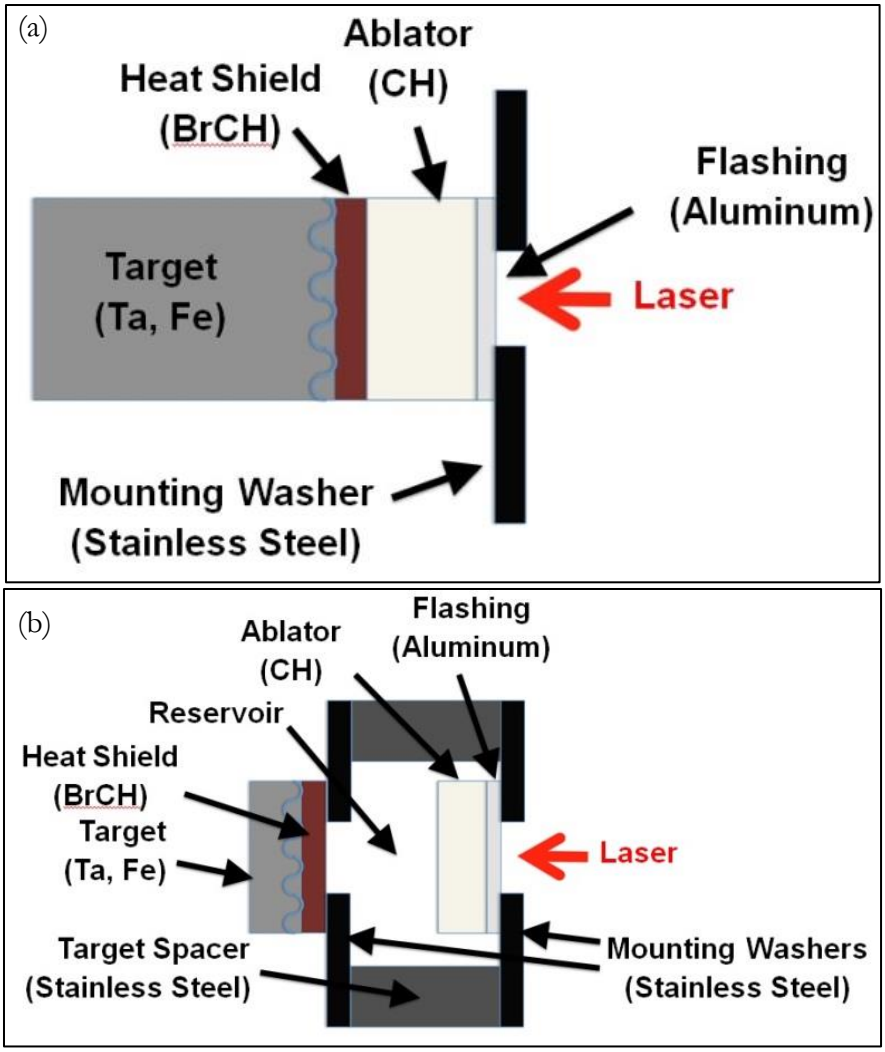

Figure 2.5: Cross sections of target stacks: (a) RM Target Stack, (b) RT Target Stack.

Experiment Design via Simulations

Experiments are designed by calibrating simulations to drive shots of similar heat shields and ablators and then predicting peak pressure and ripple growth as a function of laser energy. Hyades simulations are run first to match the VISAR/drive information to produce profiles of pressure, velocity, and temperature. Hyades is a radiation hydrodynamics simulation code for the design and analysis of laboratory high energy-density experiments created by Jon Larsen of Cascade Applied Sciences Inc. 1D Hyades simulations are calibrated to VISAR measurements, then used to design

ablators, heat shields, and laser energies. In calibrating 1D hydrodynamic simulations, VISAR velocity profiles and breakout times at the rear surface of samples are matched. Once calibrated, the 1D software is used to calculate pressure, velocity, and temperature profiles at the Heat Shield – Ablator (RM) or Heat Shield – Reservoir (RT) interface for laser energies that correspond to peak pressures of 0.500 – 3.500 Mbar in the targets.

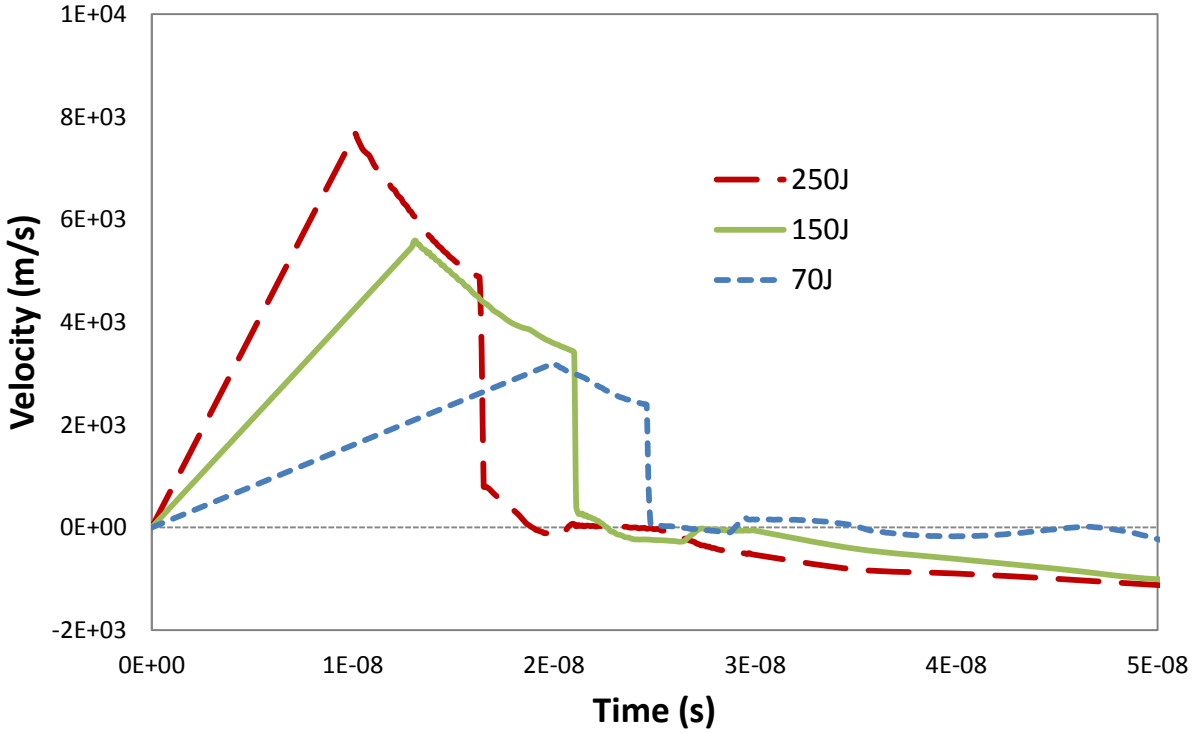

Figure 2.6: Velocity Profile output from Hyades used as input into Eureka. Hyades simulations are calibrated to VISAR and used to determine laser energies.

Ride-along Experiments

The ride-along platform has been used in recent Omega experiments and will continue to be used alongside Omega experiments in the future. In this research, the first experiment that utilized the ride-along platform is discussed. These experiments took place in April 2013 and the results are presented in Section 2.4. These experiments studied strength via the RM instability on Ta targets using a single wavelength rippled surface. The ride-along platform will also be used in upcoming experiments that study both Ta and Fe targets using a multimode ripple pattern. The purpose of the multimode is to study the non-linearity of the ripple growth. The modes will grow independently when deformation is linear, and will couple when in the non-linear growth regime. More details on the theory behind the multimode ripple are in Section 2.3.2. Figure 2.7 shows the pattern used for the multimode ripple targets.

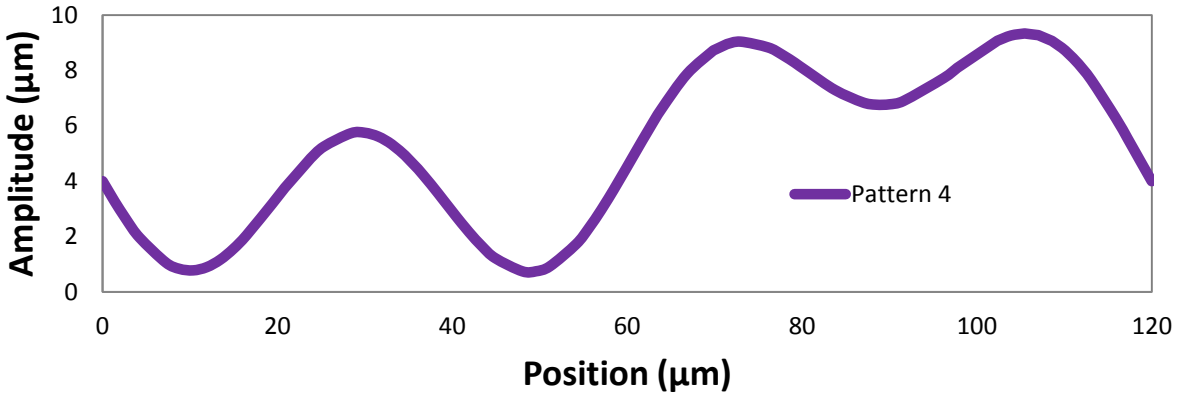

Figure 2.7: Multimode pattern used for the ride-along experiments.

The equations for the three-mode pattern are below, along with the maximum angle-of-descent.

$$\eta_{Pattern4}(x) = 2.5\sin\left(\frac{2\pi}{40}x + \frac{\pi}{3}\right) + \sin\left(\frac{2\pi}{60}x + \frac{\pi}{2}\right) + 3\sin\left(\frac{2\pi}{120}x\right) \quad (2.1)$$

$$\theta^{max} = 31° \quad (2.2)$$

The results from the ride-along experiments are presented in Section 2.4. This experiment was modeled and simulated using Eureka and an engineering model. This is discussed more in the following chapters.

2.3 Experimental Configurations

Prior to any experiment at Omega, several design decisions have to be determined months in advance. Fabrication is a timely process that must be done ahead of time, therefore design decisions must be made even sooner. Design decisions are guided by the science objectives one is hoping to gain from the experiment. The previous section discussed the two different types of experimental platforms used to study strength at Omega. This section discusses the two different types of targets that used in this research (single-mode ripples vs. multimode ripples). This section also discusses the experimental selections that are made for experiments and what type of scientific objectives the experiments are trying to obtain. Target fabrication is also included in this section, followed by an overview of the different experiments (or campaigns) that were performed in collaboration with the LLNL team to study strength of tantalum at Omega.

2.3.1 Single-Mode Ripples

To measure strength of tantalum at high pressures and strain rates, the observational parameter is the growth of the Rayleigh-Taylor instability or the Richtmyer-Meshkov instability. To do this at

Omega, targets are designed with a ripple in the material, and the growth of this ripple is measured. In the experiments, the growth is measured using face-on radiography. By measuring the growth of these ripples, a growth factor is obtained based on the initial and final amplitudes of these ripples. These growth factors are then compared to predictions from strength models such as Preston-Tonks-Wallace (PTW) or Steinberg-Guinan (SG). These can also be compared to different multiscale or engineering models such as the Caltech Eureka models.

The images in Figure 2.8 show the rippled targets. The amplitude and wavelength of the targets can be changed for each experiment. The ripple has a wavelength of 50 μm and an amplitude of 2 μm.

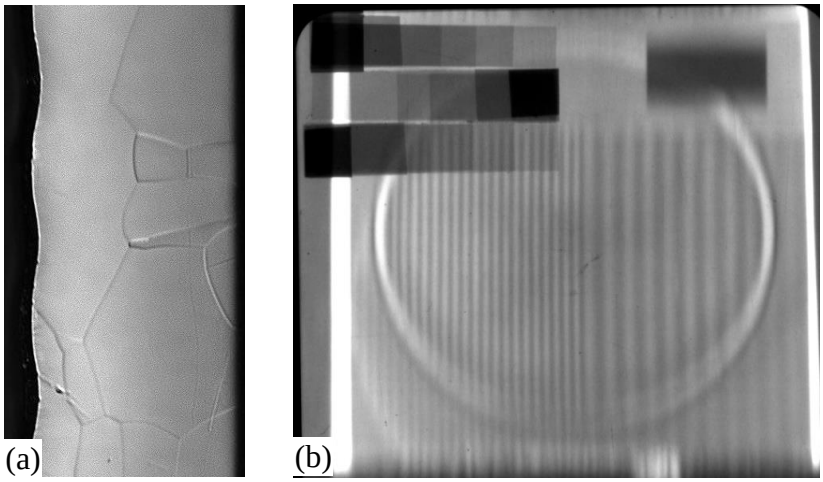

Figure 2.8: Rippled Targets: (a) Profile view of a rippled Ta target with λ = 50 um, η=2 um; (b) Face-on view of rippled target [30, 40].

2.3.2 Multimode Ripples

Background

The previous sections described experiments that were used to study and characterize the strength and behavior of metals that consisted of single-mode ripple patterns. This section discusses the use of multimode ripple patterns in experiments and simulations. Multimode patterns are introduced to study whether or not the drive exhibited linear versus nonlinear instability growth. In the linear region, the modes will grow independently; however, the modes will become coupled when in the nonlinear region [41]. Studying multimode patterns provides the ability to study both regions.

Theory

Based on Remington's study of single-mode and multimode RT experiments [41], there exists a good understanding of the evolution of the perturbations in RT experiments. Experiments have

been conducted with surface perturbations of single-mode, two-mode, and eight-mode sinusoids. The surface is perturbed by a shock transit phase. During this phase, the perturbations begin to grow, and exhibit Richtmyer-Meshkov (RM) instability-like dynamics. Next, the shock breaks out, and the perturbations continue to grow but exhibit Rayleigh-Taylor (RT) instability-like dynamics. During this RT region, while the growth is linear, a single-mode perturbation will grow exponentially in time. Once it becomes nonlinear, the perturbation will not grow as much and the sinusoidal shape of the perturbation may start to look more like a "bubble and spike", more similar to the typical "finger" visual representation given to the RT instability. However, for multimode perturbations, during the linear region, each individual mode will grow independently, but once in the nonlinear region the modes will become coupled. This coupling also results in $k_i + k_j$ "beat" modes, which result in the perturbation changing shape to broader, flatter bubbles and narrower spikes [41].

There are essentially three phases in the development of a single-mode perturbation [41]. The first phase comes when the drive pushes an initial strong shock through the material. The shock front will likely be deformed and will exhibit any imperfections that may have been found at the surface. The rippled shock front traveling through the material will resemble the RM instability. As it continues, the shock travels at different velocities depending on the thickness of the material, and the shape of the shock front will not be constant and will evolve with time. The second phase comes when the shock breaks out of the material and the compressed target accelerates. The growth of the perturbations continues now as RT instabilities. The growth is linear and the perturbation will grow exponentially. In the third phase, the perturbations will become nonlinear and will saturate, and the shape changes from sinusoidal to "bubble and spike." The three phases mentioned are characteristic of single-mode initial perturbations. However, when multiple modes are present at the start, the growth will evolve differently. The first two phases are similar, but once the perturbations enter the nonlinear region, the modes will become coupled, which results in the $k_i + k_j$ "beat" modes as mentioned before. This results in wavelengths that are longer and shorter (the bubbles are broader and flatter and the spikes are narrower), and affects the saturation of the individual modes [41]. Remington's paper discusses the experimental support for the three phases of the single-mode behavior, and initiates the evidence for the multiple-mode behavior (via two-mode and eight-mode configurations) through experiments and computations.

Multimode in Omega Experiments

Multimode patterns have been used in Omega experiments using the isentropic compression experimental platform. In the upcoming months, multimode patterns will be used via the ride-along experimental platform discussed previously. Chapter 3 and 5 discuss in great detail the simulations for the multimode ripple tests performed. The goal of the simulations was to help determine which multimode pattern to use and which energies to test on the day of the experiment. In general,

whether single ripples or multimode ripples are being used, the target fabrication and experimental platform remains the same. Only the surface of the target is changed. The multimode pattern does affect the simulations that need to be run and some of the post-processing after the experiments.

Multimode Design

Selecting the right multimode pattern must be be done months before the Omega experiments. The targets have to be coined ahead of time, so the pattern must be decided ahead of time. The Eureka simulations were critical in designing the multimode pattern for the the Omega experiments. More on the simulations for the mutlimode pattern can be found in Chapter 5. This section serves to illustrate the process for selecting the multimode pattern.

Originally, four-mode patterns were tested, as shown in Figure 2.9. Three different patterns were tested by modeling the ripples in Solidworks and running simulations in Eureka.

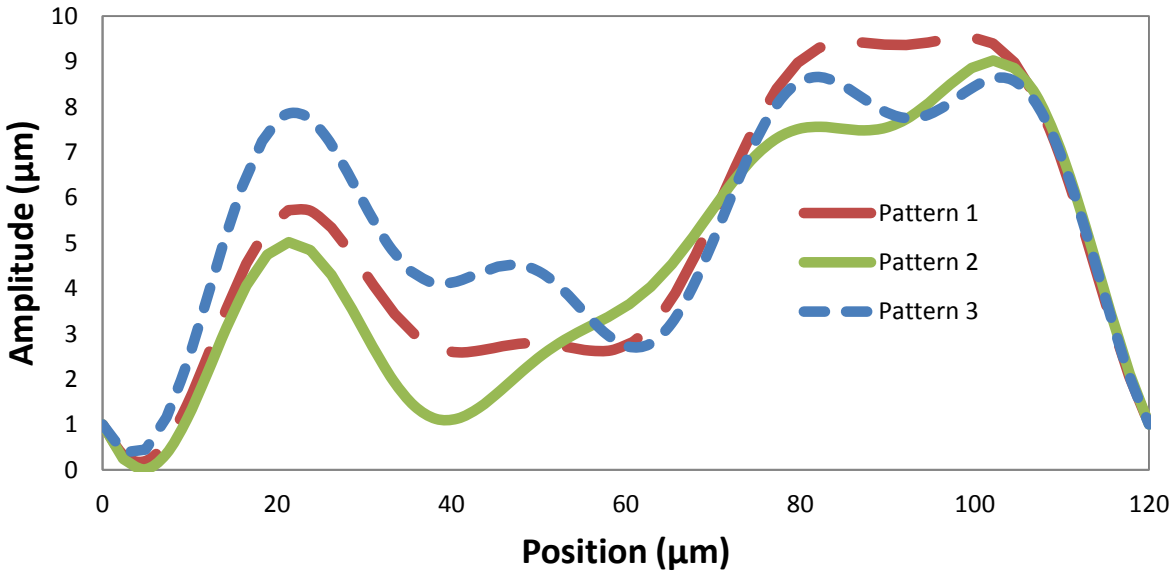

Figure 2.9: Three different four-mode patterns tested.

The three different equations for the four-mode patterns are below.

$$\eta_{Pattern1}(x) = \sin\left(\frac{2\pi}{30}x + \frac{\pi}{4}\right) + \sin\left(\frac{2\pi}{40}x + \frac{\pi}{3}\right) + 2.5\sin\left(\frac{2\pi}{60}x + \frac{\pi}{2}\right) + 3\sin\left(\frac{2\pi}{120}x\right) \quad (2.3)$$

$$\eta_{Pattern2}(x) = \sin\left(\frac{2\pi}{30}x + \frac{\pi}{4}\right) + 1.5\sin\left(\frac{2\pi}{40}x + \frac{\pi}{3}\right) + 1.5\sin\left(\frac{2\pi}{60}x + \frac{\pi}{2}\right) + 3\sin\left(\frac{2\pi}{120}x\right) \quad (2.4)$$

$$\eta_{Pattern3}(x) = 1.5\sin\left(\frac{2\pi}{30}x + \frac{\pi}{4}\right) + \sin\left(\frac{2\pi}{40}x + \frac{\pi}{3}\right) + 2.5\sin\left(\frac{2\pi}{60}x + \frac{\pi}{2}\right) + 1.5\sin\left(\frac{2\pi}{120}x\right) \quad (2.5)$$

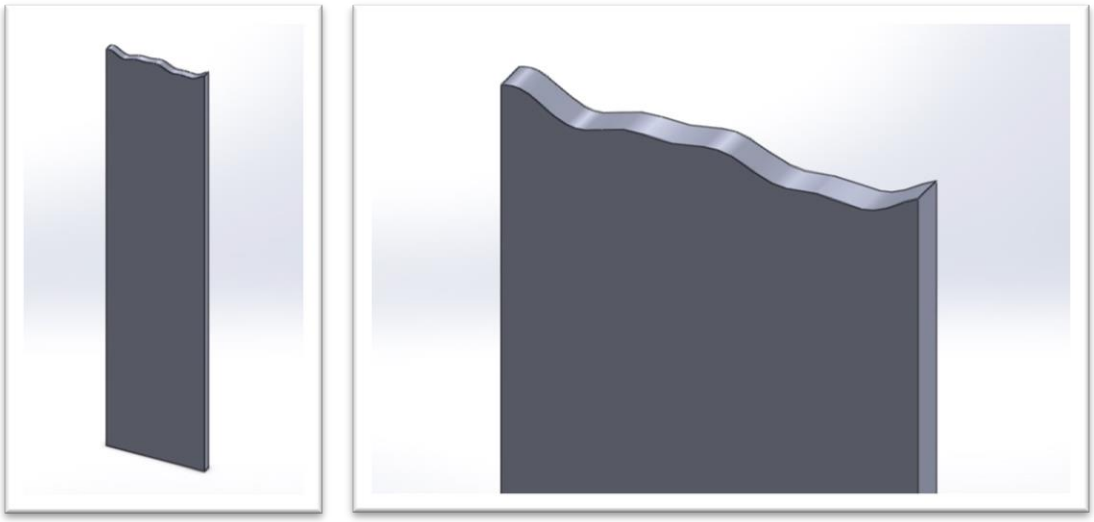

Figure 2.10: SolidWorks models for one of the four-mode ripple patterns; the image on the left is the entire model; the image on the right is zoomed in to show the rippled surface.

However, it was decided that the four-mode target patterns should be excluded, because during the simulation analysis it was difficult to dechipher the different modes. Next, three-mode patterns were tested, with the idea that this would make manufacturing and post-deformation analysis more realistic.

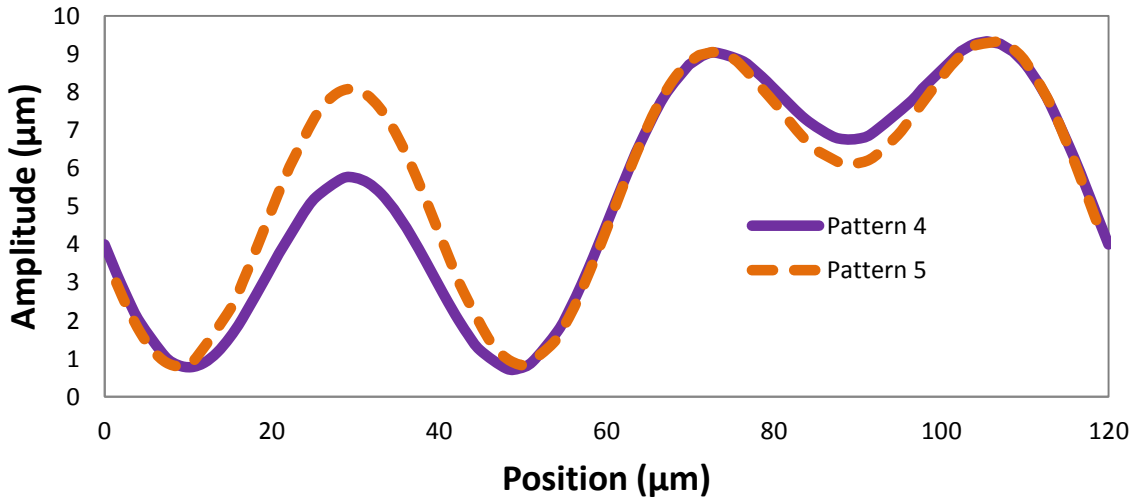

Figure 2.11: Two different three-mode patterns tested.

The two different equations for the three-mode patterns are below, along with their respective maximum angle-of-descent boundaries.

$$\eta_{Pattern4}(x) = 2.5sin\left(\frac{2\pi}{40}x + \frac{\pi}{3}\right) + sin\left(\frac{2\pi}{60}x + \frac{\pi}{2}\right) + 3sin\left(\frac{2\pi}{120}x\right) \quad (2.6)$$

$$\theta^{max} = 31° \quad (2.7)$$

$$\eta_{Pattern5}(x) = 3sin\left(\frac{2\pi}{40}x + \frac{\pi}{3}\right) + 1.5sin\left(\frac{2\pi}{60}x + \frac{\pi}{2}\right) + 2sin\left(\frac{2\pi}{120}x\right) \quad (2.8)$$

$$\theta^{max} = 34° \quad (2.9)$$

The three-mode designs were based off fabrication criteria of maximum peak-to-valley amplitude of no more than 10 um. Simulations on the two patterns showed that either would be analyzable post-deformation. Therefore, the decision of which pattern to use was based on manufacturing. The first of the two patterns shown above has a slightly lower slope or angle-of-descent, making it easier for GA to manufacture and characterize pre-shot. Figure 2.12 is an image of one of the final coined multimode targets for the Omega experiments.

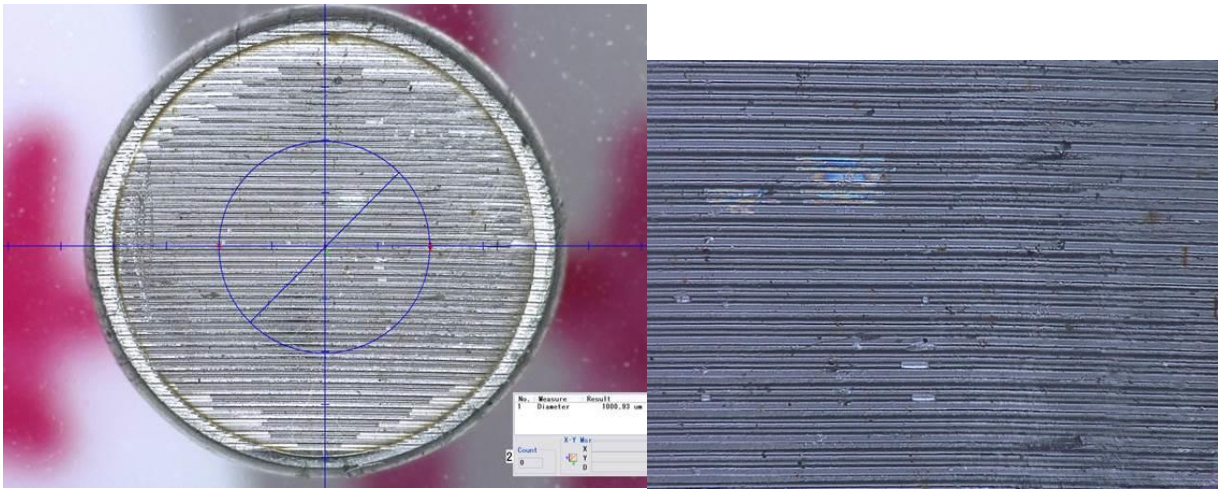

Figure 2.12: Multimode Target Pre-Shot.

Due to the small size of the ripples in the multimode patterns, it is difficult to see from the above pictures what the pattern looks like. To ensure they were coined correctly, Wyko scans were performed, as shown in the Figure 2.13.

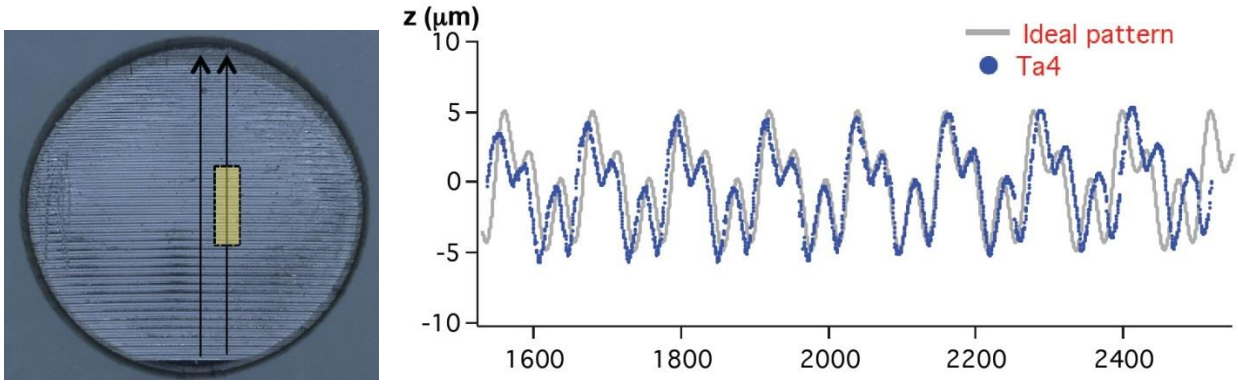

Figure 2.13: Scans of multimode targets after coining but before experiments.

2.3.3 Experimental Selections

Material Selection

Tantalum is an ideal metal to use because of its high density, high melting point, and relatively high ductility. Ta was also selected as a material because of its interest to the impact engineering area and because of its common use in academics and research, therefore data exists for it. Additionally, this material was selected because of its heritage use with the LLNL team that these experiments are done in collaboration with. As discussed in the HEDLP meeting with the collaborators of this research, Ta is a sensible material to use. It is a simpler, easier to model material, and is easily attainable from various sources. Also, Ta is a material that GA has worked with and can coin/stamp such that targets can be manufactured. There is also a parameter that the material can be harder than nitride steel. Ta can also be obtained in different grain sizes, which makes for an interesting study to see how grain size affects dynamics properties [42]. When selecting the material, different parameters, in addition to grain size, had to be considered, such as thickness. If the material is too thick, it is hard to coin. If it is too thin, it becomes brittle or will not show deformation. The geometry for the targets was decided based on the designs tested and proved to exhibit growth by the LLNL team, in combination with the design used by the Harvard team in a similar set of experiments. This design (for the single ripple, that is) is a 50 μm wavelength with a 10 μm peak-to-valley amplitude. In the future, other materials such as magnesium (Mg) and tungsten (W) are being considered. In the past, vanadium (V) has been used. The current work is focused on Ta and Fe. Fe is interesting because of the phase transition that occurs. Although some work has been on Fe, this research focuses solely on Ta.

Strength, Mechanics, and Materials Science

These experiments were ultimately performed to test the strength of metals at extremely high pressures. However, other mechanics and materials science research can come from these experiments. For instance, size scales will affect the mechanics of dislocation propagation, dislocation density, and density growth; all of these aspects affect strength [43]. Therefore, it is interesting to look at the effect of these different size scales (grains, specimens, defects) in the experiments. Dislocation dynamics is an interesting facet of this research. By looking at the microstructure, one can gain a better understanding of these dynamics, including thermal activation of dislocations (i.e. non-shock loading) and phonon drag (i.e. shock regimes). This is important to understanding the relationship between dislocation density and strain rates. In the experiments, it is not clear how a driven sample spreads its mass and velocity. This is something that modeling capabilities such as the simulations can provide. Another issue could be the temporary loss of order to the crystal structure on diffraction. Diffraction experiments and grain size effects have been

studied in some of the Omega Ta experiments, to see how they affect the yield strength. Since the size scale of these experiments is relatively fixed, the only way to compare would be to look at bulk Ta work done by others. Therefore, it is necessary to be conscious of these size effects, but keep the focus on studying strength and the mechanics of the RT instability.

In Figure 2.14, the start of the time represents the start of the laser. The laser illuminates the hohlraum and then the ablator/reservoir/gap. Here, at around 17 ns, is where the plasma drive arrives in front of the heat shield and Ta ripple sample. This time is significant because if it takes a longer time for the laser to arrive at the sample, then the shock wave has been degraded by some amount [44]. This time parameter is used because it is difficult to quantify a strain rate in these experiments, since the shock profiles vary due to the ablator and heat shield. Using simulations and experiments at Caltech, the mechanical characterization for these experiments is thus improved. The main focus, though, is to understand the mechanical properties that affect ripple growth, and how that relates to strength.

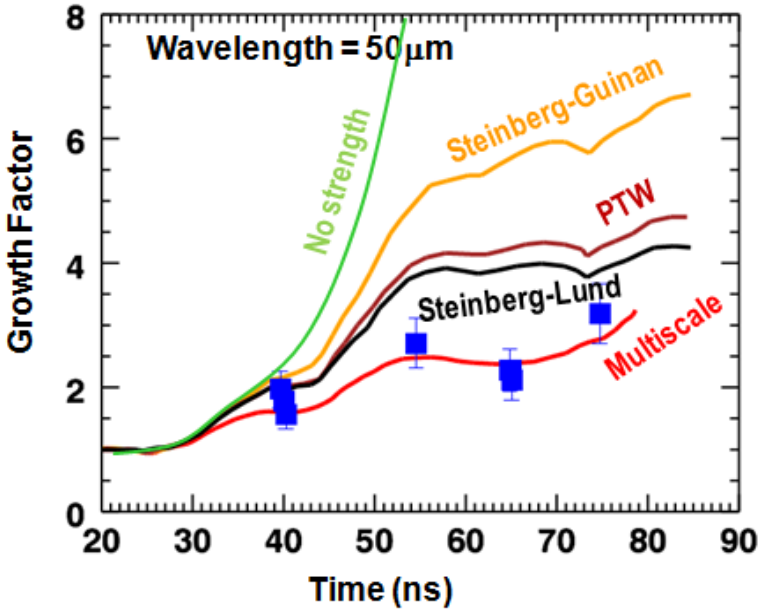

Figure 2.14: Ta Rayleigh-Taylor growth factors as a function of time. Omega data points are the blue squares. Various material strength models are plotted for comparison [30].

2.3.4 Target Fabrication & Characterization at General Atomics

Fabrication of Rippled Metals for Viscous Plastic Flow Studies

Target fabrication is a critical part of the experimental process for Omega. The small size of the targets makes them difficult and expensive to manufacture. General Atomics (GA), a company in San Diego, makes the targets. The rippled surfaces are coined by GA into targets and characterized pre and post shot. Both single and multimode ripple patterns are designed and coined into the driven surface of Ta targets. Deformation of the ripples and changes in material microstructure are

used to characterize the material strength and deformation mechanisms. Deformation of multimode targets are used to assess if the drive remained in the linear vs. nonlinear instability growth, as the modes grow independently in the linear regime, but become coupled in the nonlinear regime. As discussed, different multimode patterns were tested in Hyades and Eureka. Running simulations on the patterns helps to determine which one to coin into targets. Due to the expense and limit of shots on experiment days, only one multimode pattern is coined.

The goal of the fabrication is to produce rippled metals by micro-coining. The typical target specifications are for a metal foil thickness of ~ 1000 μm, a peak-to-valley amplitude of ~ 10 μm, and a wavelength of ~50 μm, with those parameters shown in Figure 2.15. The following procedures are performed by General Atomics and led by Greg Randall, who provided the resources [45]. The Caltech effort was led by Aaron Stebner of Caltech who also provided resources [46].

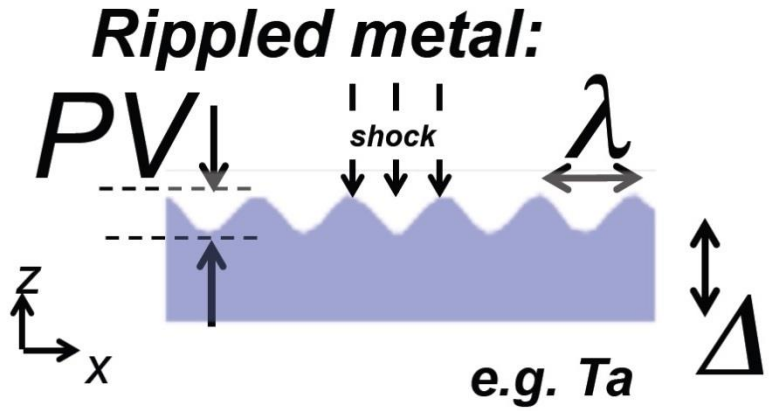

Figure 2.15: Ripple target with parameters labeled

Pre-shot micro-coining of the ripples is performed. Surface profiles of the coined metal indicate how well the pattern was transferred from a die. To obtain full pattern transfer, many parameters are important, such as the metal's thickness, hardness, texture, and work hardening behavior. The actual fabrication of the target involves many components. Figure 2.16 depicts the different layers of the target.

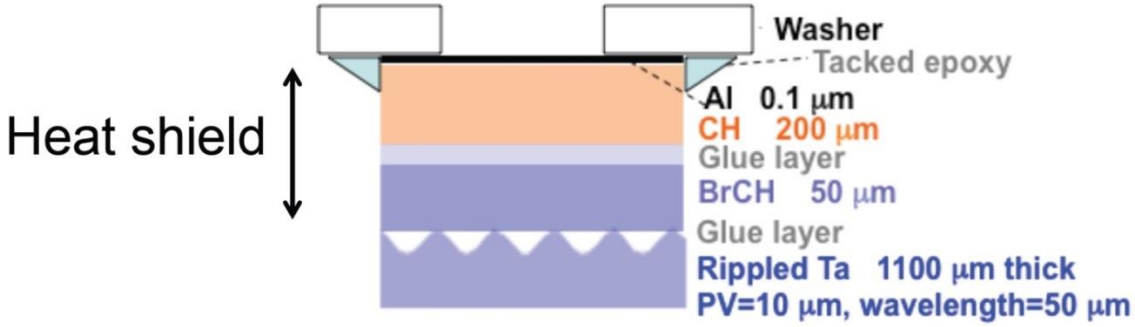

Figure 2.16: Target fabrication and the layers of the target.

Polishing also must be done to each target; however, it must be done with minimal residual work or damage such that the surface crystal structure stays intact. For die fabrication, a nitride tool steel is used as the die because it can withstand high pressure (GPa) coining stress, and it can be diamond turned. Target assembly is performed using a precision assembly station that allows for microalignment, pressing, and micropipetting of the glue, as shown in Figure 2.17.

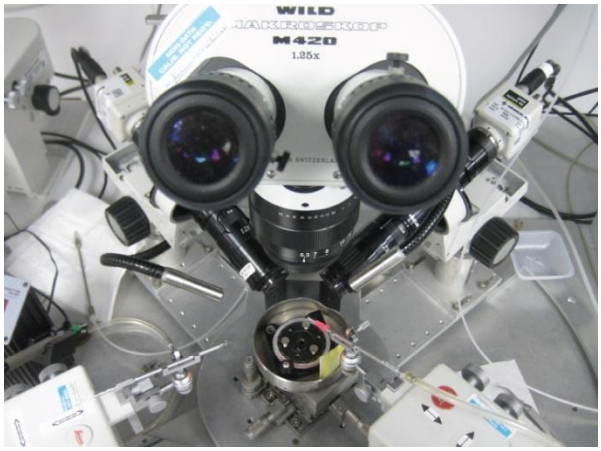

Figure 2.17: Target assembly machine.

Dual confocal lasers and interferometry thickness characterization of the glue gaps are used to ensure that the glue is thin and bubble-free within error. Figure 2.18 shows the progression building the targets.

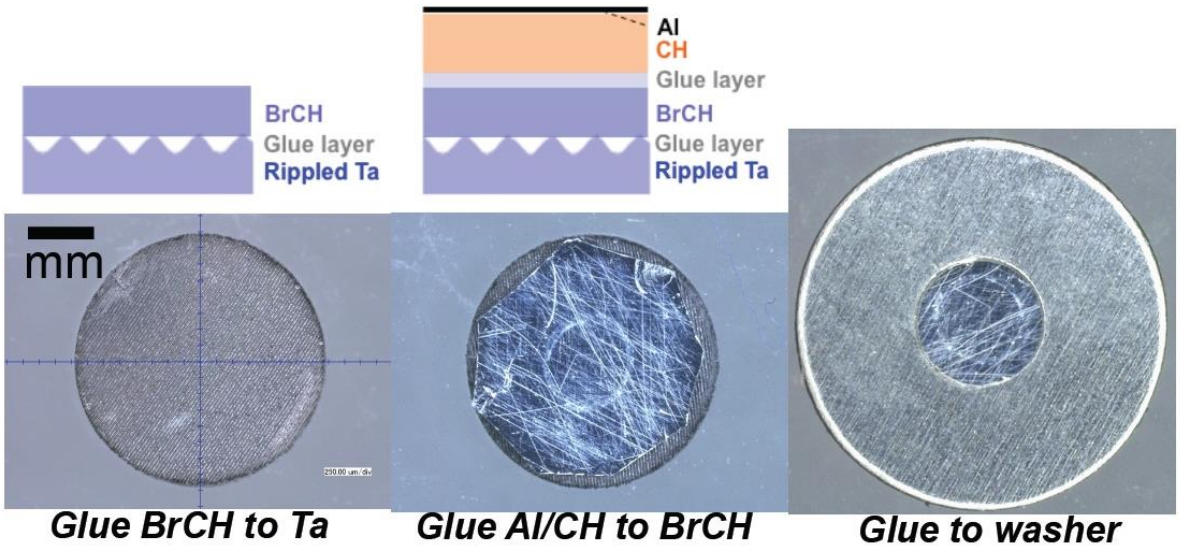

Figure 2.18: Build progression of the targets.

Target fabrication and assembly is done months before the experiments; therefore, design decisions affecting the targets must be made ahead of time. Once the targets are constructed, they are hand-carried to Omega by the experimenters. Before the experiment, they are inspected to make sure everything is intact. In certain experiments, the targets can be recovered, such as the ride-along targets. As soon as the experiments are over, the process of target characterization can begin. The following section discusses this post-experiment characterization, as well as some of the aspects of pre-shot characterization.

Target characterization – Post Experiment

Target characterization of the ripples, as well as characterization of the microstructure, is done pre- and post-shot using Wyko. This analysis provides the growth factor measurements that are used to gage the strength of the material. Characterization of the microstructure provides insight into the active deformation mechanisms in Ta and other metals tested at these high pressures of 1-4 Mbar. Pre-shot simulations are used to predict and validate the models and experimental design. Post-shot simulations are used to quantify the drives experienced by the targets and to correlate the drive characteristics to material strength including analysis of the role of RT/RM instabilities.

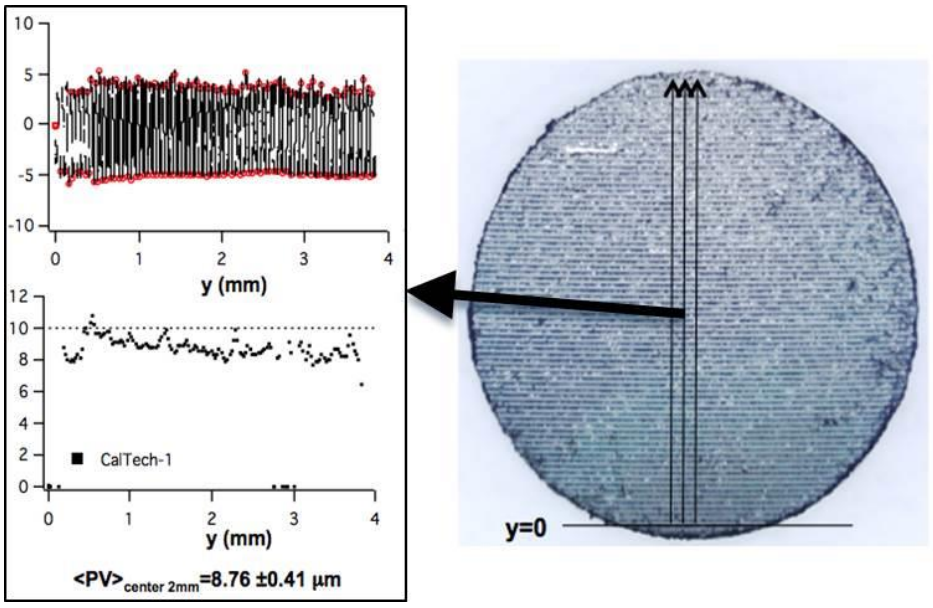

Figure 2.19: Characterization of peak-to-valley (PV) amplitudes of ripples.

Microscopy is performed to compare the pre- and post-shot microstructures. This is used to characterize dislocation density, slip system activity, grain growth, and twinning [45, 46]. This is shown in Figure 2.20.

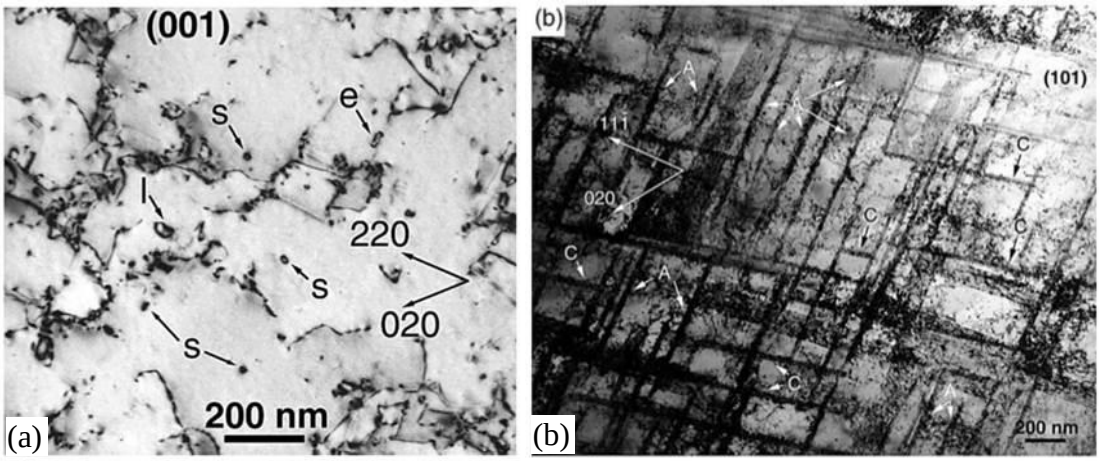

Figure 2.20: Target Characterization: (a) Slip system identification, (b) Twin identification.

Another part of the target characterization is white light interferometry. This is used to characterize the ripple patterns pre- and post-shot. Using the measurements from white light interferometry, the total growth factor may be analyzed and can then be used to understand the strength of the material. This is shown in Figure 2.21.

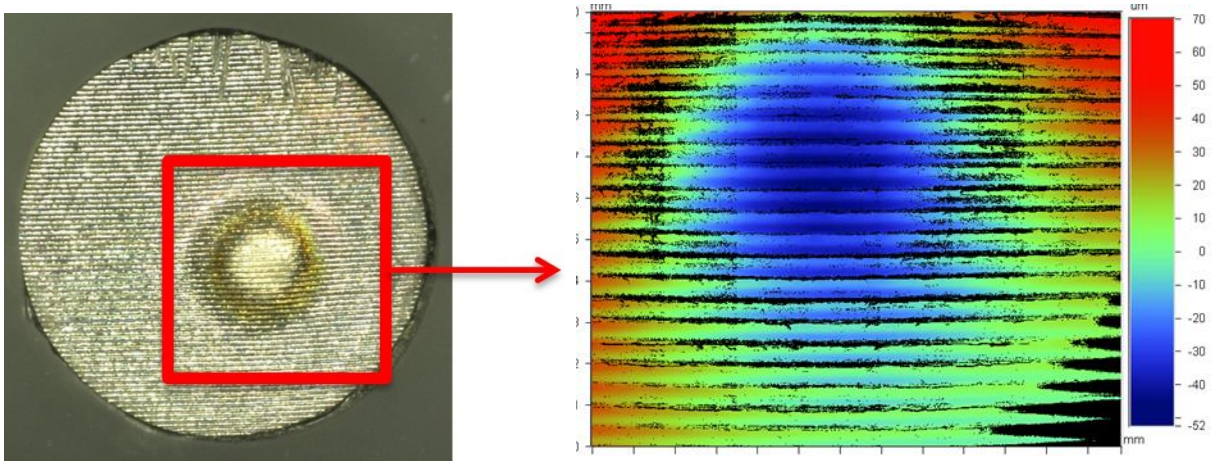

Figure 2.21: White light interferometry.

The process for obtaining the growth factors from the targets is described below.

Growth Factor Analysis Procedure:

1. Ripple peaks and valleys are identified in pre and post shot interferometry measurements.
2. Wave heights are calculated by averaging the distance between neighbor peaks and valleys.
3. Growth factors are assessed by normalizing post shot wave by pre-shot wave heights.
4. Error of the growth factors is assessed using the mean and standard deviation of multiple "line-outs" across the driven sample.

Plots showing steps from the growth factor analysis are shown in Figure 2.22.

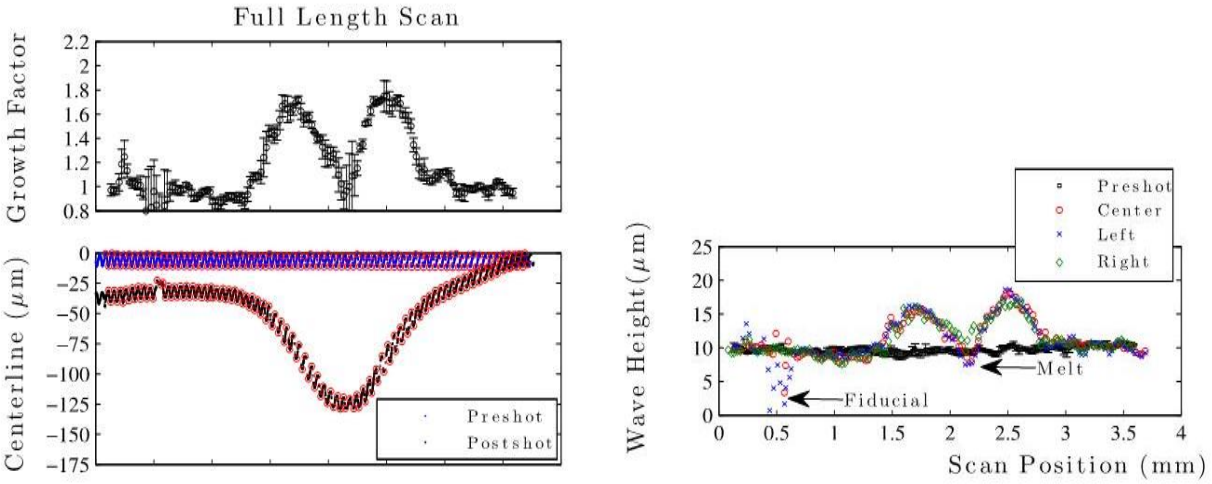

Figure 2.22: Plots for growth factor analysis.

2.4 Results of the Single-Mode Experiments

2.4.1 Analysis

Following the experiments, it is important for the targets to be recovered for post-experiment analysis to obtain growth factor measurements. This effort was led by Greg Randall of General Atomics and Aaron Stebner of Caltech. Figures 2.23 and 2.24 show what the recovered targets look like after removal from the recovery tube and after they are cleaned. The recovery tube surfaces must be ethanol rinsed, dried, and classified as Be-free. Each target is removed from each recovery tube and imaged. The targets are soaked in nitro-methane vials to remove the heat shield, and then they are re-imaged. At this point, characterization of the ripple can begin.

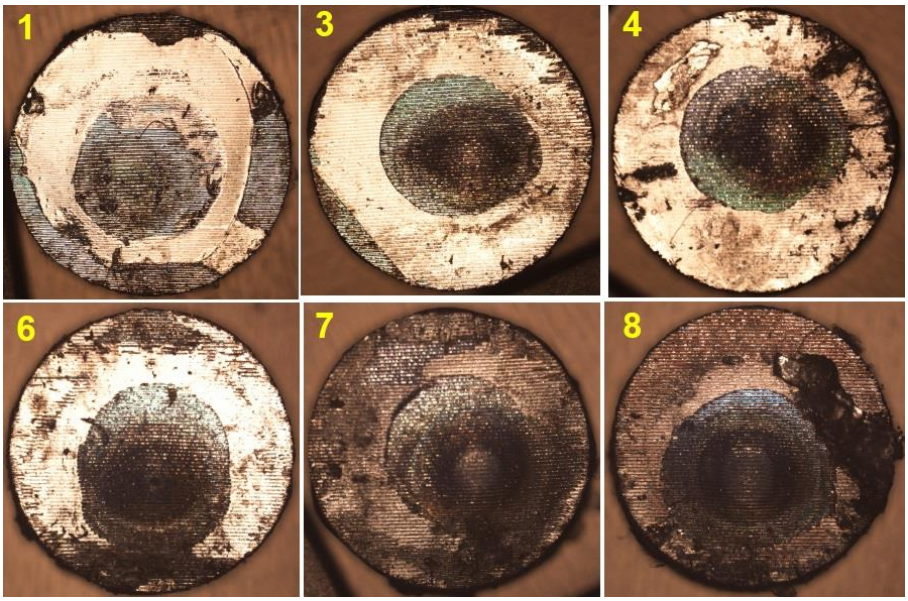

Figure 2.23: Post-shot images right after removal from recovery tube.

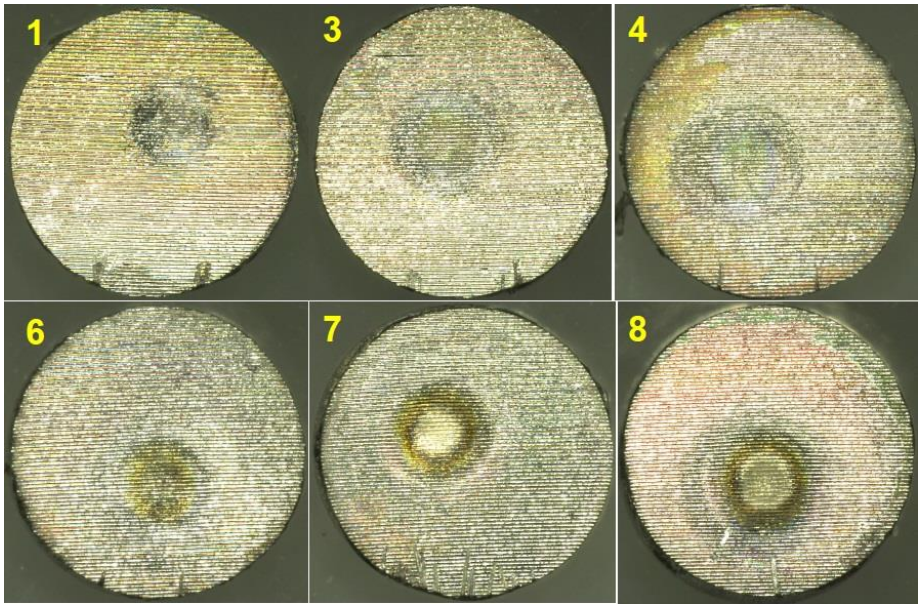

Figure 2.24: Post-shot images after nitromethane soak to remove heat shield.

Informal Analysis of the Wyko Data

Figure 2.25 is a summary of post shot Wyko done to obtain images, and therefore growth factors. This is done for each target. To be redundant, two stitched scans are done on each target. One is a long lineout and the other is a square of the shot zone. This is discussed more below.

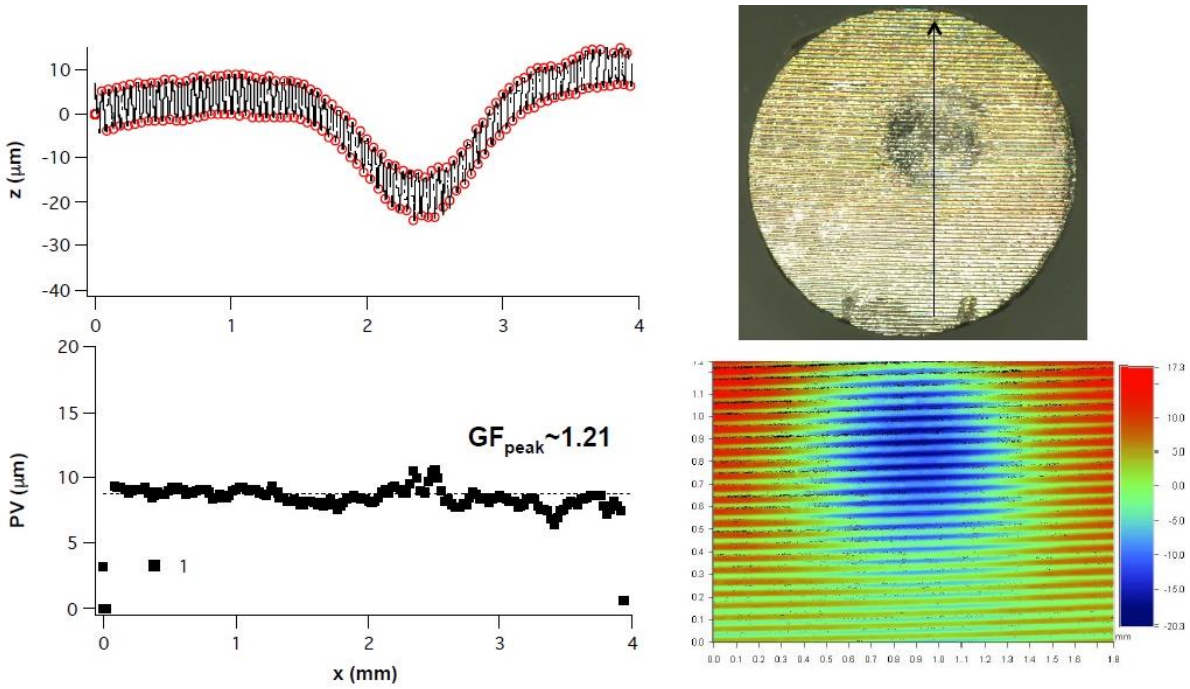

Figure 2.25: Wyko Process for obtaining GFs.

Formal Analysis of the Wyko Data

Maximum growth factors are taken from "full length" scans. Before the experiment, a scan was taken down the center of each target, and three lineouts were obtained (center, center + 0.2 mm, and center – 0.2 mm), as seen in Figure 2.26. Post-shot, two scans were taken for each target. The first scan is a full length scan taken through the center of where the shot was taken, as shown in Figure 2.26, and three lineouts are taken (center, center + 0.2 mm, and center – 0.2 mm). The second scan is window of the shot spot. From this 1 mm x 1 mm window, five lineouts can be taken (one down the center of the spot, and then 2 to either side of center, 0.05 mm apart). See Figure 2.26 for the pre- and post-shot scans.

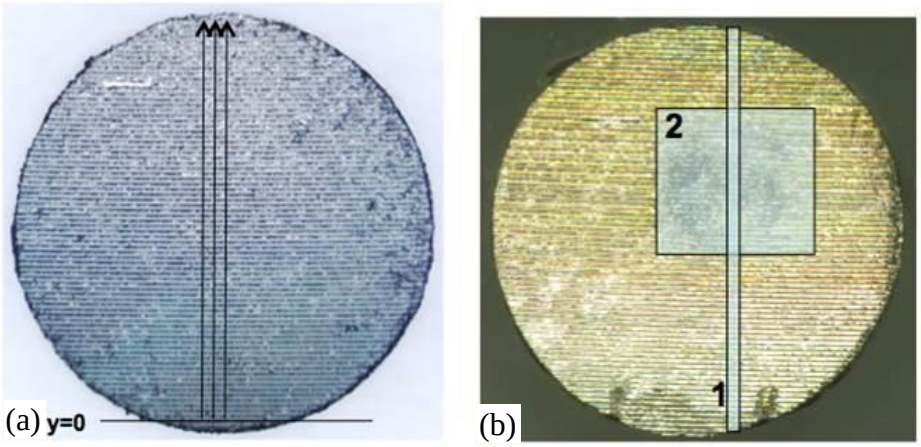

Figure 2.26: (a) Pre-shot scans, (b) Post-shot scans.

The growth factors are found using the following sequence:

1. Peaks and valleys of each wave were found for all pre and post shot lineouts described on the previous slide. On the middle set of axes in each figure, the "center" Wyko lineout data, peaks, and valleys are plotted for each scan (pre & post shot full length scans on left, post-shot spot scan on right). For each pattern, the y-axis data is shifted such that the global maximum data point corresponds to a vertical position of zero. For the spot analysis data, the x-axis position is shifted such that the minimum data point for the "center" spot scan aligns with the minimum data point for the "center" full length scan.
2. From these peaks and valleys, wave heights were found by taking the average distance between each peak & its two neighboring valleys (or vice-versa for valleys). The pre-shot wave heights plotted on the bottom axes are plotted as the mean of the three lineouts, with the standard deviation used as the error bar. The post-shot wave heights are plotted individually for each of the eight lineouts. For the "spot scan" data, the same x-axis shift was applied to all 5 scans.
3. To calculate growth factors, the wave height data is interpolated for each scan to a uniform x-axis grid. The post-shot wave height was then divided by the mean of the three pre-shot wave heights at each grid point for each of the eight post-shot measurements. In these figures, the growth factors are reported as the mean GF of each of the two scans, with the standard deviation used as the error bar.

In the six plots of Figure 2.27, the results of the two different types of scans are shown below. The left column of plots shows the full length scans and the right column shows the spot scans. Step 1 in the above procedure is represented by the second row of plots. Step 2 is represented by the third row of plots. Step 3 is represented by the first row of plots.

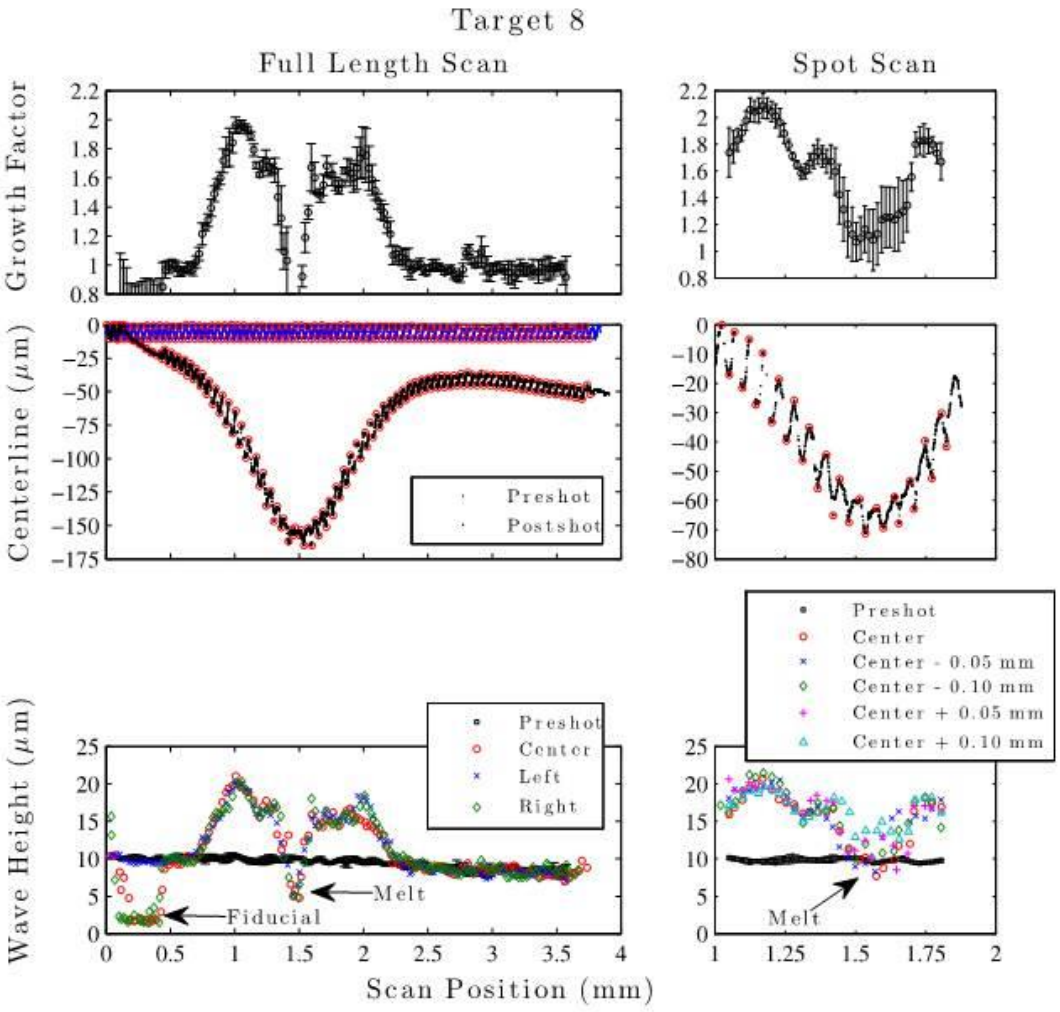

Figure 2.27: Target analysis results. (Left column) Result of analyzing the full-length scan, (Right column) Result of analyzing the spot scan.

This process was done to obtain the growth factor results for all targets. In the ride-along experiments this was done for all six targets. The results are discussed in the following section.

2.4.2 Results

This section summarizes the results from the ride-along experiments at Omega. The analysis for the plots provided is described in the previous section. For each target, there are plots of growth factor, centerline, and wave height for full length scans and spot scans. For each target, the energy requested and the energy obtained is provided, as well as the peak pressure as predicted by simulations described in Chapter 3.

Table 2.3: Summary of Omega Experiments on Single-Mode Ripples of Tantalum

Target	GF_{approx}	Energy (J)	Pressure (Mbar)
1	1.26	56.6	.98
3	1.43	95.4	1.23
4	1.43	118.9	1.52
6	1.58	153.5	1.96
7	1.72	202.3	2.68
8	1.97	252.9	3.41

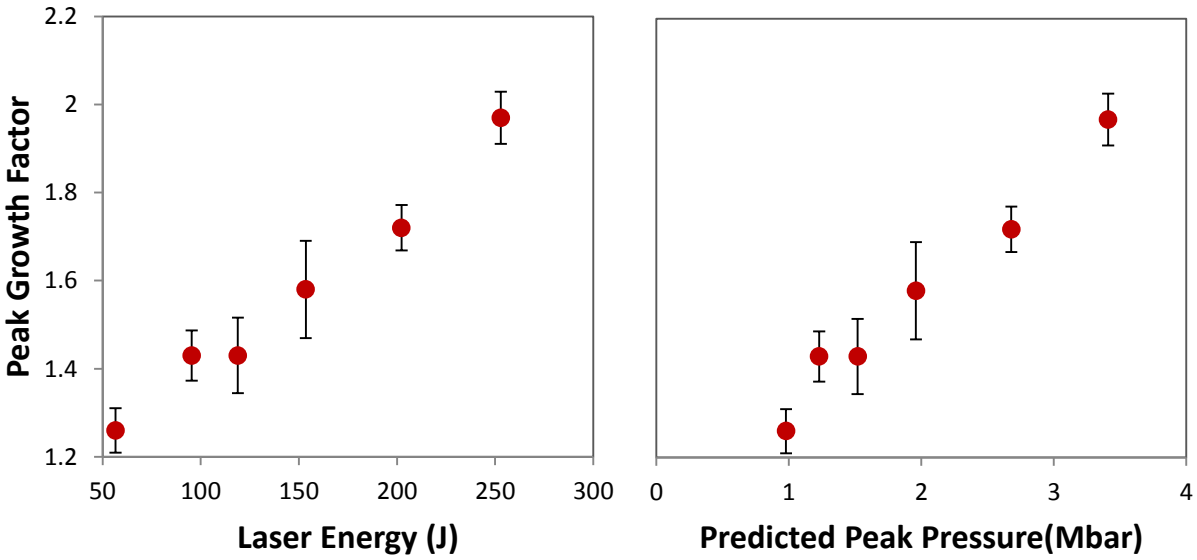

Figure 2.28: Summary of maximum growth factors in from April Omega experiments.

Target 1:
Energy: 70 J request, 56.6 J actual
Pressure: 0.98 Mbar predicted peak pressure (Eureka)
Growth Factor (approx.): 1.26

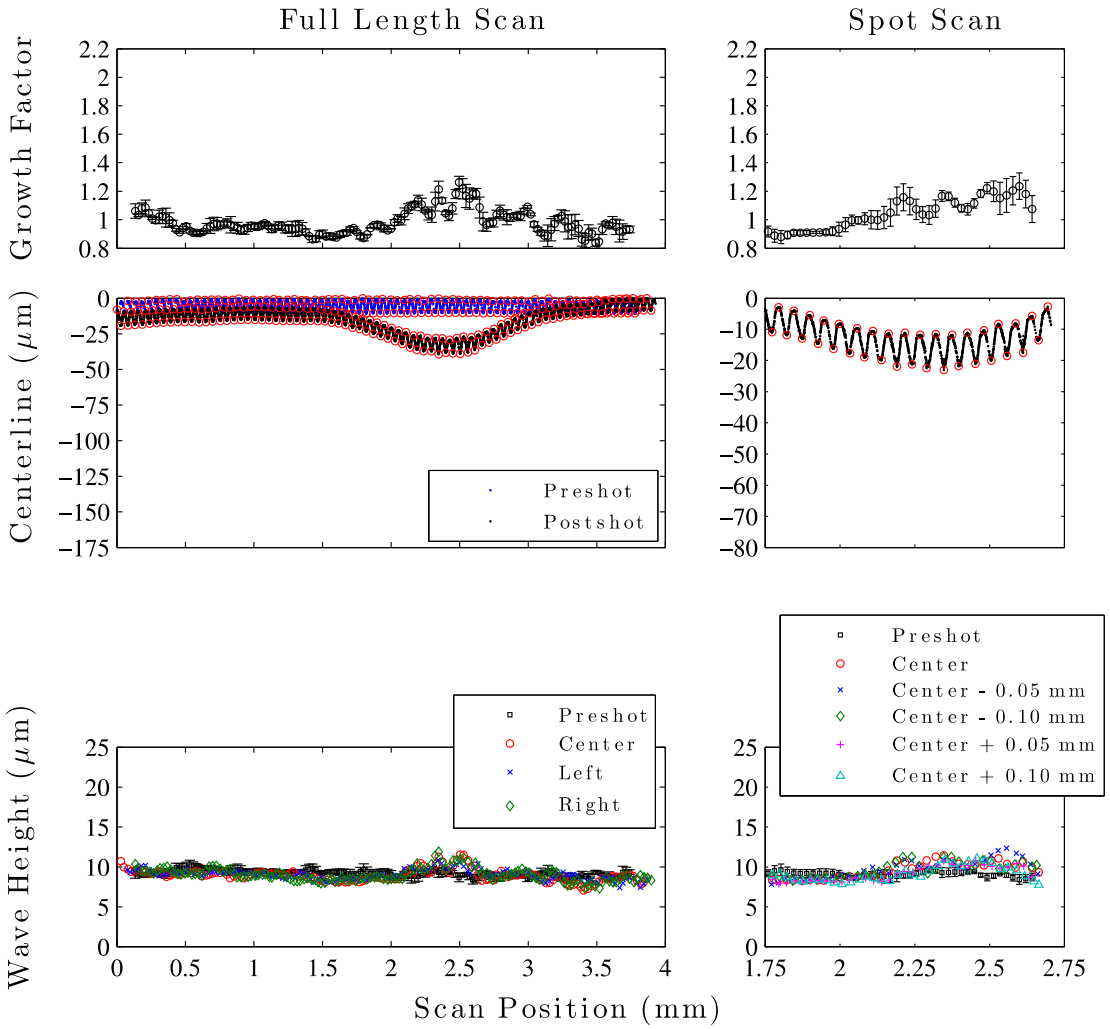

Figure 2.29: Target 1 Results. (Left column) Results from full-length scan, (Right column) Results from spot scan.

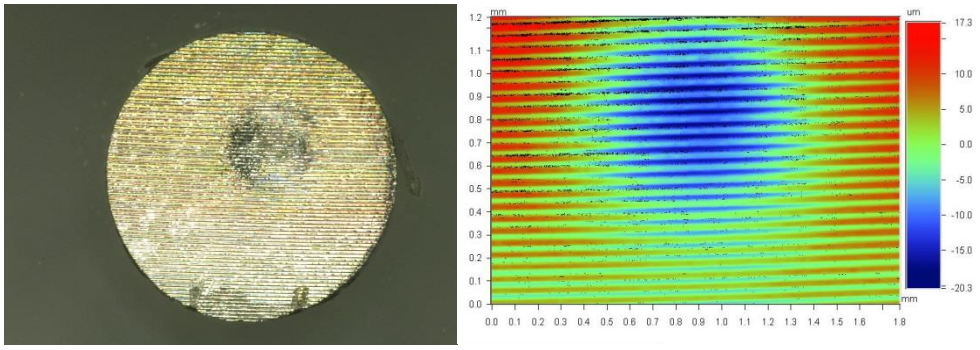

Figure 2.30: Target 1. (Left) Post-shot, (Right) Wyko for shot spot area.

Target 3:
Energy: 100 J request, 95.4 J actual
Pressure: 1.23 Mbar predicted peak pressure (Eureka)
Growth Factor (approx.): 1.43

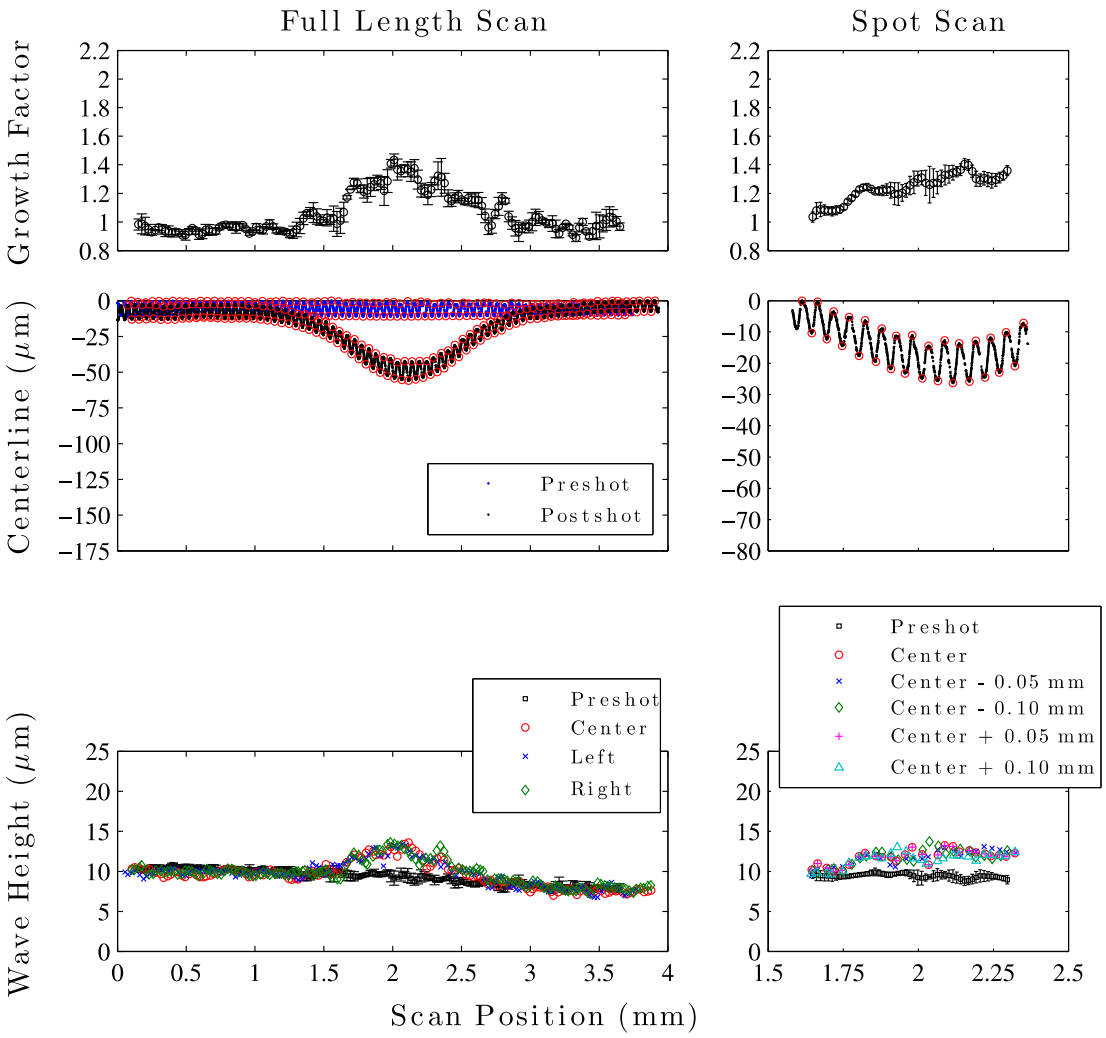

Figure 2.31: Target 3 Results. (Left column) Results from full-length scan, (Right column) Results from spot scan.

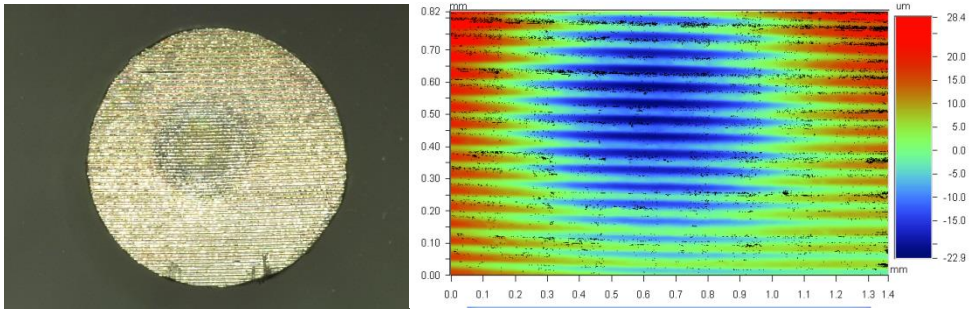

Figure 2.32: Target 3. (Left) Post-shot, (Right) Wyko for shot spot area.

Target 4:
Energy: 120 J request, 118.9 J actual
Pressure: 1.52 Mbar predicted peak pressure (Eureka)
Growth Factor (approx.): 1.43

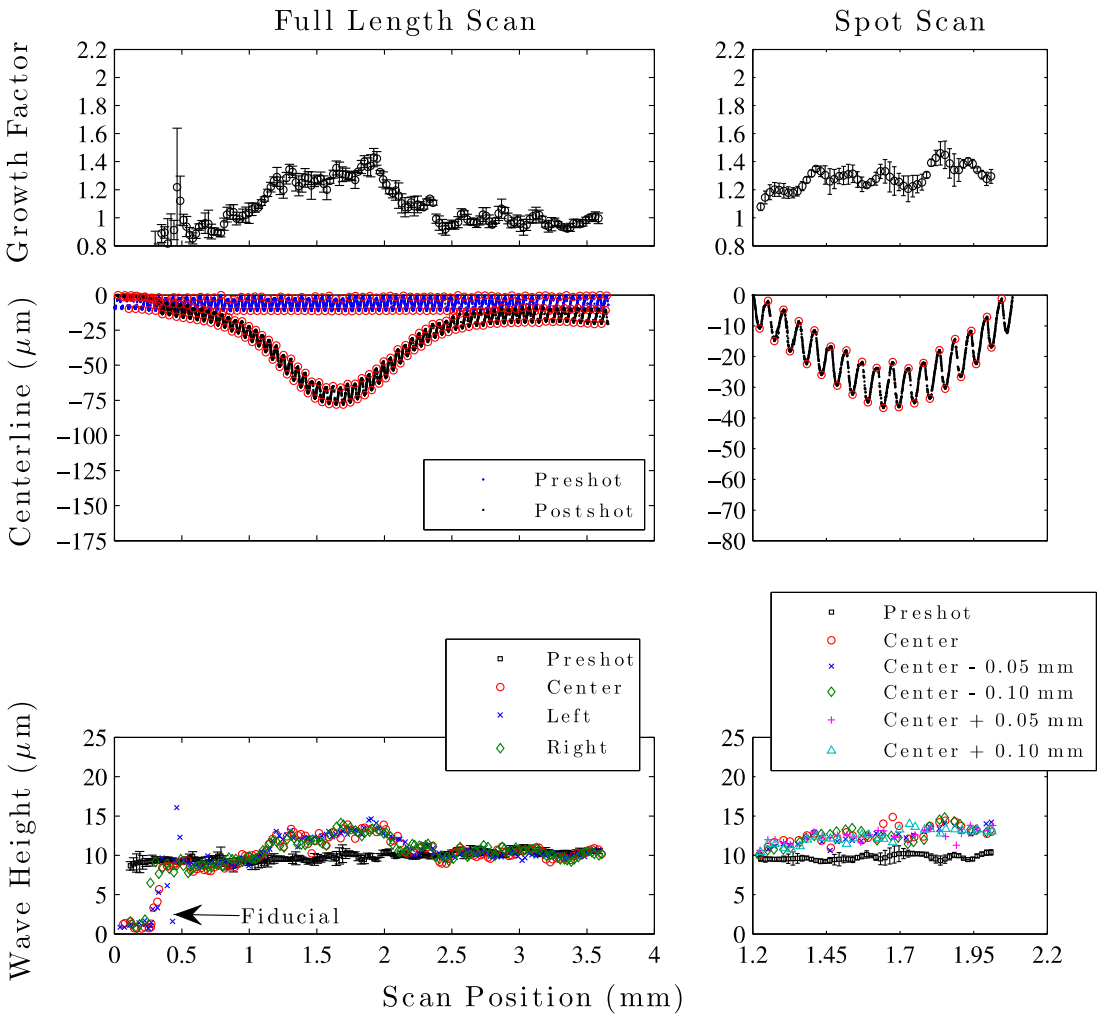

Figure 2.33: Target 4 Results. (Left column) Results from full-length scan, (Right column) Results from spot scan.

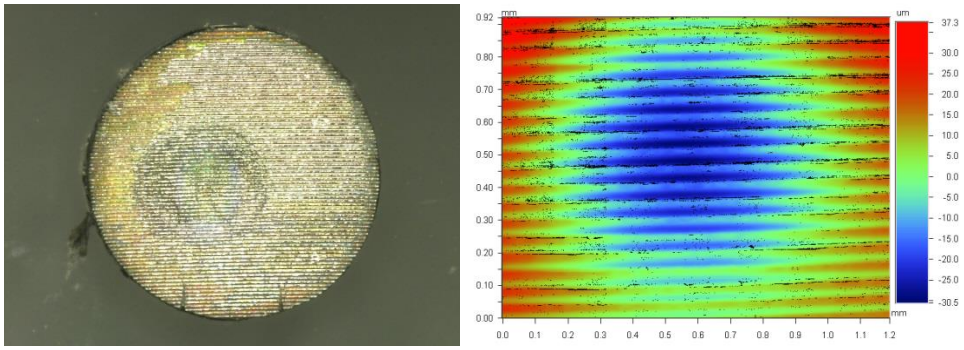

Figure 2.34: Target 4. (Left) Post-shot, (Right) Wyko for shot spot area.

Target 6:
Energy: 150 J request, 153.5 J actual
Pressure: 1.96 Mbar predicted peak pressure (Eureka)
Growth Factor (approx.): 1.58

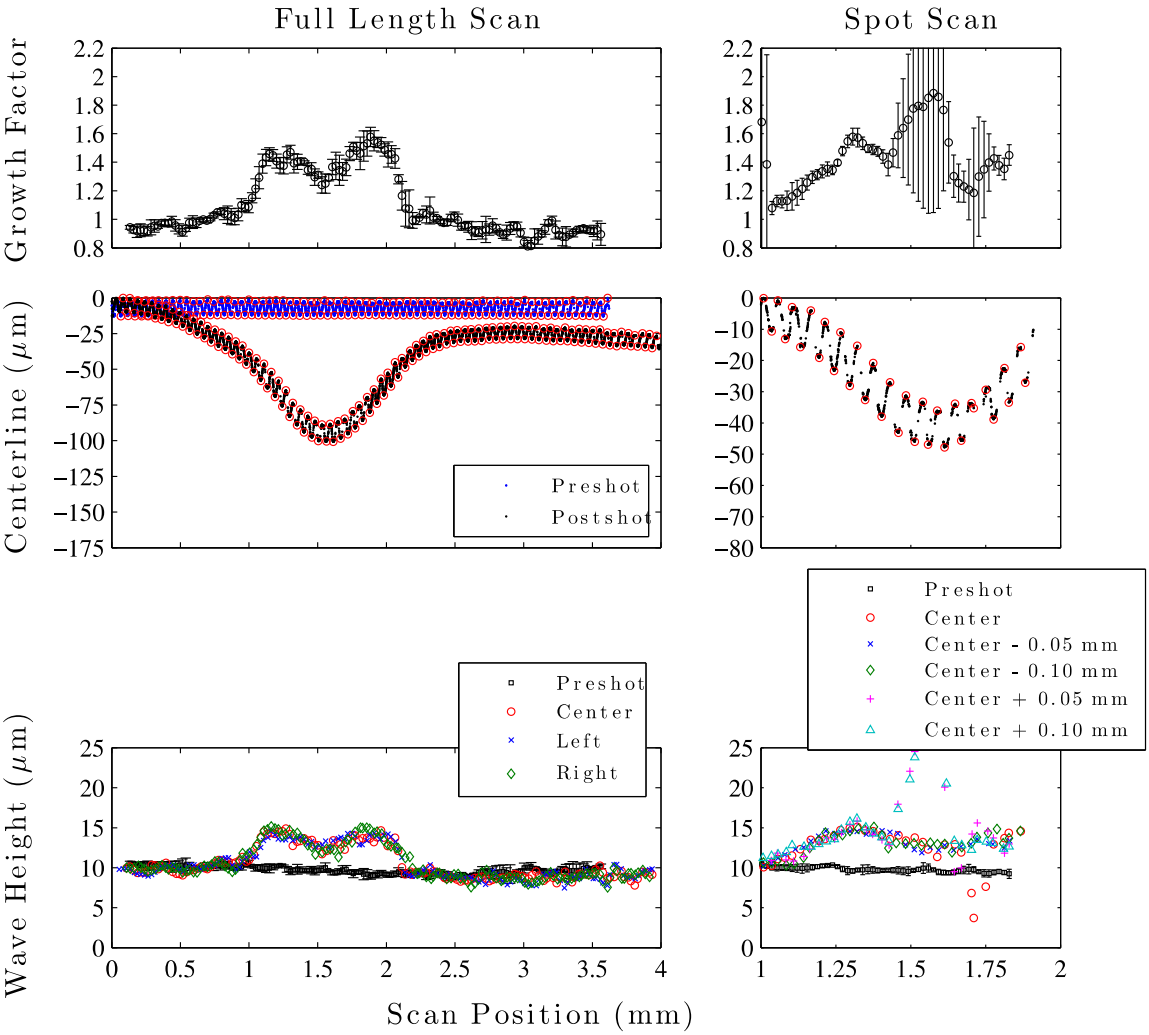

Figure 2.35: Target 6 Results. (Left column) Results from full-length scan, (Right column) Results from spot scan.

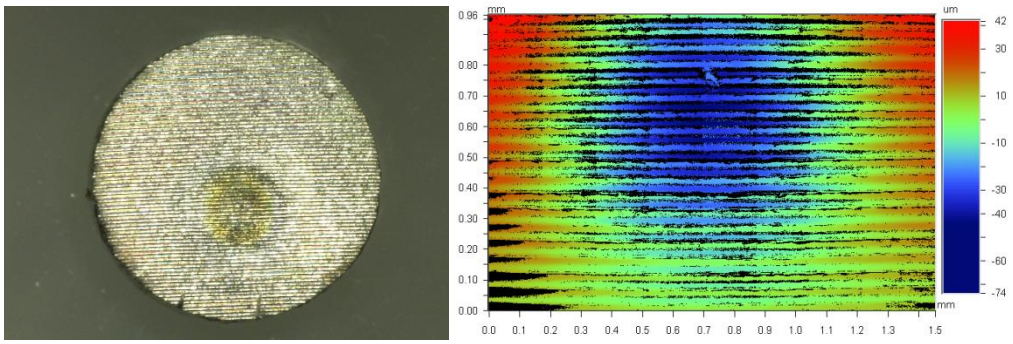

Figure 2.36: Target 6. (Left) Post-shot, (Right) Wyko for shot spot area.

Target 7:
Energy: 200 J request, 202.3 J actual
Pressure: 2.68 Mbar predicted peak pressure (Eureka)
Growth Factor (approx.): 1.72

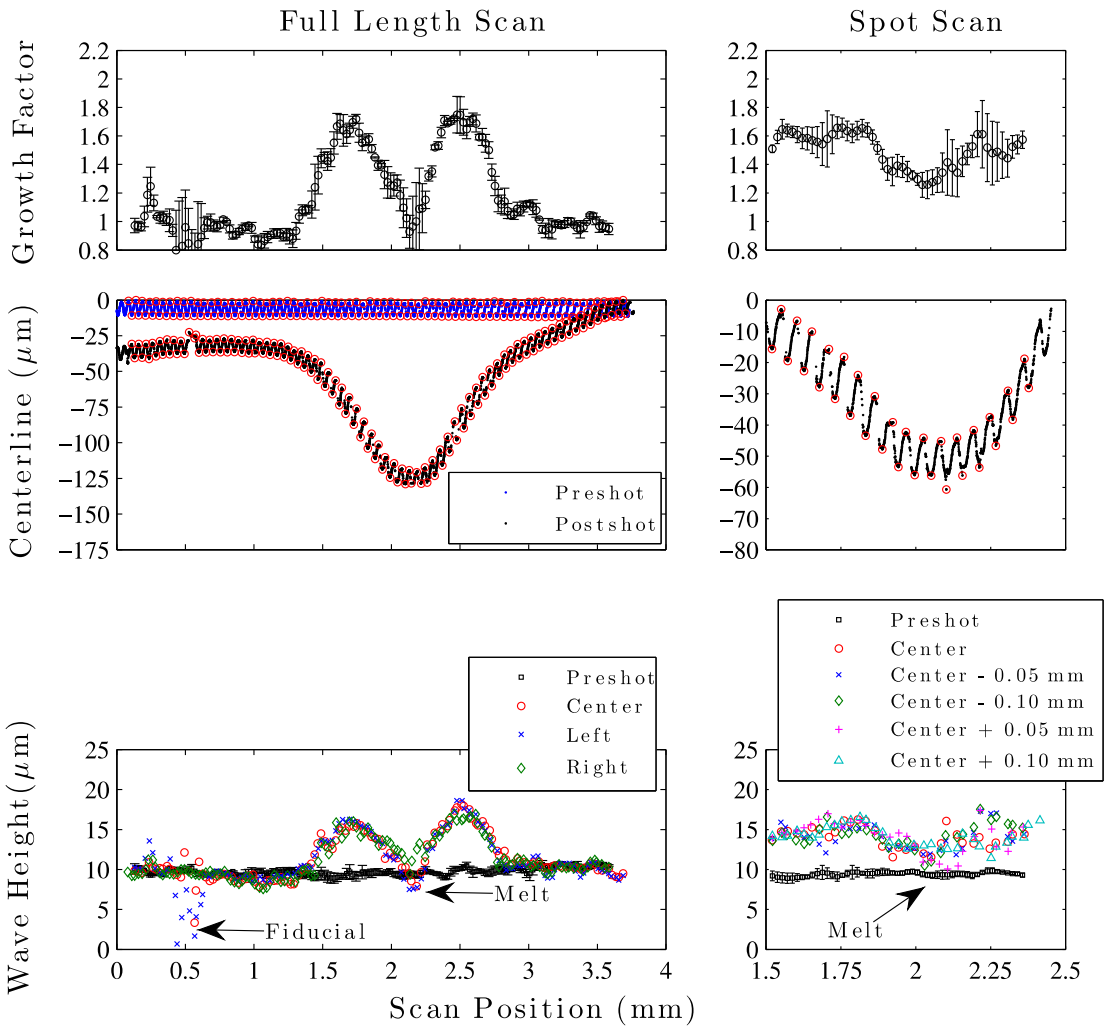

Figure 2.37: Target 7 Results. (Left column) Results from full-length scan, (Right column) Results from spot scan.

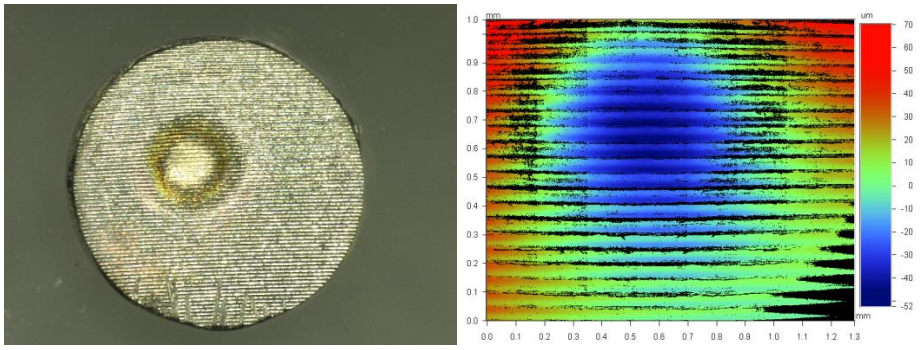

Figure 2.38: Target 7. (Left) Post-shot, (Right) Wyko for shot spot area.

Target 8:
Energy: 250 J request, 252.9 J actual
Pressure: 3.41 Mbar predicted peak pressure (Eureka)
Growth Factor (approx.): 1.97

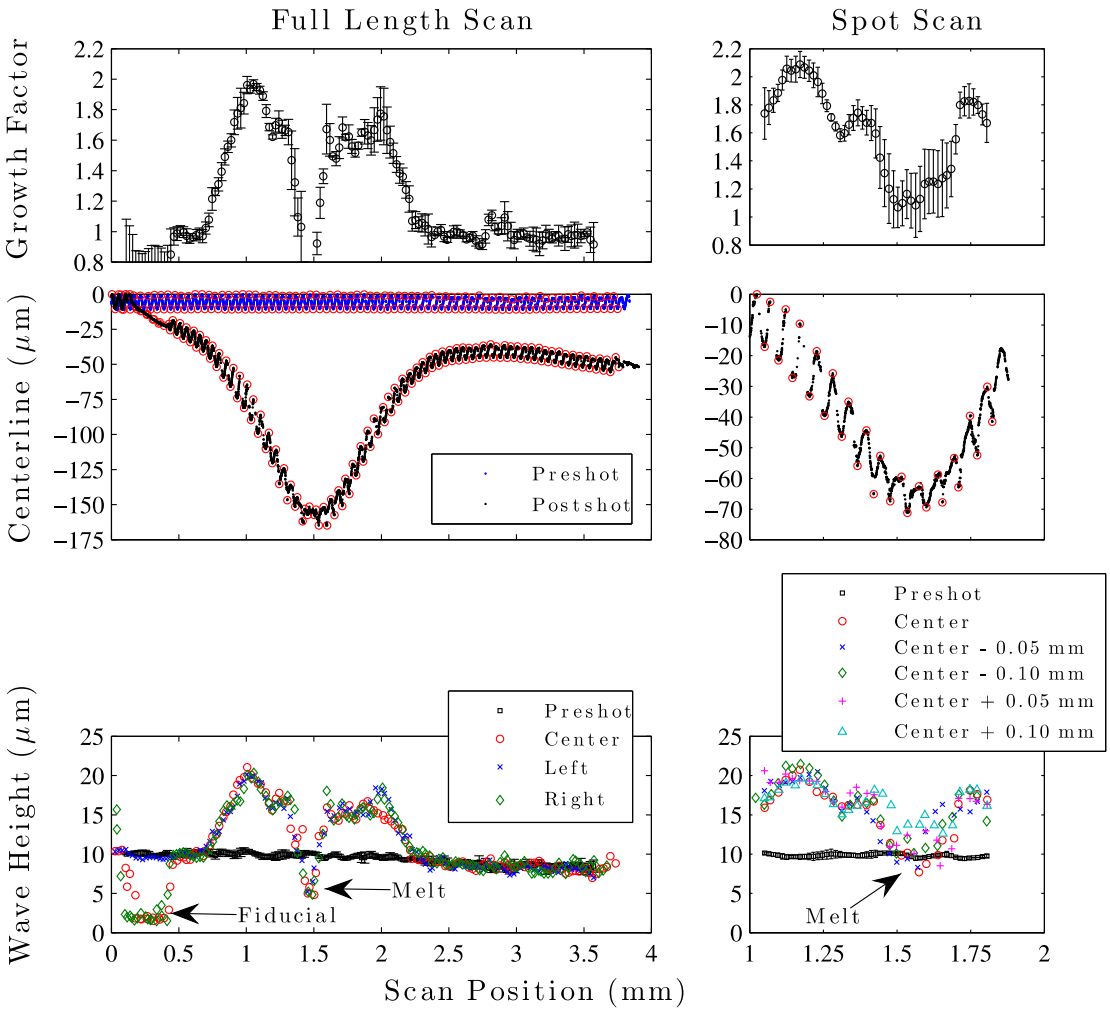

Figure 2.39: Target 8 Results. (Left column) Results from full-length scan, (Right column) Results from spot scan.

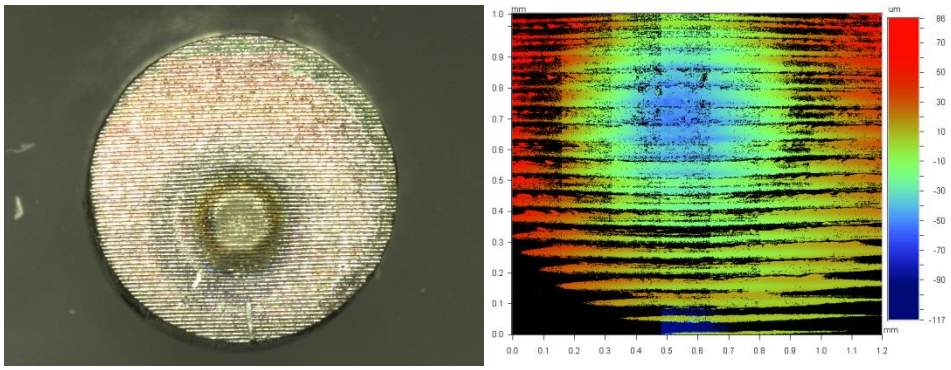

Figure 2.40: Target 8. (Left) Post-shot, (Right) Wyko for shot spot area.

These single-mode ripple tests have provided a reliable platform for studying the strength of tantalum at high pressures and strain rates.

2.5 Summary

By performing experiments on the Omega laser, a much better understanding of the strength of tantalum has been achieved. From grain sizes to crystal orientation to amplitude to wavelength, a variety of parameters have been studied that affect growth and therefore strength. By using simulations in conjunction with these experiments, both the experimental outcomes and the simulation predictions have been improved. The knowledge gained from the Omega experiments is critical to studying Ta strength at these high pressures. The following chapters cover the simulations that have been performed to assist in designing, predicting, and understanding these Omega experiments.

Chapter 3

Simulations of Richtmyer-Meshkov Instabilities

3.1 Background

The Richtmyer-Meshkov instabilities (Chapter 1) are used to infer the strength of tantalum at high pressures (>1 Mbar (100 GPa)) and high strain rates (>10^7 s^{-1}) using the ride-along experimental platform described in Chapter 2. To characterize and predict the response of materials at these conditions of high pressures and deformation rates, advanced simulations capabilities are utilized. These capabilities have been developed at Caltech by Professor Michael Ortiz's group over the last decade. The extreme conditions of this type of material behavior mean that experimental data is critical to developing the models for plastic flow and failure which are critical to predicting the experiments [47, 48, 49]. The simulations are based on a platform that consists of constitutive and failure models derived from first principles and empirical models. These simulations provide information at the nanoscale that is used to represent certain mechanisms in order to create models that are validated against experimental data, as well as microstructural characterization. This iterative process improves both the models (and thus predictive capabilities) and the experiments. Multiscale modeling is becoming increasingly important in the understanding of material behavior under extreme conditions, such as when matter is subjected to high energy density [9, 36, 38] and hypervelocity impact [50, 51].

3.1.1 Optimal Transportation Meshfree (OTM) Method

The Optimal Transportation Meshfree (OTM) method was developed as the numerical solver to simulate solid continuum mechanics problems including large deformations, hypervelocity impact, and fracture. The OTM method is based on optimal transportation theory. This is a tool used to generate geometrically exact discrete Langrangians for flow problems. It gives exact conservation properties, such as linear and angular momentum conservation [51, 52]. In addition to optimal transportation theory, it utilizes material point sampling and max-ent meshfree interpolation. The following characteristics of the OTM development make it viable for simulating large deformation and fracture problems. The OTM "generalizes the Benamou-Brenier differential formulation of optimal mass transportation problems to problems including arbitrary geometries and constitutive behavior, it enforces mass transport and essential boundary conditions exactly and is free from

tension instabilities, and it exactly conserves linear and angular momentum and its convergence characteristics are verified in standard benchmark problems" [51].

The goals of the OTM include a "Lagrangian method for extremely large deformation problems, imposition of essential boundary conditions in meshfree methods, numerical integration in meshfree methods, dynamic contact algorithm in meshfree methods, fracture and fragmentation algorithm in meshfree methods, and hypervelocity impact simulations via the OTM method" [51]. For the simulations of Richtmyer-Meshkov instabilities using a phenomenological engineering constitutive model, a critical element is the J2 isotropic plasticity model with power law hardening and thermal softening that is described in the next section.

OTM has been used to simulate and predict hypervelocity impact phenomena with qualified margins and uncertainties. Hypervelocity impact is considered a grand challenge in scientific computing and requires dynamics, high-energy density, multiphase flows (solid, fluid, gas, and plasma), and free boundaries plus dynamic contact. To take into account fracture, fragmentation, and perforation, complex material phenomena must be taken into account such as HED/extreme conditions, ionization, excited states, plasma, multiphase equation of state, transport, viscoplasticity, thermomechanical coupling, brittle/ductile fracture, and more [53].

The time integration aspect, in addition to the optimal transportation theory, involves discrete mechanics, variational time integrators, variational material updates, inelasticity, and incremental variational structure. The spatial discretization, in addition to utilizing local max-ent meshfree interpolation, involves material point sampling, numerical quadrature, material history, and dynamic reconnection [53].

The optimal transportation theory, based on the work of Gaspard Monge of Paris in the late 1700s and Leonid Kantorovich in the mid-1900s, is used to generate geometrically-exact discrete Langrangians for flow problems. The inertial part of the discrete Langrangian is used to measure the distance between consecutive mass densities. The variational time integration scheme is time reversible and symplectic, meaning it is differentiable with a closed, non-degenerate form. It gives exact conservation properties (momentum, energy) and a strong variational gamma convergence [54]. A max-ent spatial interpolation is used. The shape functions are determined directly by the nodes (i.e. meshfree). It is smooth, local (rapid decay), and monotonic. The Kronecker delta property at the boundary allows for essential boundary conditions. As shown in the Figure 3.2, the interpolation at material point p is determined by nodes in a local environment. These environments are determined "on-the-fly" by range searches and evolve through the flow [54].

OTM is based on optimal transportation theory and utilizes material point sampling and max-ent meshfree interpolation. Its advantages and characteristics include the ability to use an arbitrary geometry, constitutive behavior, free from tension instability, applies essential boundary conditions, and conserves mass, linear, angular momentum exactly [52, 53]. Figure 3.1 shows the evolution of the nodes and material points.

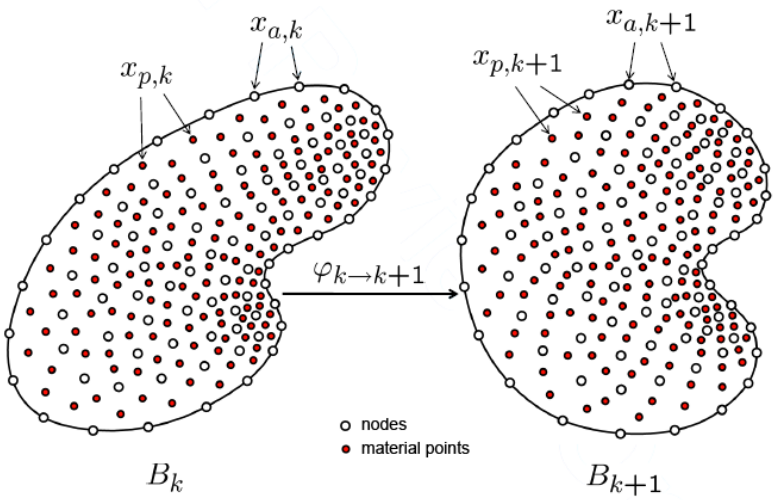

Figure 3.1: Illustration of OTM method evolution of nodes and material points [55]

It is assumed that the nodal kinematic variables and material points are given at time t_k to t_{k+1}. The explicit nodal coordinates, velocity, and acceleration will update as follows [53]:

$$\mathrm{x}_{k+1} = \mathrm{x}_k + (t_{k+1} - t_k)\left(\mathrm{v}_k + \frac{t_{k+1}-t_k}{2}\mathrm{a}_k\right) \tag{3.1}$$

$$\mathrm{a}_{k+1} = \mathrm{M}^{-1}\mathrm{f}_{k+1} \tag{3.2}$$

$$\mathrm{v}_{k+1=} = \mathrm{v}_k + \frac{1}{2}(t_{k+1} - t_k)(\mathrm{a}_{k+1} + \mathrm{a}_k) \tag{3.3}$$

The material point will also update [53]:

$$\mathrm{x}_{p,k+1} = \varphi_{h,k\to k+1}(\mathrm{x}_{p,k}) \tag{3.4}$$

$$\mathrm{F}_{p,k+1} = \nabla\varphi_{h,k\to k+1}(\mathrm{x}_{p,k})\mathrm{F}_{p,k} \tag{3.5}$$

$$V_{p,k+1} = \det[\nabla\varphi_{h,k\to k+1}(\mathrm{x}_{p,k})]V_{p,k} \tag{3.6}$$

$$\rho_{p,k+1} = m_p/V_{p,k+1} \tag{3.7}$$

This process is shown in the flow chart in Figure 3.2. This process represents the steps of explicit nodal coordinate updating, material point updating, constitutive updating at the material points, failure based on energy release rate criteria, and range searches.

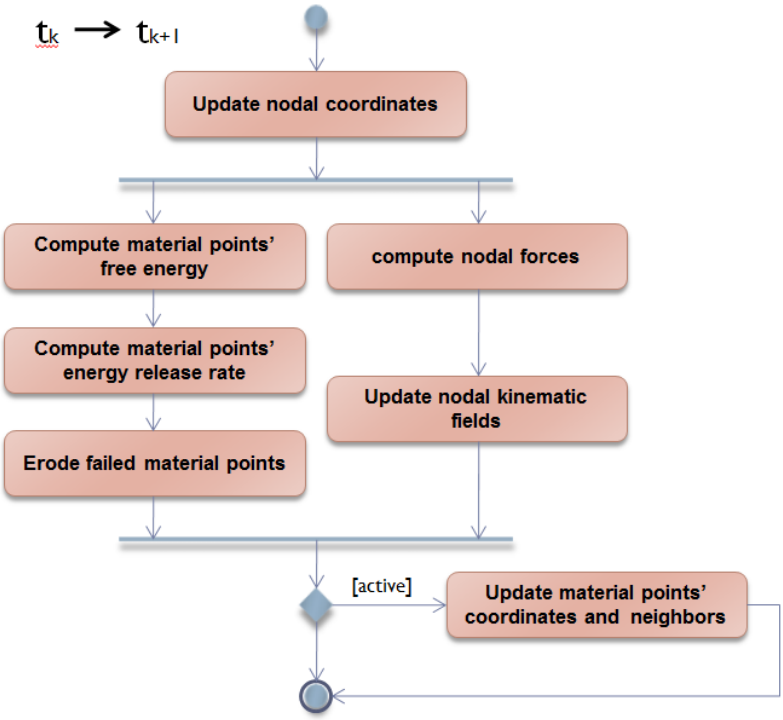

Figure 3.2: Flow chart for how OTM process works [53]

Parallel OTM: An advantage of OTM is its ability to run parallel such that calculations can be carried out simultaneously. It utilizes a shadow scheme and communication map. It looks for shadow nodes that are defined as shared nodes by two processes such that an overlap region of the range boxes exists, as shown in Figure 3.3.

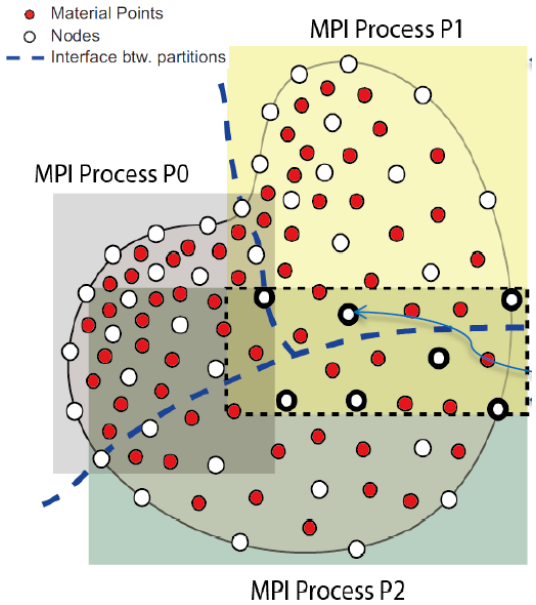

Figure 3.3: Parallel Computing of OTM via shadow scheme and communication map [53]

It is assumed that nodal and material point information, range boxes, and communication maps at time t_k are given from t_k to t_{k+1} for each partition [53]. For each core at every time step, range boxes are constructed. This is altered by the number of material points for each core. A communication map is constructed based on the range boxes, number of nodes that each core will receive from the next, and a sparse matrix. Using a communication map, the shadow nodal information includes coordinates, velocity, acceleration, and mass point-to-point [53].

Implementation in Eureka: Eureka is the object-oriented computational mechanics code created by Professor Michael Ortiz and his group at Caltech. Eureka is written in C++ and uses the MPI core, which is the interface between Eureka and the MPI implementation. MPI or Message Passing Interface is a system in parallel computing in which messages can be passed between systems and programs. It involves a core of library routines that can be accessed by users with C programming language or other language capabilities. Figure 3.4 is a schematic showing how Eureka interfaces with MPI, and Figure 3.5 is a representation of the parallel OTM with Eureka and uncertainty quantification [53].

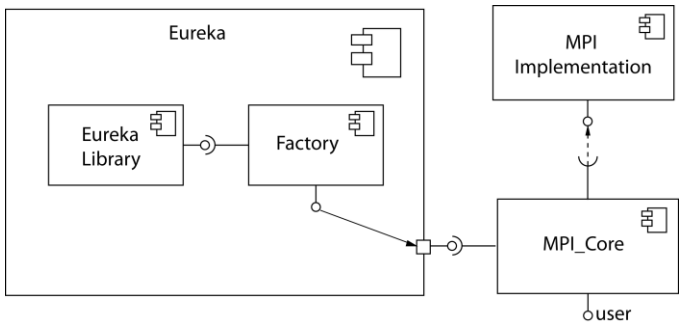

Figure 3.4: Schematic of Eureka interfacing with MPI [53]

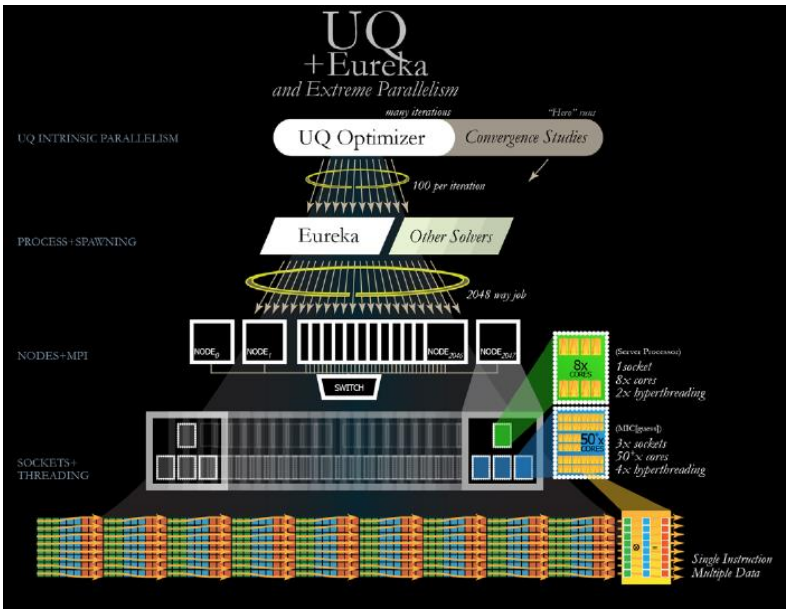

Figure 3.5: Representation of Parallel OTM with Eureka and UQ [53]

Eureka contains a series of different experimental tests with a suite of mechanics models. Those relevant to this research are discussed in the following sections. The performance of the OTM can be represented by the number of material points, nodes, and simulation time. For instance, a 60,000 material point, 12,000 nodes, 20 μs test would take 166 minutes with 1 core. Understandably, this number will go down if more cores are used. On the other hand, a test involving 1 million material points, 200,000 nodes, and only 1 μs, could take as long as 7 hours using 64 cores. In all, the OTM has proven to be a robust system for running large deformation problems such as hypervelocity impact.

3.1.2 Engineering Model

Within Eureka, different types of material models can be implemented. In this case, a phenomenological engineering constitutive model is utilized. This is the variational thermomechanical coupling material model created by Professor Michael Ortiz's group at Caltech. The goal of this model was to be a thermomechanical model applicable to both solid and liquid phases. The following equations give a brief overview of the model.

Overview of variational thermomechanical coupling material model: The variational thermomechanical coupling material model uses variational updates for a dissipative system [56, 57, 58, 59, 60]:

$$\Phi[\varphi_{n\to n+1}] = \int_{\Omega_0}\left[\frac{\rho_0}{2\Delta t^2}\,|\varphi_{n\to n+1}|^2 + W_n\left(\mathrm{F}_{n+1};\mathrm{F}_n,T_n,\mathrm{Z}_n\right)\right]dV \tag{3.8}$$

The incremental energy density per unit volume, W_n, is defined as [56]:

$$\begin{aligned}&\mathrm{W_n}\left(\mathrm{F_{n+1}};\mathrm{F_n},\mathrm{T_n},\mathrm{Z_n}\right) = \\ &\sup_{\mathrm{T_{n+1}}}\left\{\inf_{\mathrm{Z_{n+1}}}\left\{\mathrm{A_{n+1}}-\mathrm{A_n}+\eta_\mathrm{n}(\mathrm{T_{n+1}}-\mathrm{T_n})+\right.\right.\\ &\left.\left.\Delta\mathrm{t}\Psi^*\left(\frac{\mathrm{T_{n+1}}}{\mathrm{T_n}}\dot{\mathrm{Z}}_{\mathrm{n,n+1}}\right)\right\}+\Delta\mathrm{t}\Phi^*\left(\frac{\mathrm{T_{n+1}}}{\mathrm{T_n}}\frac{\Delta\mathrm{F}}{\Delta\mathrm{t}}\right)\right\}\end{aligned} \tag{3.9}$$

where A_{n+1} is the internal energy or the Helmholtz free energy and η_n is the entropy per unit volume. The Ψ^* term represents rate sensitivity and dissipation pseudo-potential that determines the evolution of the Taylor-Quinney factor. The Φ^* term represents the viscous dissipation potential.

For the Helmholtz free energy, an additive decomposition of the energy is assumed [56]:

$$A = W^e(\mathrm{C}^e,T) + W^p(\bar{\epsilon}^p,T) + W^h(T) \tag{3.10}$$

which can be broken into W^e (elastic strain energy), W^p (stored energy of plastic work), and W^h (stored heat). Elastic strain energy is defined as:

$$W^e(\mathrm{C}^e,T) = f(J,T) + G(J,T)\,\|\mathrm{e}^e\|^2 \tag{3.11}$$

where $f(J,T)$ is the Equation of State (EOS) and e^e represents the deviatoric elastic response.

The stored energy of plastic work is represented as a Hardening Law:

$$W^p(\bar{\epsilon}^p, T) = \frac{n}{n+1}\sigma_0(T)\bar{\epsilon}_0^p\left(1+\frac{\bar{\epsilon}^p}{\bar{\epsilon}_0^p}\right)^{\frac{n+1}{n}} \tag{3.12}$$

The thermal softening, $\sigma_0(T)$, is given a value of zero unless the temperature, T remains below the melt temperature, T_m, as follows:

$$\sigma_0(T) = \begin{cases} \sigma_y\left(1-\left(\frac{T-T_0}{T_m-T_0}\right)^a\right) & if\ T < T_m \\ 0 & \text{otherwise} \end{cases} \tag{3.13}$$

The stored heat is defined as:

$$W^h(T) = C_0 T\left(1-\log\frac{T}{T_0}\right) \tag{3.14}$$

The variational thermomechanical coupling material model can be tested and validated for specific materials. In this case, Ta was tested and validated for pure polycrystalline Ta in the quasi-static and dynamic range. The stress-strain curves used for validation of pure polycrystalline are shown in Figure 3.6.

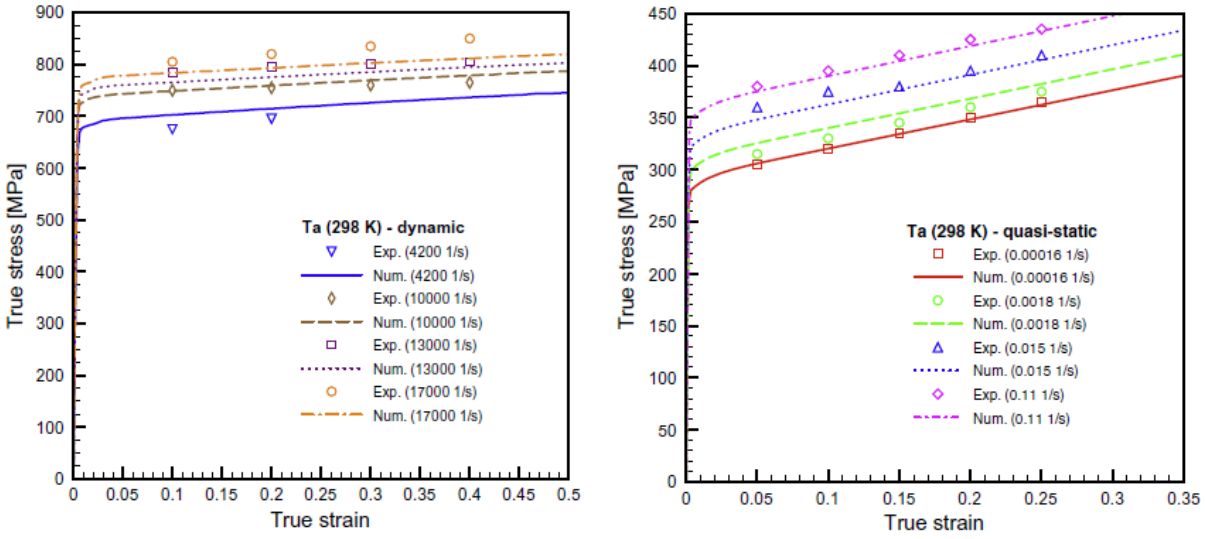

Figure 3.6: Stress–strain curves for pure polycrystalline Ta (no annealing), in the quasi-static range (isothermal conditions) and dynamic range (adiabatic conditions) from Stainier and Ortiz 2010. Experimental results taken from Rittel et al. (2007). [56, 61]

EOS & the SESAME Database: As discussed earlier, the elastic strain energy component of the additive decomposition of the Helmlholz free energy is represented as:

$$W^e(\mathrm{C}^e, T) = f(J,T) + G(J,T)\|\mathrm{e}^e\|^2 \tag{3.15}$$

where $f(J,T)$ is the Equation of State (EOS), J is the volumetric deformation, and T is the temperature. This volumetric contribution must be accessed from the SESAME EOS database of

Los Alamos National Laboratory (LANL). Eureka is built such that it can access certain materials within this database. For these simulations, tantalum EOS is required and accessible. The data points in the *(J,T)* space are extracted in tabular form and interpolated linearly in each cell of the domain, as shown in Figure 3.7, for the elastic strain energy [60, 62].

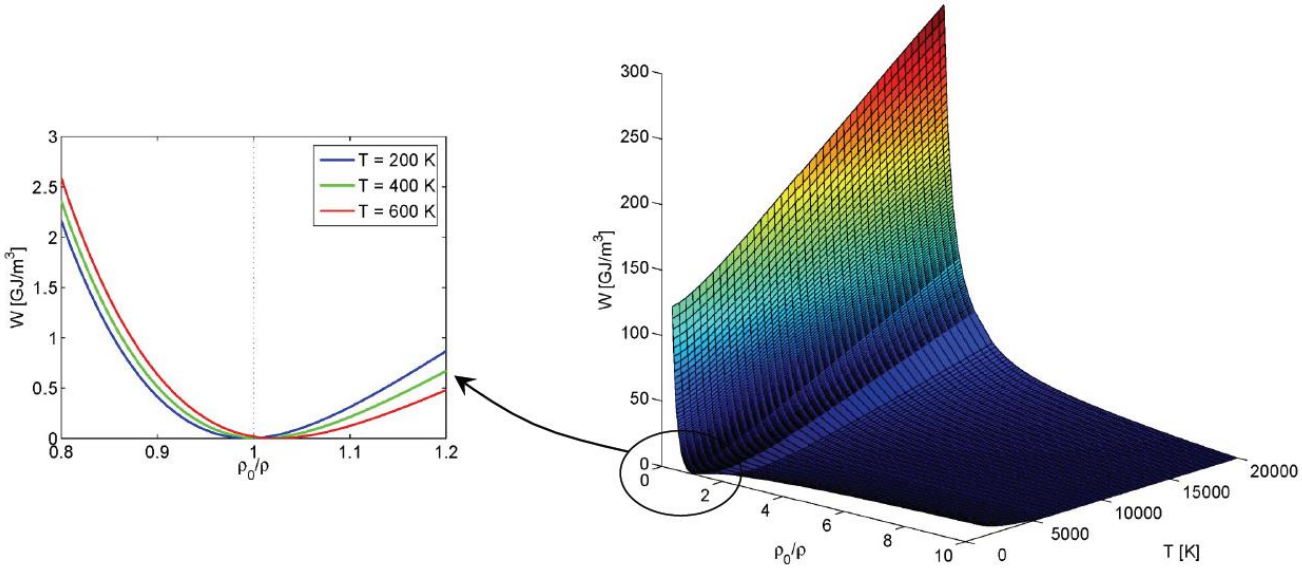

Figure 3.7: The SESAME EOS data points for elastic strain energy must be extracted in tabular form and interpolated linearly [62].

Similarly, the pressure must be accessed from the SESAME EOS database for tantalum. The pressure is also a function of the volumetric deformation *(J)* and the temperature *(T)* and must be extracted in tabular form and interpolated linearly in each cell of the domain, as shown in Figure 3.8.

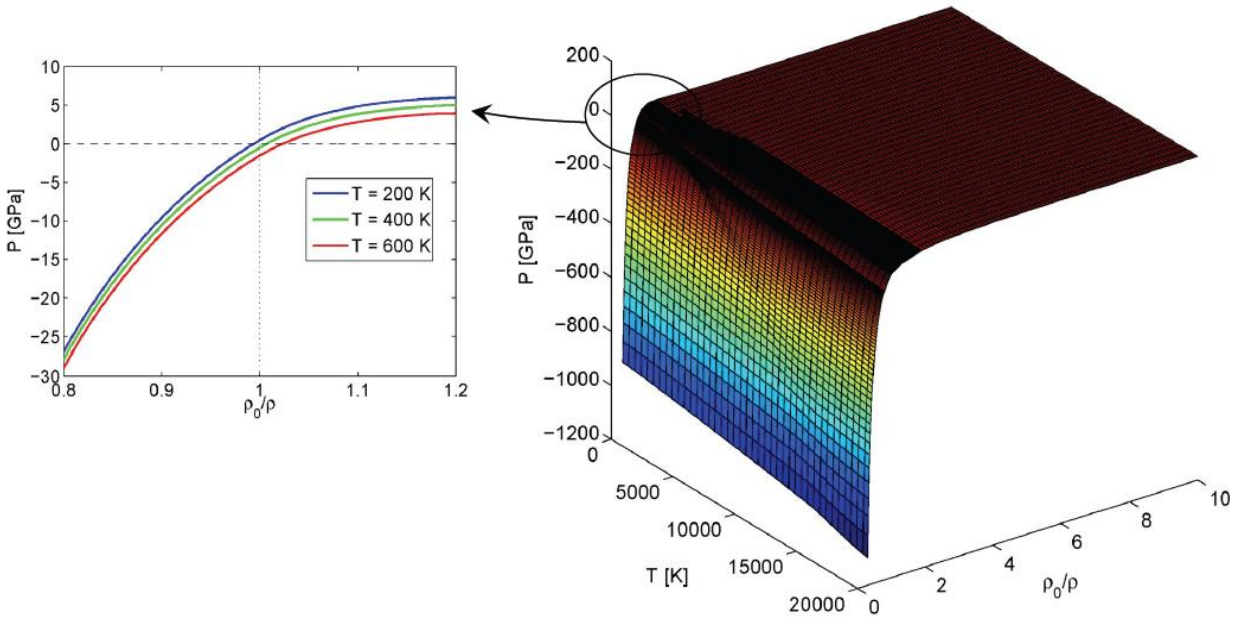

Figure 3.8: The SESAME EOS data points for pressure must be extracted in tabular form and interpolated linearly [62].

3.2 Pre-processing and Post-processing

To use Eureka, certain pre-processing and post-processing must be done. The following subsections go over the different programs and steps that are required to run simulations. Prior to using Eureka, three different important tools must be used: Modeling (which is done in SolidWorks), Meshing (which is done in Femap), and running hydro codes (which is done in Hyades). Next, Eureka itself can be used to run the simulations. Following the simulations, a post-processing visualization tool called Paraview is used. These sections will go over how and why these different steps are used. Following these five steps, analysis techniques are used. These are discussed more at the end of this chapter. Figure 3.9 is an illustration of how the different components of running simulations come together.

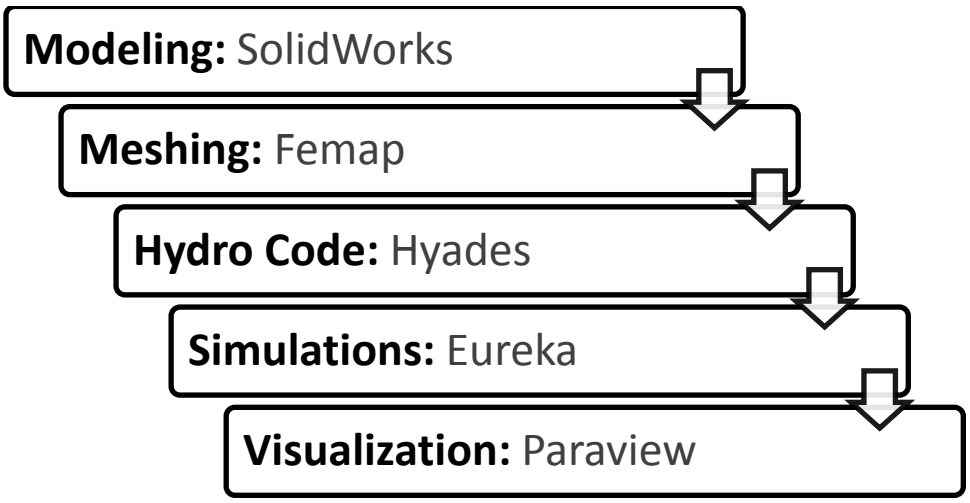

Figure 3.9: The different components of running simulations.

3.2.1 Modeling

The first step is to create the geometry that will be used in Eureka. The choice for the geometry is driven by the experimental test that needs to be simulated. In this case, the simulations aim to capture instability growth in rippled surfaces, so geometries with a specific wave function representing the ripple are created, as shown in Figures 3.14 – 3.15. In this design, geometric concerns include the height of the sample, the amplitude and wavelength of the ripple, and the width of the sample. For modeling purposes, one ripple or even one half of a ripple can be modeled and then post-processing can be used to create a series of ripples. The models are 3D models but are designed such that they are thin 3D models with the proper boundary condition applied to the faces to emulate plane strain.

SolidWorks is the software used to create these models using the geometries that have been chosen. SolidWorks is a 3D mechanical computer-aided design (CAD) program. It operates on Microsoft Windows. SolidWorks was chosen because of the author's substantial experience using this program, and because it is commonly used by engineers, universities, designers, and companies worldwide. Additionally, SolidWorks files are sent to the machine shop in the department where they can use those files to create actual models. SolidWorks files have also been used with a 3D printer, where custom equipment is printed out of a polymer. Figure 3.10 and 3.11 show views of the different models used for the simulations, including both single ripples and multimode ripples of the samples used in the laser driven Richtmyer-Meshkov experiments.

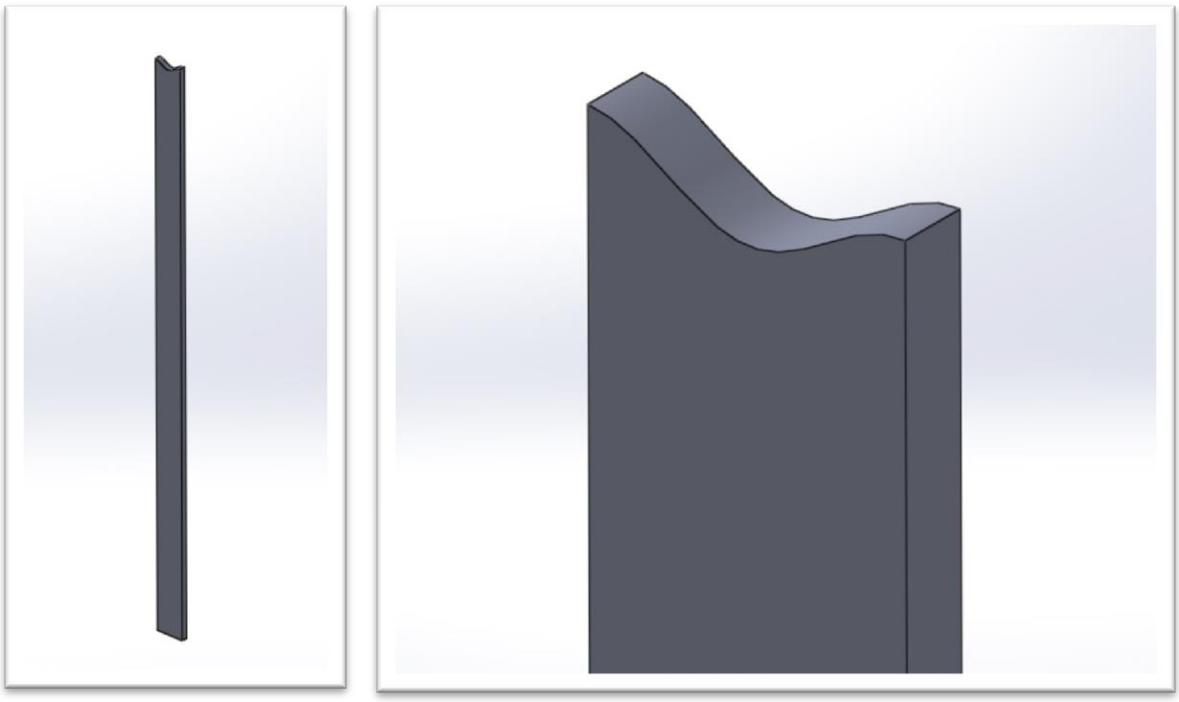

Figure 3.10: SolidWorks model for the single ripple in a laser driven Richtmyer-Meshkov experiment; the image on the left is the entire model; the image on the right is zoomed in to show the rippled surface.

Before determining which multimode pattern to use, each pattern had to be modeled in SolidWorks. The first set of multimode patterns tested had four modes. Three different patterns were tested.

Figure 3.11: SolidWorks models for the four-mode ripple patterns in a laser driven Richtmyer-Meshkov experiment; the images on the left are the entire model; the images on the right are zoomed in to show the rippled surfaces.

For the multimode patterns, after being simulated in Eureka it was determined the growth of the different modes would not be clearly distinguishable during analysis. Therefore, three-mode patterns were created in SolidWorks that were tested in Eureka. Of the two patterns in Figure 3.12, the first pattern was selected. Both patterns exhibited growth that could be measured, but the former pattern was easier to manufacture. After the SolidWorks models have been created, they are then brought into a program called Femap for meshing.

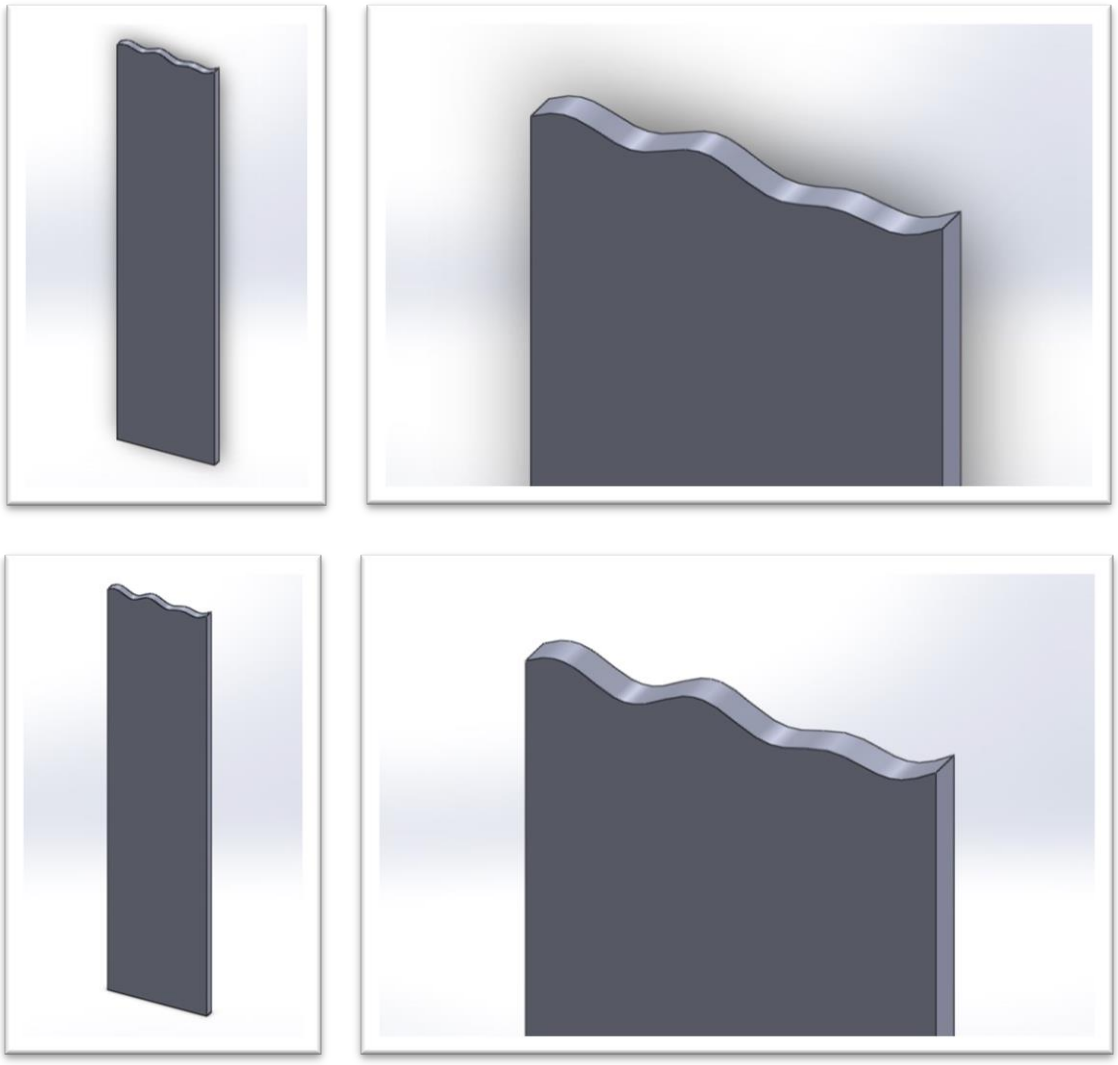

Figure 3.12: SolidWorks models for the three-mode ripple patterns in a laser driven Richtmyer-Meshkov experiment; the images on the left are the entire model; the images on the right are zoomed in to show the rippled surfaces.

3.2.2 Meshing

The second step is to create the meshes. Once the geometry has been created in SolidWorks, the files are imported into Femap. Once the mesh files are created in Femap, a meshed file can be exported. Femap, or Finite Element Modeling and Post-processing, is an engineering analysis

software program that runs on Microsoft Windows. It can create finite element analysis models for complex engineering systems and can virtually model the components. Because Femap is CAD-independent, the geometry can be imported from SolidWorks so as to use Femap solely for its finite element meshing capabilities. Femap uses 3D solid and surface meshers to "generate high-quality meshes, providing well-shaped elements to ensure accurate results" [63]. With Femap, there is complete control over which meshing parameters to use, including mesh size, meshing of small features, and varying meshes for more complex areas. For the elements, 3D linear tetrahedrons are used. Tetrahedrons mesh more easily than other geometries such as quads. Within Eureka, the method is meshfree, so as long as the points are evenly spaced, the type of elements used does not matter. Figure 3.13 shows some images of the meshes from Femap. Each of the succeeding images is more zoomed in to show more detail of the mesh. Once the meshes have been created using Femap, the meshed file can be exported. A Python script written by Dr. Bo Li is used to convert the Femap mesh into a mesh that is readable by Eureka.

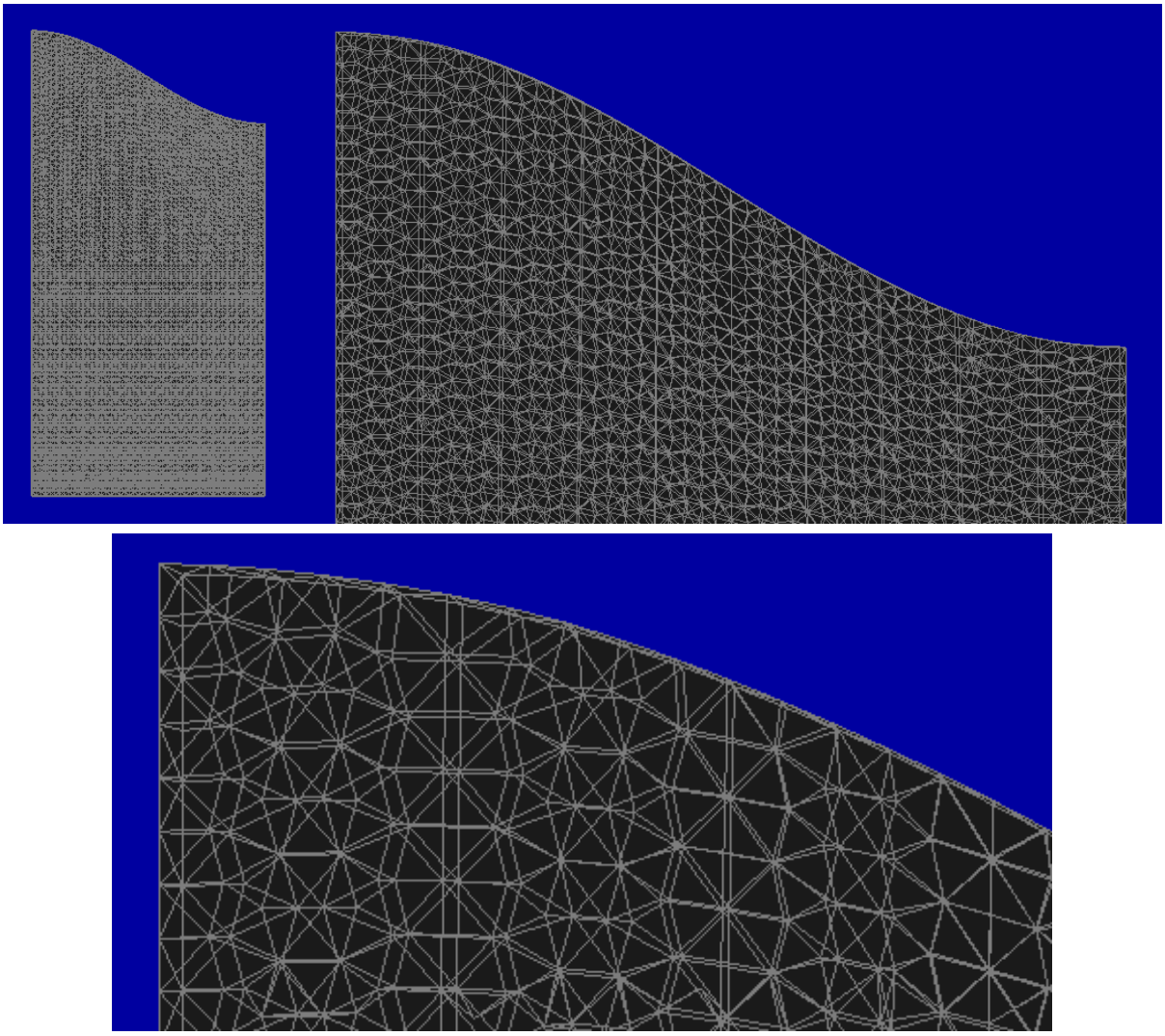

Figure 3.13: Meshes of a model for the ripple using Femap. Each subsequent image is more zoomed in to show more detail of the mesh. 3D tetrahedrons are used.

3.2.3 Rad-Hydro Code

For using Eureka, a boundary condition is needed to simulate the drive imparted on the ripples and heat shield by the laser impinging on the ablator of the target package used in the experiments. A one-dimensional radiation-hydrodynamics (rad-hydro) code simulating laser-material interaction is used to obtain the boundary condition on the heat shield, which drives the ripples in the RM experiments. The 1-D rad-hydro code Hyades [64] is used to create the drive profiles in the form of particle velocity that are used as inputs during the Eureka simulations. Simple simulations using velocity drives such as step or ramp functions can be used in Eureka without using Hyades. However, to get the most accurate simulations, the drives obtained using a specific laser energy in Hyades are used. This is not done in conjunction or relation to the modeling or meshing, but is carried out before the simulations are run in Eureka. Hyades is a 1D hydrodynamic software created by Jon Larson of Cascade Applied Sciences, Inc. For obtaining the boundary conditions for the present simulations of RM experiments, Hyades simulations were performed by Dr. Aaron Stebner. The Hyades simulations have been calibrated using the VISAR (particle velocity) measurements in laser experiments. The simulations are calibrated to drive shots of similar heat shields and ablators that are used in the experiments. Hyades simulations can also be used to design ablators, heat shields, and laser energies. The goal is to calibrate the simulations such that VISAR velocity profiles and breakout times at the rear surface of the samples are matched. Once calibrated, the 1D software is used to calculate pressure, velocity, and temperature profiles at the heat shield – ablator (RM) or heat shield – reservoir (RT) interface for laser energies that correspond to peak pressures of 0.500 – 3.500 Mbar in the targets. These profiles are then used as inputs into Eureka. Figure 3.14 shows sample velocity profiles output from Hyades for various laser input energies than can be used as boundary conditions on the heat shield in Eureka.

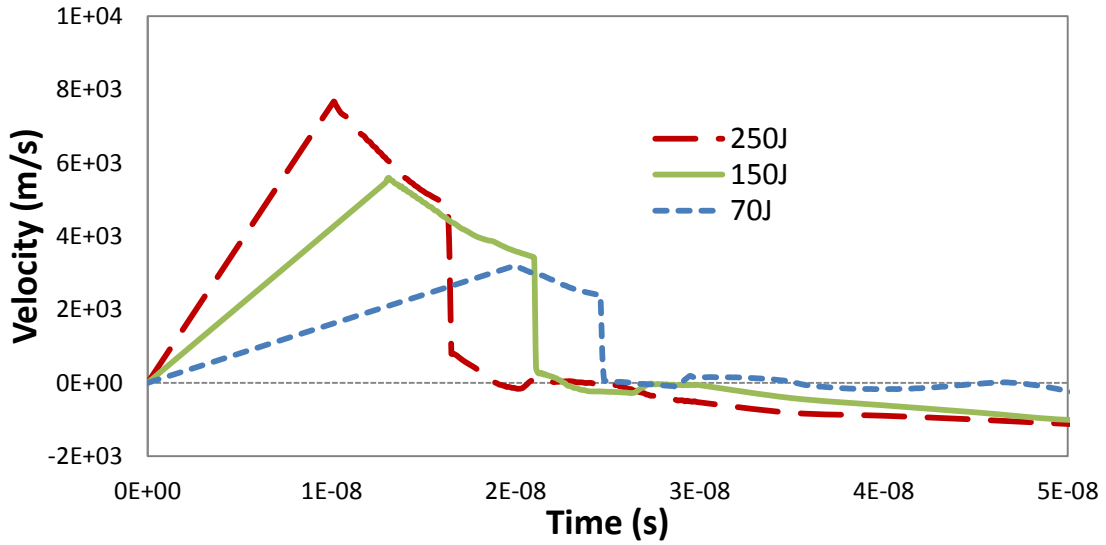

Figure 3.14: Velocity profiles for three different laser energies. These are obtained using the 1D rad-hydro code Hyades, and used as the inputs for the velocity boundary conditions in Eureka.

Rad-Hydro Codes to Design Laser Experiments: The purpose of using Hyades is to reduce the need for incorporating radiation-hydrodynamics into Eureka. Essentially, the experiment is modeled in Hyades until a certain point (the heat shield interface), where Eureka takes over. These RT and RM experiments were designed using radiation-hydrodynamics codes, so the experimental setup and the components (ablators, heat shields, and energy) are already established.

These rad-hydro codes are used to model the flow of energy from the Omega lasers to the pressure drive that accelerates the rippled interface, which thereby drives the RT or RM growth [50]. These codes utilize hydrodynamics, radiation transport, opacities, and equations of state via SESAME. Simulations using advanced rad-hydro codes performed by LLNL are performed to determine the plasma drive. The plasma drive is a pressure boundary condition necessary in the experiments and can be used in the Caltech simulations [50]. It is critical in these simulations to be able to model the experiments that involve reaching the desired pressure and remaining at that pressure for long enough for the ripple to show growth. The rad-hydro codes can also ensure that the sample remains solid. Eureka can also be used to verify that melting has not occurred. In these experiments, the loading starts with a weak shock and the amplitude of that shock must stay low enough such that shock heating does not melt the sample [50]. The codes can also be used to understand the timing of any subsequent shocks or reflections. By using these rad-hydro codes, designers can make choices that optimize the experiment. This includes whether to use direct drive or indirect drive, what ablator materials to use, and how thick different components such as heat shields and ablators should be [50]. In the actual Omega experiments, the simulations give insight into timing for diagnostics such as radiography, diffraction, and backlighters.

To simulate dynamic experiments, current hydro-codes are more advanced than previous codes that treated solids as fluids [50]. Before, codes neglected components of stress other than pressure, but now these codes involve some form of strength. They utilize the conservation of momentum equations relating to the divergence of the full stress tensor including shear components [50]. Strength models provide the constitutive response of the material and can be modeled in the form of Steinberg-Guinan, PTW, or other first-principle models [6, 7].

Hyades Profiles into Eureka: The main purpose for Hyades in the simulations is to obtain the drive profiles. These Hyades files which are provided as data files must be preprocessed before going into Eureka. A Maple file is utilized to preprocess the input files so that they can be read into the RT or RM test within Eureka. Figure 3.14 shows some of the velocity profiles used when determining which drives to use for Omega experiments. By running through several different profiles, the ones that exhibit growth can be determined. After drives are taken from Hyades and modified in Maple, they are ready for input into Eureka. The following section covers some of the aspects of using Eureka.

3.2.4 Visualization

Once simulations have finished running in Eureka, they must be viewed visually in order to perform post-processing and analysis. For this analysis, a program called Paraview is used. This provides a way to import the data files from the simulations into a visualization program.

Paraview is a data analysis and visualization program. The program is open-source and widely used by engineers and scientists to build visualizations of their large data sets to analyze both qualitatively and quantitatively. Data analysis can be done interactively by viewing the 3D data, or it can be done programmatically using the batch processing capabilities [65]. Paraview is built on top of a VTK library. VTK, or visualization tool kit, is a type of data file or library used to provide visualization for data. Paraview uses shared-memory and clusters or can be used on individual computers when the data sets are not too large. Figure 3.15 is an image of the Paraview interface used for visualizing the results of the simulations. In this case, a half ripple was being tested.

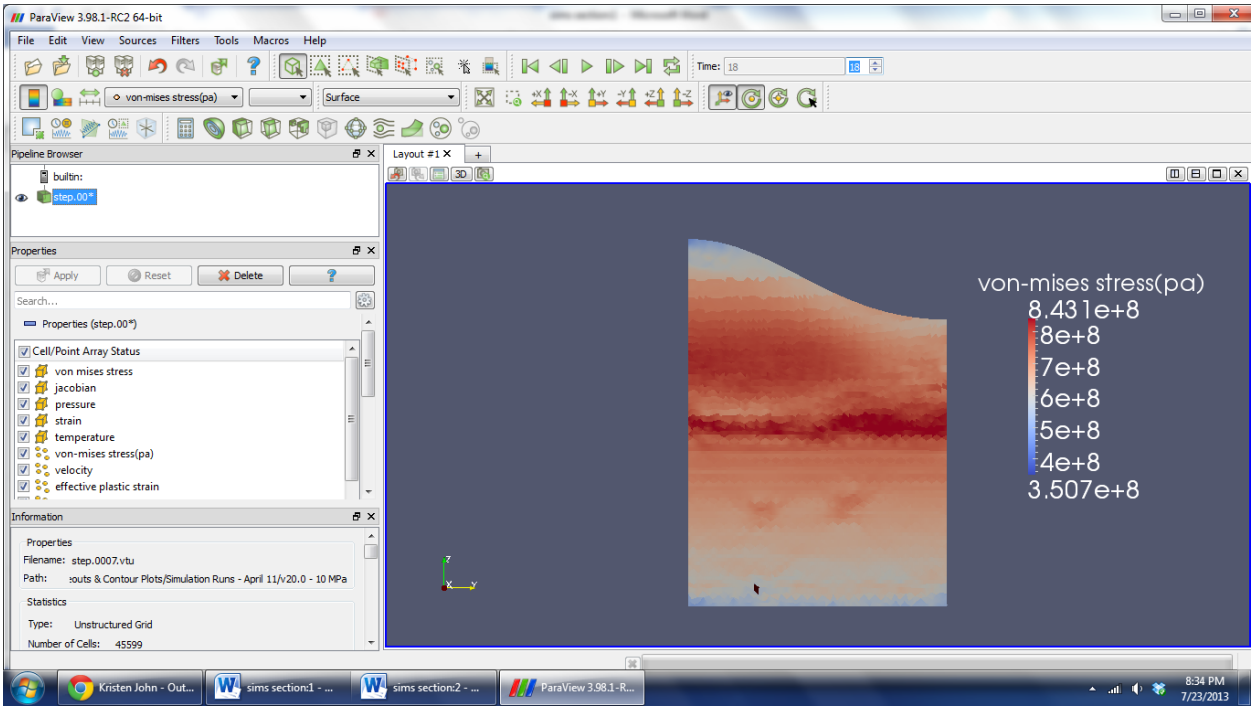

Figure 3.15: Paraview interface used for visualizing the results of the simulations.

Paraview allows for visualization of the results of the experiment as time progresses throughout the experiment. The simulation can be viewed in its entirety, it can be viewed time step by time step, or it can focus on one particular time step of interest. Paraview also allows for visualization of the simulation from any point of view. The color maps on the side provide real time data that updates with each time step. Many parameters of interest can be visualized, including von mises stress, Jacobian, pressure, strain, temperature, effective plastic strain, velocity, etc. Additionally, it provides the ability to visualize several different representations of the model, including surface,

outline, points, edges, volume, or wireframe. Within Paraview, movies or animations can be created of the progression of the simulation.

The visualization is used to understand several different values as a function of time, including pressure, velocity, and stress. The most critical measurement is how the ripple grows as a function of time. Paraview allows for visualization of the growth and provides a means of quantifying growth when nodal displacements are not available. The results of the ripple growth and other aspects of the simulations will be discussed in the following two chapters. Figure 3.16 is an example of how Paraview allows for visualization of growth as a function of time.

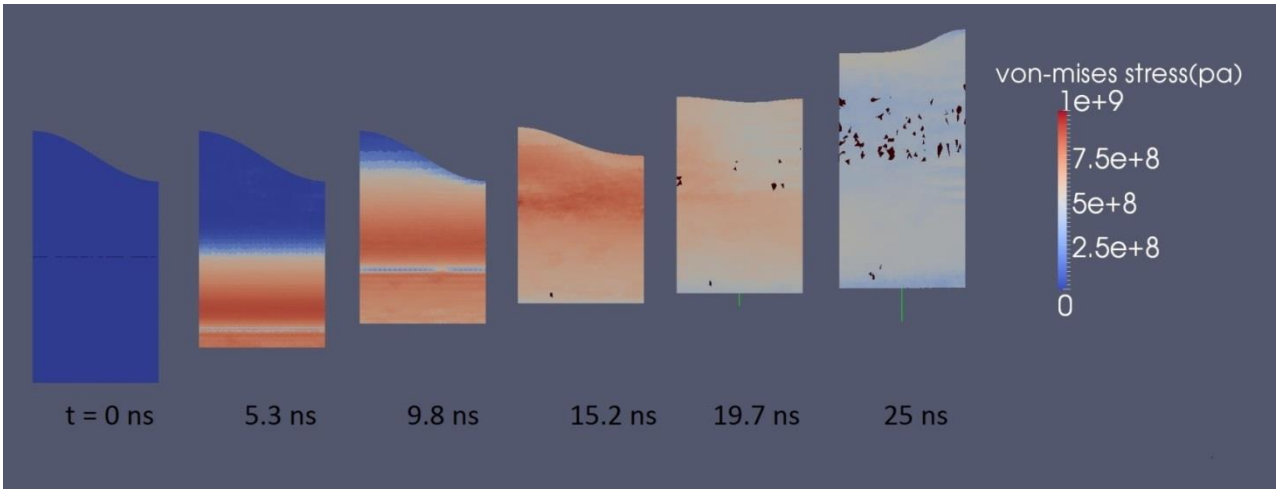

Figure 3.16: Using Paraview, the ripple growth as a function of time can be observed, as well as certain quantities of interest, such as von-mises stress in this case.

The last several sections have discussed the methods and programs needed to effectively use Eureka for simulating laser driven Richtmyer-Meshkov experiments. This included modeling in SolidWorks, meshing in Femap, creating the boundary conditions in Hyades, and using Paraview for visualization. The next section will focus on using Eureka itself.

3.3 Using Eureka

3.3.1 CACR & SHC

Eureka is implemented in its parallel version via Caltech's CACR or the Center for Advanced Computing Research. The purpose of CACR is to provide Caltech users with state-of-the-art computational science resources. CACR has several systems available. SHC (or the Shared Heterogeneous Cluster) is used to provide the necessary computational capabilities to run the simulations. CACR's shared cluster model is "optimized for parallel numerical codes that can sustain over 1 trillion floating point operations per second" [66]. SHC consists of 352 2.2Ghz AMD Opteron cores, 308 2.4 GHz AMD Opteron cores, ~1.3 TB of memory, all interconnected by an Infiniband networking fabric that can move 160+ Gigabytes/s between the compute nodes" [66].

The 'sharing' in the shared cluster comes from the fact that it is used by several partner groups, each receiving on allocation of time. By doing this, each group gets better pricing, staff that can administer the cluster, and a much larger machine than each would have on their own. To access SHC, one must 'ssh' in. To perform edits, compiles, builds, and job submissions, users do this at the front end. The system configuration for SHC includes "163 dual core/dual processor nodes and 66 quad core/dual processor nodes, connected via Voltaire's Infiniband and a Force-10 Gigabit Ethernet Switch" [66]. MPI, or message passing interface, is the programming model used within SHC and it uses a flexible queue policy to allow for runs in an organized method.

To access the SCH cluster and work on the CACR computers, login is required using SSH. SSH or secure shell is a secure method of data communication using remote command line log in and remote command line execution. On one's personal computer, there must be a terminal compatible with SSH to log in. Once logged into the SHC, a series of different folders will exist for each user. Here, Eureka can be accessed. Within Eureka, updates to input files and configuration files can be made based on the needs of the simulation. Eureka has a large collection of capabilities. Only those related to the simulations need to be in the folders. These folders will contain the setups of the different simulations, where the model/mesh will be called. The different configurations used for the simulations in this research, such as the RTI or the RMI, are discussed more in following sections. Essentially, all the input files, configuration files, and test files needed to run a simulation will be located in these folders. By going to these folders, adjustments can be made to the values or the files can be replaced with new ones. Once all the parameters are set, a job can be submitted. A job submission will fail if something has been done incorrectly. Once the job is successfully submitted, it is put into a queue where the status can be monitored. Depending on the number of nodes and cores called for when setting up the test, the simulation could take anywhere from seconds to days to run.

Within the test setups, an objective is to change and look at several different aspects within the test. Oftentimes, the drive input is changed. These drives can come from Hyades rad-hydro code, or a simple drive, such as a ramp or step drive, can be used. Either way, the drive profile is one of the input files that must be created for each test. This drive actually initiates the growth in the ripple, which is what the simulations are trying to achieve. Eureka is also configured such that it calls the proper EOS based on the material (i.e. Ta) that is input. Permission to use the SESAME EOS for Ta was granted such that the Ta EOS is among others in the database Eureka can access. As discussed earlier, the EOS data points are in the *(J,T)* space and are extracted in tabular form and interpolated linearly in each cell of the domain. In addition to changing the drive and accessing the EOS, different material and configuration parameters can be altered. These are discussed in the following section. Before every simulation job is submitted, these files must be updated with the relevant parameters.

3.3.2 Boundary Conditions and Sample Configuration

Geometry of Sample Configurations and Heat Shield: The geometry of the Ta sample depends on the simulation being performed. Both single-mode and multimode configurations of the Richtmyer-Meshkov instability are simulated in this research. Chapter 4 focuses on the simulations involving single-modes, and Chapter 5 focuses on the simulations involving the multimode ripples. The dimensions of the single-mode ripple are a length of 50 μm, a width of 0.5 μm, and a height of 200 μm. The dimensions of the multimode ripples are a length of 120 μm (this represents one period of the prescribed pattern), a width of 2.0 μm, and a height of 500 μm. For both configurations, the length and width of the heat shield are the same as the Ta sample, but the height is 50 μm. These are illustrated in their respective chapters (see Figure 4.1(a) for the single-mode dimensions and Figure 5.3(a) for the multimode dimensions).

Boundary Conditions: In these simulations, the boundary condition on the top surface of the heat shield is a prescribed velocity profile, which corresponds to the results obtained from the 1D rad-hydro code simulation (Section 3.2.3) of the laser interaction with ablator (Figures 2.1, 2.5). At the bottom of the tantalum sample, the boundary condition is set to be traction-free to emulate the experimental conditions. Only a single ripple is simulated and periodic boundary conditions are used to model the lateral sides of the sample. The simulations are performed in 3D, but the third direction is set to have a unit thickness with lateral surfaces constrained to emulate plane strain.

3.3.3 Material Parameters

One of the key inputs into the simulations is the material parameters. In these simulations, different experiments are being analyzed, such as the Richtmyer-Meshkov instability (RMI) setup. The following sections discuss the different setups in more detail. When the simulations run, they rely upon different inputs such as the material parameters. By changing the values of these parameters, parametric studies can be performed to see their effect on phenomena of interest, e.g. growth rate of ripples. However, for the most part, these parameters are held constant as they are fit to experimental data. The parameters include material type, shear moduli, Lame constant, Young's modulus, Poisson's ratio, density, initial yield stress, reference plastic strain, hardening constant, hardening exponent, reference plastic strain rate, rate-dependent hardening constant, rate-dependent hardening exponent, reference temperature, melting temperature, heat capacity, linear thermal expansion coefficient, thermal-softening exponent, Taylor-Quinney coefficient, and the critical energy release rate. Table 3.1 shows typical material parameter inputs used for tantalum.

Table 3.1: Material parameters for tantalum used in simulations.

Material Parameter	Units	Value
Material Type	N/A	Tantalum
Young's modulus	(Pa)	211.0e9
Poisson's ratio	N/A	0.34
Density	(mg/μm^3)	16.65e-9
Initial Yield stress	(Pa)	100.0e6
Reference plastic strain	N/A	0.12
Hardening constant	(Pa)	100.0e6
Hardening exponent	N/A	0.4
Reference plastic strain rate	N/A	0.0005
Rate-dependent hardening constant	(Pa)	187.0e6
Rate-dependent hardening exponent	N/A	0.0685
Reference Temperature	(K)	273.0
Melting Temperature	(K)	3290.0
Heat capacity	(J/(kg*K) or 1.0e12*J/(g*K))	140.0e12
Linear thermal expansion coefficient	(/K)	6.6e-6
Thermal-softening exponent	N/A	2.0
Taylor-Quinney coefficient	N/A	0.9
Critical energy release rate	(N/m or 1.0e6 * N/mm)	1.31e7

To perform a sensitivity analysis and parametric studies, these parameters can be altered. For instance, by changing the initial yield stress and the hardening constant, it can be determined how the strength affects the growth of the ripples. Similarly, by changing the rate-dependent hardening constant, the effect of the rate sensitivity can be observed. As noted, these parameters are fit to experimental data. To view and alter these parameters, they are located within the plate_material.dat file in the test package.

3.4 Definition and Derivation of Growth Factor

Defining growth factor in the RM simulations was an important step. For each simulation, a set of outputs was provided. These outputs needed to be defined ahead of time so that they could be called in the code and recorded. The values for growth factor were calculated after the simulations using certain values that were stored in the output files. To do this, it was necessary to clearly define growth factor to make sure the correct parameters were recorded in each simulation.

Properties of a Wave or Ripple: Before defining the growth factor, it is necessary to define the terms being used. This is shown in Figure 3.17.

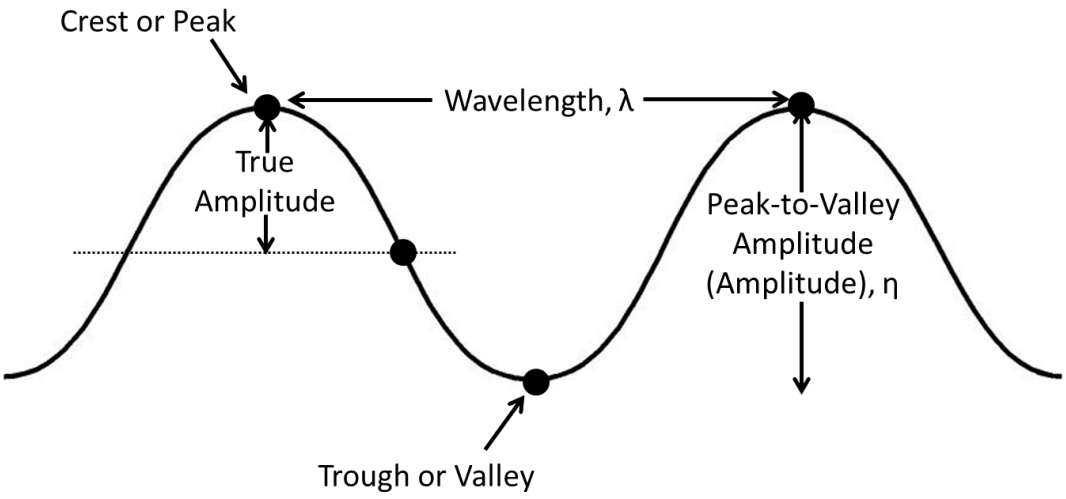

Figure 3.17: Schematic of a ripple

The crest or peak of a wave is the highest point. The trough or valley is the lowest point. The wavelength is the distance between two crests or two troughs, or can be thought of as the horizontal distance of one ripple or wave. Typically, amplitude is defined as the maximum vertical distance between the crest of the wave and the baseline (baseline being the dotted line or "equilibrium" in Figure 3.17). However, that will be referred to as true amplitude, and from this point forward this property is not used to avoid confusion. The peak-to-valley amplitude is of primary interest in the simulations and experiments and is actually twice the true amplitude. The peak-to-valley amplitude represents the vertical distance from a crest to a trough. In this case, it is the height of one ripple. Henceforth, when referring to amplitude, this is the peak-to-valley amplitude. Figure 3.18 shows a typical illustration of a ripple from the simulations with the peak-to-valley amplitude labeled.

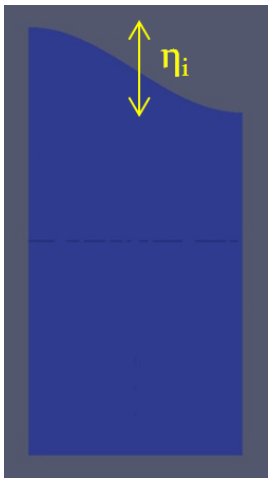

Figure 3.18: A typical ripple in the simulations, with η_i representing the peak-to-valley amplitude.

Standard Growth Factor with no inversion: Typically, defining growth factor is simple. It is the ratio of the current ripple amplitude to its initial value. Assuming the initial amplitude is known (which it

is in both experiments and simulations), then the growth factor can be calculated as long as the current amplitude is known. In experiments, this means only the final growth factor is determined, because the ripple amplitude can only be obtained after the experiment has concluded and not throughout the evolution of the experiment. However, in simulations the current amplitude can be obtained at any point in the simulation, so final growth factor can be quantified, as well as growth factor as a function of time. This is certainly an advantage of the simulations.

Standard growth factor refers to current amplitude over initial amplitude. In many simulations and experiments, this will suffice. In these situations, the wave or ripple does not become inverted, as shown in the illustrations in Figure 3.19. In these cases, the propagation of the ripple is such that the crest always remains ahead of the trough.

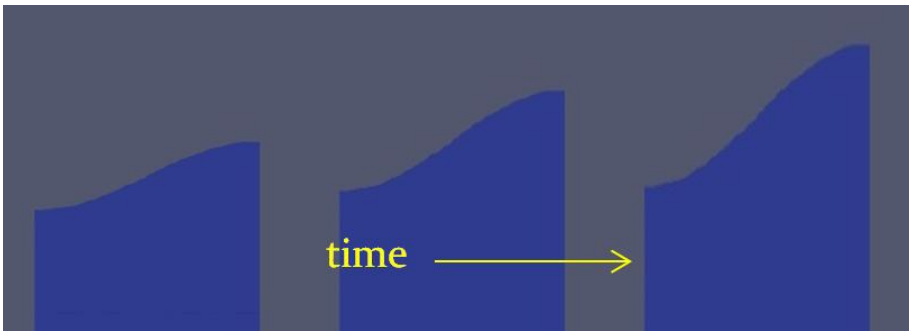

Figure 3.19: Standard growth with no inversion.

The equation for this type of growth is:

$$GF_{final} = \frac{\eta_f}{\eta_i} \tag{3.16}$$

Here, growth factor is represented as GF. The amplitude is represented by η. The final amplitude is represented by η_f. The initial amplitude is represented by η_i. Again, when referring to amplitude, this is the peak-to-valley amplitude. So the final growth factor is the perturbed amplitude or current amplitude over the initial amplitude. In cases where growth factor is measured as a function of time, the equation remains the same.

$$GF(t) = \frac{\eta(t)}{\eta_i} \tag{3.17}$$

Growth Factor with inversion: In several situations, the growth of the ripple or wave is such that it becomes inverted. In these cases, the trough of the wave overcomes the crest, and then the trough continues to grow. In these situations, a new definition is needed for growth factor to account for the compression of the ripple and the subsequent growth, which is shown in the illustration in Figure 3.20.

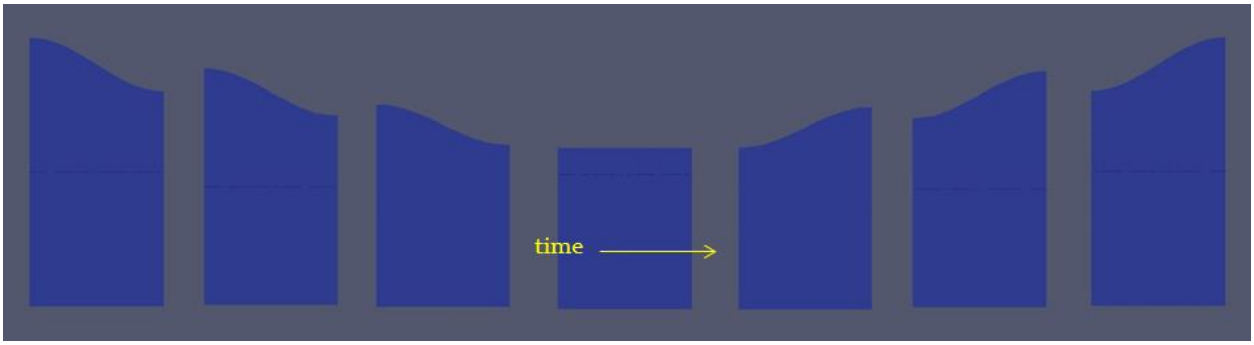

Figure 3.20: Ripple growth with inversion.

As time progresses, the original valley or trough evolves such that it becomes a peak or crest. The total growth needs to be accounted for in the definition for growth factor. Until the trough overtakes the crest, it is referred to as "standard" growth. Standard growth can occur when the crest always stays above the trough, and the crest grows more than the trough. Alternatively, this can occur when the ripple is compressed but the crest is still above the trough. The growth is quantified by the delta of the crest to the trough. During inverted growth, at some point in time, the trough will overtake the crest. Then the trough will become the new crest. In any case, both the standard growth and the inverted growth need to be accounted for in the growth factor calculation, as shown in Figure 3.21, with sample values.

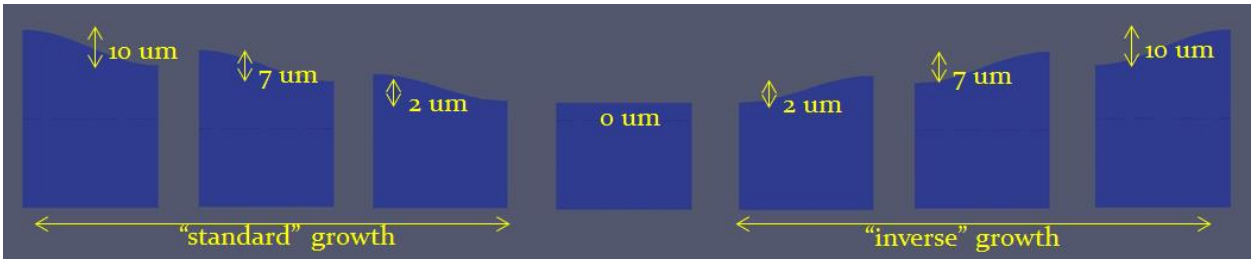

Figure 3.21: Ripple growth with standard growth and inverse growth.

For instance, if the initial amplitude is 10 μm and then the ripple becomes inverted such that the trough overtakes the crest and the final difference is another 10 μm, then both the original difference in amplitude and the final difference in amplitude need to be accounted for. Based on the work by Park and the LLNL team [32, 33], and to avoid a classification scheme that uses negative numbers or fractions, it is defined that a ripple with no growth has a GF of 1. The derivation for growth factor is given in the following section. Since the original crest and trough essentially trade places, the terminology can become unclear. Therefore, the left and right sides of the ripple are defined. Figure 3.22 helps depict the variables.

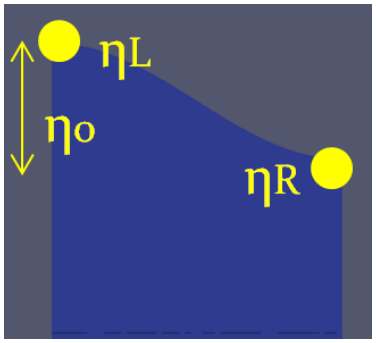

Figure 3.22: New nomenclature for variables to avoid confusion of inverted crests and troughs.

The peak-to-valley amplitude is defined by η. As per the illustration in Figure 3.27, η_0 is defined as the initial amplitude. This is constant, whereas the other values of amplitude are a function of time.

$$\eta = \eta(t) \tag{3.18}$$

The change in amplitude changes as a function of time. Therefore, the change in amplitude as follows is defined as follows.

$$\Delta\eta = \eta_0 - \eta_c \tag{3.19}$$

Here, η_c represents the current amplitude at any given time of interest. The current amplitude is defined by the difference of the crest and trough or the leftmost and rightmost points of the ripple at any given time.

$$\eta_c = \eta_L - \eta_R \tag{3.20}$$

Therefore, the growth factor is defined by the following equation.

$$GF = \frac{\eta_0 + |\Delta\eta|}{\eta_0} \tag{3.21}$$

This accounts for any growth that occurs before and after inversion. This equation will also work for instances with no inversion. This equation also follows the rule that LLNL uses, which is that a ripple with no growth has a GF of 1. For instance, if the initial amplitude is 10 μm, then following Equation 3.21, since $\Delta\eta$ is 0, the GF will be 10/10 or 1. If the left and right points of the ripple are equal, then η_c will equal 0, so $\Delta\eta$ will equal 10, giving a GF of 2. If the ripple becomes inverted such that the amplitude on the right hand side is now 10 μm, then η_c will equal -10, so $\Delta\eta$

will equal 20, giving a GF of 3. The illustration in Figure 3.23 shows sample amplitudes and the growth factors associated with the resulting growth.

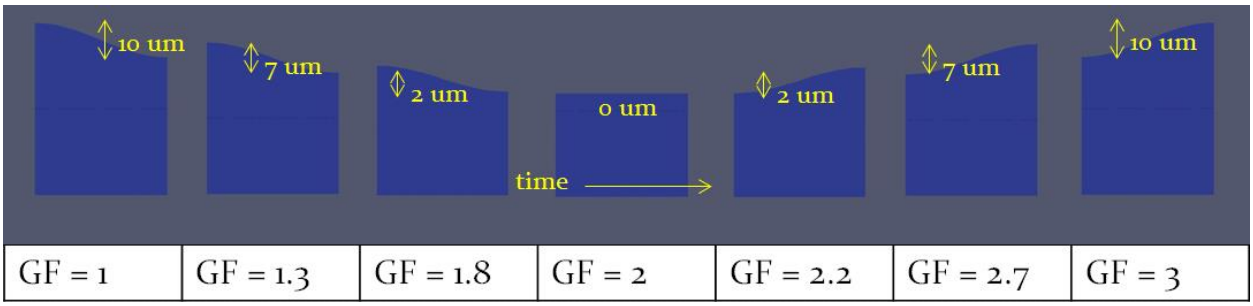

Figure 3.23: Verification of the growth factor definition.

As discussed earlier, the definition of growth factor is important to know before running simulations so that the correct variables can be recorded during the test. Essentially, the definition of growth factor depends on initial amplitude, the leftmost amplitude at any time, and the rightmost amplitude at any time.

$$GF = f\{\eta_0, \eta_L(t), \eta_R(t), t\} \tag{3.22}$$

In the simulations, initial amplitude is known, and an output file is created that contains the left and right points of the ripple at a series of different time steps. This information can be used to calculate final growth factor and growth factor as a function of time.

Chapter 4

Richtmyer-Meshkov Instabilities in Single-Mode Ripples

This chapter describes the results and analysis of simulations performed using a single-mode ripple configuration of the Richtmyer-Meshkov instability experiments. These results are compared to experimental data obtained using the Omega facility on tantalum (Ta) samples described in Chapter 2. Simulations were performed for the six different energies used in the experiments at Omega. The first part of this chapter discusses the simulations, followed by a comparison of the results to each other and to the experiments. This analysis also serves as validation of the engineering model described in Chapter 3.

4.1 Single-Mode Simulations

Before running the simulations using the Eureka code, the configuration was modeled, meshed, and input into Eureka (see Chapter 3). An image of the unperturbed single-mode ripple before the start of the simulation is shown in Fig. 4.1.

In Figure 4.1, the red region is the Ta ripple and the grey region is the BrCH heat shield. These images are at time t=0 (start of the simulation) and hence the ripple pattern has not been deformed. In the Richtmyer-Meshkov (RM) configuration, the drive comes from the top down such that the heat shield is driven into the Ta sample, i.e., light medium accelerating into heavy medium. The dimensions of the single-mode ripples are a length of 50 μm, a width of 0.5 μm, and a height of 200 μm. For the heat shield, the length and width are the same as the Ta sample (length of 50 μm, width of 0.5 μm) but the height is 50 μm. Therefore, ripples have a wavelength of 50 μm, as well as a peak-to-valley height of 10 μm.

4.1.1 Boundary Conditions

In these simulations, the boundary condition on the top is a prescribed velocity profile, which corresponds to the results obtained from the 1D rad-hydro code simulation (see Chapter 3) of the laser interaction with ablator (Figures 2.1, 2.5). At the bottom of the sample, the boundary condition is set to be traction free to emulate the experimental conditions. Only a single ripple is simulated and periodic boundary conditions are used to model the entire sample. The simulations

are performed in 3D, but the third direction is set to have a unit thickness with lateral surfaces constrained to emulate plane strain.

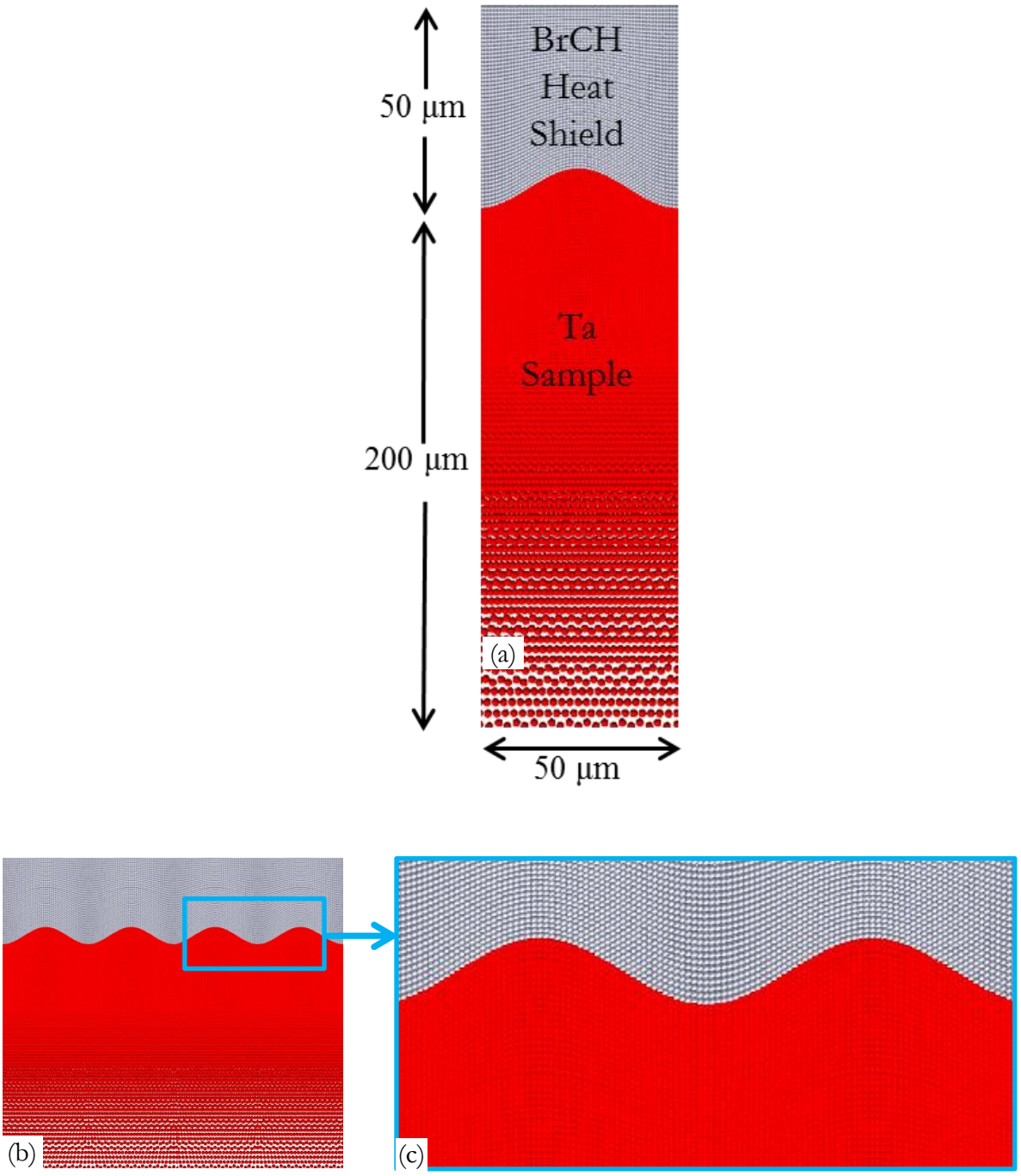

Figure 4.1: Particle model of the single-mode ripple of tantalum used in the Richtmyer-Meshkov instability experiments: (a) full ripple with dimensions, (b) and (c) details of the interface of the ripple and heat shield. The width of the sample and heat shield is 0.5 µm.

To simulate each pattern at different energies, different velocity profiles are applied in the form of the boundary condition on the top. The velocity profile corresponding to three different laser energies (70, 150 and 250 J) are shown in Fig. 4.2.

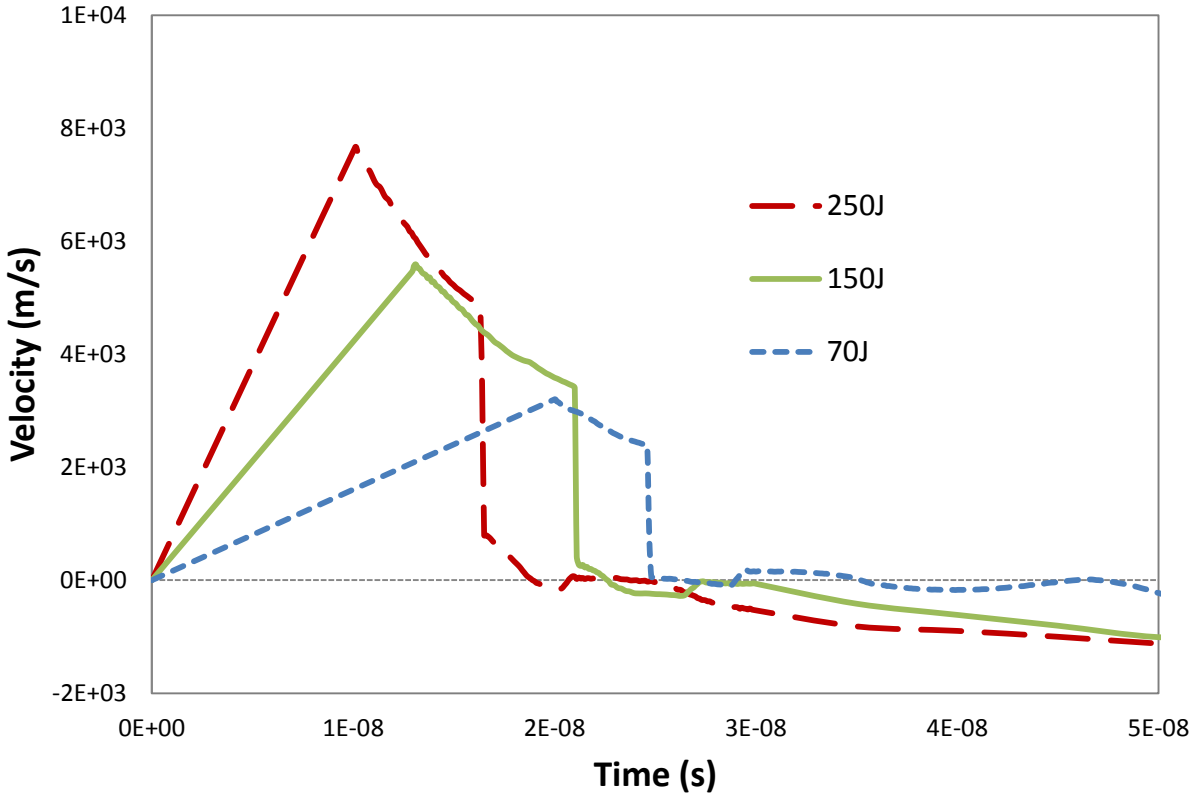

Figure 4.2: Velocity profiles corresponding to three different laser energies, which are used as the boundary condition on the heat shield.

The shape of the velocity profile is designed to counter the effects of the waves and reflections within the heat shield. The initial profile will compress the heat shield, but the reflections at the interface will at later stages lead to tension on the top surface where the loading is applied, causing the heat shield to expand. Additionally, a concern in these experiments and simulations is the reflection of the waves on the free (rear) surface of the Ta sample. Therefore, the thickness of the sample is large enough that interactions from reflections do not affect the results. In a few of the simulations, the wave does reach the back surface of the sample and begins to reflect back toward the interface. However, this does not affect the values for growth factor as the wave does not reach the interface. This will be addressed in the applicable sections.

4.1.2 Growth Factors

To determine growth factor from these simulations, it is necessary to know where the peaks and valleys of the ripples. By tracking the location of the peaks and valleys over time, growth factors are calculated. Growth factor (GF) is defined as the current peak-to-valley height (η_c) over the initial peak-to-valley height (η_i):

$$GF = \frac{\eta_c(t)}{\eta_i} \tag{4.1}$$

In Eq. (4.1), the current height (η_c) is a function of time. Initial height (η_i) is constant and is the peak-to-valley height before deformation (before the simulations begins).

4.2 Results

The results from the simulations for six different laser energies are described in the following section. This is followed by a comparison of the trends for the growth factor for the various drives.

4.2.1 70 J Drive

A simulation was performed for the single-mode configuration with 70 J of energy for the drive. At the conclusion of the simulation, the data was collected and visualized. An animation was created for the simulation, as well as snapshots of the deformed configuration. In the simulations, a series of data files were generated. The data files provide the current locations of the nodes on the ripple surface. From this information, the nodal displacements were obtained and the growth factor was calculated. Figure 4.3 shows a selection of the images from the simulation with approximately 6.3 ns between successive images. In these images, the red region is the Ta sample and the grey region is the heat shield. In the Richtmyer-Meshkov configuration, the drive comes from the top down such that the heat shield is driven into the Ta sample.

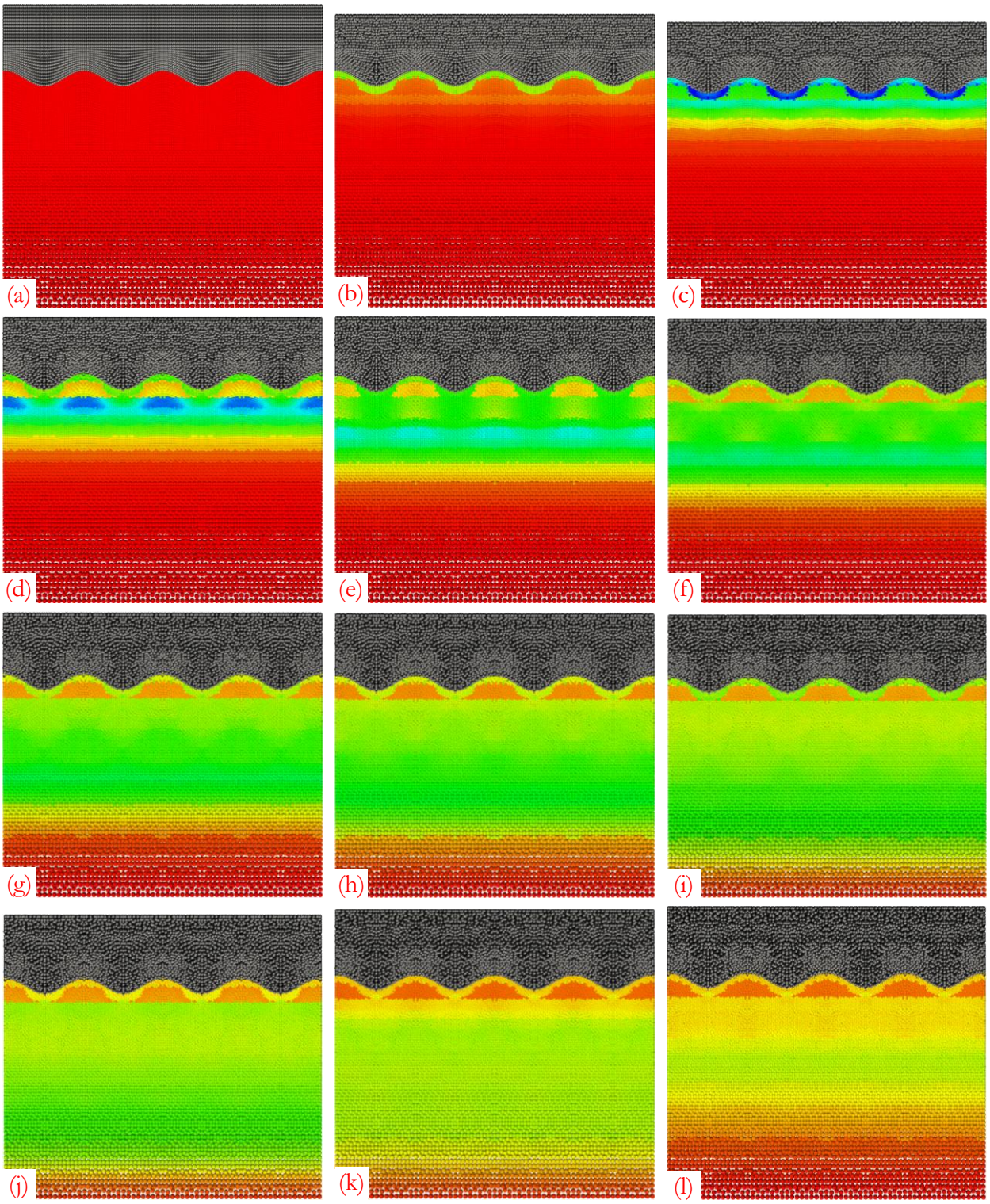

Figure 4.3: Evolution of single-mode ripple in time for a laser energy of 70 J. The images (a)-(l) are snapshots of the ripples starting from time t=0 to t= 69.02 ns, with 6.3 ns between the images.

The velocity boundary condition corresponding to the 70 J laser energy (Fig. 4.2) is applied to the top, which represents the top of the heat shield. It can be seen in the first few images (Fig.

4.3(a)-(c)) that the heat shield is compressing. It can be seen in the last few images (Fig. 4.3(j)-(l)) that the heat shield begins to expand. This is the result of the reflections within the heat shield. It should be noted that the impedance of the heat shield is much smaller than that of Ta. In the earlier images, once the wave reaches the interface of the heat shield and the Ta sample, the Ta sample appears to be compressing. This continues throughout the simulation; however, it is hard to see if deformation of the ripples is occurring. In the last two images (Fig. 4.3 (k)-(l)), the wave reaches the free end of the Ta sample and begins to reflect back toward the interface. However, this reflected wave does not reach the interface, so this does not affect the values for growth factor.

Using the displacements of the peaks and valleys from the simulations, the growth factor is computed using the procedure outlined in Section 3.4. Figure 4.4 shows the growth factor as a function of time for the 70 J drive.

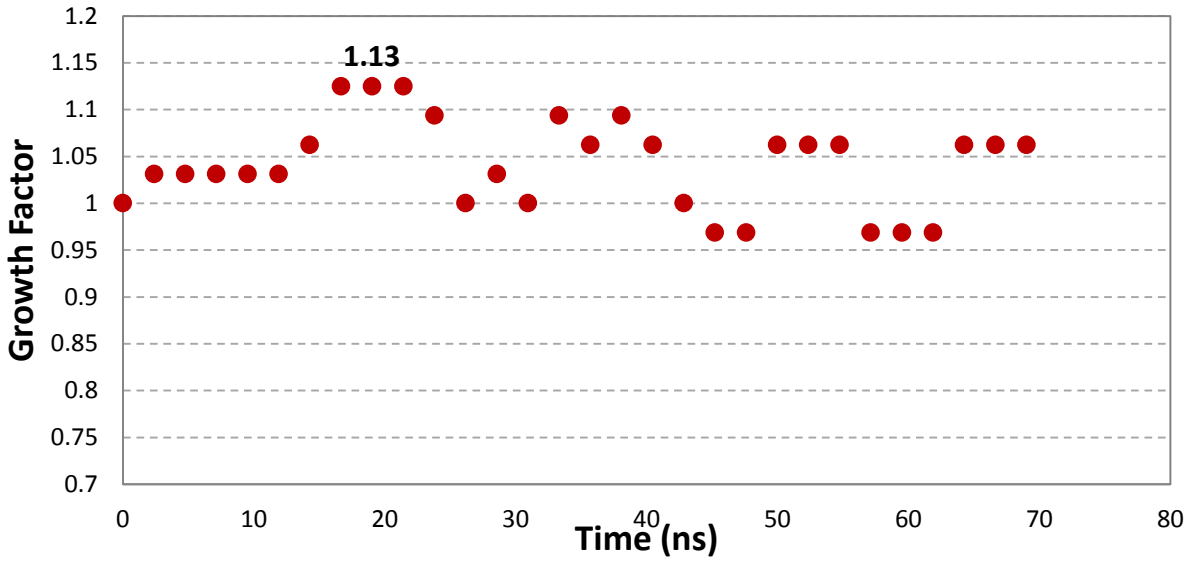

Figure 4.4: Growth factor vs. time for a drive corresponding to laser energy of 70J.

It can be seen from Fig. 4.4 that the growth factor peaks at a value of 1.13 at about 20 ns. Because the growth factor is small in this simulation, as is expected for such low laser energy, the opportunity for error is greater. This is because the growth factor is calculated as current height over initial height (Eq. (4.1)), and information at only a limited number of nodes is available. The value given for the position of the node is an approximation of the location of that point on the surface. For a smaller difference between heights, more error is present because fewer nodes exist and more issues for rounding arise. One way to reduce this would be to create a finer discretization. For a few of the following simulations, this was done, however it did not affect the values for peak growth factor. Rather, it just gave a more accurate representation of the trend. Overall, the trend of growth factor versus time, as well as the peak value of 1.13, appears reasonable for a 70 J driver.

4.2.2 100 J Drive

A simulation was performed for the single-mode configuration with 100 J of energy for the drive. Figure 4.5 shows a selection of the images from the simulation with approximately 6.5 ns

between successive images. In these images, the red region is the Ta sample and the grey region is the heat shield. In the Richtmyer-Meshkov configuration, the drive comes from the top down such that the heat shield is driven into the Ta sample.

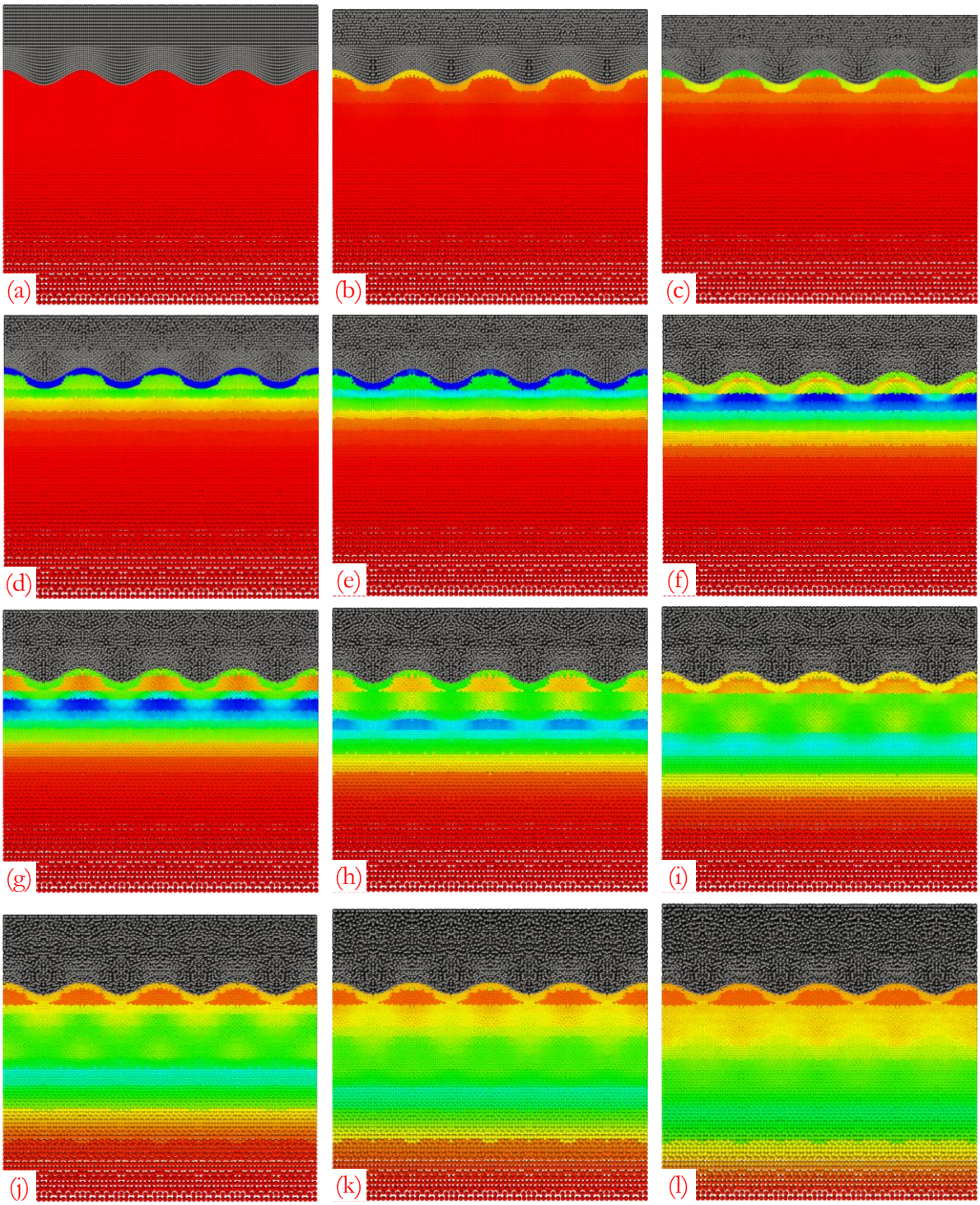

Figure 4.5: Evolution of single-mode ripple in time for a laser energy of 100 J. The images (a)-(l) are snapshots of the ripples starting from time t=0 to t= 71.4 ns, with 6.5 ns between the images.

As seen earlier for the 70 J driver, the heat shield compresses in the beginning, the wave propagates from the heat shield to the interface then down the length of the Ta sample, compressing the sample, and toward the end the heat shield begins to expand because of the reflection of waves within the heat shield.

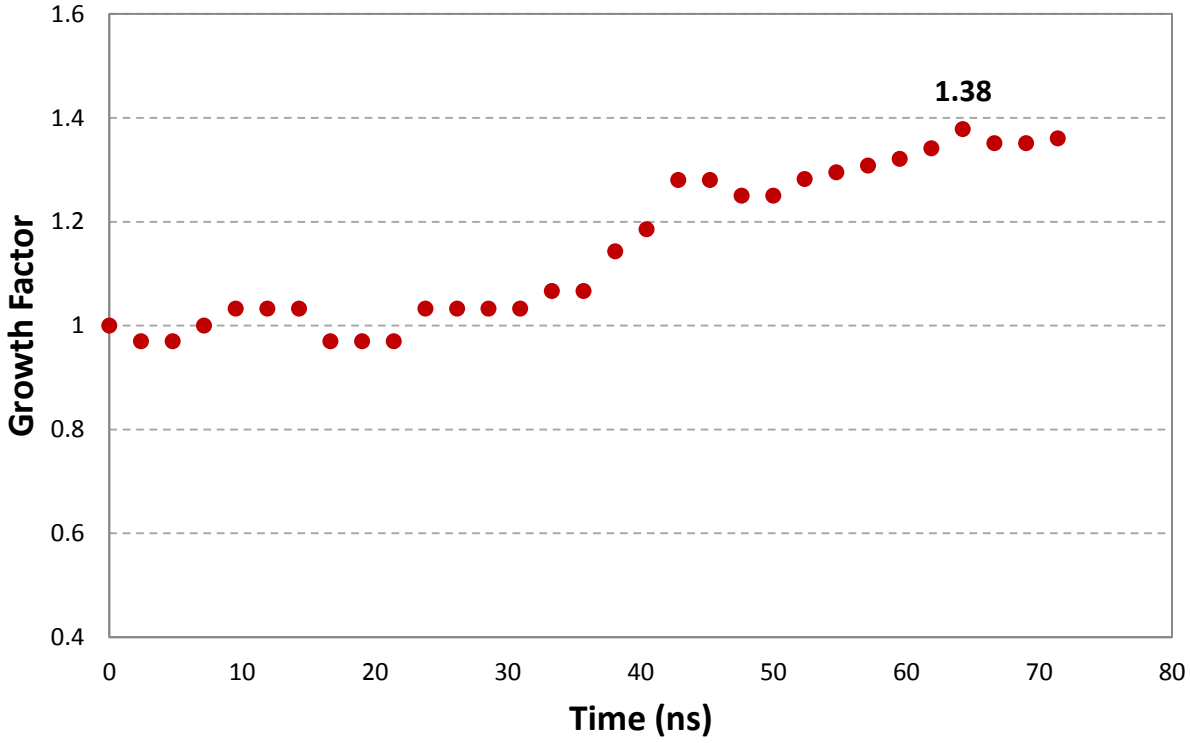

Figure 4.6: Growth factor vs. time for a drive corresponding to laser energy of 100 J.

Figure 4.6 shows the growth factor as a function of time for the 100 J drive. In this simulation, the growth factor peaks closer to the end at about 65 ns with a value of 1.38. This is higher than the 1.13 peak associated with the 70 J, which is as expected. In this case, the values for growth factor generally increase over time

4.2.3 120 J Drive

A simulation was performed for the single-mode configuration with 120 J of energy for the drive. Figure 4.7 shows a selection of images from the simulation with approximately 11 ns between successive images. In these images, the red region is the Ta sample and the grey region is the heat shield. In the Richtmyer-Meshkov configuration, the drive comes from the top down such that the heat shield is driven into the Ta sample.

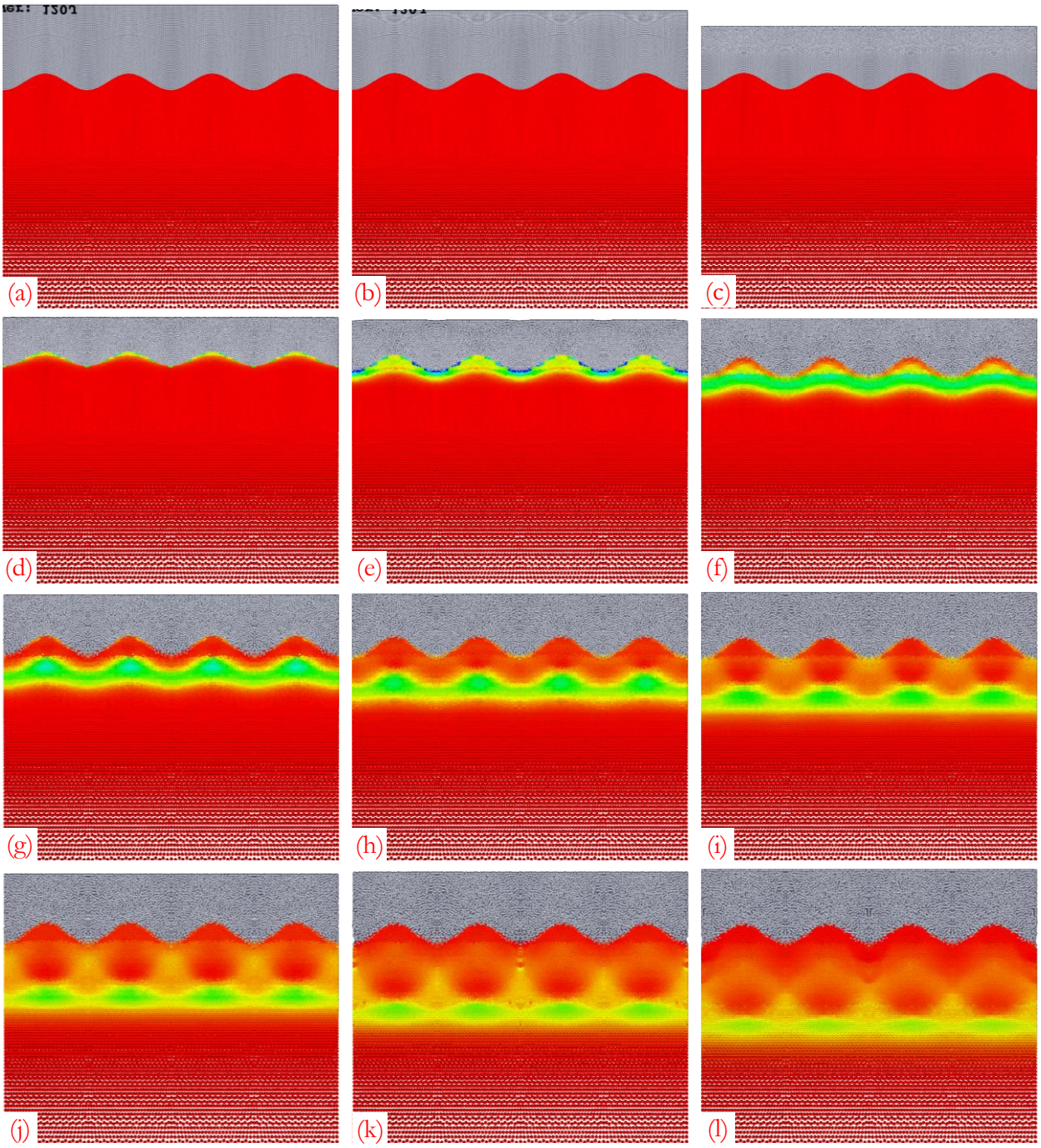

Figure 4.7: Evolution of single-mode ripple in time for a laser energy of 120 J. The images (a)-(l) are snapshots of the ripples starting from time t=0 to t= 121.9 ns, with 11 ns between the images.

As seen in earlier simulations, the heat shield compresses in the beginning, the wave propagates through the interface, and the Ta sample begins to compress. More so than in the last two simulations, the growth of the ripples is evident from the images.

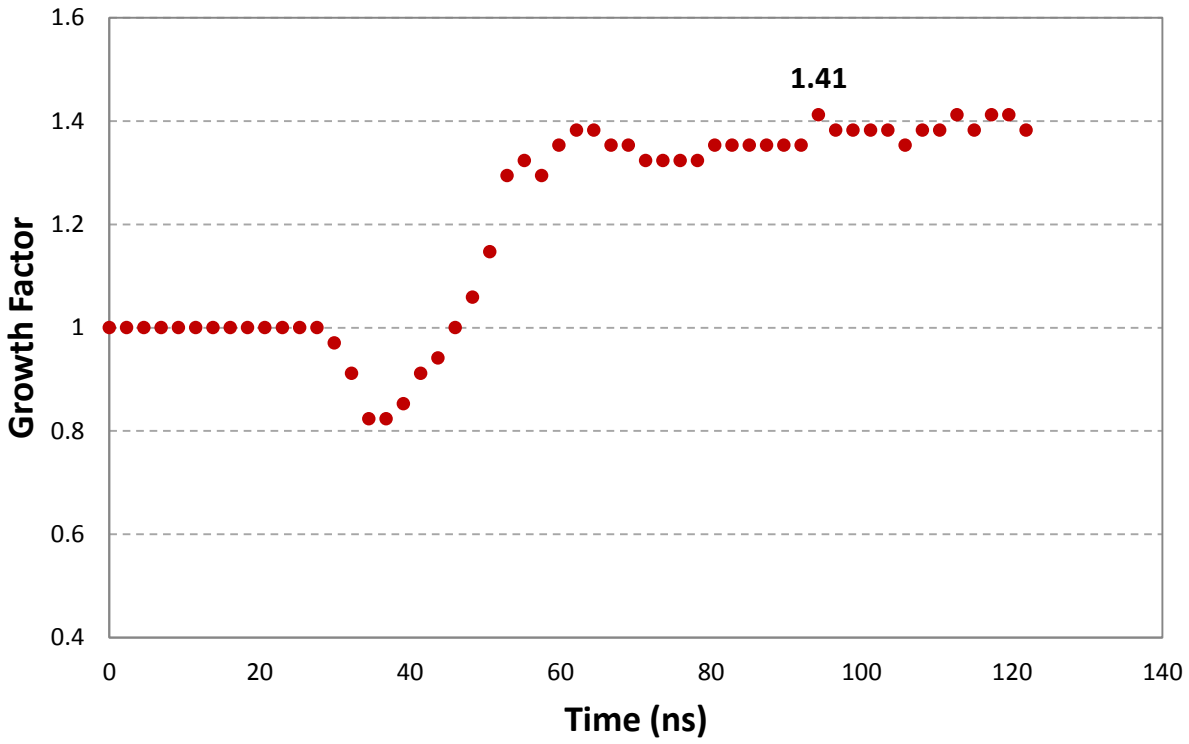

Figure 4.8: Growth factor vs. time for a drive corresponding to laser energy of 120 J.

Figure 4.8 shows the growth factor as a function of time for the 120 J driver. The results of this simulation show a trend for growth factor that follows more closely with what was expected.

Growth does not occur in the beginning as the heat shield is compressing. At about 30 ns, the ripples are compressed and then begin to expand. The growth factor peaks at 1.41 at about 100 ns, but at around 60 ns onward the growth factor remains in this range. For this simulation, a finer mesh was used, providing more frequent data points in the timeframe of the simulation. This allows for more accurate calculation of growth factor, as evident from the smooth transition of data from point to point. Also, because this simulation is at a higher energy, more growth is expected, which is also easier to quantify. It is important to note that for the 120 J case, both coarse and fine meshes were simulated. The results did not affect the value for peak growth factor, but the finer mesh provided more precise calculation of overall growth factors.

4.2.4 150 J Drive

A simulation was performed for the single-mode configuration with 150 J of energy for the drive. Figure 4.9 shows a selection of the images from the simulation with approximately 7.3 ns between successive images. In these images, the red region is the Ta sample and the grey region is

the heat shield. In the Richtmyer-Meshkov configuration, the drive comes from the top down such that the heat shield is driven into the Ta sample.

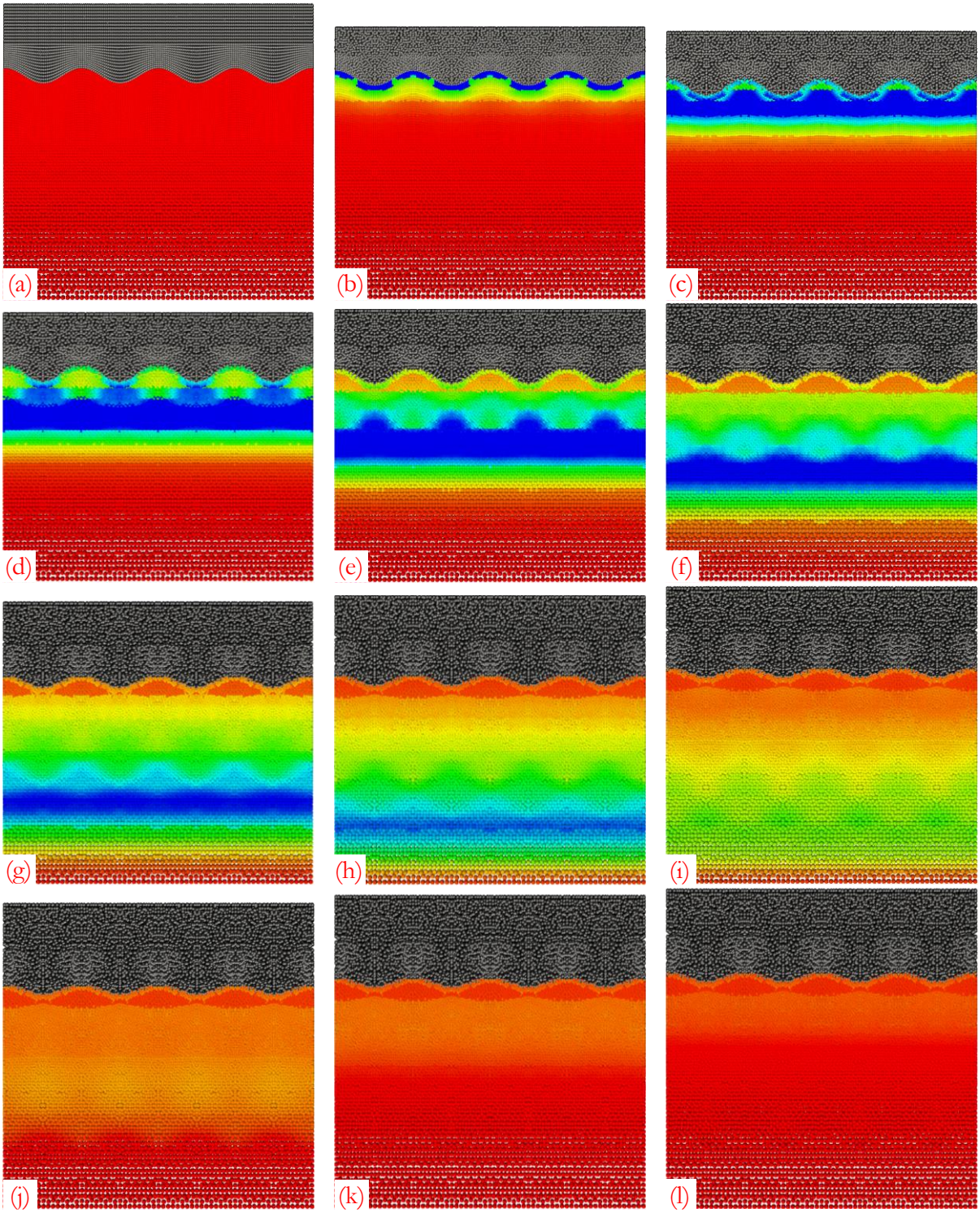

Figure 4.9: Evolution of single-mode ripple in time for a laser energy of 150 J. The images (a)-(l) are snapshots of the ripples starting from time t=0 to t= 80.92 ns, with 7.3 ns between the images.

As observed in the other simulations, the heat shield compresses initially, the wave travels through the interface, reflections within the heat shield causes it to expand, and the Ta sample compresses downward throughout the duration of the simulation. Reflection in the Ta sample occurs at the rear free surface which then travels back toward the interface. Examining the last image (fig. 4.9(l)), it is possible that this wave may affect the values for growth factor in the final stage of the simulation.

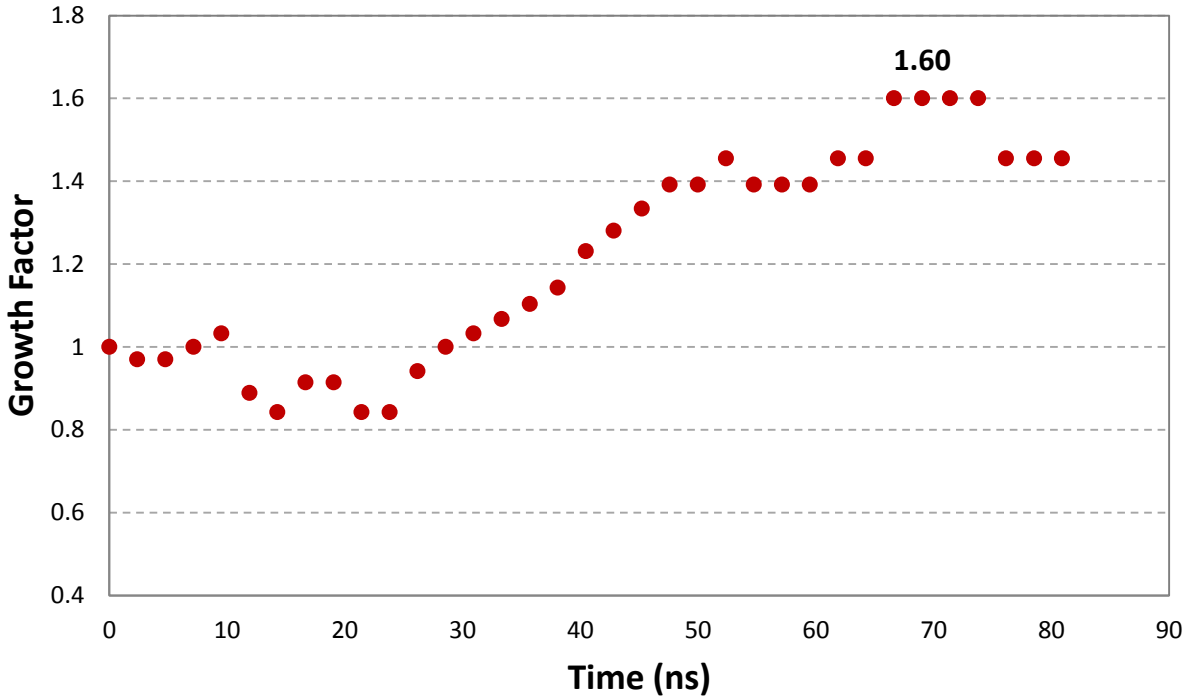

Figure 4.10: Growth factor vs. time for a drive corresponding to laser energy of 150 J.

Figure 4.10 shows the growth factor as a function of time for the 150 J driver. The growth factor steadily increases in this simulation, peaking toward the end at about 70 ns with a growth factor of 1.60. As noted above in the discussion of the images from the simulations, a reflection against the free surface seems to make its way toward the ripple interface. This is potentially the cause for the drop to a growth factor of 1.45 in the final 10 ns of the simulation.

4.2.5 200 J Drive

A simulation was performed for the single-mode configuration with 200 J of energy for the drive. Figure 4.11 shows a selection of the images from the simulation with approximately 16.7 ns between successive images. In these images, the red region is the Ta sample and the grey region is the heat shield. In the Richtmyer-Meshkov configuration, the drive comes from the top down such that the heat shield is driven into the Ta sample.

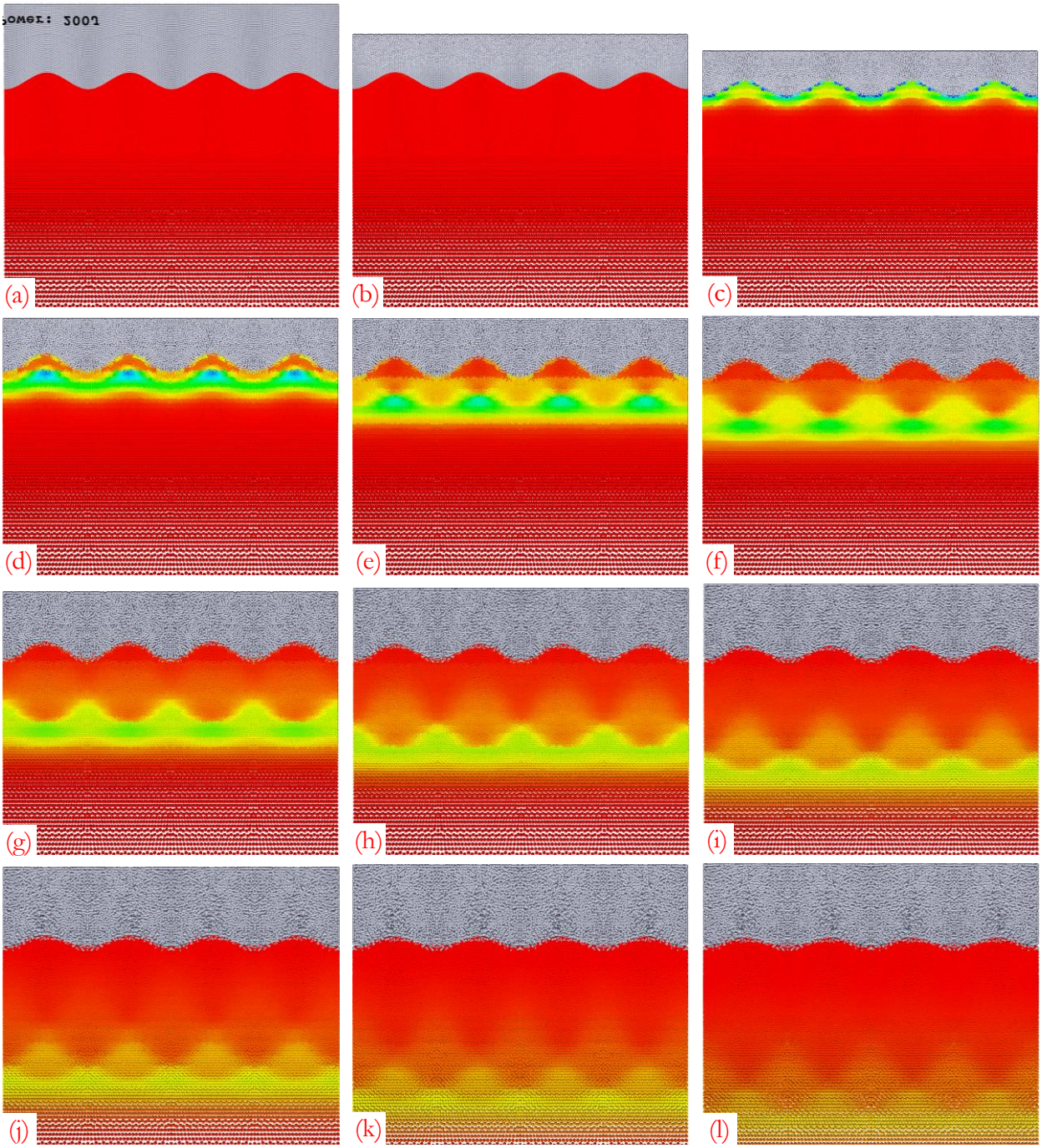

Figure 4.11: Evolution of single-mode ripple in time for a laser energy of 200 J. The images (a)-(l) are snapshots of the ripples starting from time t=0 to t= 184 ns, with 16.7 ns between the images.

Similar to other simulations, the expected physics are shown here involving the compression and expansion of the heat shield, as well as the propagation of the wave through the interface and sample. The growth of the ripples is more evident from these images, especially in Fig. 4.11(d)-(e). The images also show compression of the ripple surface over time.

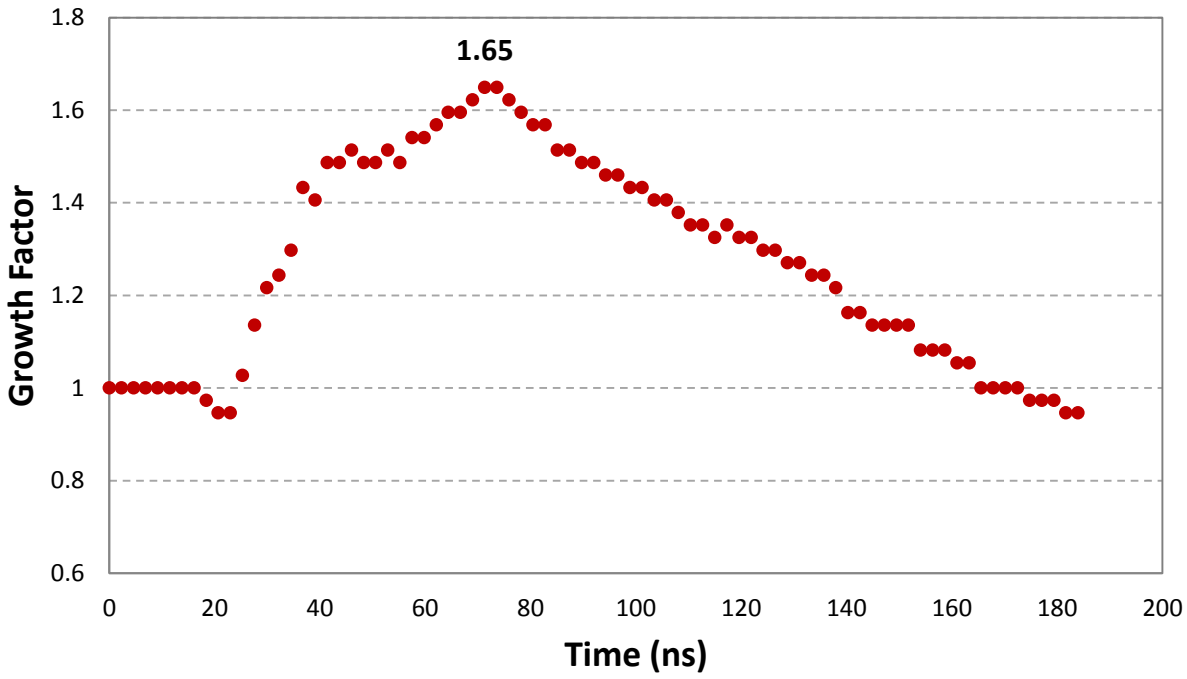

Figure 4.12: Growth factor vs. time for a drive corresponding to laser energy of 200 J.

Figure 4.12 shows the growth factor as a function of time for the 200 J driver. The value for peak growth factor for this simulation is 1.65 at about 70 ns. The trend of growth factor over time follows more closely with expectations. At the start while the heat shield is compressing, growth of the ripple does not occur. Following this, a slight compression occurs followed by a steady increase in growth factor until it peaks at 70 ns. After it peaks, the growth factor steadily decreases until the end of the simulation. As with the 120 J driver simulation, a finer mesh was used for this simulation, providing more accurate measurements for growth factor as evident from the smooth transition of data from point to point. Also, as expected, a higher energy driver results in more growth, which is easier to quantify and results in less error.

4.2.6 250 J Drive

A simulation was performed for the single-mode configuration with 250 J of energy for the drive. Figure 4.13 shows a selection of the images from the simulation with approximately 15.5 ns between successive images. In these images, the red region is the Ta sample and the grey region is the heat shield. In the Richtmyer-Meshkov configuration, the drive comes from the top down such that the heat shield is driven into the Ta sample.

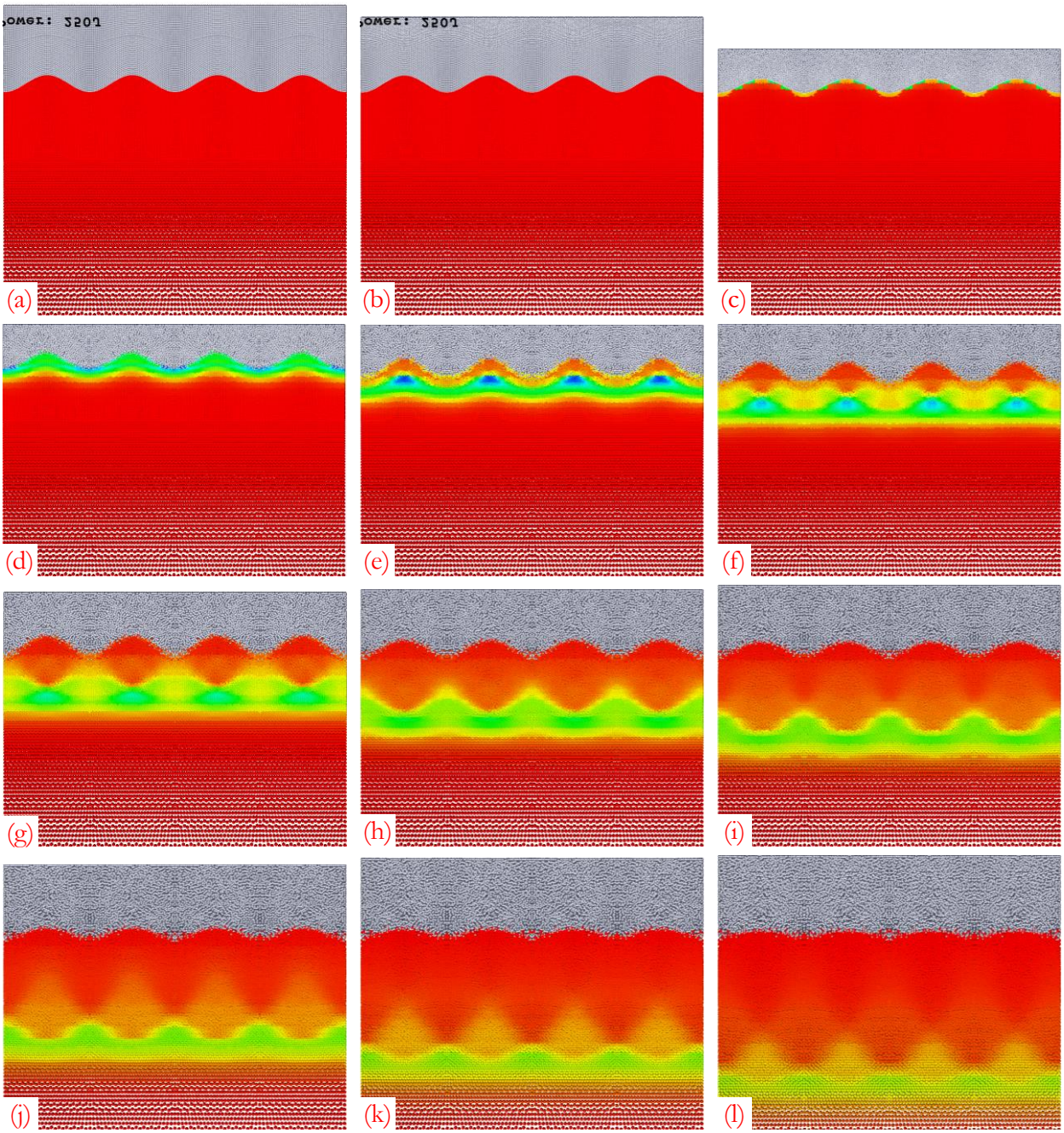

Figure 4.13: Evolution of single-mode ripple in time for a laser energy of 250 J. The images (a)-(l) are snapshots of the ripples starting from time t=0 to t= 170.2 ns, with 15.5 ns between the images.

The results of this simulation are very similar to the 200 J simulation. The expected physics regarding the compression and expansion of the heat shield occur. The heat shield seems to expand even more, which is to be expected for a higher energy drive. The wave propagates through the heat shield and through the ripple interface. The growth of the ripples is much more apparent here, especially in Figs. 4.13 (d) and (e). Towards the later stages of the simulation, the ripple surface shows considerable compression.

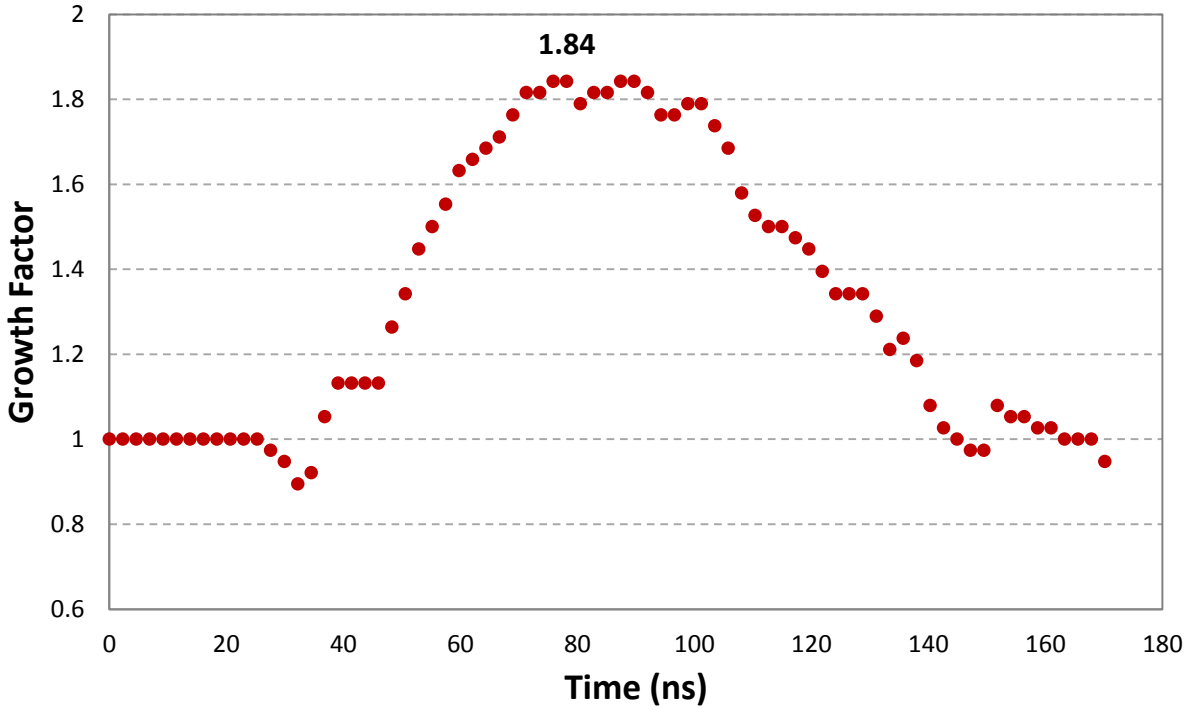

Figure 4.14: Growth factor vs. time for a drive corresponding to laser energy of 250 J.

Figure 4.14 shows the growth factor as a function of time for the 250 J driver. In this simulation, the growth factor peaks at a value of 1.84 at about 80 ns. The trend of growth factor over time is similar to the simulation for 200 J. The initial growth factors remain constant at 1 as the heat shield compresses. This is followed by a slight drop, and then a steady increase in growth factor. The growth factor peaks and remains at that point for over 10 ns before steadily decreasing. Again, a finer mesh was used in this simulation as with the 120 J and 200 J simulations. This does not affect peak growth factor, but provides more accurate values for growth factor as seen above from the smooth transition of data from point to point. This simulation showed the highest growth factor of all the simulations, as expected.

4.3 Discussion

In all, six different simulations were performed for the single ripple configuration of the Richtmyer-Meshkov instability experiment with drives corresponding to laser energies (70 to 250 J) used in the experiments. This section compares the results of the different simulations. Each successive simulation was performed at higher drive energy, and it is expected that with increasing energy, the growth factor increases. The data for the growth factor (GF) from the simulations are summarized in Table 4.1. It is seen that the peak growth factor increases with increasing laser energy.

Table 4.1: Summary of growth factors for single-mode ripple Richtmyer-Meshkov simulations

Energy (J)	Peak GF	GF at the end	Mesh
70	1.13	1.06	Coarse
100	1.38	1.36	Coarse
120	1.41	1.38	Fine
150	1.58	1.45	Coarse
200	1.65	0.95	Fine
250	1.84	0.95	Fine

The values for peak growth factor increase with increasing laser energy, as expected. The final value for growth factor at the conclusion of the simulation does not show the same trend as the peak growth factor. For the laser energies ranging from 70 to 150 J, the growth factor at the end increases. For the laser energies 200 and 250 J, the growth factor at the end decrease, but as discussed above (see Sections 4.2.5 and 4.2.6), the ripples are compressed substantially after the initial growth. Two different mesh sizes were used during these simulations. Initially, the lower laser energy drives (70 to 150 J) were simulated using a coarser mesh. Then a finer mesh was used on the 120 J case. Since both meshes were used on this case, the analysis concluded that the mesh size did not affect the values for peak growth factor. However, due to the increased number of material points in the simulation, there was less error in the growth factor. This has to do with the fact that growth factor is measured by taking current height over initial height (peak to valley) of the ripple. The higher laser energy drives (200 and 250 J) were simulated using the finer mesh. The growth factor is plotted as a function of time for all the laser energies shown in Table 4.1 in Fig. 4.15.

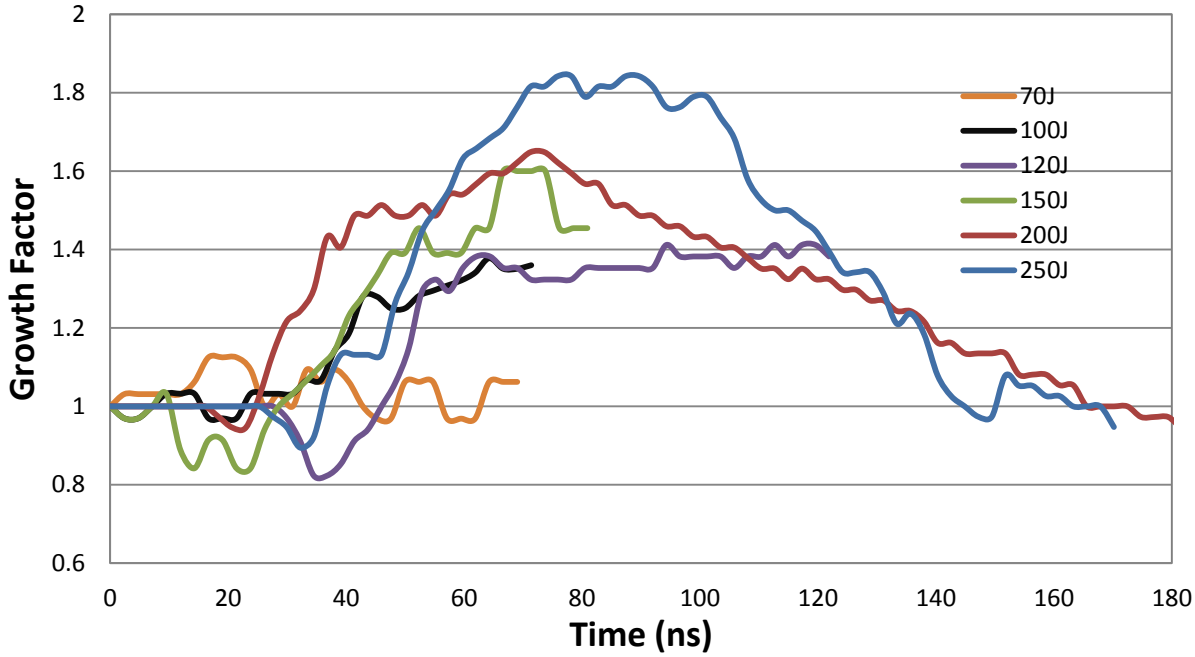

Figure 4.15: Growth factor versus time obtained from simulations for different laser energies.

It can be seen from Fig. 4.15 that with increasing energy, the growth factor generally increases initially up to a t=70 ns (Fig. 4.16). Also, for the longer simulations, it is seen that the growth factor will peak at some point and then begin to decrease. The peak growth factor as a function of the laser energy of the drive is plotted in Fig. 4.17. As energy increases, the peak growth factor increases, as expected.

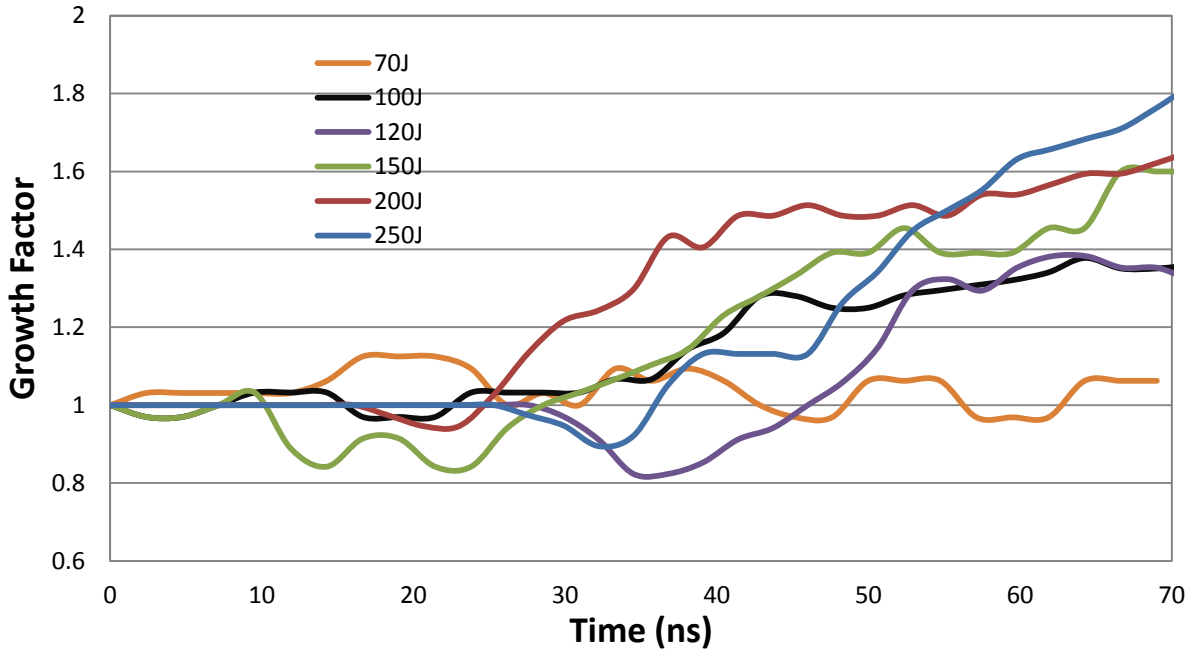

Figure 4.16: Growth factor versus time obtained from simulations for different laser energies. Only the data for the first 70 ns of the simulations are shown.

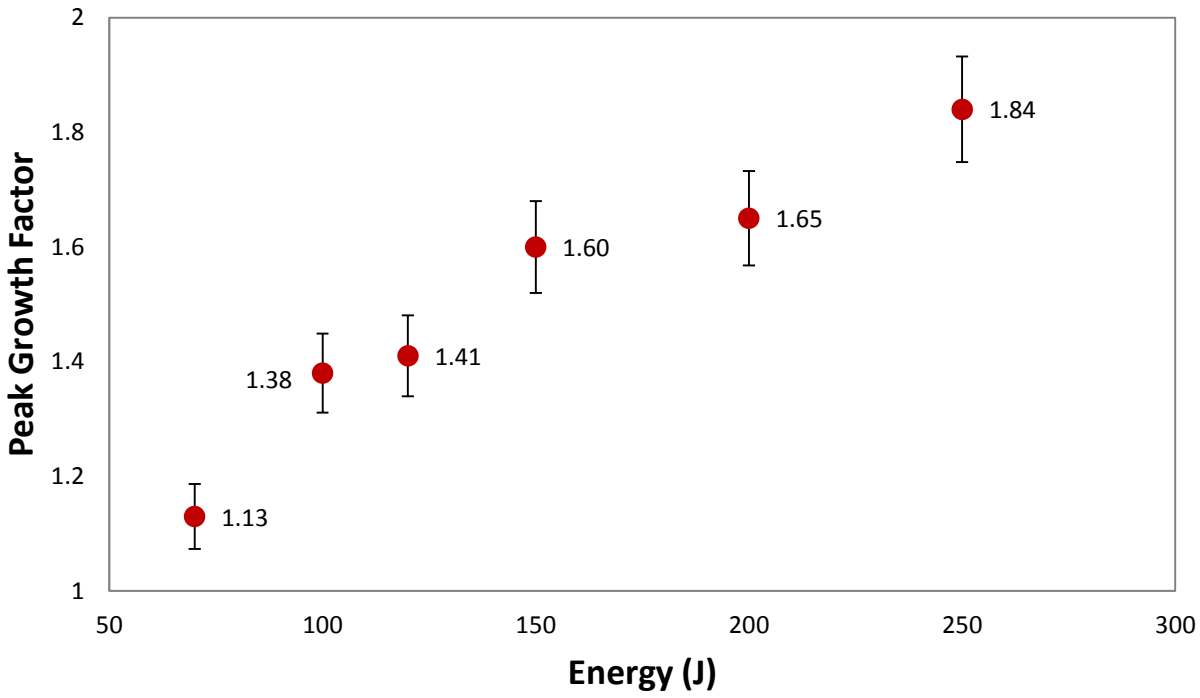

Figure 4.17: Peak growth factor as a function of laser energy of the drive.

Table 4.2 summarizes the predictions of peak pressure both in the rad-hydro code, Hyades, and the present simulations. Values for pressure are not available from the experiments because of the nature of the ride-along experiments. Only the laser energy is known, but VISAR data is not available. The Hyades simulations are calibrated to past experiments that have similar heat shield and ablator designs using the corresponding VISAR data. Then the Hyades simulations are performed on the current targets to obtain pressure and velocity profiles that are used as the inputs into the Eureka simulations.

Table 4.2: Predictions of Peak Pressure using Hyades and Eureka

Energy (J)	Predicted Peak Pressure using Hyades (Mbar)	Peak Pressure in simulations (Mbar)
70	0.98	1.0
100	1.23	1.0
120	1.52	1.5
150	1.96	1.5
200	2.68	2.5
250	3.41	3.5

The peak pressures agree reasonably well with each other. Having two sets of predictions from two different tools is useful given the absence of experimental data for pressure. The images in Fig.

4.18 show the pressure contours within the sample at a specific time for three different laser energies, 120, 200 and 250 J. The images selected are when peak pressures are reached during the simulation.

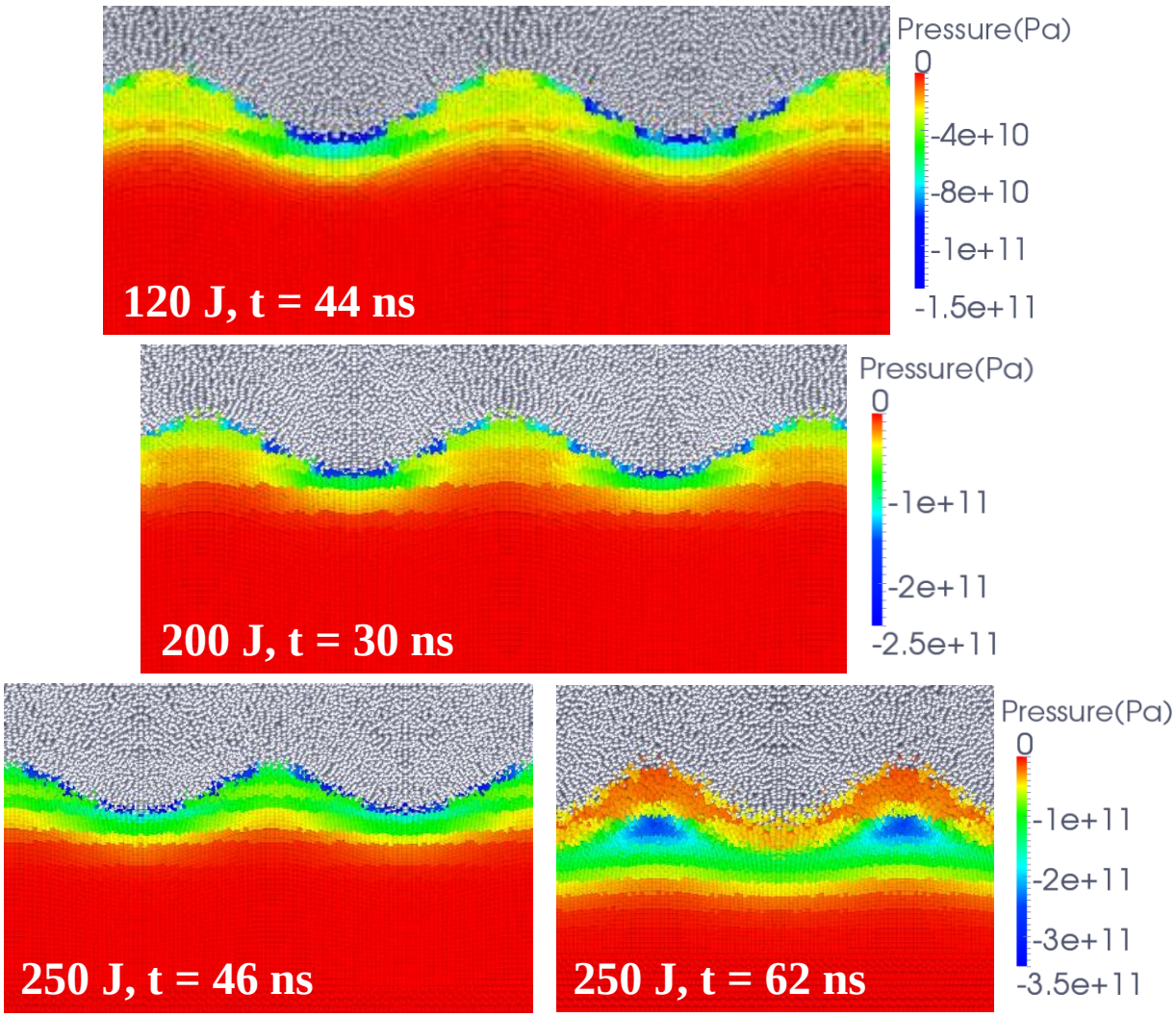

Figure 4.18: Peak pressures attained during simulations for three different laser energies – 120, 200 and 250 J.

For the three laser energies shown in Fig. 4.18, pressure is at a maximum right at the interface of the ripple and the heat shield. For the 250 J case later in the simulation, another peak pressure occurs in the area below the ripples. This is likely due to the pressure gradients associated with the waves propagating through the sample and the compression and growth of the ripple interface. For 120, 200, and 250 J, the peak pressure values of 1.5, 2.5, and 3.5 Mbar, respectively, agree reasonably well with the Hyades predictions. The Hyades predictions for peak pressure are at the location between the ablator and the heat shield interface.

4.4 Comparison to Experiments

The following section compares the simulation results to the experimental data obtained from the single-mode laser experiments performed using the ride-along experimental platform in Omega, as described in Chapter 2. Table 4.3 provides a comparison of the results of the peak growth factor from the simulations to growth factors from experimental data. This data is from experiments performed at Omega on single-mode ripples in tantalum in April 2013, as discussed in Chapter 2. As described in Chapter 2, the measurements for growth factor in the experiments are made after the experiments were completed. Therefore, only the final growth factor is obtained from these experiments.

Table 4.3: Growth Factor (GF) results from simulations and experiments

Shot Energy (J) Request/Actual	GF Simulations	GF Experiments
70/56.6	1.13	1.26
100/95.4	1.38	1.43
120/118.9	1.41	1.43
150/153.5	1.60	1.58
200/202.3	1.65	1.72
250/252.9	1.84	1.97

As seen from the table, the energy requested on the day of the shot is not always obtained on Omega. Therefore, the values shown for growth factor for the simulations are not necessarily at the same energies as in the experiments. In general, there is reasonable agreement between the data from the simulations and the experiments, as seen in Figure 4.19.

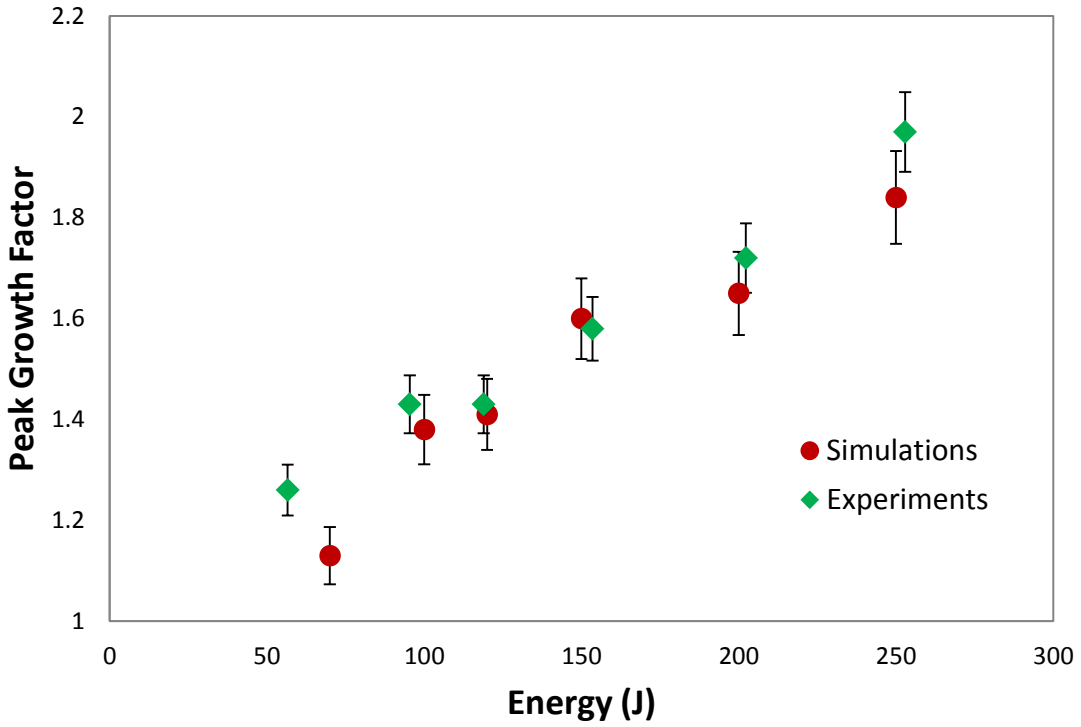

Figure 4.19: Comparison of peak growth factors for the simulations to experimental data.

The peak growth factors from the simulations and the experiments are plotted as a function of laser energy in Fig. 4.19. The values for peak growth factor at various energies agree very well from simulations to experiments except for the lowest laser energy, 70 J.

This combined experimental and simulation effort proved to be a useful validation of the code Eureka, as well as the engineering model for tantalum used in the code. Additionally, these results indicate that the simulations provide valuable information that can be used as predictions for growth factors for future experiments. Furthermore, simulations can be performed prior to experiments at various laser energies to guide the decision of what energy drivers to use for the experiments.

Chapter 5

Richtmyer-Meshkov Instabilities in Multimode Ripples

The results and analysis of simulations performed in the design of a multimode configuration of the Richtmyer-Meshkov (RM) instability experiment are presented.

The previous chapter described simulations that were used to study and characterize the behavior and growth of ripples in tantalum in single-mode ripple patterns. Single-mode means only one initial wavelength is designed into the surface of the sample. This section discusses the use of multimode ripple patterns in simulations. Multimode implies that a number of different wavelength modes are present in the initial amplitudes. Multimode patterns are introduced to study whether or not the drive exhibited linear versus nonlinear instability growth. In the linear region, the modes will grow independently; however, the modes will become coupled when in the nonlinear region [41]. Studying multimode patterns provides the ability to study both regions. The RM single-mode case is simpler to model and may provide insight into the interaction of the shock and the interface of the two mediums, along with the resulting perturbations of the initial amplitudes [20]. However, the RM multimode case provides insight into the nonlinearity of the growth, and serves to represent a more random, realistic model of the types of imperfections and irregularities that may be found at the interfaces of two interacting materials [20].

The goal of these simulations is to assist in the design and prediction of the growth factors for experiments conducted on tantalum in the Omega laser facility described in Chapter 2. Using the Eureka code as described in Chapter 3, simulations have been performed to examine various multimode configurations. The simulations were undertaken to determine which configuration is best suited for a multimode campaign at Omega, and determine which laser energies to use for the drives. This experiment, as described in more detail in Section 2.2.2, is a collaboration between Caltech, LLNL, and General Atomics. General Atomics manufactures the targets used in the laser experiments several months in advance. Therefore, prior to the experiments, it is necessary to determine which multimode configuration to use. By analyzing various configurations in the simulations using the Eureka code, it was determined which one General Atomics should manufacture, based on the insights gained from the simulations. The decision was based on which multimode ripple pattern would exhibit growth while also allowing us to evaluate this growth throughout the simulation and, most importantly, be able to characterize it post-experiment.

Additionally, by simulating various energies and predicting the growth associated with each one, the decision could be made as to which energies to use for the experiments. The goal was to find a range of energies that were each large enough to cause growth in the sample, but not so large that melting would occur in the tantalum samples.

5.1 Multimode Simulations

The growth of laser driven RM instabilities for both four-mode and three-mode ripple patterns in tantalum was simulated. The criteria used to select the equations which describe the ripple patterns for the multimode targets were largely defined by the limits of the manufacturing process. The peak-to-valley of the ripples could be no larger than 10 μm and the angle of the slope of the ripples (angle-of-descent boundary) was limited to about 40°. Past multimode experiments performed by the LLNL team were also factors in selecting the ripple patterns [67, 68, 69]. After creating a series of combinations of multimode patterns, the ones that looked feasible to analyze post-experiment were selected for analysis and simulations. For the four-mode scenario, three different patterns were selected. After these four-mode patterns were analyzed, as discussed in the following sections, two different three-mode patterns were created. These patterns were simulated using Eureka, and one of them was determined to be the best option, which was the pattern used by General Atomics in the manufacturing of the tantalum samples. The four-mode ripple patterns and the corresponding equations describing them are shown in Figure 5.1 and Equations 5.1 – 5.3.

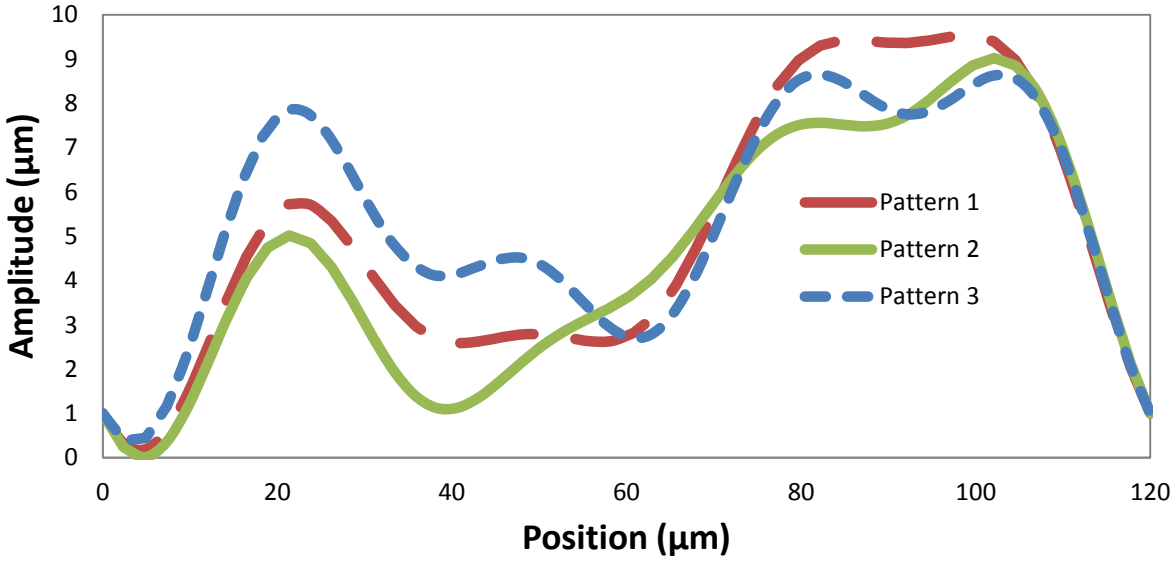

Figure 5.1: Four-mode ripple patterns considered for the laser driven Richtmyer-Meshkov instability experiments.

Each of the four-mode patterns in Figure 5.1 has a more distinctive first peak, followed by a smaller second peak that is slanted, and ending with two peaks at the end that each have a small and

large valley on either side. The three different equations for the four-mode patterns are given below. For the single-mode simulations, one half of a ripple was modeled. However, for the multimode simulations it is necessary to simulate one full period of the pattern, which is 120 μm. Therefore, in the equations below, x represents the position of the tantalum sample with units of μm.

$$\eta_{Pattern1}(x) = \sin\left(\frac{2\pi}{30}x + \frac{\pi}{4}\right) + \sin\left(\frac{2\pi}{40}x + \frac{\pi}{3}\right) + 2.5\sin\left(\frac{2\pi}{60}x + \frac{\pi}{2}\right) + 3\sin\left(\frac{2\pi}{120}x\right) \quad (5.1)$$

$$\eta_{Pattern2}(x) = sin\left(\frac{2\pi}{30}x + \frac{\pi}{4}\right) + 1.5sin\left(\frac{2\pi}{40}x + \frac{\pi}{3}\right) + 1.5sin\left(\frac{2\pi}{60}x + \frac{\pi}{2}\right) + 3sin\left(\frac{2\pi}{120}x\right) \quad (5.2)$$

$$\eta_{Pattern3}(x) = 1.5sin\left(\frac{2\pi}{30}x + \frac{\pi}{4}\right) + sin\left(\frac{2\pi}{40}x + \frac{\pi}{3}\right) + 2.5sin\left(\frac{2\pi}{60}x + \frac{\pi}{2}\right) + 1.5sin\left(\frac{2\pi}{120}x\right) \quad (5.3)$$

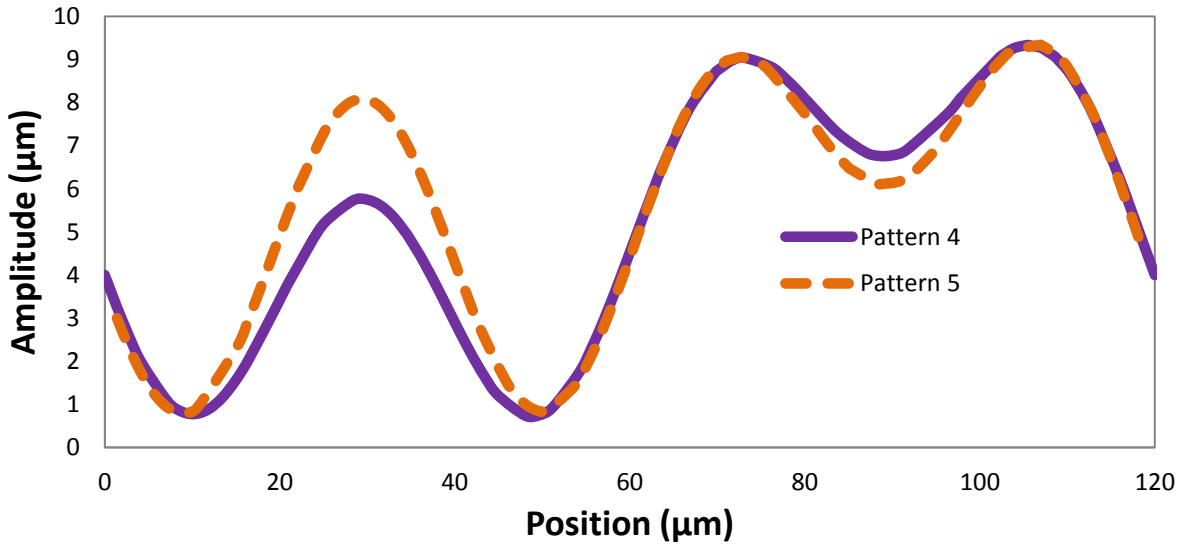

Figure 5.2: Three-mode ripple patterns considered for the laser driven Richtmyer-Meshkov instability experiments.

As seen from Figure 5.2, the three-mode patterns are very similar to each other, but with variations in the height of the amplitudes of the three different peaks. The wavelengths of these peaks remain the same, so the higher amplitudes result in a higher angle for the slope of the ripples. This is referred to as the angle-of-descent boundary and is represented by θ. The two different equations describing the three-mode patterns in Figure 5.2 are below, along with their respective maximum angle-of-descent boundaries. For the multimode simulations, it is necessary to simulate one full period of the pattern, which is 120 μm. Therefore, in the equations below, x represents the position of the tantalum sample with units of μm.

$$\eta_{Pattern4}(x) = 2.5\sin\left(\frac{2\pi}{40}x + \frac{\pi}{3}\right) + \sin\left(\frac{2\pi}{60}x + \frac{\pi}{2}\right) + 3\sin\left(\frac{2\pi}{120}x\right) \quad (5.4)$$

$$\theta^{max} = 31° \quad (5.5)$$

$$\eta_{Pattern5}(x) = 3\sin\left(\frac{2\pi}{40}x + \frac{\pi}{3}\right) + 1.5\sin\left(\frac{2\pi}{60}x + \frac{\pi}{2}\right) + 2\sin\left(\frac{2\pi}{120}x\right) \quad (5.6)$$

$$\theta^{max} = 34° \quad (5.7)$$

Each of the multi-mode ripple patterns in Figures 5.1 and 5.2 is simulated at different laser energies. Before running the simulations, the patterns are modeled, meshed, and input into the Eureka code. Images of the unperturbed ripple before the start of the simulation are shown in Figure 5.3.

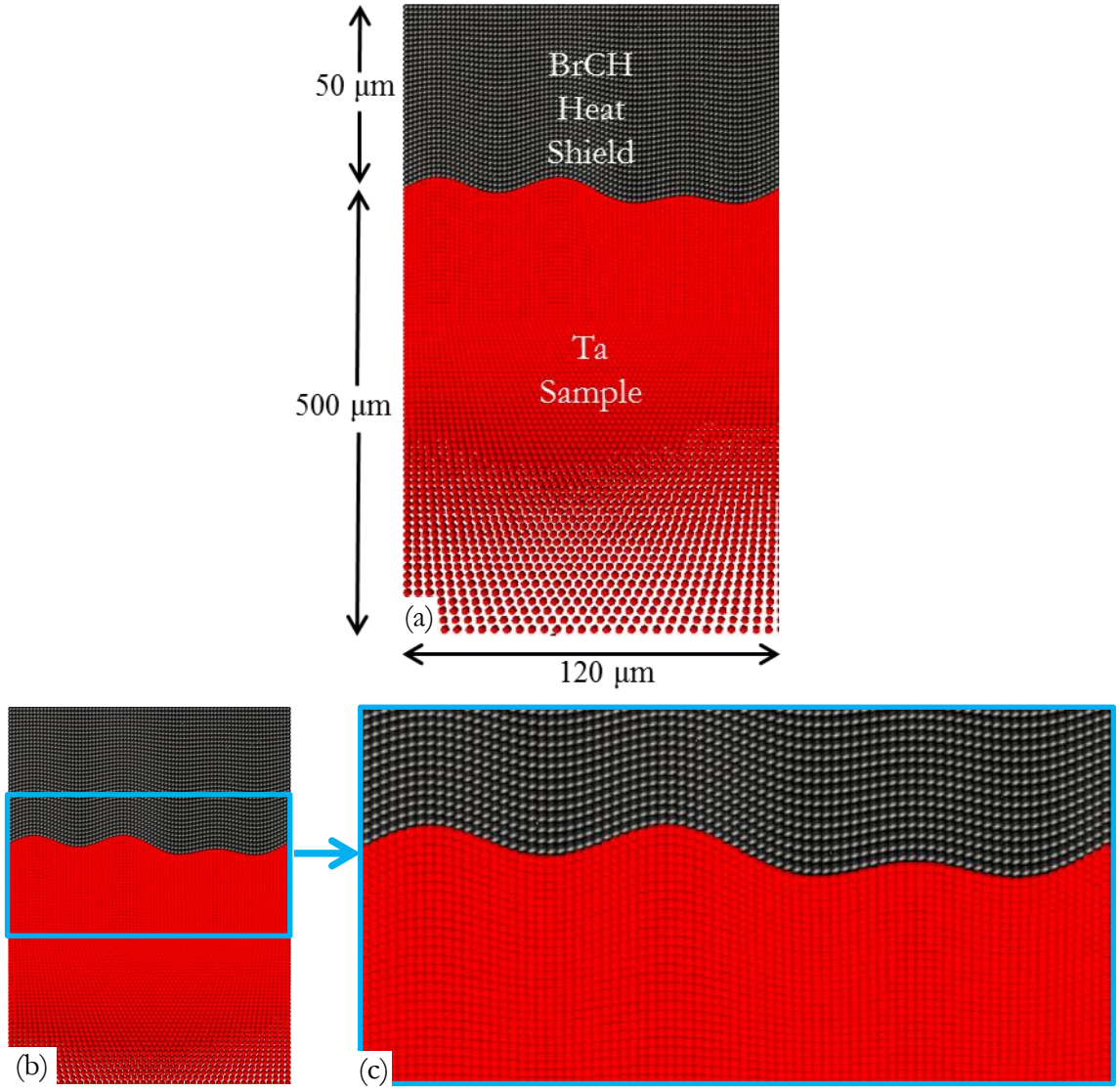

Figure 5.3: Three-mode ripple (Pattern # 4): (a) full ripple with dimensions, (b) and (c) details of the interface of the ripple and heat shield. The width of the sample and heat shield is 2 µm.

In Figure 5.3, the region marked red is the tantalum (Ta) ripple and the grey region is the BrCH heat shield. These images are at time t=0 before the start of the simulation, when the ripple pattern has not been deformed. In the Richtmyer-Meshkov configuration, the pressure drive comes from

the top down such that the heat shield is driven into the Ta sample. The dimensions of the multimode ripples are a length of 120 μm (this represents one period of the prescribed pattern), a width of 2.0 μm, and a height of 500 μm. For the heat shield, the length and width are the same as the Ta sample (length of 120 μm, width of 2.0 μm) but the height is 50 μm.

5.1.1 Boundary Conditions

In all the simulations, a velocity profile is prescribed as the boundary condition at the top of the heat shield. At the bottom of the rippled Ta sample, the boundary condition sets it as a free surface. The two sides of the images shown in Figure 5.3 have periodic boundary conditions. These simulations are actually 3D, but the third direction is set to have unit thickness (one element) and are fixed at the lateral edges, simulating plan strain conditions.

The velocity profile, which is applied as the boundary condition, is correlated to the laser drive energy using the rad-hydro code, Hyades. The generation of the velocity profile from the laser interaction with the target is discussed more in Section 3.2.3. To simulate each pattern at different laser energies, different velocity profiles are applied in the form of the boundary condition on the top of the heat shield. The velocity profile corresponding to the 100 J laser energy drive is shown in Figure 5.4.

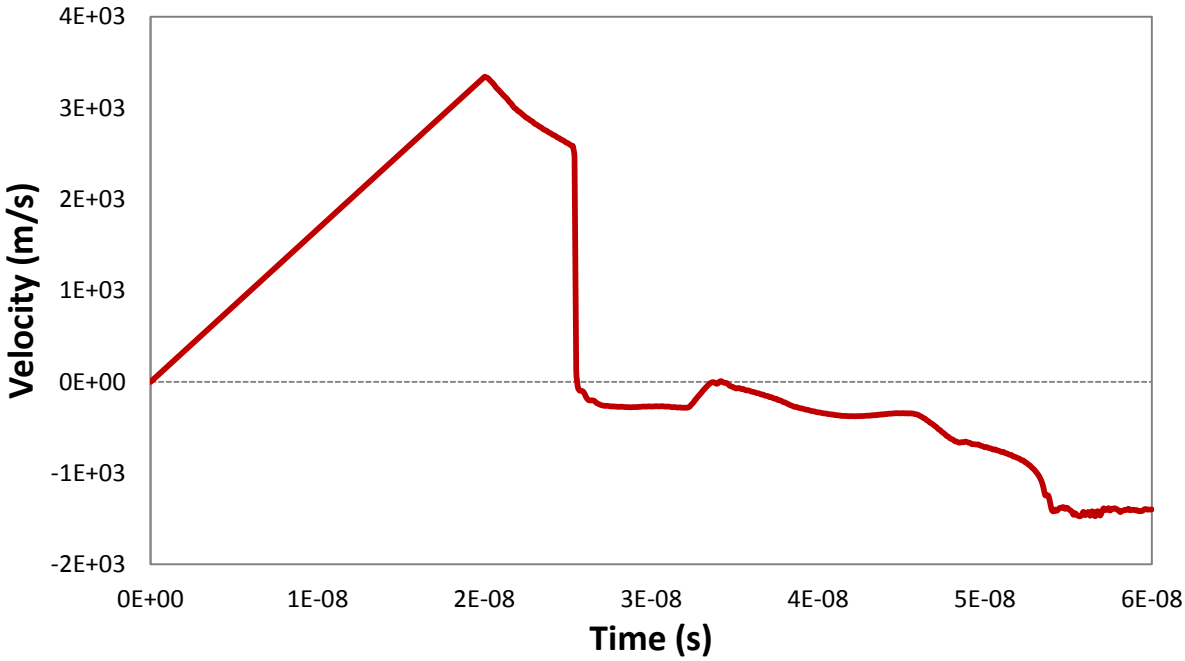

Figure 5.4: Velocity profile corresponding to the 100 J laser energy drive applied as the boundary condition.

The shape of the velocity profile is designed to counter the effects of the waves and reflections within the heat shield. The initial profile will compress the heat shield, but the reflections at the

interface will lead to tension on the initial surface, causing the heat shield to expand. Additionally, a concern in these experiments and simulations is the reflection of the waves from the free surface of the Ta sample. Therefore, the height of the sample is large enough so that interactions from reflections do not affect the growth and instabilities of the ripples.

5.1.2 Growth Factors

To determine the growth factor in the multimode patterns, it is necessary to know where the peaks and valleys are. By tracking the location of the peaks and valleys over time in the simulation, growth factors are calculated.

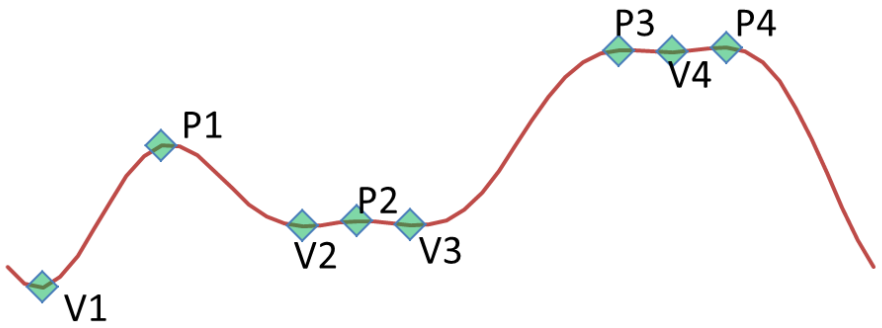

Figure 5.5: Locations on the multimode patterns for tracking the peaks and valleys to calculate the growth factor.

Growth factor (GF) is defined as the current peak-to-valley height (η_c) over the initial peak-to-valley height (η_i):

$$GF = \frac{\eta_c(t)}{\eta_i} \tag{5.8}$$

In Eq. (5.8), the current height (η_c) is a function of time. Initial height (η_i) is constant and is the peak-to-valley height before deformation (before the simulations begins). In single-mode ripples, the computation of growth factor is straightforward, as there is simply one peak and one valley. However, as seen in Figure 5.5, a four-mode ripple has four peaks and four valleys, and therefore eight different measurements of growth (eight because each peak has two different valleys – one on either side) can be obtained.

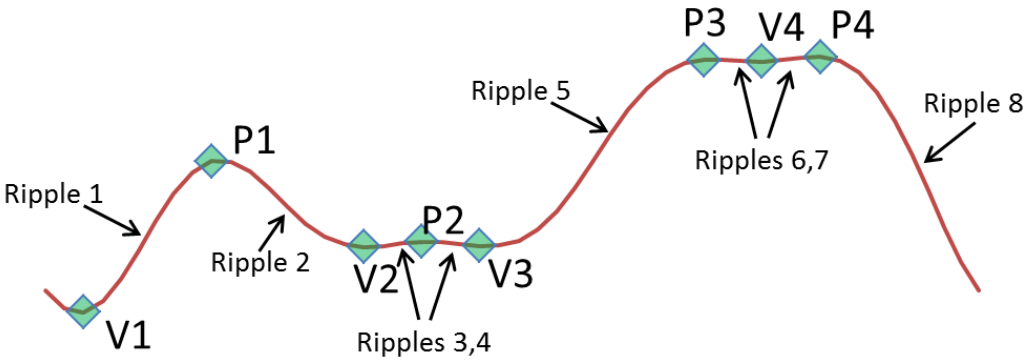

Figure 5.6: Identifying the eight unique peak-to-valley heights that can be obtained from four peaks and valleys.

The equations for the eight different peak-to-valley heights are defined below.

$$\eta_{c1} = P1 - V1 \tag{5.9}$$
$$\eta_{c2} = P1 - V2 \tag{5.10}$$
$$\eta_{c3} = P2 - V2 \tag{5.11}$$
$$\eta_{c4} = P2 - V3 \tag{5.12}$$
$$\eta_{c5} = P3 - V3 \tag{5.13}$$
$$\eta_{c6} = P3 - V4 \tag{5.14}$$
$$\eta_{c7} = P4 - V4 \tag{5.15}$$
$$\eta_{c8} = P4 - V1 \tag{5.16}$$

The locations of peaks (P) and valleys (V) are captured as a function time; therefore the growth factor is obtained as a function of time. For each simulation, the growth factors are plotted for each of the eight different ripples, #1 through #8.

Similarly, for the three-mode patterns, each combination of the three peaks and three valleys has to be accounted for, as shown in Figure 5.7. The equations for the three-mode are the same for η_{c1} through η_{c5}, $\eta_{c6} = P3 - V1$, and η_{c7} and η_{c8} do not exist.

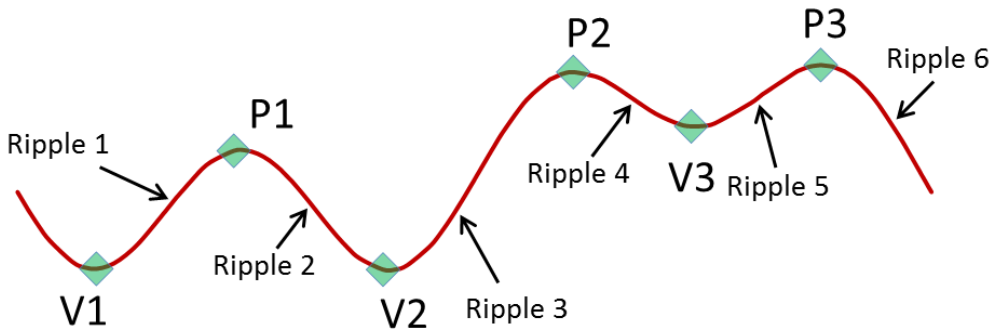

Figure 5.7: Identifying the six unique peak-to-valley heights that can be obtained from three peaks and valleys.

5.2 Four-Mode Configuration Results

Three different patterns (Figure 5.1, Equations 5.1, 5.2, and 5.3) were considered for the four-mode configuration. Each pattern was simulated twice by subjecting the ripple to drives corresponding to laser energies of 100 and 150 J.

5.2.1 Pattern # 1

Four-mode Pattern # 1 is represented by the following equation:

$$\eta_{P1}(x) = \sin\left(\frac{2\pi}{30}x + \frac{\pi}{4}\right) + \sin\left(\frac{2\pi}{40}x + \frac{\pi}{3}\right) + 2.5\sin\left(\frac{2\pi}{60}x + \frac{\pi}{2}\right) + 3\sin\left(\frac{2\pi}{120}x\right) \qquad (5.17)$$

5.2.1.1 Pattern # 1 – 100 J

A simulation was performed for the four-mode Pattern # 1 configuration with 100 J of energy for the drive. At the conclusion of the simulation, the data was collected and visualized. An animation was created for the simulation, as well as snapshots of the deformed configuration. In the simulations, a series of data files were generated. The data files provide the current locations of the nodes on the ripple surface. From this information, the nodal displacements were obtained and the growth factor was calculated. Figure 5.8 shows a selection of the images from the simulation to show the evolution of the deformation of the target with approximately 7.3 ns between successive images. In these images, the red region is the Ta sample and the grey region is the heat shield. In several of the images shown in the following sections, only part of the Ta sample (in red) is depicted in the images. This was done to more clearly convey the deformation of the interface between the sample and the heat shield. In the Richtmyer-Meshkov configuration, the drive comes from the top down such that the heat shield is driven into the Ta sample.

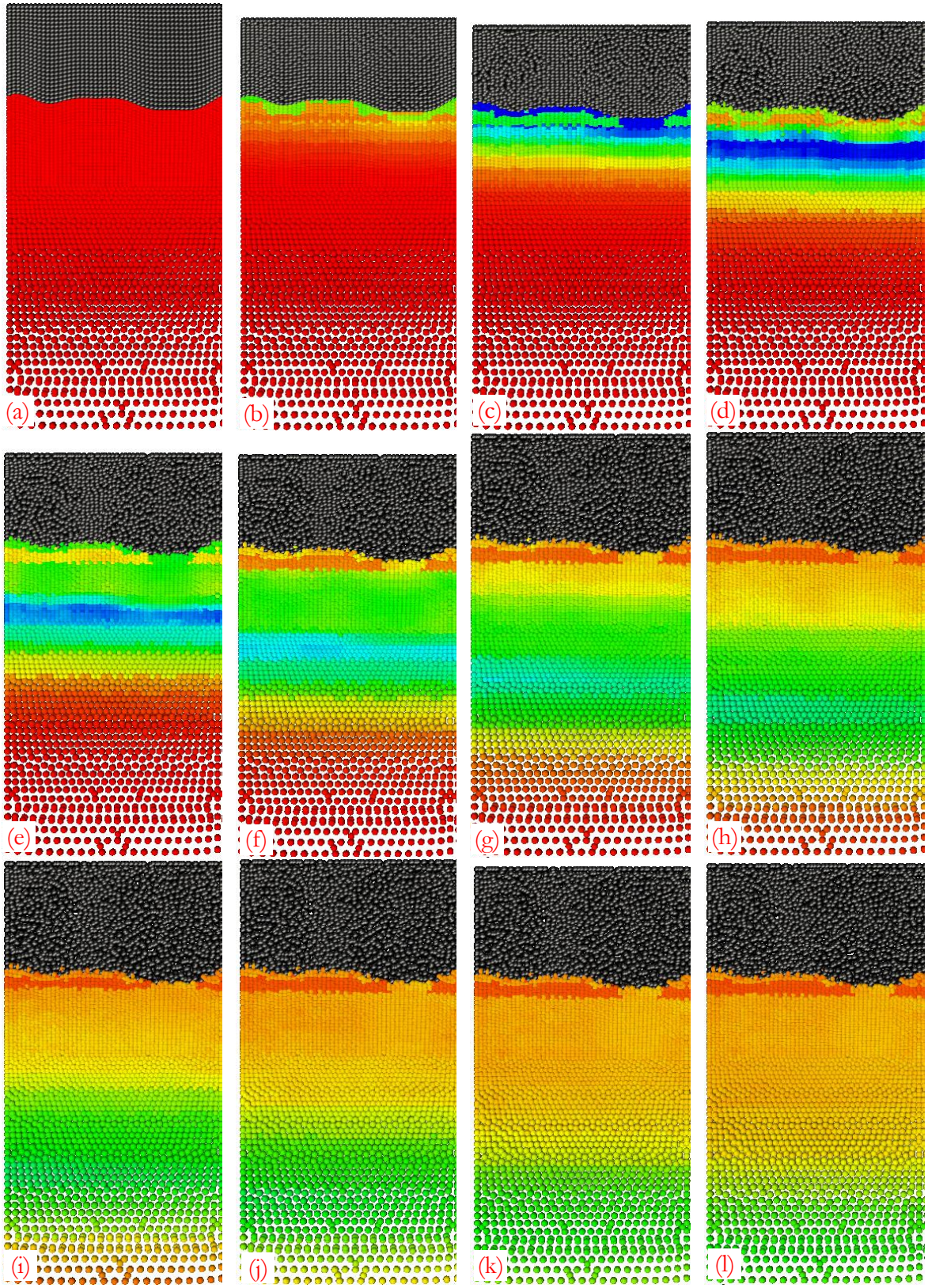

Figure 5.8: Four-mode Pattern # 1 subjected to a drive corresponding to a laser energy of 100 J – Evolution of the ripple and target in time. The images (a)-(l) are snapshots of the ripples starting from time t=0 to t= 80 ns, with 7.3 ns between the images.

The drive is applied in the form of a velocity profile to the top surface of the BrCH heat shield. In the first three to four images (Figure 5.8(a)-(d)), the heat shield can be seen to be undergoing compression. Between the 6th and 7th image (Figure 5.8(f)-(g)), the heat shield suddenly expands. This is the result of the reflection from the top surface of the heat shield causing tension of the heat shield. Also, soon after the expansion occurs, the velocity profile boundary condition ends, rendering it to be a free surface. The velocity profile provides the initial motion but does not continue driving the heat shield during the entire duration of the simulation. As seen in the velocity profile in Figure 5.4, the drive ends at about 60 ns. The expansion of the heat shield occurs somewhere between the 6th and 7th images (Figure 5.8(f)-(g)), which corresponds to the time in the range of 37-45 ns.

Even after the loading ends, the heat shield still continues to compress (Figure 5.8(k)-(l)) and interact with the Ta rippled sample. For the first half of the simulation, the Ta sample appears to be compressing. Although the entire sample seems to stop compressing, the deformation of the ripples continues throughout the entire simulation. The evolution of the ripple surface plotted using the displacements of the nodes at the surface is shown in Figure 5.9.

The vertical axis in Figure 5.9 represents the distance along the direction of the loading. Each line represents the location of the ripple surface at a particular time during the simulation. In these plots, the drive is coming from the bottom up, i.e. the lowermost curve represents the four-mode ripple pattern before loading at t=0.

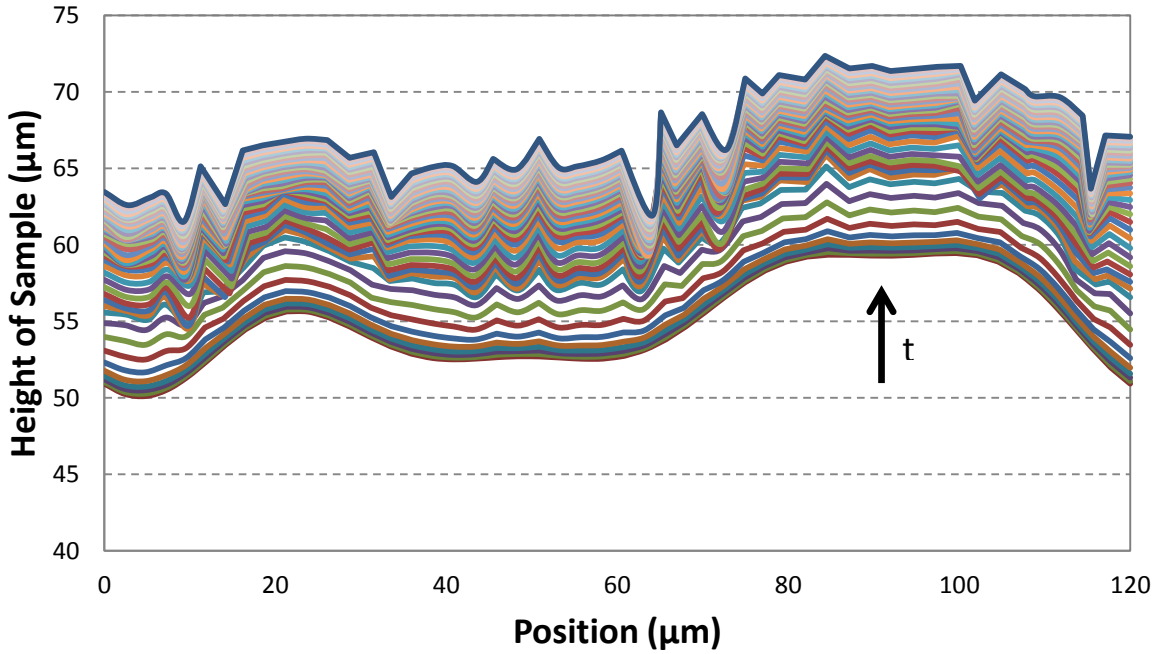

Figure 5.9: Four-mode Pattern # 1 subjected to a drive corresponding to a laser energy of 100 J – Evolution of the ripple surface as a function of time.

As time increases, the ripple surface moves further along the direction of loading, as expected. In the early stage of loading, the surface remains smooth. As time progresses, the ripple surface begins to show wrinkles and is no longer smooth and continuous. The plot in Figure 5.10 shows the same evolution of the ripple surface in Figure 5.9, but with only the 12 data points of interest.

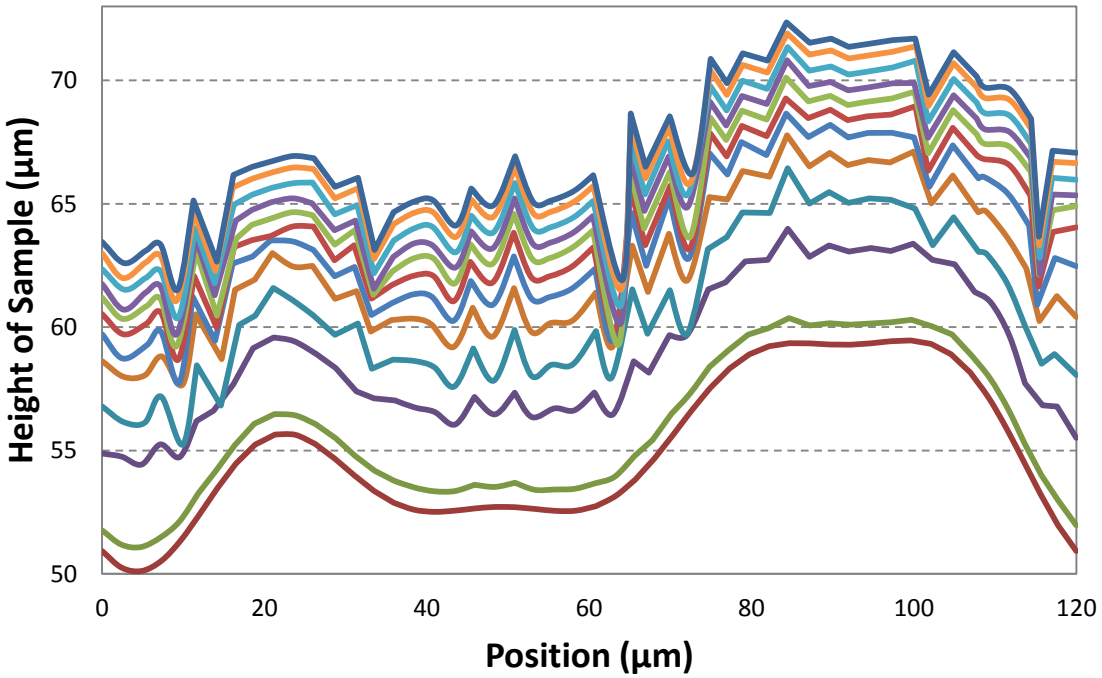

Figure 5.10: Four-mode Pattern # 1 subjected to a drive corresponding to a laser energy of 100 J – Evolution of the ripple surface as a function of time plotted with only 12 points of interest from Figure 5.9.

Each of the data sets on the plot in Figure 5.10 represents every 4th output in time, giving approximately 7.5 ns between each line. Although the time between lines is equal, the change in displacement between each time interval is not constant. Between the first two time points the change is slow, because the heat shield is still being compressed. Between the second and third time points, the change of displacement of the surface is at a maximum. As time continues, the ripple surface continues to move up but at a slower rate.

Figure 5.11 shows the growth factors computed using Equation 5.8 as a function of time for each of the eight different ripples. This is followed by Figure 5.12, which shows the plots of the growth factors for a few of the selected ripples from Figure 5.11.

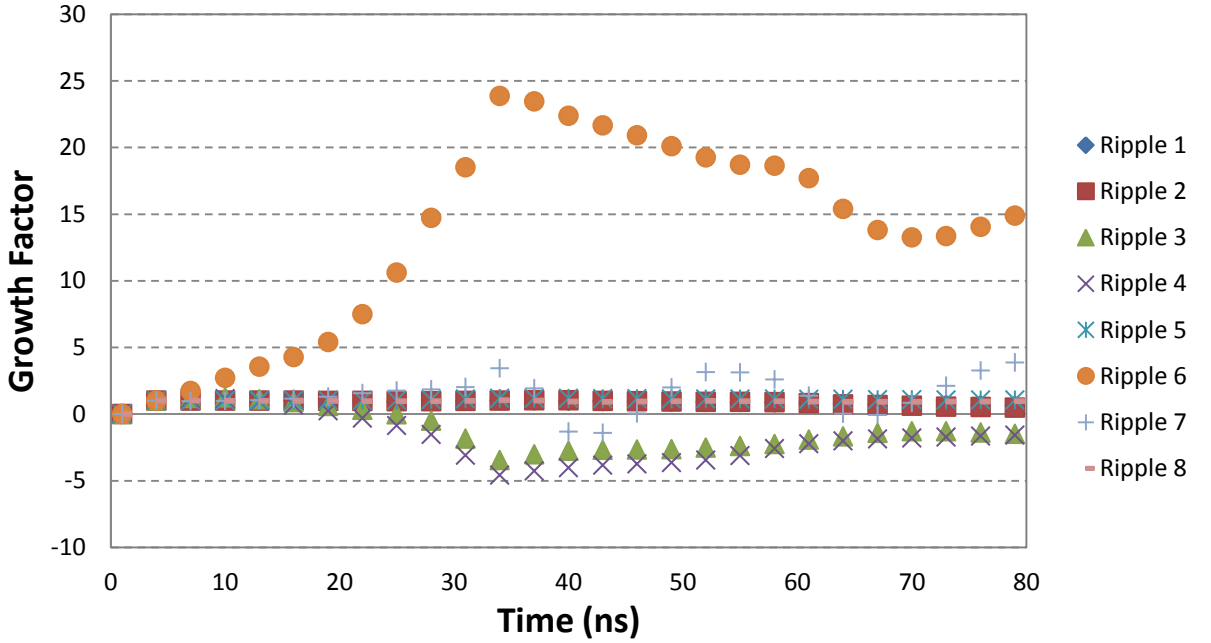

Figure 5.11: Growth Factor vs. time for four-mode Pattern # 1 subjected to a drive corresponding to a laser energy of 100 J.

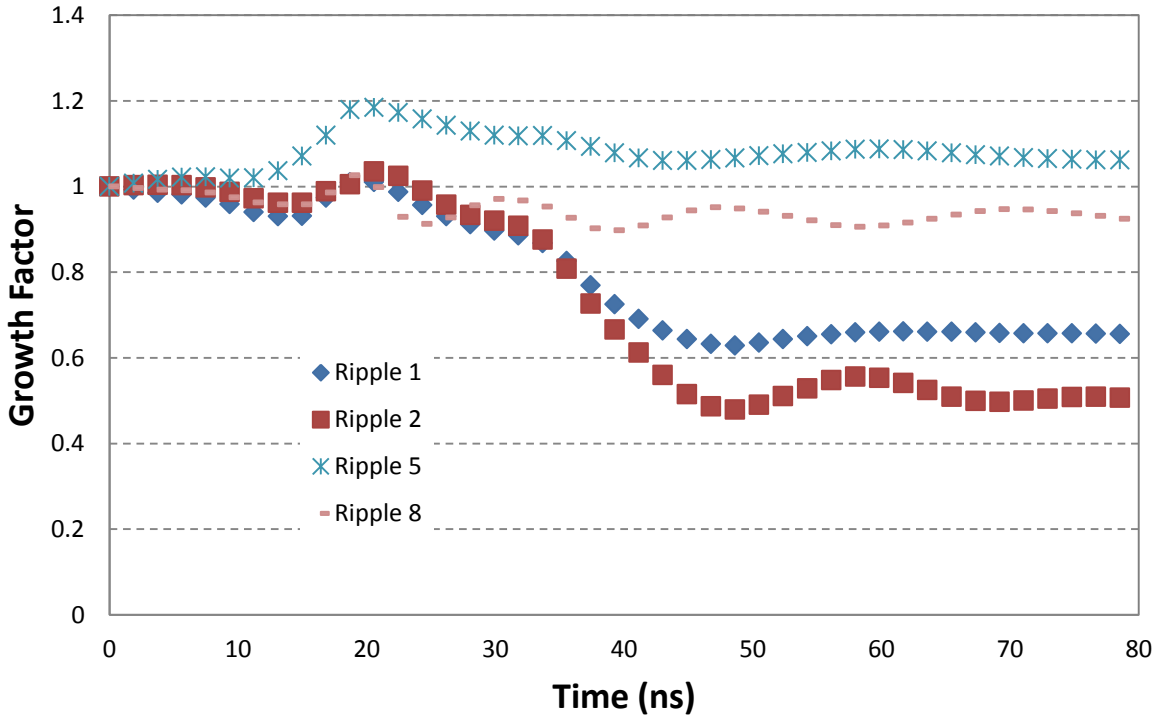

Figure 5.12: Growth Factor vs. time for selected ripples of interest for four-mode Pattern # 1 subjected to a drive corresponding to a laser energy of 100 J.

Figure 5.11 shows a growth factor of nearly 25 for Ripple # 6. Clearly, this is not realistic as the growth factors seen in experiments are typically not much higher than 2. This is not a failure of the simulation, but is due to error in the calculation of the growth factor using the nodal displacements. Ripple #s 3, 4, 6, and 7, as seen in the Figure 5.11, have very small amplitudes to begin with. Therefore, when calculating growth factor, which is current height over initial height, any errors in the height will magnify the errors in growth factors. A possible solution to decreasing this error would be to use a finer mesh and more nodes; however, this is costly and timely in computing capabilities. Also, these small peak-to-valley heights, such as those for Ripple # 6, will cause the same issue in experiments when measuring the ripple growth post-experiment. This is certainly a disadvantage with this pattern.

As seen in Figure 5.12, for the other ripples, the growth looks more normal, showing peak growth factors of just over 1 for Ripple #s 1, 2, and 8, and a growth of 1.2 for Ripple # 5. It would be ideal to have larger growth factors, and this led to exploring other patterns at higher energies. The following section contains the same pattern discussed here, but was subjected to a drive corresponding to a laser energy of 150 J instead of 100 J.

5.2.1.2 Pattern # 1 – 150 J

A simulation was performed for the four-mode Pattern # 2 configuration with 150 J of energy for the drive. Figure 5.13 shows a selection of the images from the simulation with approximately 7.3 ns between successive images. In these images, the red region is the Ta sample and the grey region is the heat shield. In the Richtmyer-Meshkov configuration, the drive comes from the top down such that the heat shield is driven into the Ta sample.

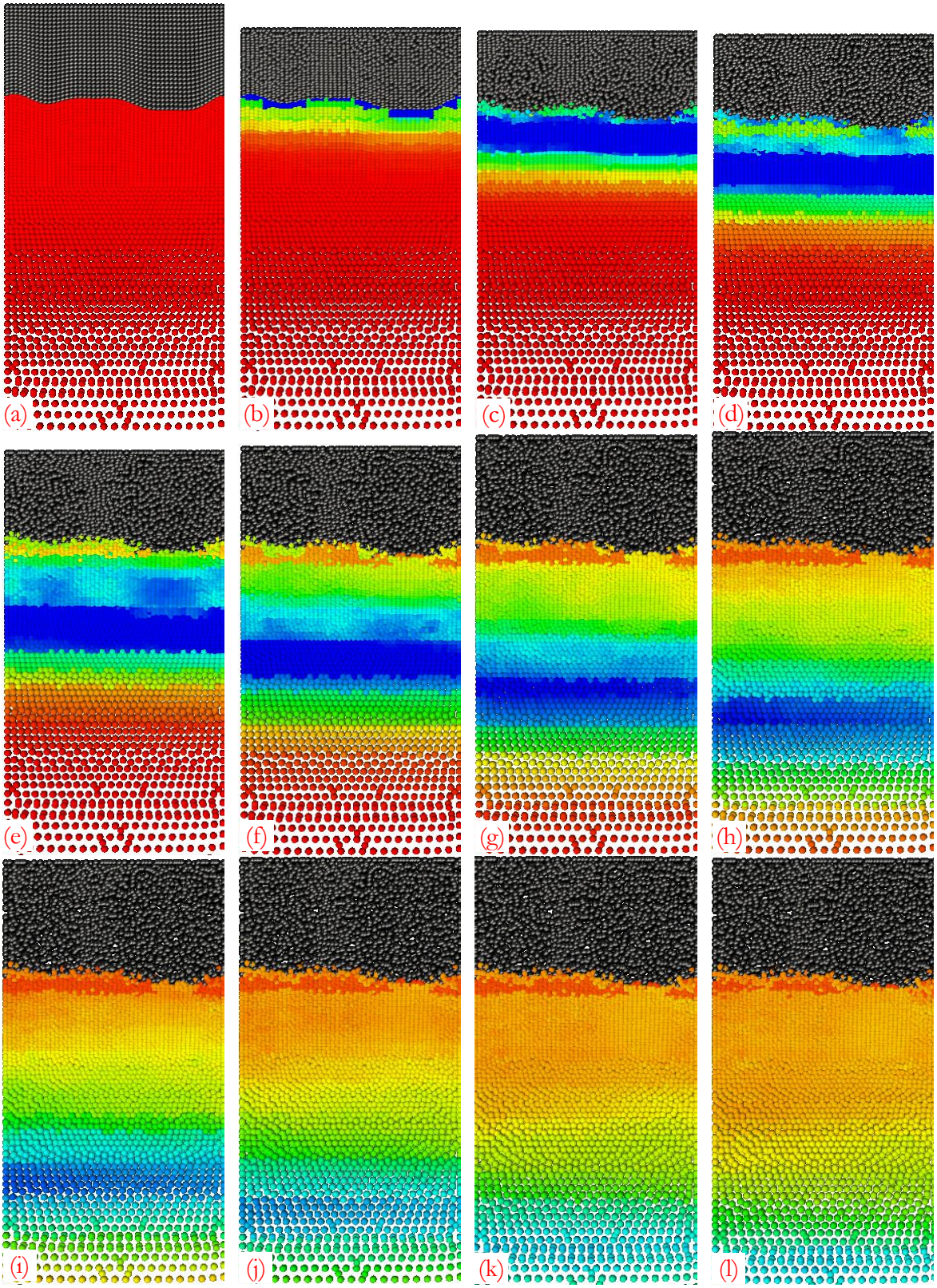

Figure 5.13: Four-mode Pattern # 1 subjected to a drive corresponding to a laser energy of 150 J – Evolution of the ripple and target in time. The images (a)-(l) are snapshots of the ripples starting from time t=0 to t= 80 ns, with 7.3 ns between the images.

As expected in Figure 5.13, the heat shield can be seen to be undergoing compression in the beginning and eventually the waves reach the interface of the heat shield and Ta sample, causing the Ta sample to compress. About halfway through, as expected, the heat shield expands, but the interface continues to move downward. With each successive image, the interface becomes less defined and growth of the ripples is not necessarily evident.

The vertical axis in Figure 5.14 represents the distance along the direction of the loading. Each line represents the location of the ripple surface at a particular time during the simulation. In these plots, the drive is coming from the bottom up, i.e. the lowermost curve represents the four-mode ripple pattern before loading at t=0.

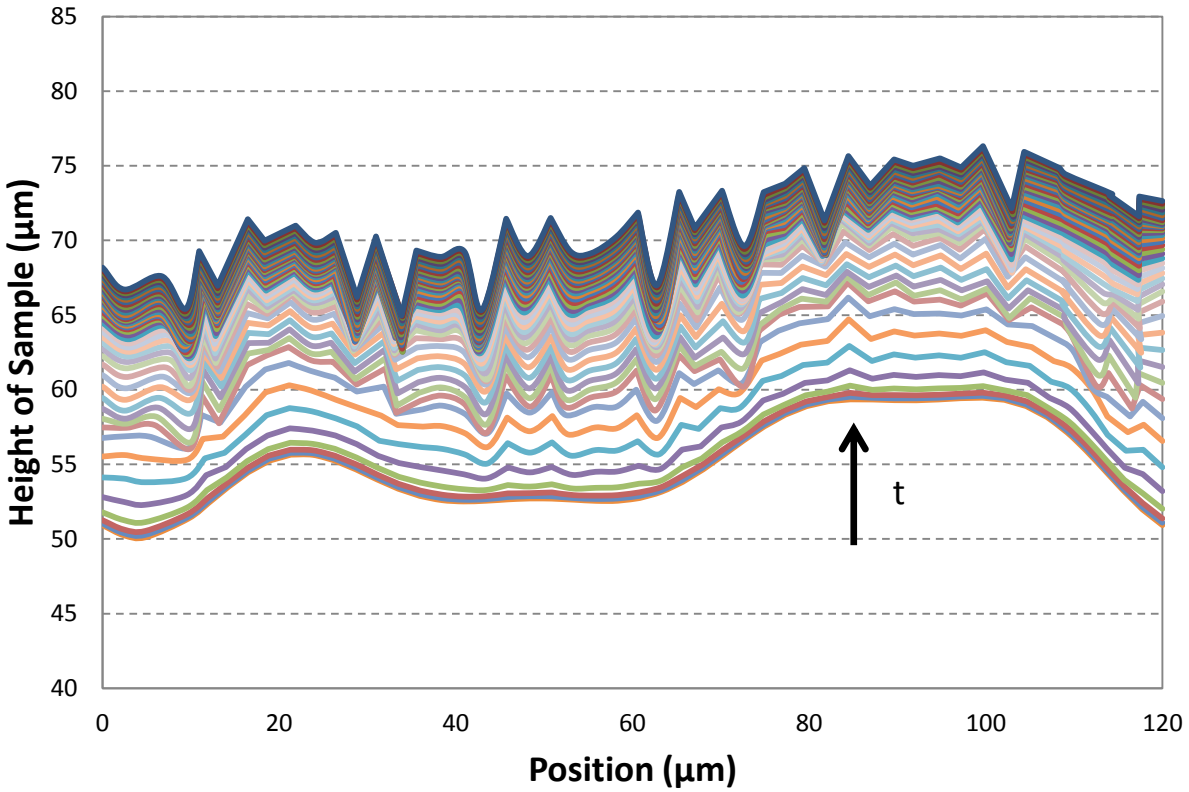

Figure 5.14: Four-mode Pattern # 1 subjected to a drive corresponding to a laser energy of 150 J – Evolution of the ripple surface as a function of time.

As time increases, the ripple surface moves further along the direction of loading, as expected. In the early stage of loading, the surface remains smooth. The plot in Figure 5.15 shows the same evolution of the ripple surface in Figure 5.14, but with only the 12 data points of interest.

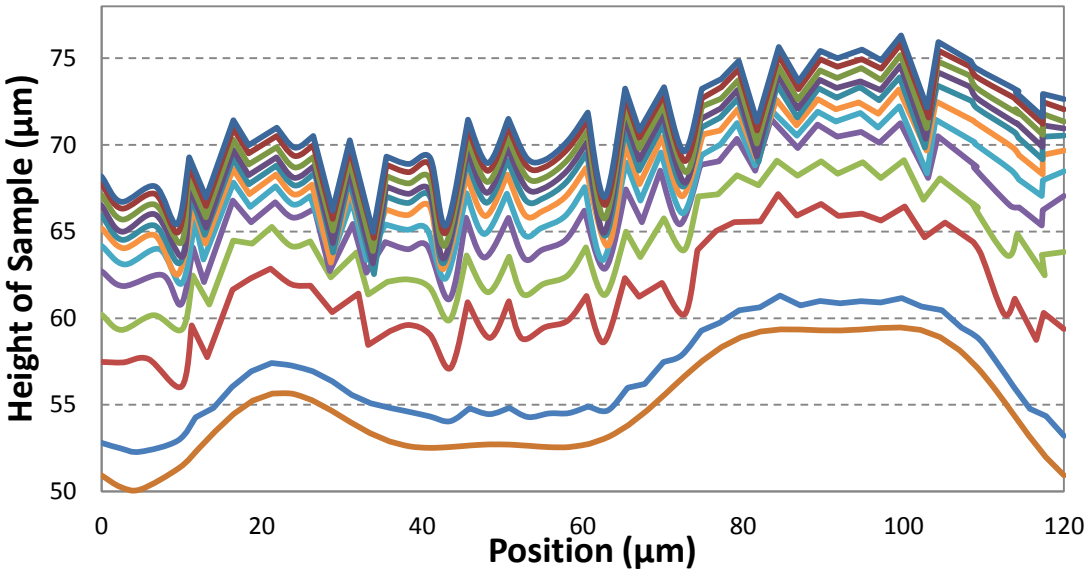

Figure 5.15: Four-mode Pattern # 1 subjected to a drive corresponding to a laser energy of 150 J – Evolution of the ripple surface as a function of time plotted with only 12 points of interest from Figure 5.14.

Similarly to the 100 J drive, the evolution of the ripple surface as seen in Figures 5.14 and 5.15 starts out smooth. Likewise, as time progresses, the ripple surface begins to show wrinkles and is no longer smooth and continuous. Each of the data sets in Figure 5.15 is about 7.5 ns later. The first two time points show less growth because of the compression of the heat shield. Between the second and third time points, the progression of the surface is at a maximum, and as time progresses, the ripple surface continues to move up, but at a slower rate.

Figure 5.16 shows the growth factors computed using Equation 5.8 as a function of time for each of the eight different ripples. This is followed by Figure 5.17, which shows the plots of the growth factors for a few of the selected ripples from Figure 5.16.

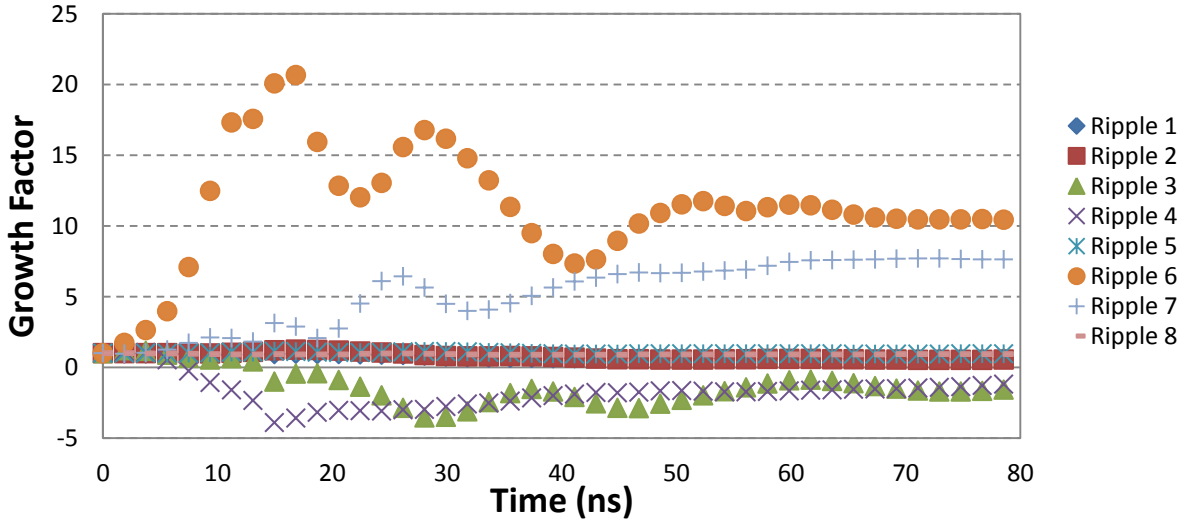

Figure 5.16: Growth Factor vs. time for four-mode Pattern # 1 subjected to a drive corresponding to a laser energy of 150 J.

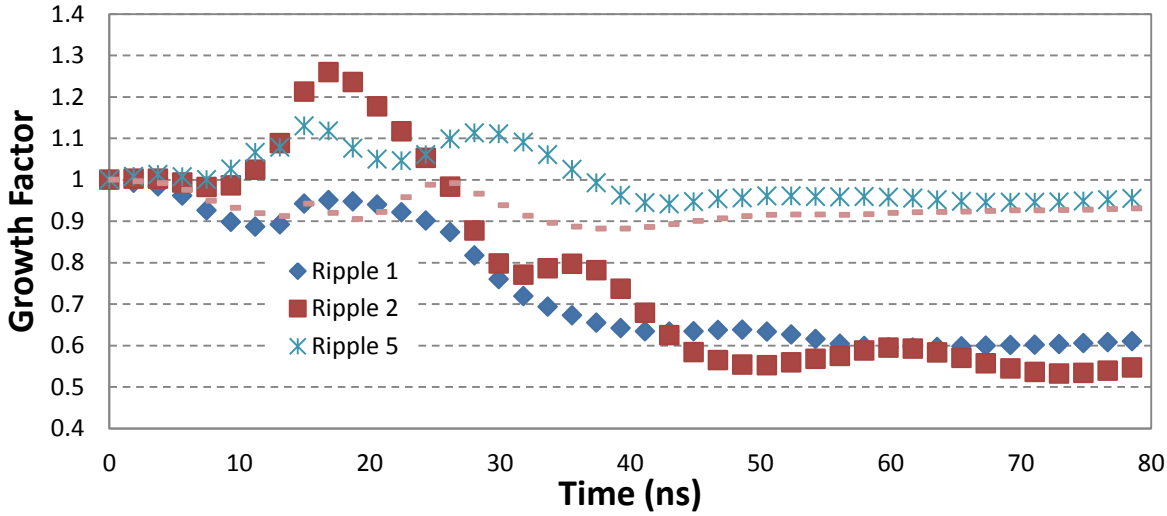

Figure 5.17: Growth Factor vs. time for selected ripples of interest for four-mode Pattern # 1 subjected to a drive corresponding to a laser energy of 150 J.

As seen in Figure 5.16, Ripple # 6, just as in the 100 J case, shows an anomalously high growth factor of over 20 because of the error related to the small initial height. Even Ripple # 7 shows a growth factor of 7, which is not realistic. Figure 5.17 focuses on the larger ripples, and the values for growth factor (1 – 1.3) are more realistic. However, the ideal pattern would exhibit even more growth. The following section presents the results of the two different energies studied for Pattern # 1 side by side.

5.2.1.3 Four-mode Pattern # 1 Comparison

The four-mode ripple Pattern # 1 was subjected to drives corresponding to laser energies of 100 and 150 J. Figure 5.18 shows the time history of two of the ripples at each energy. It is expected that higher energy will result in more growth.

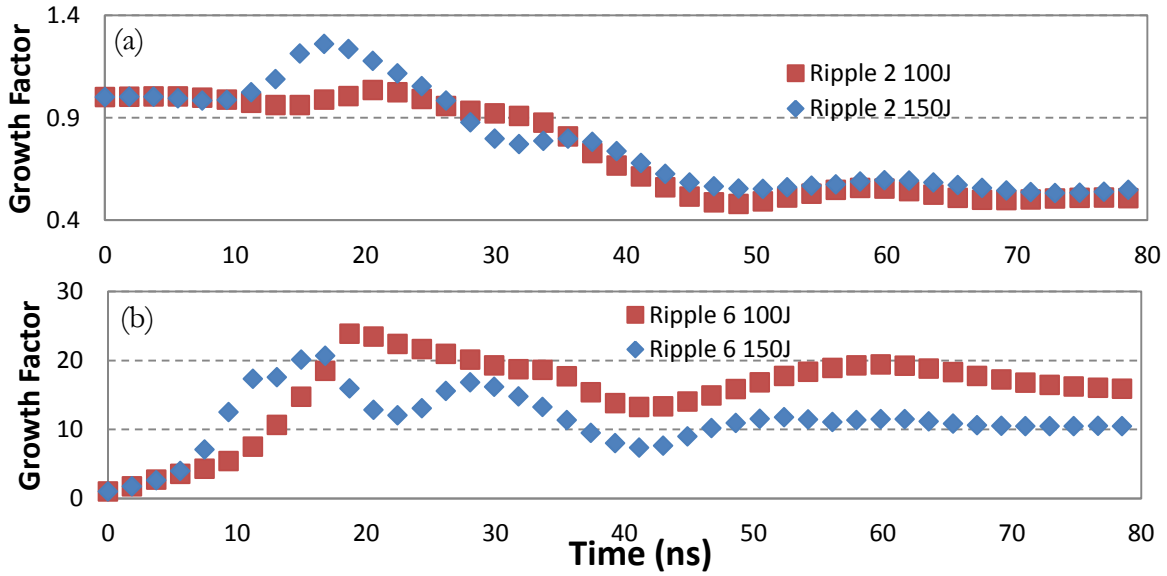

Figure 5.18: Comparison of Growth Factor vs. time for four-mode Pattern # 1 subjected to two different energies, 100 and 150 J for (a) Ripple # 2 and (b) Ripple # 6.

For Ripple # 2, the 150 J drive shows more growth than the 100 J drive, as expected (Figure 5.18(a)). However, neither exhibits large growth factors. Also, Ripple # 6 does not follow the expected trend and indeed just the opposite, i.e. the growth factor for the 100 J drive is actually higher than that for the 150 J drive (Figure 5.18(b)). Both of these cases are exhibiting anomalously high growth factors that are too high because Ripple # 6 has too small of an initial peak-to-valley height. A slight change in the peak or valley makes a large difference and a larger error in the nodal displacement analysis. It can be inferred that the unexpected observation of ripples subjected to the 100 J drive growing more than the 150 J drive is due to the large errors associated with Ripple #s 3, 4, 6, and 7. The results of this pattern and issues that arise during these simulations suggest that four-mode Pattern # 1 is not ideal. The higher energy cases do not always show the expected trend, the smaller ripples are giving unrealistic growth factors, and the images and video show that the interface becomes unresolved over time. For this reason, different patterns were simulated, as discussed in the following sections.

5.2.2 Pattern # 2

Four-mode Pattern # 2 is represented by the following equation:

$$\eta_{P2}(x) = \sin\left(\frac{2\pi}{30}x + \frac{\pi}{4}\right) + 1.5\sin\left(\frac{2\pi}{40}x + \frac{\pi}{3}\right) + 1.5\sin\left(\frac{2\pi}{60}x + \frac{\pi}{2}\right) + 3\sin\left(\frac{2\pi}{120}x\right) \quad (5.18)$$

5.2.2.1 Pattern # 2 – 100 J

A simulation was performed for the four-mode Pattern # 2 configuration with 100 J of energy for the drive. Figure 5.19 shows a selection of the images from the simulation with approximately 7.8 ns between successive images. In these images, the red region is the Ta sample and the grey region is the heat shield. In the Richtmyer-Meshkov configuration, the drive comes from the top down such that the heat shield is driven into the Ta sample.

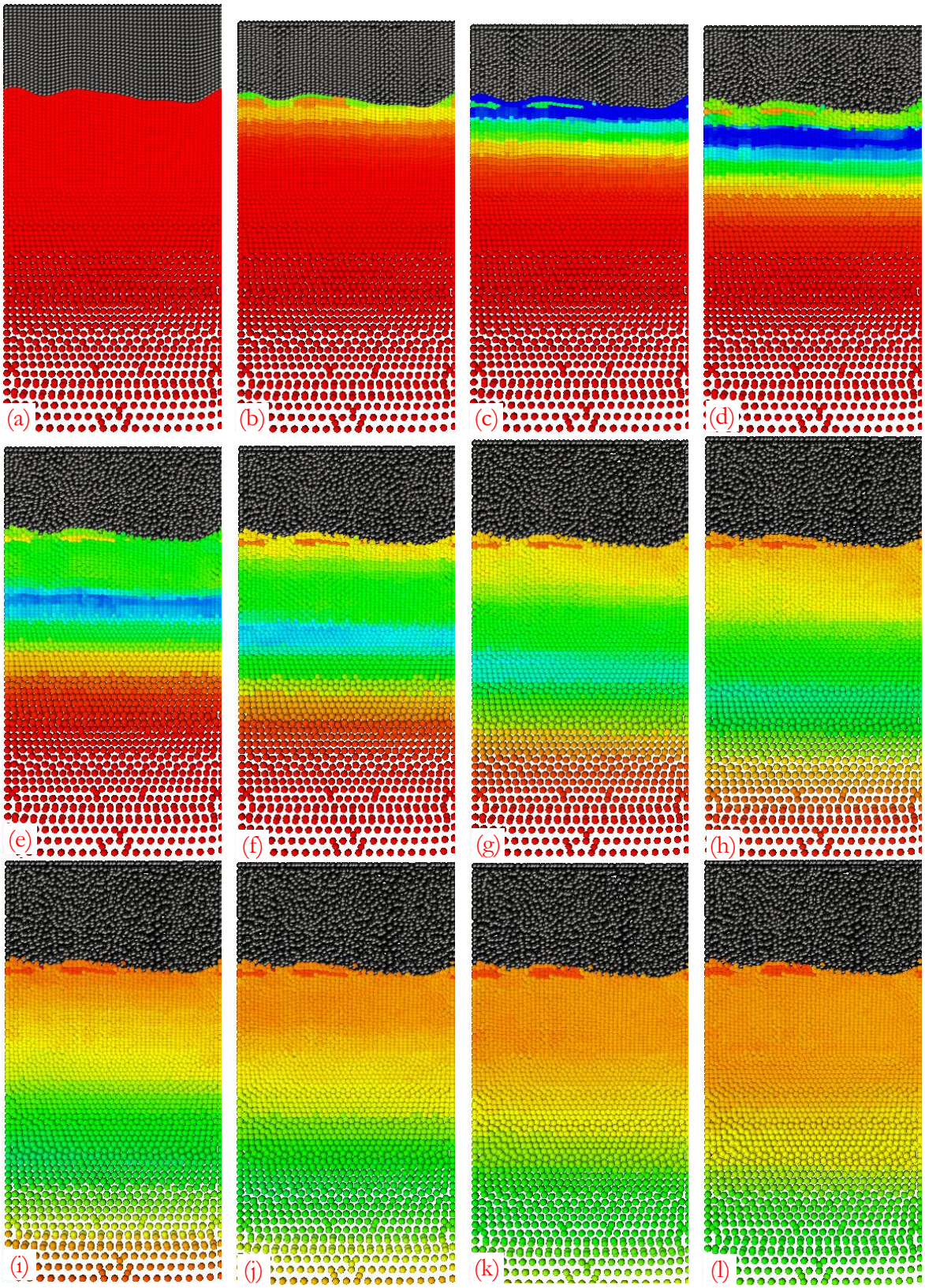

Figure 5.19: Four-mode Pattern # 2 subjected to a drive corresponding to a laser energy of 100 J – Evolution of the ripple and target in time. The images (a)-(l) are snapshots of the ripples starting from time t=0 to t= 86 ns, with 7.8 ns between the images.

Just as in four-mode Pattern # 1, the heat shield is initially compressed, the wave reaches the interface and the growth begins, and the heat shield expands about halfway through the simulation. In this case, as the interface evolves, the shape seems to remain intact unlike in the previous simulation.

The vertical axis in Figure 5.20 represents the distance along the direction of the loading. Each line represents the location of the ripple surface at a particular time during the simulation. In these plots, the drive is coming from the bottom up, i.e. the lowermost curve represents the four-mode ripple pattern before loading at t=0.

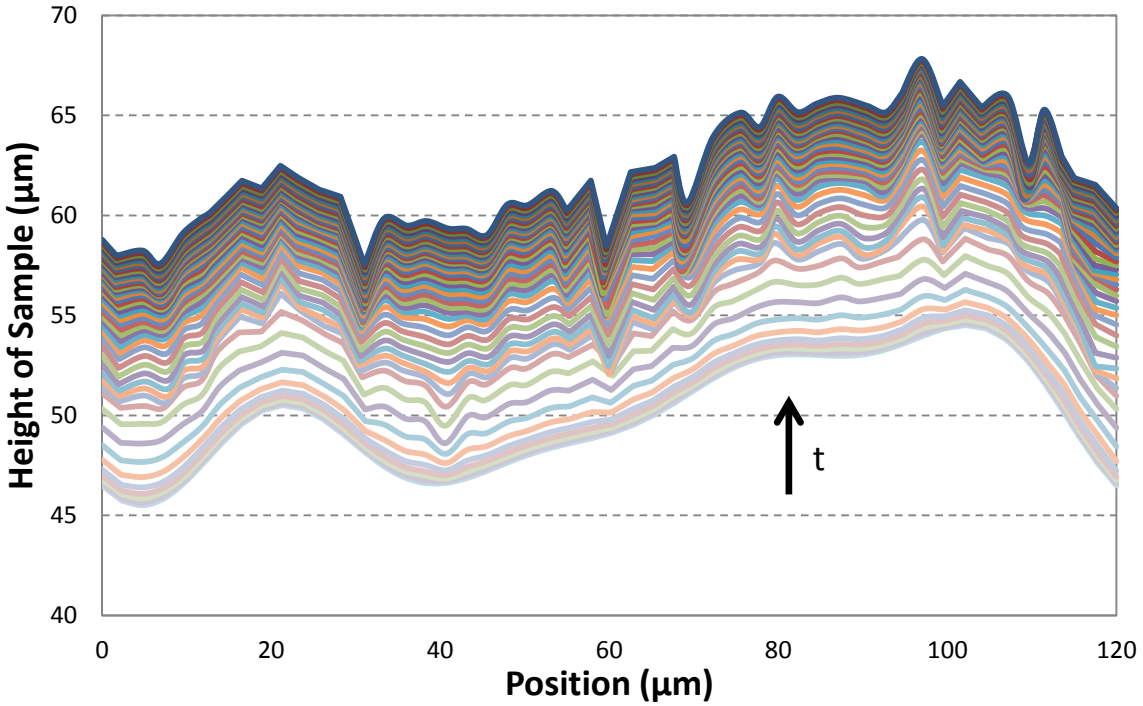

Figure 5.20: Four-mode Pattern # 2 subjected to a drive corresponding to a laser energy of 100 J – Evolution of the ripple surface as a function of time.

As time increases, the ripple surface moves further along the direction of loading, as expected. In the early stage of loading, the surface remains smooth. The plot in Figure 5.21 shows the same evolution of the ripple surface in Figure 5.20, but with only the 12 data points of interest.

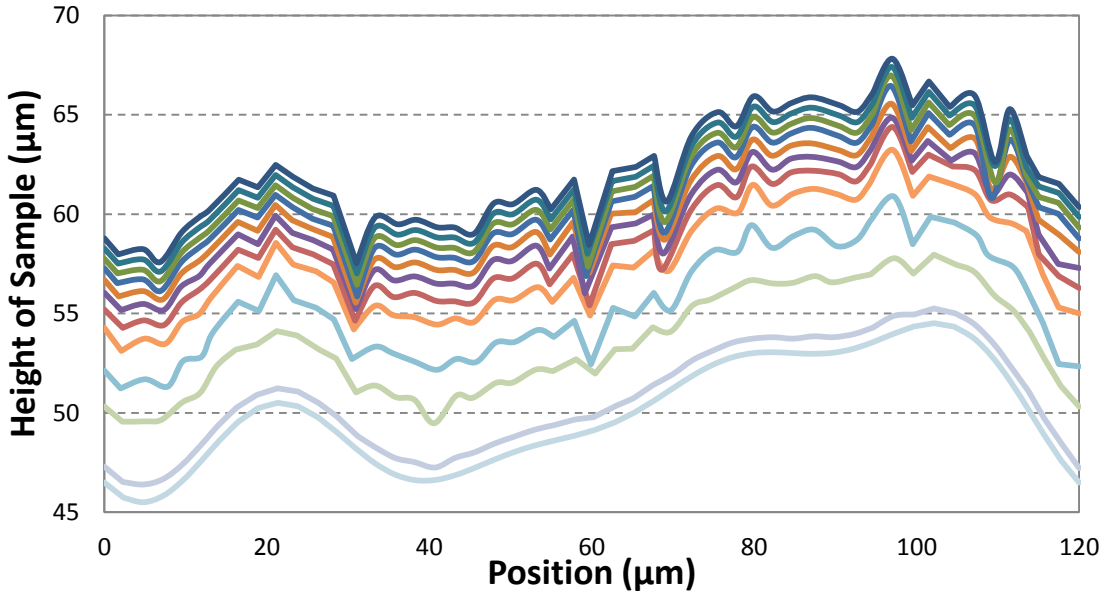

Figure 5.21: Four-mode Pattern # 2 subjected to a drive corresponding to a laser energy of 100 J – Evolution of the ripple surface as a function of time plotted with only 12 points of interest from Figure 5.20.

Figures 5.20 and 5.21 show that at the start of the simulation the ripple surface stays smooth, and as time continues the ripple surface begins to show wrinkles and is no longer smooth and continuous. Just as in Pattern # 1, the first two time points show less growth because of the compression of the heat shield. Between the second and third time points, the progression of the surface is at a maximum, and as time progresses the ripple surface continues to move up, but at a slower rate.

Figure 5.22 shows the growth factors computed using Equation 5.8 as a function of time for each of the eight different ripples. This is followed by Figure 5.23, which shows the plots of the growth factors for a few of the selected ripples from Figure 5.22.

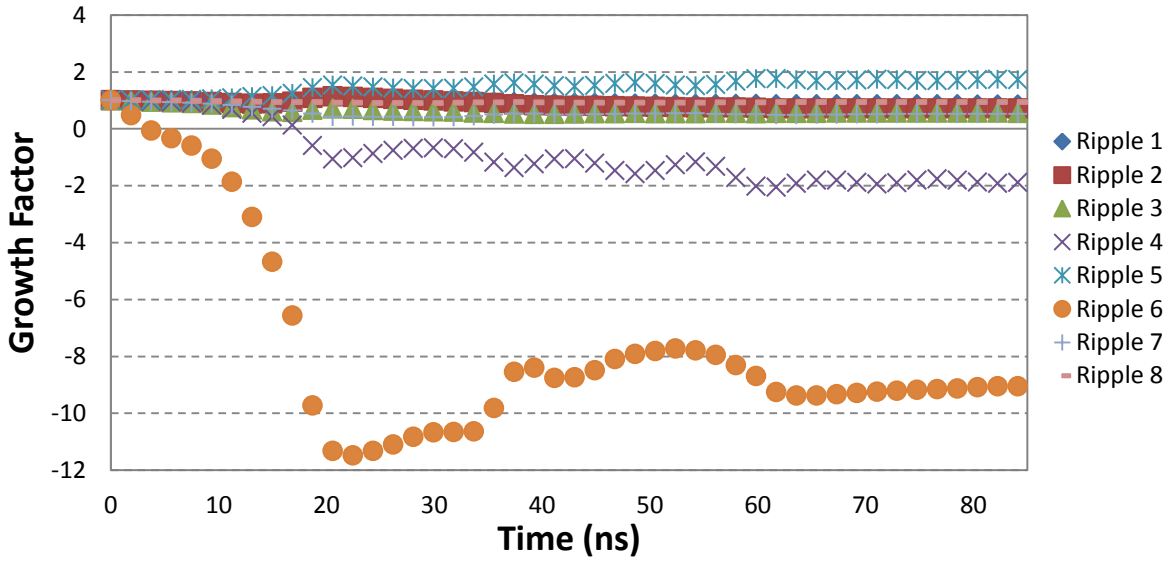

Figure 5.22: Growth Factor vs. time for four-mode Pattern # 2 subjected to a drive corresponding to a laser energy of 100 J.

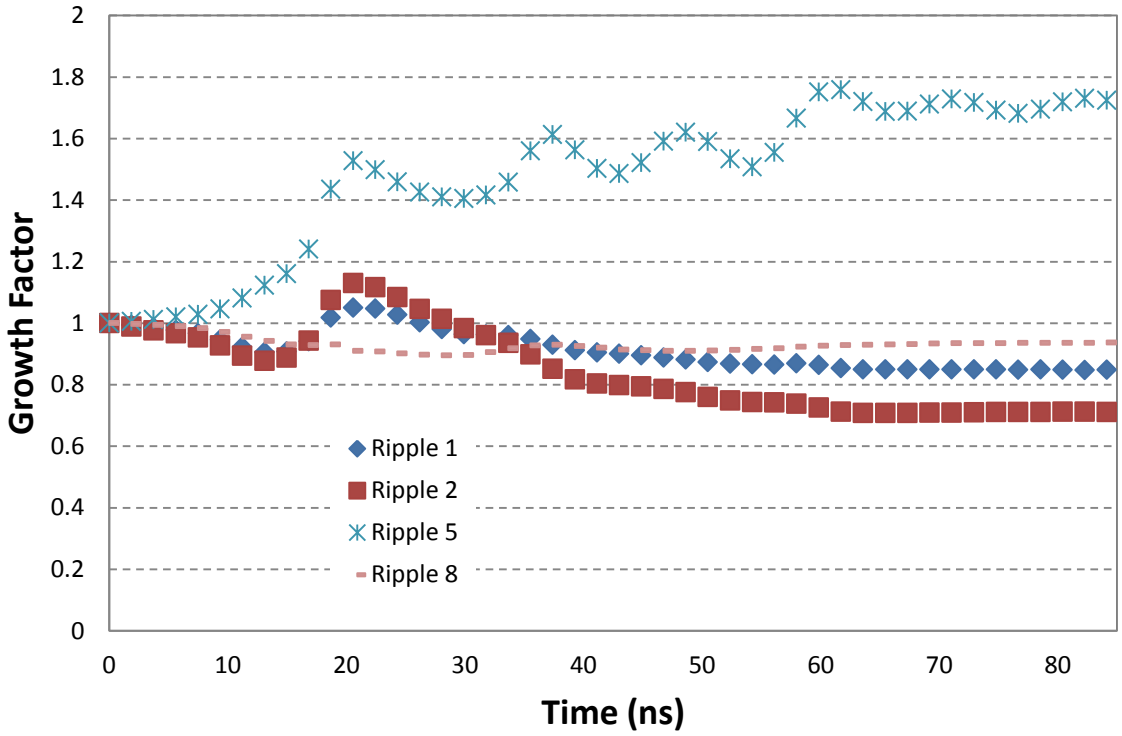

Figure 5.23: Growth Factor vs. time for selected ripples of interest for four-mode Pattern # 2 subjected to a drive corresponding to a laser energy of 100 J.

As seen in Figure 5.23, the values for growth factor are more in the range of what was expected, as compared to Pattern # 1. Figure 5.22 shows that Ripple # 6 is again an outlier and is showing an anomalously high growth factor. This pattern also had small amplitudes for Ripple #s 3, 4, 5, and 6, which is why Figure 5.23 focuses on the ripples with initially larger amplitudes. Ripple #s 1 and 2 show peak growth factors of nearly 1.1 and 1.2, respectively. Ripple # 8 does not grow and only shows compression. Ripple # 5 shows a growth factor peaking at nearly 2 towards the end. The other ripples peak at about 20 ns, where Ripple # 5 has a growth factor of about 1.5. This agrees well with the single-mode results of ripple growth at this energy.

5.2.2.2 Pattern # 2 – 150 J

A simulation was performed for the four-mode Pattern # 2 configuration with 150 J of energy for the drive. Figure 5.24 shows a selection of the images from the simulation with approximately 7.8 ns between successive images. In these images, the red region is the Ta sample and the grey region is the heat shield. In the Richtmyer-Meshkov configuration, the drive comes from the top down such that the heat shield is driven into the Ta sample.

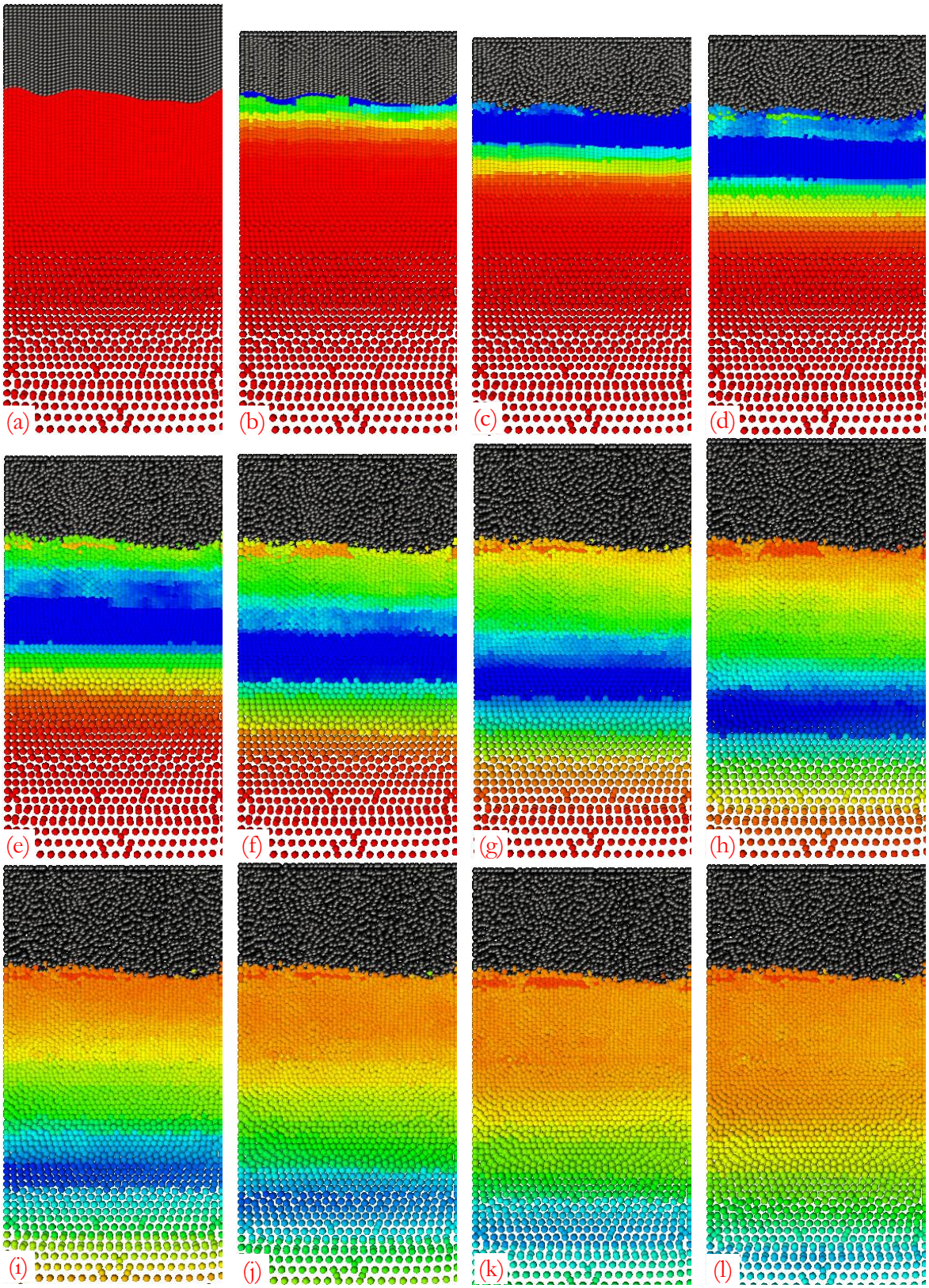

Figure 5.24: Four-mode Pattern # 2 subjected to a drive corresponding to a laser energy of 150 J – Evolution of the ripple and target in time. The images (a)-(l) are snapshots of the ripples starting from time t=0 to t= 86 ns, with 7.8 ns between the images.

Figure 5.24 shows the expected physics, as in the other simulations. The heat shield is initially compressed, the wave reaches the interface and the growth begins, and the heat shield expands about halfway through the simulation. However, unlike in the 100 J drive, as the interface evolves it becomes more blurred, making the initial pattern harder to decipher.

The vertical axis in Figure 5.25 represents the distance along the direction of the loading. Each line represents the location of the ripple surface at a particular time during the simulation. In these plots, the drive is coming from the bottom up, i.e. the lowermost curve represents the four-mode ripple pattern before loading at t=0.

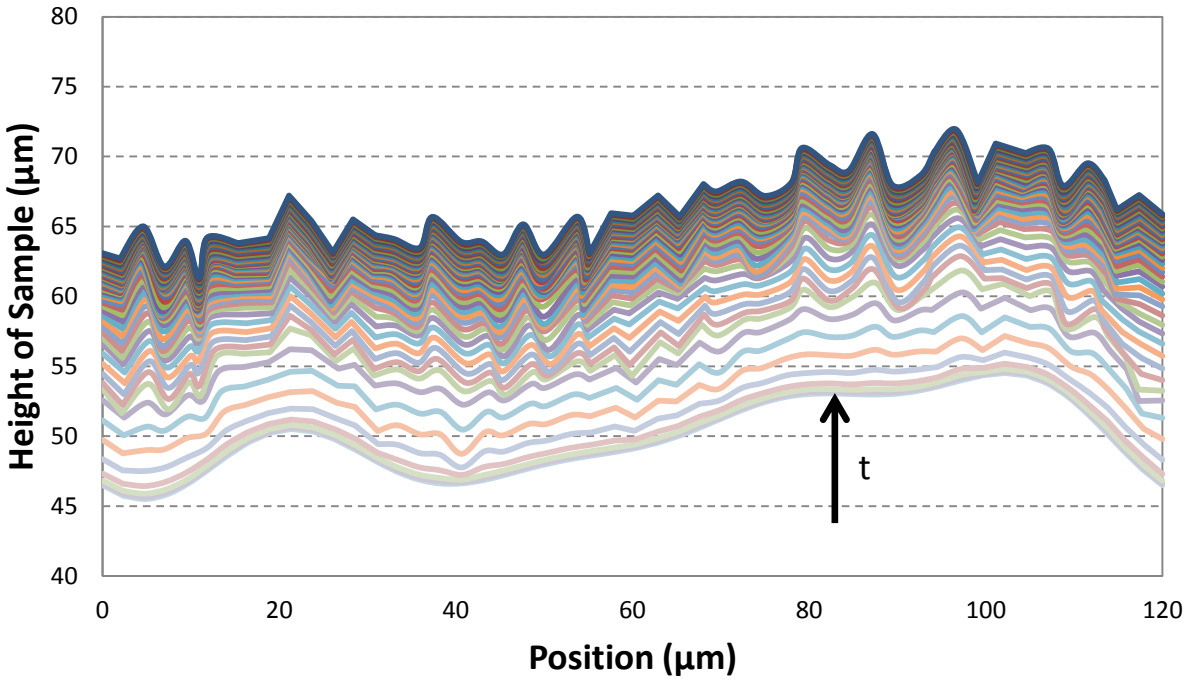

Figure 5.25: Four-mode Pattern # 2 subjected to a drive corresponding to a laser energy of 150 J – Evolution of the ripple surface as a function of time.

As time increases, the ripple surface moves further along the direction of loading, as expected. In the early stage of loading, the surface remains smooth. The plot in Figure 5.26 shows the same evolution of the ripple surface in Figure 5.25, but with only the 12 data points of interest.

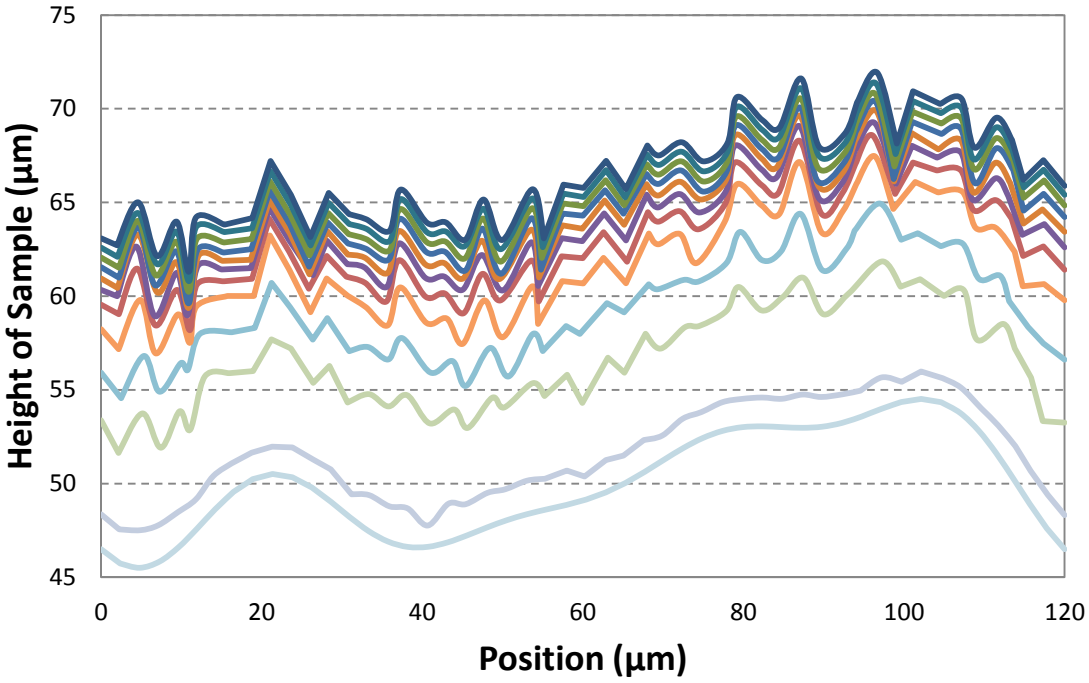

Figure 5.26: Four-mode Pattern # 2 subjected to a drive corresponding to a laser energy of 150 J – Evolution of the ripple surface as a function of time plotted with only 12 points of interest from Figure 5.25.

The plots in Figures 5.25 and 5.26 of the evolution of the ripple surface show the same trend as for the 100 J drive. In the early stage of loading, the surface remains smooth. As time progresses, the ripple surface begins to show wrinkles and is no longer smooth and continuous. Likewise, the first two time points show the compression of the heat shield, and the subsequent time points show the progression of the surface as faster in the beginning and slower at the end.

Figure 5.27 shows the growth factors computed using Equation 5.8 as a function of time for each of the eight different ripples. This is followed by Figure 5.28, which shows the plots of the growth factors for a few of the selected ripples from Figure 5.27.

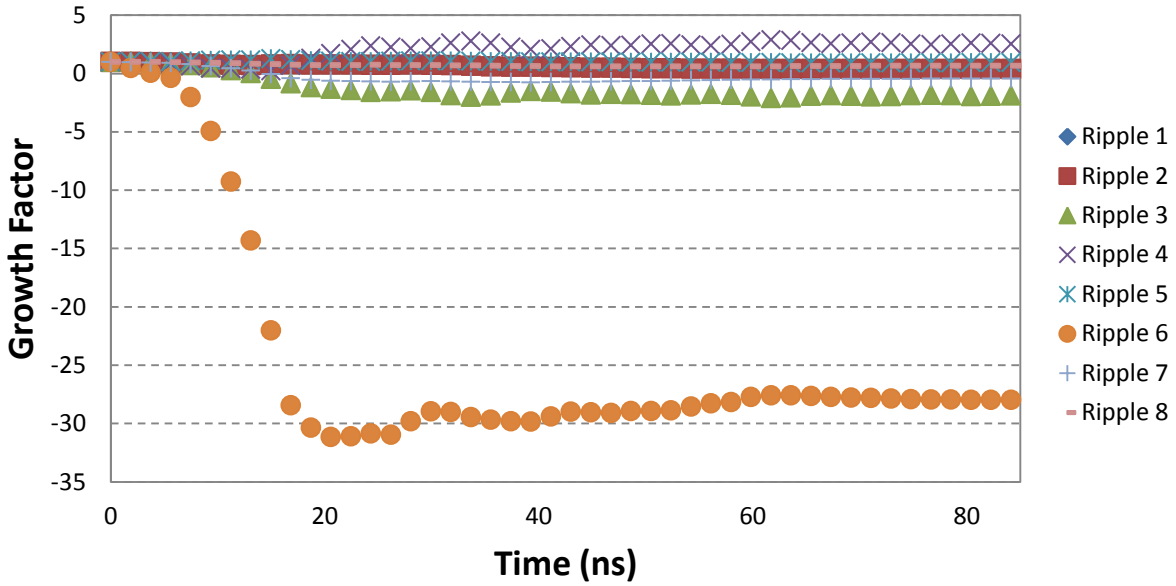

Figure 5.27: Growth Factor vs. time for four-mode Pattern # 2 subjected to a drive corresponding to a laser energy of 150 J.

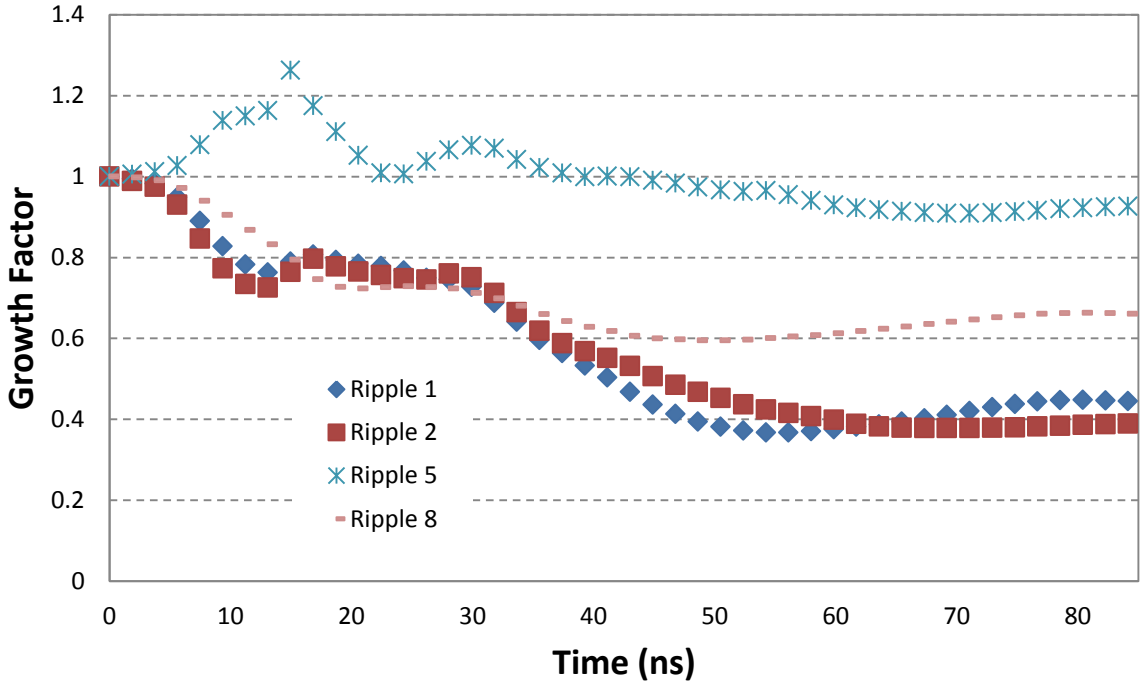

Figure 5.28: Growth Factor vs. time for selected ripples of interest for four-mode Pattern # 2 subjected to a drive corresponding to a laser energy of 150 J.

Figure 5.27 shows that Ripple # 6 is the outlier with an anomalously high growth factor. Figure 5.28 focuses on the four ripples that start with a larger amplitude. Ripple # 5 has a growth factor of 1.3, which is not as high as expected. Ripple #s 1, 2, and 8 do not show positive growth. The likely

reason for the suppressed growth in Ripple # 5 and the negative growth in the other ripples is the noted distortion in the interface as time progresses. This may be a result of the pattern and the amount of energy, but the interface of the heat shield and Ta sample becomes distorted over time, making it more difficult to obtain accurate growth factors. The results of this simulation suggest that four-mode Pattern # 2 is not ideal for experiments. The following section compares the results of Pattern # 2 at the two different energies.

5.2.2.3 Four-mode Pattern # 2 Comparison

The four-mode ripple Pattern # 2 was subjected to drives corresponding to laser energies of 100 and 150 J. Figure 5.29 shows the time history of two of the ripples at each energy. It is expected that higher energy will result in more growth.

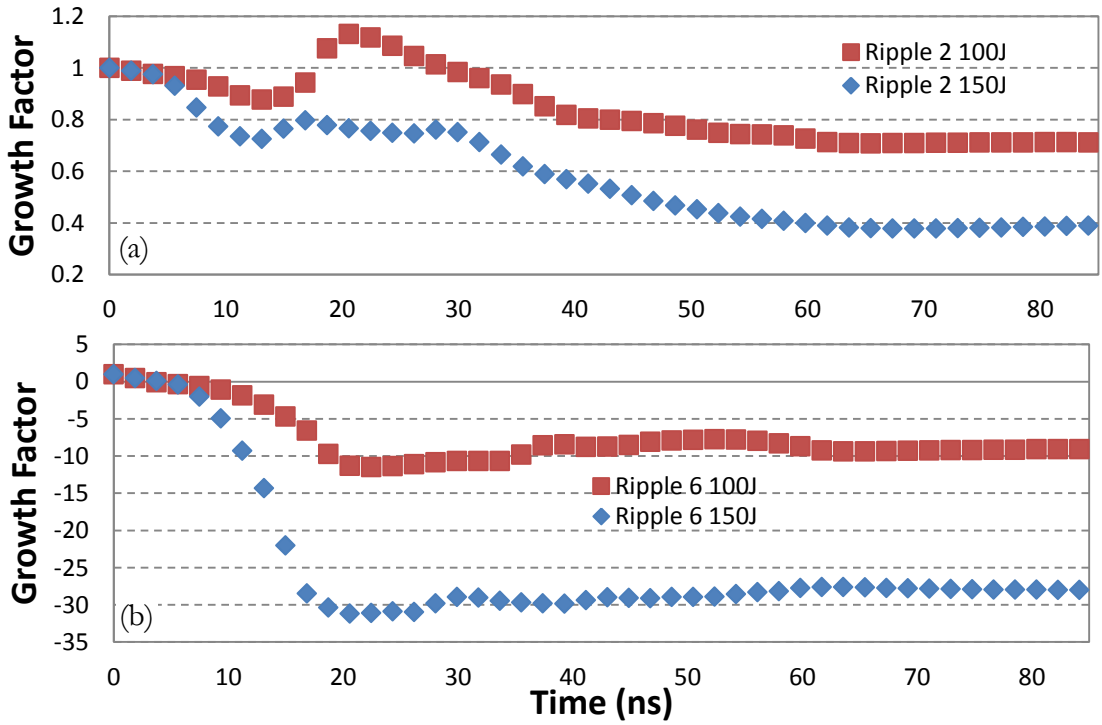

Figure 5.29: Comparison of Growth Factor vs. time for four-mode Pattern # 2 subjected to two different energies, 100 and 150 J for (a) Ripple # 2 and (b) Ripple # 6.

For Ripple # 2, the 100 J drive shows more growth than the 150 J drive, which is not expected (Figure 5.29(a)). This is likely due to the distortion of the interface of the ripple. Ripple # 6 at the 150 J drive shows more growth than the 100 J drive, however it is in compression (Figure 5.29(b)). Also, the Ripple # 6 growth factors are anomalously high, just as they were in Pattern # 1, because of the error associated with the initially smaller peak-to-valley height. Overall, in this simulation the ripples are being shrinking instead of growing. In both ripples above there is more compression for the 150 J drive than for the 100 J drive, which is expected with higher energies. However, this confirms that four-mode Pattern # 2 is not an ideal configuration to perform experiments on. It is

possible that the distortion of the interface and the resulting compression is a result of the four-mode patterns. Trying to distinguish four modes in such a small width makes it difficult to characterize the growth. The following pattern is also a four-mode pattern. If the same results are observed, this would suggest that the four-mode pattern should not be tested.

5.2.3 Pattern # 3

Four-mode Pattern # 3 is represented by the following equation:

$$\eta_{P3}(x) = 1.5\sin\left(\frac{2\pi}{30}x + \frac{\pi}{4}\right) + \sin\left(\frac{2\pi}{40}x + \frac{\pi}{3}\right) + 2.5\sin\left(\frac{2\pi}{60}x + \frac{\pi}{2}\right) + 1.5\sin\left(\frac{2\pi}{120}x\right) \quad (5.19)$$

5.2.3.1 Pattern # 3 – 100 J

A simulation was performed for the four-mode Pattern # 3 configuration with 100 J of energy for the drive. Figure 5.30 shows a selection of the images from the simulation approximately 7.5 ns between successive images. In these images, the red region is the Ta sample and the grey region is the heat shield. In the Richtmyer-Meshkov configuration, the drive comes from the top down such that the heat shield is driven into the Ta sample.

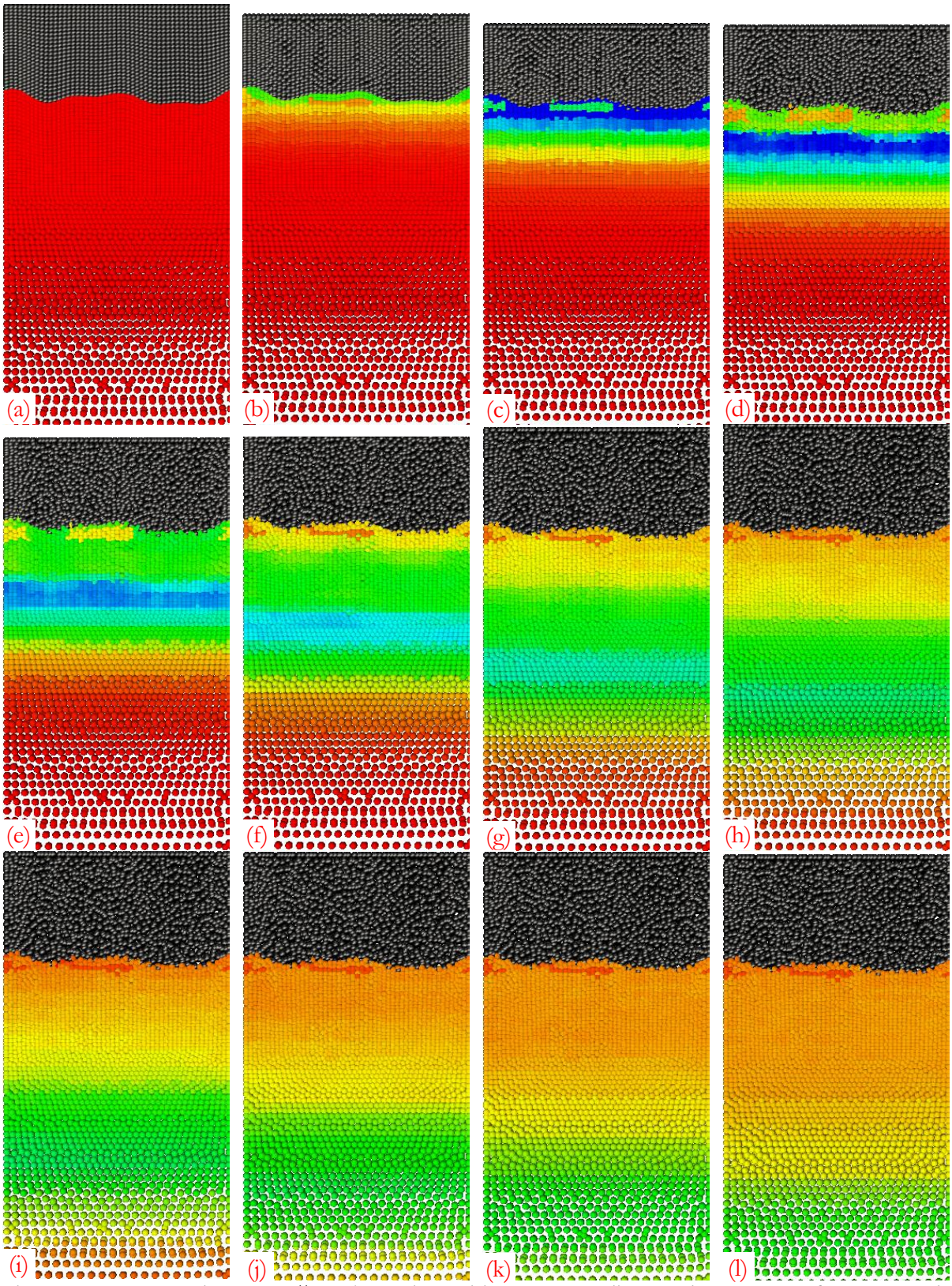

Figure 5.30: Four-mode Pattern # 3 subjected to a drive corresponding to a laser energy of 100 J – Evolution of the ripple and target in time. The images (a)-(l) are snapshots of the ripples starting from time t=0 to t= 82 ns, with 7.5 ns between the images.

Pattern # 3 shows the same physics as Patterns # 1 and # 2. The heat shield is initially compressed, the wave reaches the interface and the growth begins, and the heat shield begins to expand at about halfway through the simulation.

The vertical axis in Figure 5.31 represents the distance along the direction of the loading. Each line represents the location of the ripple surface at a particular time during the simulation. In these plots, the drive is coming from the bottom up, i.e. the lowermost curve represents the four-mode ripple pattern before loading at t=0.

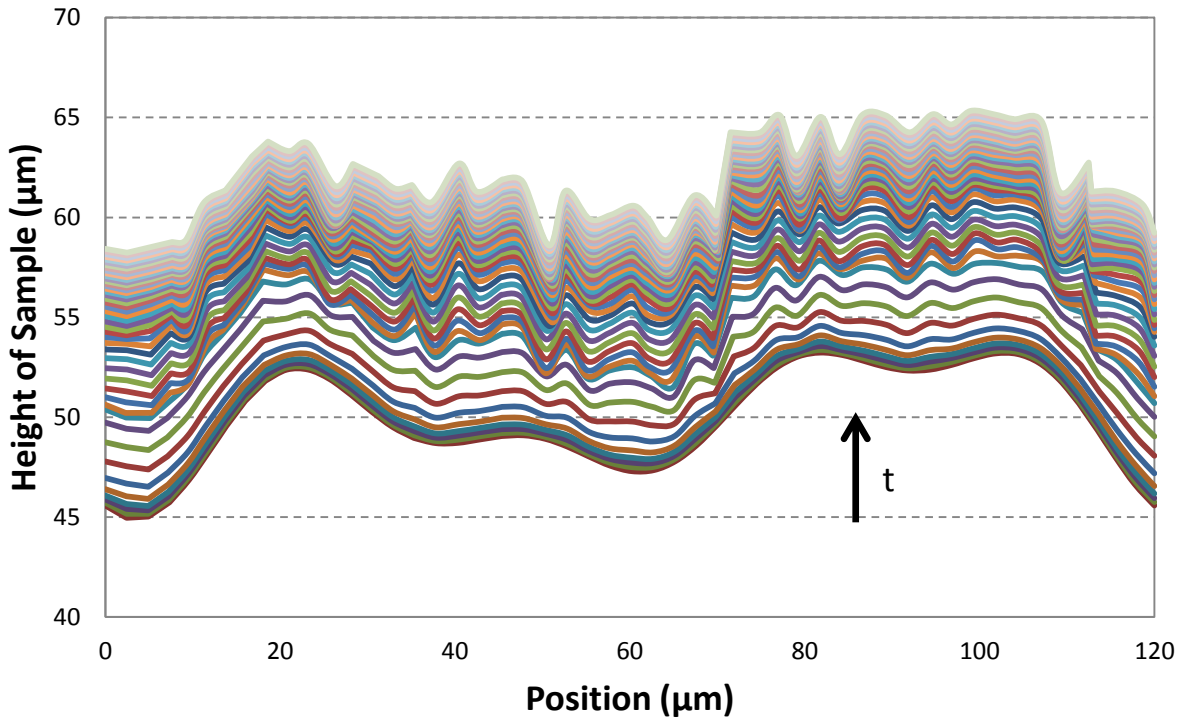

Figure 5.31: Four-mode Pattern # 3 subjected to a drive corresponding to a laser energy of 100 J – Evolution of the ripple surface as a function of time.

As time increases, the ripple surface moves further along the direction of loading, as expected. In the early stage of loading, the surface remains smooth. The plot in Figure 5.32 shows the same evolution of the ripple surface in Figure 5.31, but with only the 12 data points of interest.

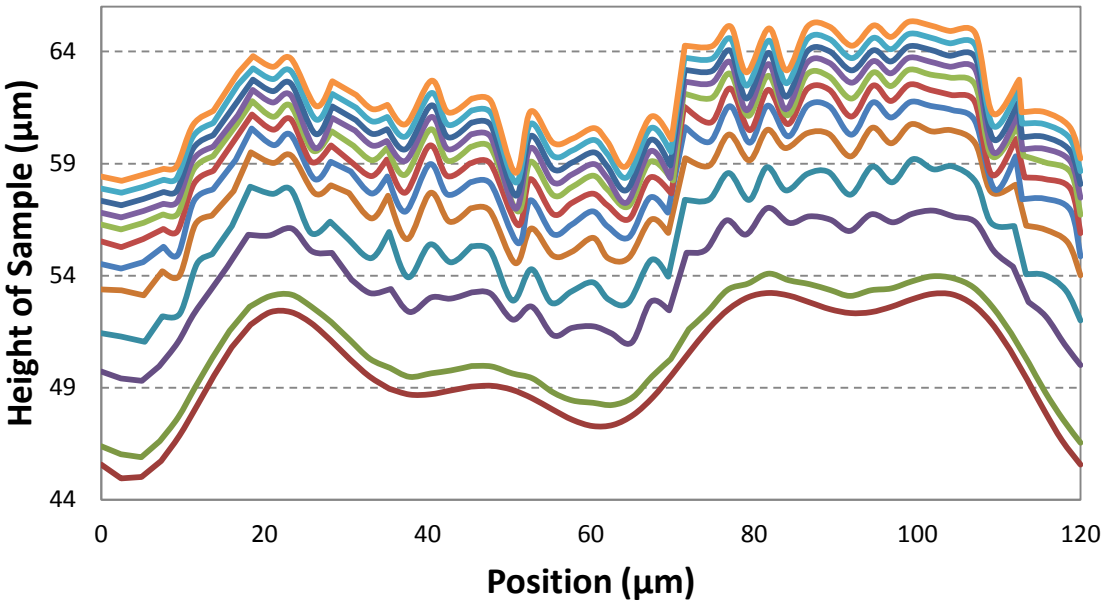

Figure 5.32: Four-mode Pattern # 3 subjected to a drive corresponding to a laser energy of 100 J – Evolution of the ripple surface as a function of time plotted with only 12 points of interest from Figure 5.31.

In Figures 5.31 and 5.32, the same behavior is shown as in Patterns # 1 and # 2. At the start of the simulation the ripple surface stays smooth, and as time continues the ripple surface begins to show wrinkles and is no longer smooth and continuous. The first two time points show less growth because of the compression of the heat shield. Between the second and third time points, the progression of the surface is at a maximum, and as time progresses the ripple surface continues to move up, but at a slower rate.

Figure 5.33 shows the growth factors computed using Equation 5.8 as a function of time for each of the eight different ripples. This is followed by Figure 5.34, which shows the plots of the growth factors for a few of the selected ripples from Figure 5.33.

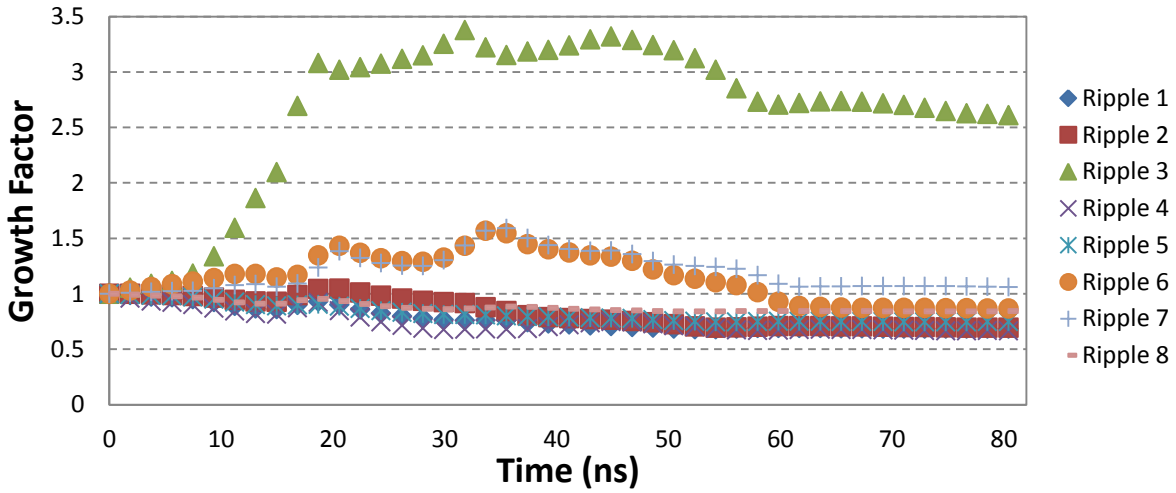

Figure 5.33: Growth Factor vs. time for four-mode Pattern # 3 subjected to a drive corresponding to a laser energy of 100 J.

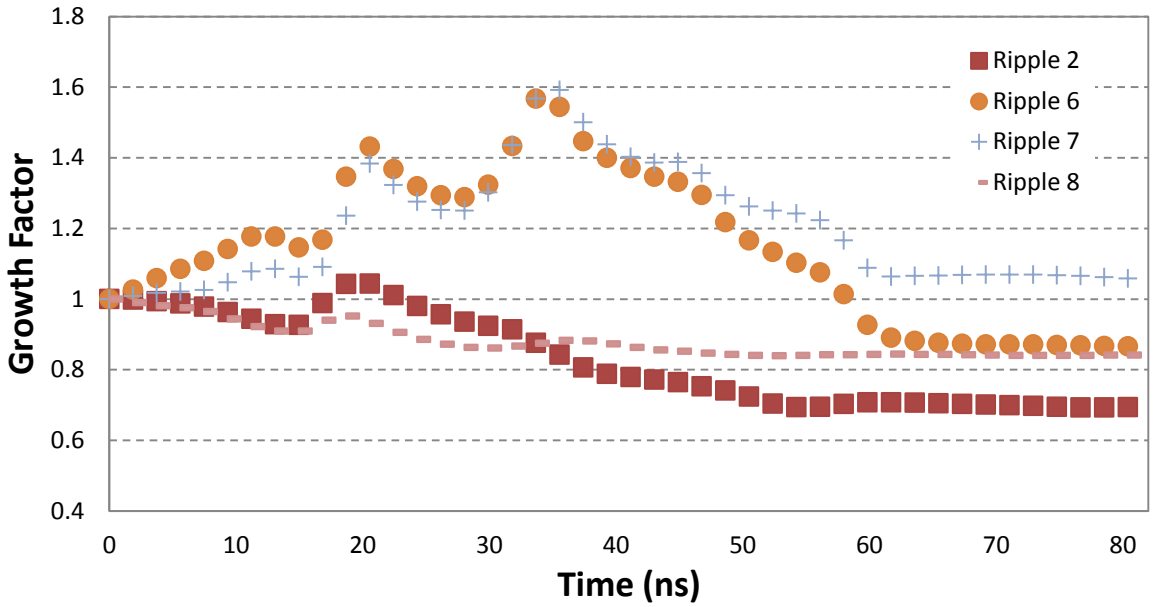

Figure 5.34: Growth Factor vs. time for selected ripples of interest for four-mode Pattern # 3 subjected to a drive corresponding to a laser energy of 100 J.

Figure 5.33 and 5.34 show that the values for the growth factor are more in the range of what is expected as opposed to Patterns # 1 and # 2. In Figure 5.33, although not as distinct an outlier as Ripple # 6 was in previous patterns, it can be inferred that Ripple # 3 is an outlier here, because it is one of the smaller initial amplitude ripples and a growth factor of 3.5 is much higher than expected. In Figure 5.34, looking at the other ripples, the types of growth factors expected are observed. Ripple #s 6 and 7 peak at 1.6 and Ripple # 2 is nearly at 1.1. Ripple # 8 peaks at the same time (about 20 ns) as the other ripples but does not have positive growth.

5.2.3.2 Pattern # 3 – 150 J

A simulation was performed for the four-mode Pattern # 3 configuration with 150 J of energy for the drive. Figure 5.35 shows a selection of the images from the simulation with approximately 3.3 ns between successive images. In these images, the red region is the Ta sample and the grey region is the heat shield. In the Richtmyer-Meshkov configuration, the drive comes from the top down such that the heat shield is driven into the Ta sample.

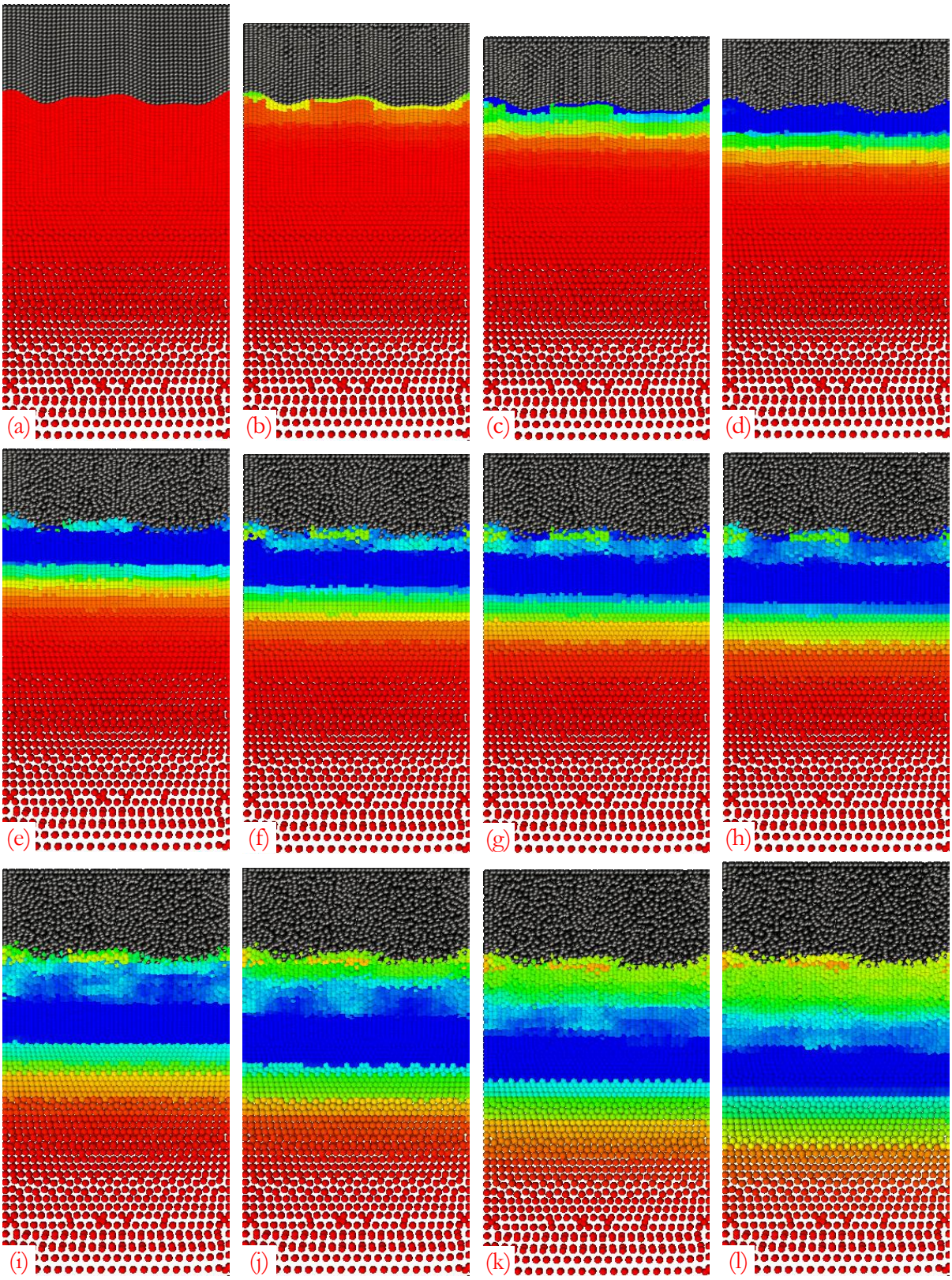

Figure 5.35: Figure 5.30: Four-mode Pattern # 3 subjected to a drive corresponding to a laser energy of 150 J – Evolution of the ripple and target in time. The images (a)-(l) are snapshots of the ripples starting from time t=0 to t= 37 ns, with 3.3 ns between the images.

Figure 5.35 shows the expected physics regarding the heat shield, Ta sample, and interface. Unlike in Pattern # 2, as the interface evolves the initial pattern does not become too distorted, which should result in more accurate measurements for growth factor.

The vertical axis in Figure 5.36 represents the distance along the direction of the loading. Each line represents the location of the ripple surface at a particular time during the simulation. In these plots, the drive is coming from the bottom up, i.e. the lowermost curve represents the four-mode ripple pattern before loading at t=0.

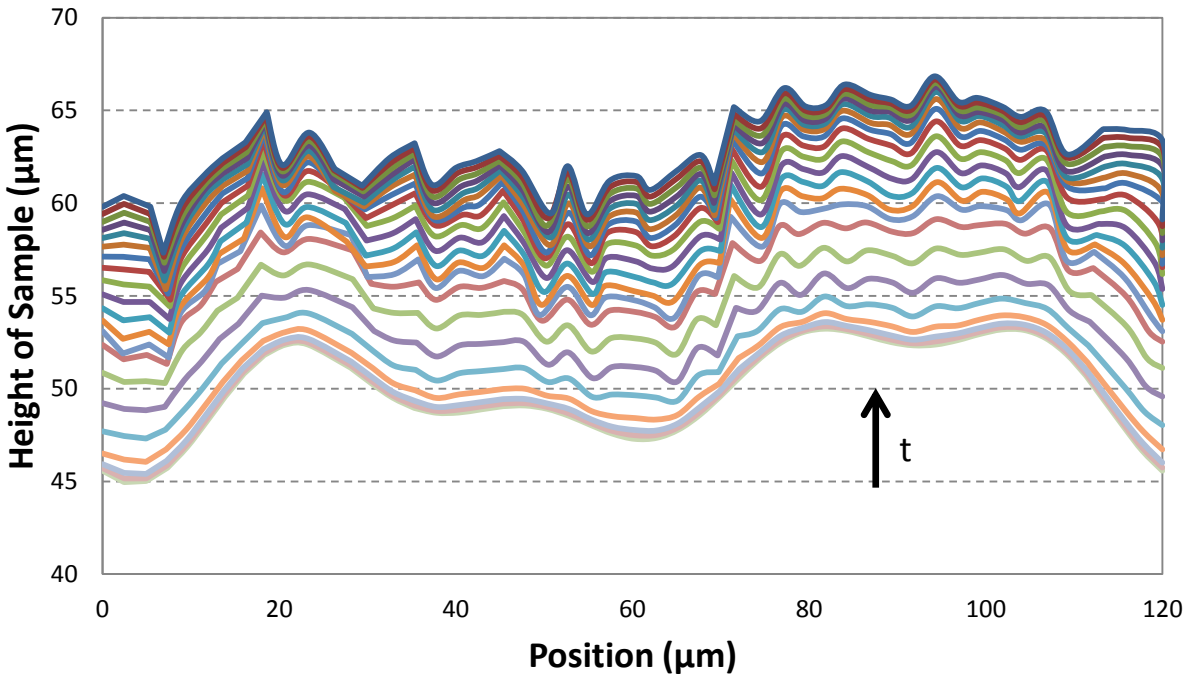

Figure 5.36: Four-mode Pattern # 3 subjected to a drive corresponding to a laser energy of 150 J – Evolution of the ripple surface as a function of time.

As time increases, the ripple surface moves further along the direction of loading, as expected. In the early stage of loading, the surface remains smooth. The plot in Figure 5.37 shows the same evolution of the ripple surface in Figure 5.36, but with only the 12 data points of interest.

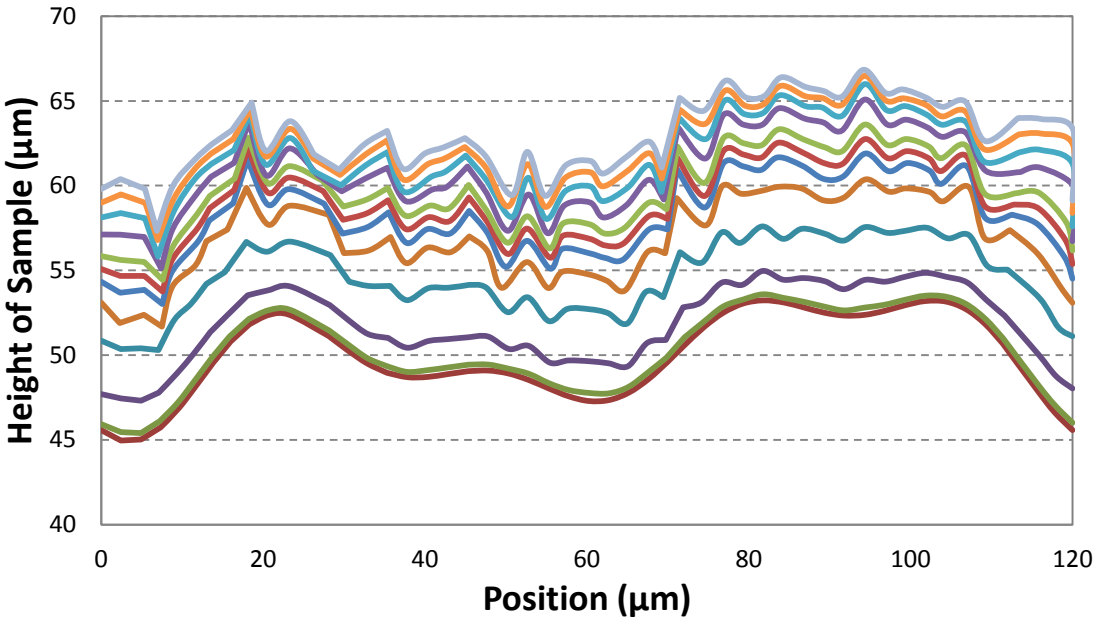

Figure 5.37: Four-mode Pattern # 3 subjected to a drive corresponding to a laser energy of 150 J – Evolution of the ripple surface as a function of time plotted with only 12 points of interest from Figure 5.36.

The plots in Figure 5.36 and 5.37 of the evolution of the ripple surface show the same trends as previous energies and patterns, as expected.

Figure 5.38 shows the growth factors computed using Equation 5.8 as a function of time for each of the eight different ripples. This is followed by Figure 5.39, which shows the plots of the growth factors for a few of the selected ripples from Figure 5.38.

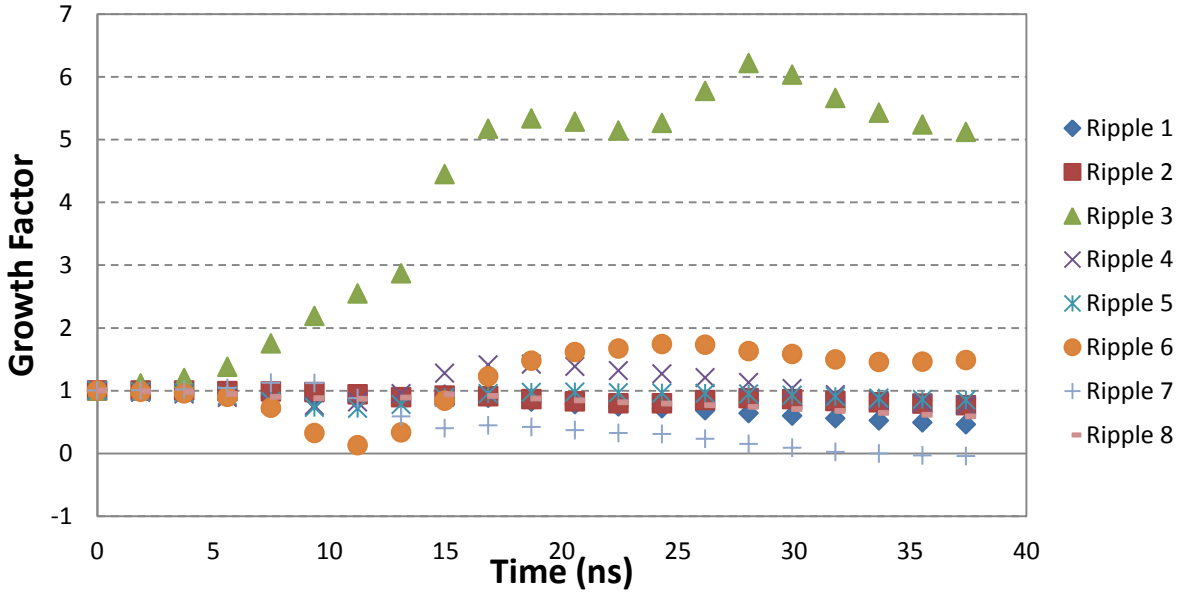

Figure 5.38: Growth Factor vs. time for four-mode Pattern # 3 subjected to a drive corresponding to a laser energy of 150 J.

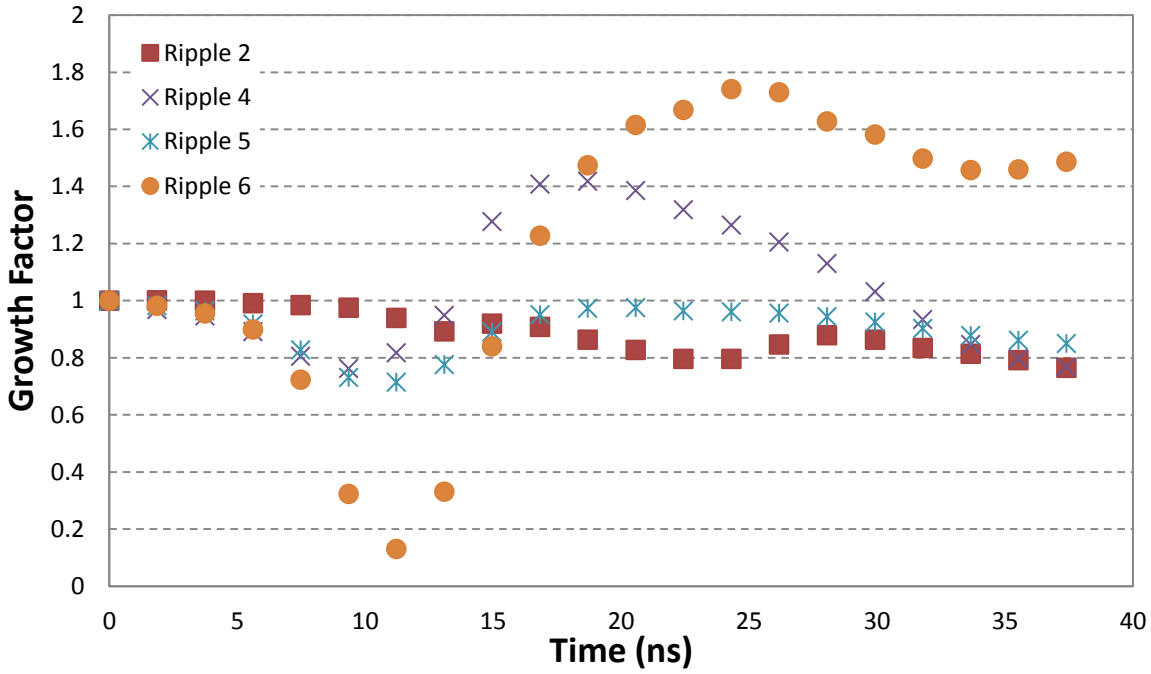

Figure 5.39: Growth Factor vs. time for selected ripples of interest for four-mode Pattern # 3 subjected to a drive corresponding to a laser energy of 150 J.

Figures 5.38 and 5.39 show that, as with the 100 J case, the growth factors are more in the range of what is expected, as opposed to Patterns # 1 and # 2. As seen in Figure 5.38, Ripple # 3 is again an outlier. As seen in Figure 5.39, Ripple #s 4 and 6 have peak growth factors of 1.4 and 1.7, respectively. Ripple #s 2 and 5 do not show positive growth. In general, the peak growth factors are more agreeable to experimental data in this pattern as opposed to other patterns. However, growth is not consistent among all the ripples. The next section compares the two different energies from Pattern # 3.

5.2.3.3 Four-mode Pattern # 3 Comparison

The four-mode ripple Pattern # 3 was subjected to drives corresponding to laser energies of 100 and 150 J. Figure 5.40 shows the time history of two of the ripples at each energy. It is expected that higher energy will result in more growth.

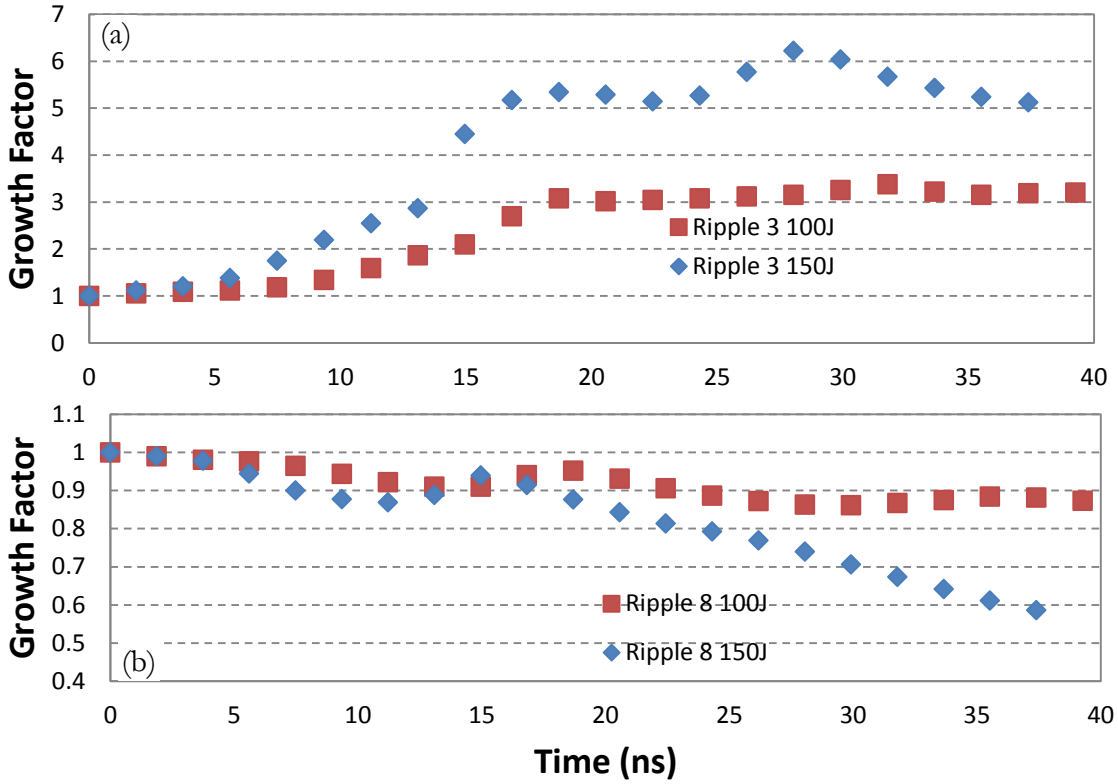

Figure 5.40: Comparison of Growth Factor vs. time for four-mode Pattern # 3 subjected to two different energies, 100 and 150 J for (a) Ripple # 3 and (b) Ripple # 8.

For Ripple # 3, the 150 J drive shows more growth than the 100 J drive, as expected; however, this ripple is one of the smaller initial peak-to-valley height ripples, which results in more error (Figure 5.40(a)). Ripple # 8 does not show positive growth but, as expected, the 150 J drive compresses more than the 100 J drive (Figure 5.40(b)). However, within this pattern, the growth is not consistent. Some of the ripples grow while others do not. Overall, this analysis suggests the four-mode patterns are not ideal for the experiments. Also, ripples with initially small peak-to-valley heights are too difficult to measure and result in too much error. Therefore, it is necessary to perform simulations on new patterns. These patterns will only have three modes and all of the resulting six amplitudes need to be large enough to accurately measure growth factor.

5.3 Three-Mode Configuration Results

Two different patterns were simulated for the three-mode configuration. Both patterns are similar and contain the same wavelengths such that the peaks and valleys are in the same horizontal location. However, Pattern # 5 has slightly larger amplitudes, resulting in steeper slopes. These two patterns can be seen together earlier in Figure 5.2. Pattern # 4 was selected as the configuration to be used in the Omega experiments, so more results are shown here than for other patterns.

5.3.1 Pattern # 4

Three-mode Pattern # 4 is represented by the following equation, where θ represents the angle-of-descent:

$$\eta_{P4}(x) = 2.5\sin\left(\frac{2\pi}{40}x + \frac{\pi}{3}\right) + \sin\left(\frac{2\pi}{60}x + \frac{\pi}{2}\right) + 3\sin\left(\frac{2\pi}{120}x\right) \quad (5.20)$$

$$\theta^{max} = 31° \quad (5.21)$$

5.3.1.1 Pattern # 4 – 150 J

A simulation was performed for the three-mode Pattern # 4 configuration with 150 J of energy for the drive. Figure 5.41 shows a selection of the images from the simulation to show the evolution of the deformation of the target with approximately 6 ns between successive images. In these images, the red region is the Ta sample and the grey region is the heat shield. In the Richtmyer-Meshkov configuration, the drive comes from the top down such that the heat shield is driven into the Ta sample.

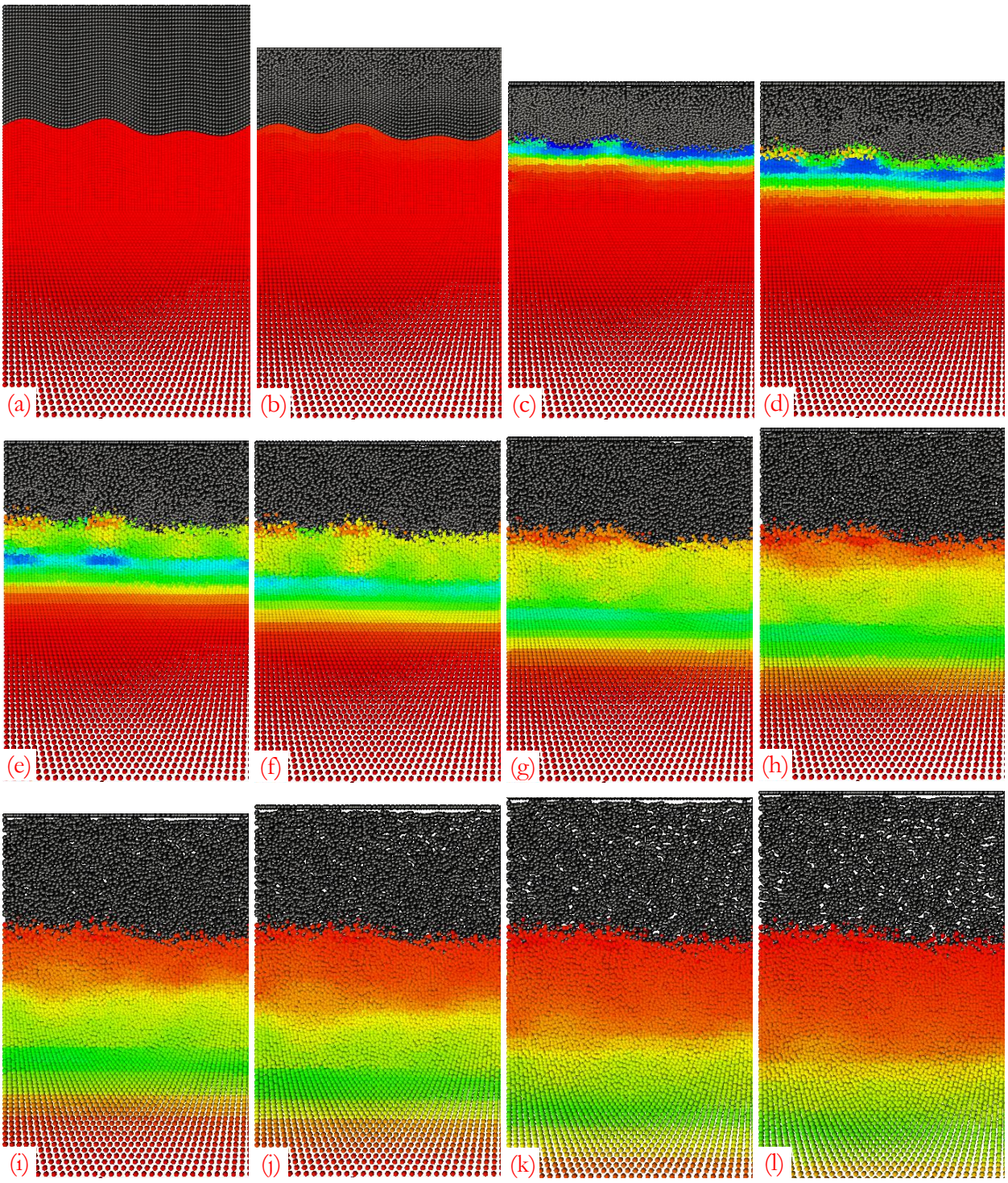

Figure 5.41: Three-mode Pattern # 4 subjected to a drive corresponding to a laser energy of 150 J – Evolution of the ripple and target in time. The images (a)-(l) are snapshots of the ripples starting from time t=0 to t= 67 ns, with 6 ns between the images.

In Figure 5.41, the drive is applied in the form of a velocity profile to the top surface of the BrCH heat shield. In the first three images (Figure 5.41(a)-(c)), the heat shield can be seen to be undergoing compression. About halfway through the simulation, the heat shield expands. As discussed in the three-mode patterns, this is the result of the reflection from the top surface of the heat shield resulting in tension of the heat shield. In Figure 5.41(c), the wave has passed the interface and is traveling through the Ta sample. As the simulation continues, the Ta sample continues to compress and the interface continues to evolve. The results in Figures 5.42 – 5.45 will show whether growth occurred in the ripples.

The vertical axis in Figure 5.42 represents the distance along the direction of the loading. Each line represents the location of the ripple surface at a particular time during the simulation. In these plots, the drive is coming from the bottom up, i.e. the lowermost curve represents the three-mode ripple pattern before loading at t=0.

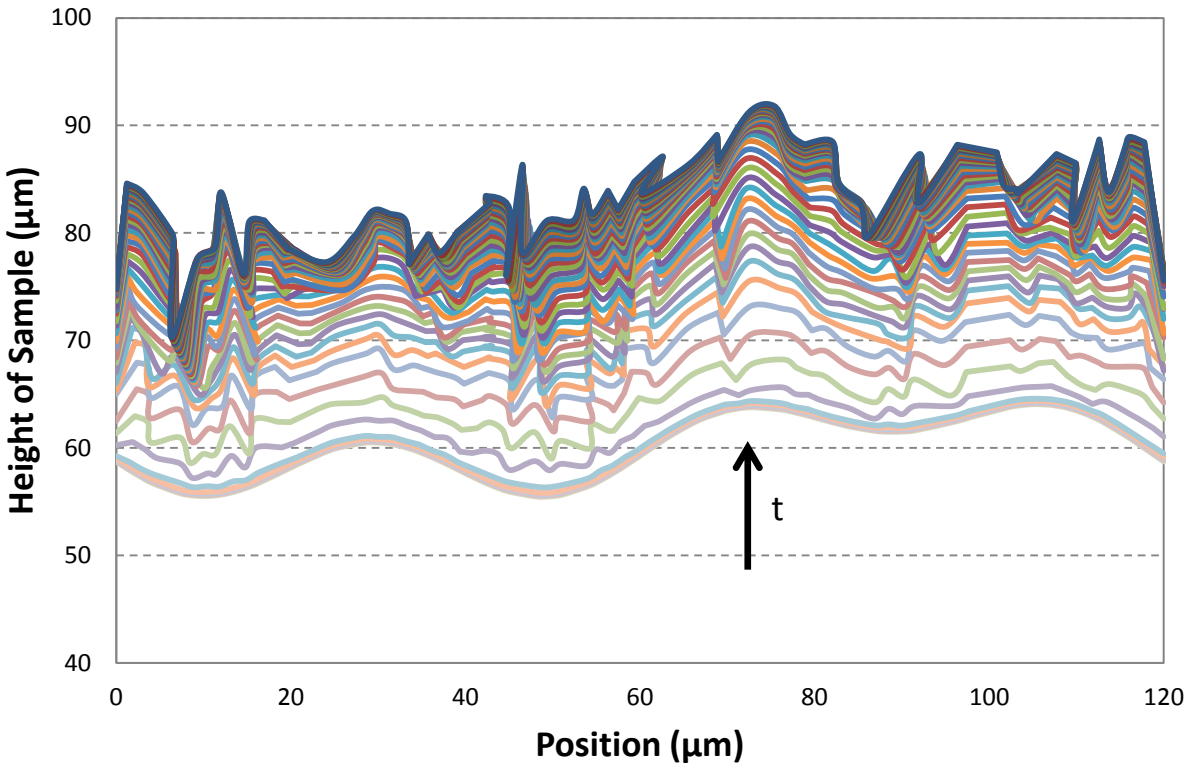

Figure 5.42: Three-mode Pattern # 4 subjected to a drive corresponding to a laser energy of 150 J – Evolution of the ripple surface as a function of time.

As time increases, the ripple surface moves further along the direction of loading, as expected. In the early stage of loading, the surface remains smooth. As time progresses, the ripple surface

begins to show wrinkles and is no longer smooth and continuous. The plot in Figure 5.43 shows the same evolution of the ripple surface in Figure 5.42, but with only the 12 data points of interest.

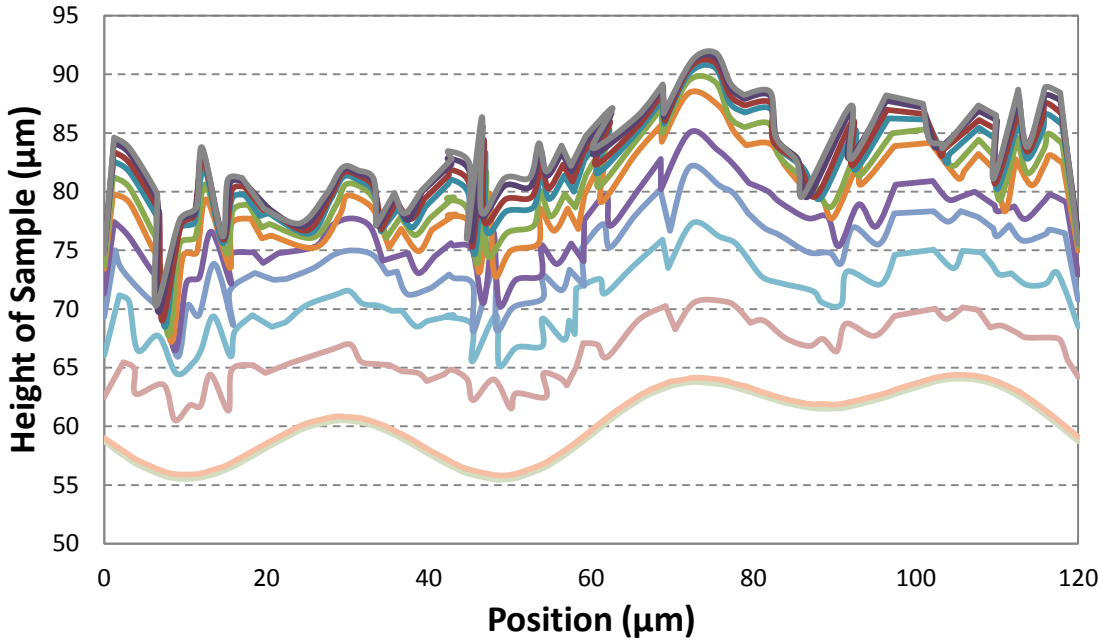

Figure 5.43: Three-mode Pattern # 4 subjected to a drive corresponding to a laser energy of 150 J – Evolution of the ripple surface as a function of time plotted with only 12 points of interest from Figure 5.42.

Each line represents approximately every 3rd or 4th output in time, giving approximately 11 ns between each line. Although the time between lines is equal, the change in displacement between each time interval is not constant. Between the first two time points, the change is slow, because the heat shield is still being compressed. Between the second and third time points, the change of displacement of the surface is at a maximum. As time continues, the ripple surface continues to move up but at a slower rate.

The growth factors from the three-mode Pattern # 4 simulation for the drive corresponding to a laser energy of 150 J are shown in Table 5.1. The second column shows the peak growth factor in the simulation. The third column shows the growth factor at the end of the simulation. In the experiments, only one data point for growth factor is given; therefore the growth factor as a function of time is not known. It is also not known if the growth factor fluctuates in the experiments as it does in simulations. Therefore, when comparing to experiments, it is standard to use the peak growth factor experienced during the test or simulation.

Table 5.1: Summary of Growth Factors for three-mode Pattern # 4 – 150 J

	Peak GF	GF at End
Ripple # 1	1.22	0.44
Ripple # 2	1.33	0.29
Ripple # 3	1.87	1.57
Ripple # 4	4.31	4.31
Ripple # 5	1.71	1.02
Ripple # 6	1.17	0.76

Figure 5.44 shows the growth factors computed using Equation 5.8 as a function of time for each of the six different ripples. This is followed by Figure 5.45, which shows the plots of the growth factors for a few of the selected ripples from Figure 5.44.

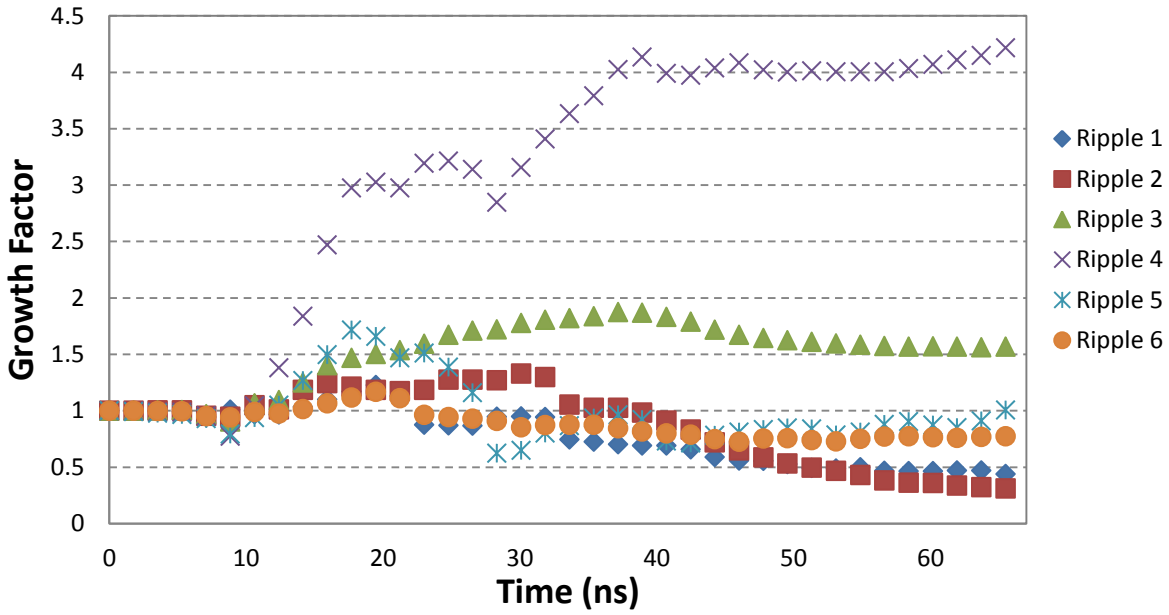

Figure 5.44: Growth Factor vs. time for three-mode Pattern # 4 subjected to a drive corresponding to a laser energy of 150 J.

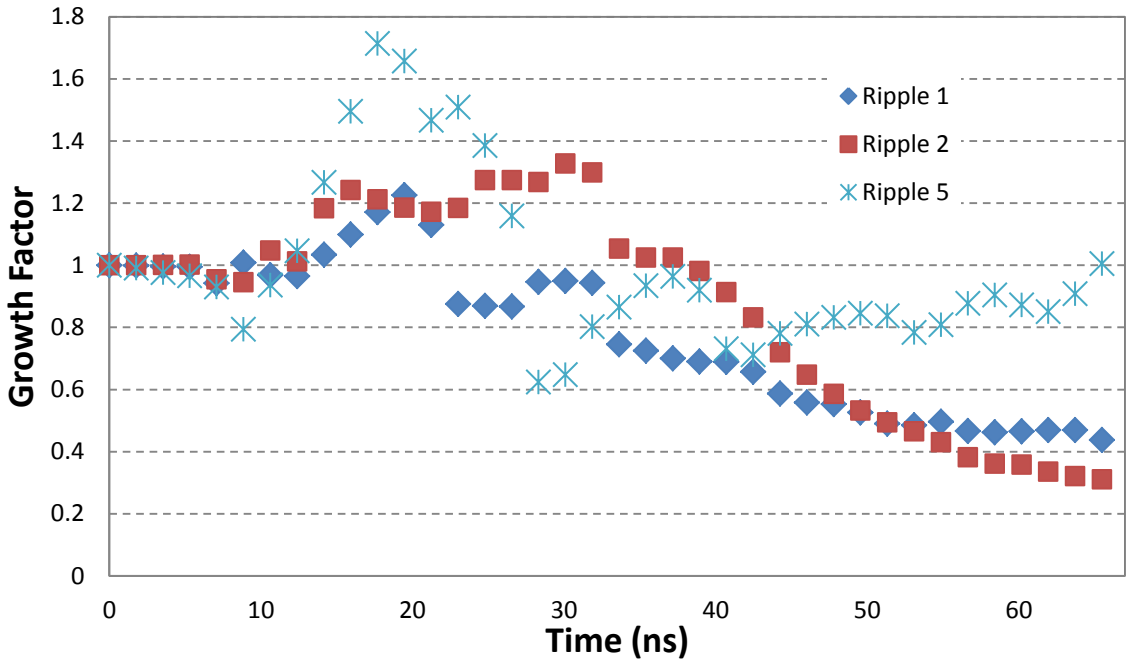

Figure 5.45: Growth Factor vs. time for selected ripples of interest for three-mode Pattern # 4 subjected to a drive corresponding to a laser energy of 150 J.

In Figure 5.44, Ripple # 4 shows a growth factor of over 4, which is anomalously high. Other than Ripple # 4, the values for growth factor are reasonable and agreeable to experiments. Figure 5.45 shows growth factor versus time for select ripples. Each of the ripples peak at about the same time (20-30 ns timeframe). Ripple # 5 has a peak growth factor of 1.71, Ripple # 2 peaks at 1.33, and Ripple # 1 peaks at 1.22. At the end of this section, these values are compared to the 200 J simulation to see if this data agrees with single-mode data.

5.3.1.2 Pattern # 4 – 200 J

A simulation was performed for the three-mode Pattern # 4 configuration with 200 J of energy for the drive. Figure 5.46 shows a selection of the images from the simulation with approximately 5 ns between successive images. In these images, the red region is the Ta sample and the grey region is the heat shield. In the Richtmyer-Meshkov configuration, the drive comes from the top down such that the heat shield is driven into the Ta sample.

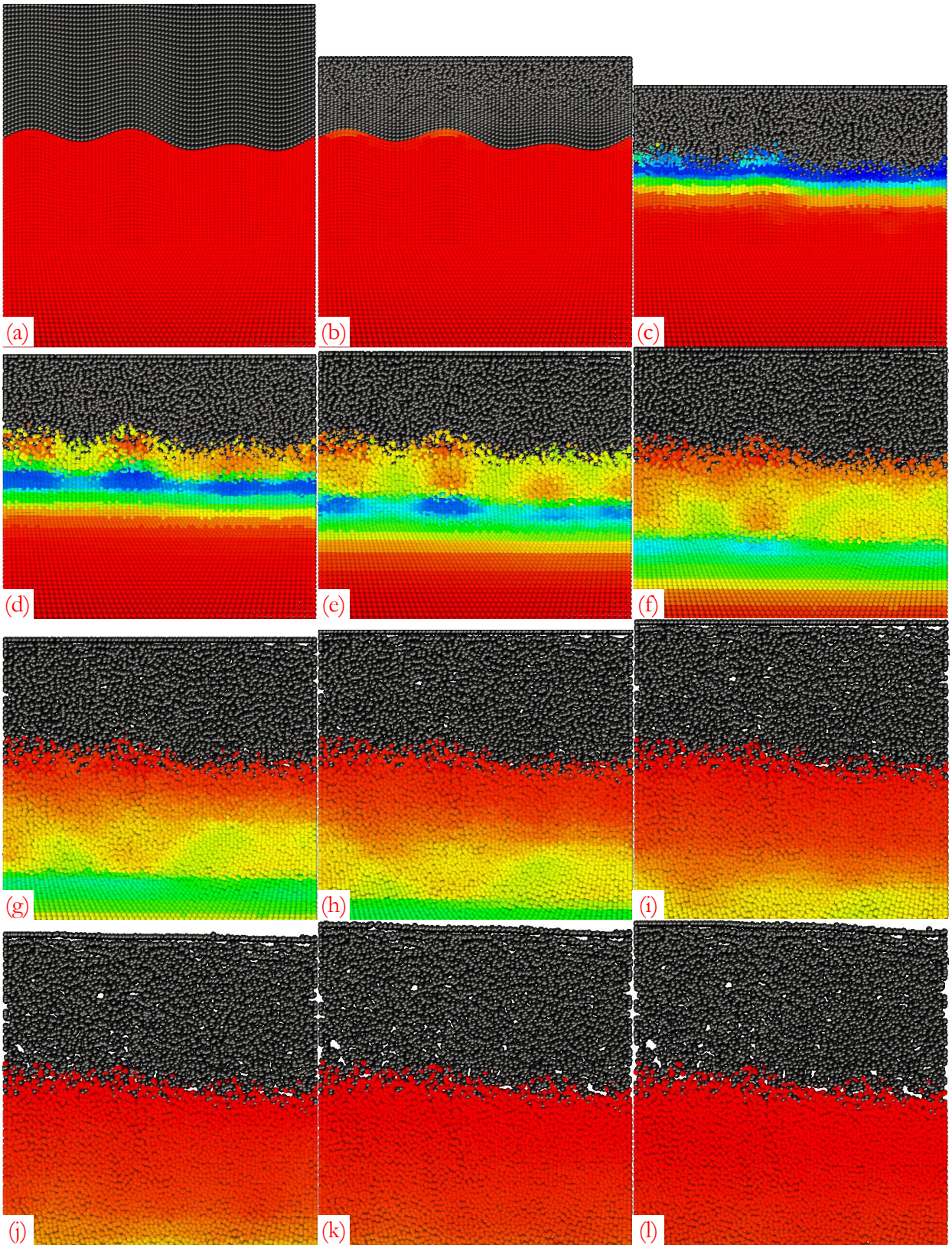

Figure 5.46: Three-mode Pattern # 4 subjected to a drive corresponding to a laser energy of 200 J – Evolution of the ripple and target in time. The images (a)-(l) are snapshots of the ripples starting from time t=0 to t= 55 ns, with 5 ns between the images.

Similarly to the 150 J simulation, the same expected physics are shown in this simulation in Figure 5.46. The heat shield is initially compressed, the wave reaches the interface and the growth begins, and the heat shield expands. Although unlike past simulations, it seems to start expanding even sooner. Also, in the first half of the simulation, the interface is clear and the growth is evident. However, during the second half, the interface becomes more blurred. This is likely the result of using a higher energy drive, and it is possible the ripples begin to grow together. Performing these simulations is necessary to understanding what might happen in the experiments. In this simulation, for instance, the data may suggest that going to 200 J is too high of a drive, or it may indicate that 200 J shows interesting phenomena that would be worthwhile to see in the laboratory.

The vertical axis in Figure 5.47 represents the distance along the direction of the loading. Each line represents the location of the ripple surface at a particular time during the simulation. In these plots, the drive is coming from the bottom up, i.e. the lowermost curve represents the three-mode ripple pattern before loading at t=0.

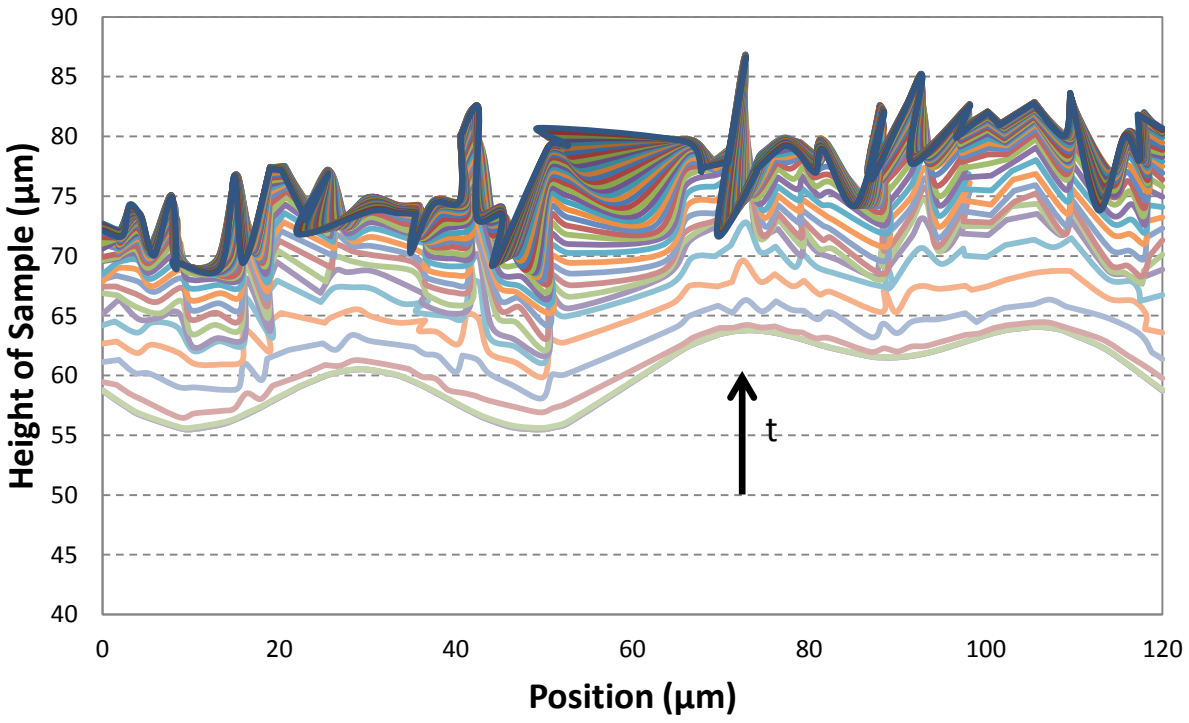

Figure 5.47: Three-mode Pattern # 4 subjected to a drive corresponding to a laser energy of 200 J – Evolution of the ripple surface as a function of time.

As time increases, the ripple surface moves further along the direction of loading, as expected. In the early stage of loading, the surface remains smooth. The plot in Figure 5.48 shows the same evolution of the ripple surface in Figure 5.47, but with only the 12 data points of interest.

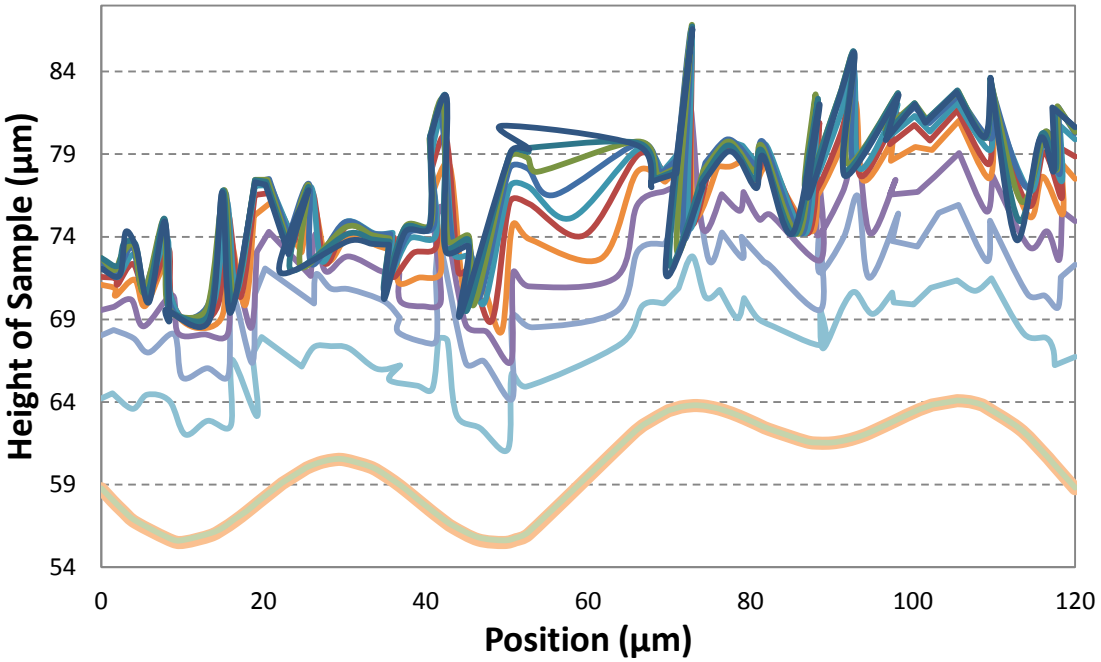

Figure 5.48: Three-mode Pattern # 4 subjected to a drive corresponding to a laser energy of 200 J – Evolution of the ripple surface as a function of time plotted with only 12 points of interest from Figure 5.47.

In Figures 5.47 and 5.48, examining the evolution of the ripple surface shows the same trend as for the other simulations. In the early stage of loading, the surface remains smooth. As time progresses, the ripple surface begins to show wrinkles and is no longer smooth and continuous. The first two time points show the compression of the heat shield, and the subsequent lines show the progression of the surface as faster in the beginning and slower at the end.

The growth factors from the three-mode Pattern # 4 simulation, including both the peak growth factors and the growth factors at the end of the simulation for the drive corresponding to a laser energy of 200 J, are shown in Table 5.2.

Table 5.2: Summary of Growth Factors for three-mode Pattern # 4 – 200 J

	Peak GF	GF at End
Ripple # 1	1.28	0.97
Ripple # 2	1.41	0.90
Ripple # 3	2.09	2.09
Ripple # 4	4.52	4.52
Ripple # 5	2.50	2.50
Ripple # 6	1.62	1.62

Figure 5.49 shows the growth factors computed using Equation 5.8 as a function of time for each of the six different ripples. This is followed by Figure 5.50, which shows the plots of the growth factors for a few of the selected ripples from Figure 5.49.

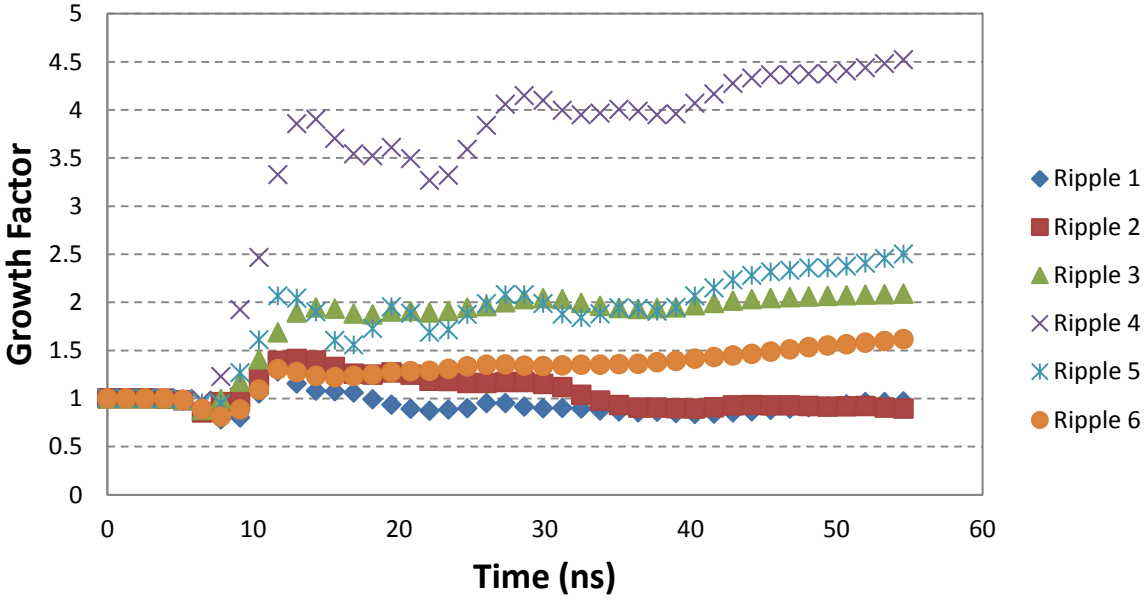

Figure 5.49: Growth Factor vs. time for three-mode Pattern # 4 subjected to a drive corresponding to a laser energy of 200 J.

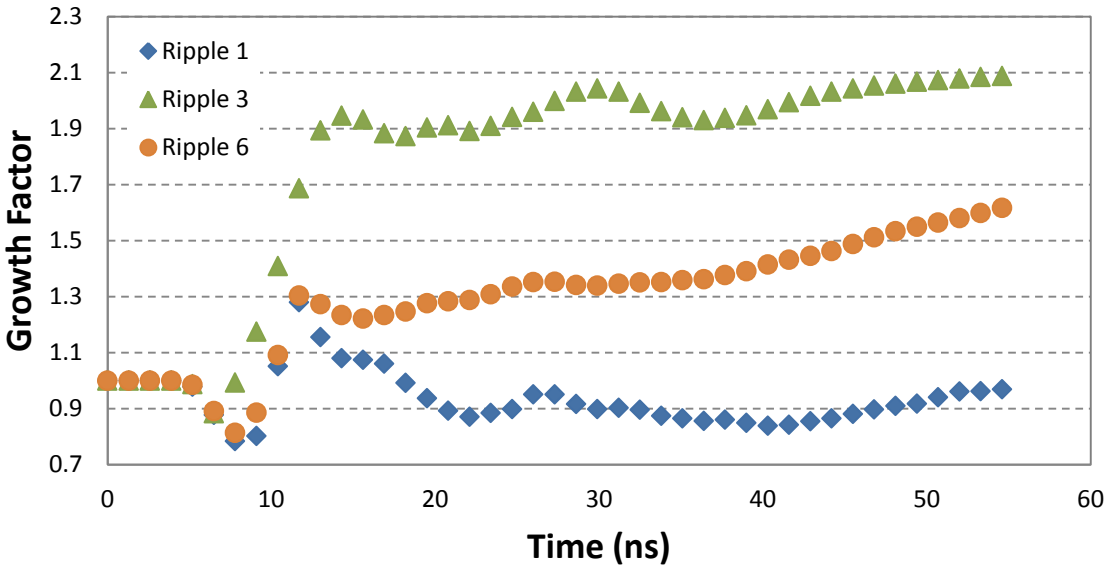

Figure 5.50: Growth Factor vs. time for selected ripples of interest for three-mode Pattern # 4 subjected to a drive corresponding to a laser energy of 200 J.

As seen in Figure 4.49, just as with the 150 J case, Ripple # 4 is anomalously high, but the other values for growth factor are reasonable and agreeable to experiments. Figure 5.50 shows growth factor versus time for Ripple #s 1, 3, and 6. Each ripple follows the same trend and has a peak at about the same place (13 ns). Unlike with other experiments, the growth factors continue upward with time. Typically, after the initial peak, the growth steadily decreases. In this case, the growth increases. As mentioned in the discussion of the images from the simulation, the last half of the simulation seems to show that at the interface the ripples become unresolved. It is possible that the ripples are beginning to grow together, which is supported by this upward trend in growth factor. This is the type of phenomena to look for during a multimode configuration.

5.3.1.3 Three-mode Pattern # 4 Comparison

The three-mode ripple Pattern # 4 was subjected to drives corresponding to laser energies of 150 and 200 J. The growth factors from the three-mode Pattern # 4 simulations, including both the peak growth factors and the growth factor at the end of the simulation for the two drives corresponding to laser energies of 150 and 200 J, are shown in Table 5.3.

Table 5.3: Summary of Growth Factors for three-mode Pattern # 4

	Peak GF		GF at End	
	150 J	200 J	150 J	200 J
Ripple # 1	1.22	1.28	0.44	0.97
Ripple # 2	1.33	1.41	0.29	0.90
Ripple # 3	1.87	2.09	1.57	2.09
Ripple # 4	4.31	4.52	4.31	4.52
Ripple # 5	1.71	2.50	1.02	2.50
Ripple # 6	1.17	1.62	0.76	1.62

Figure 5.51 shows the time history of the six different ripples at each energy. It is expected that higher energy will result in more growth.

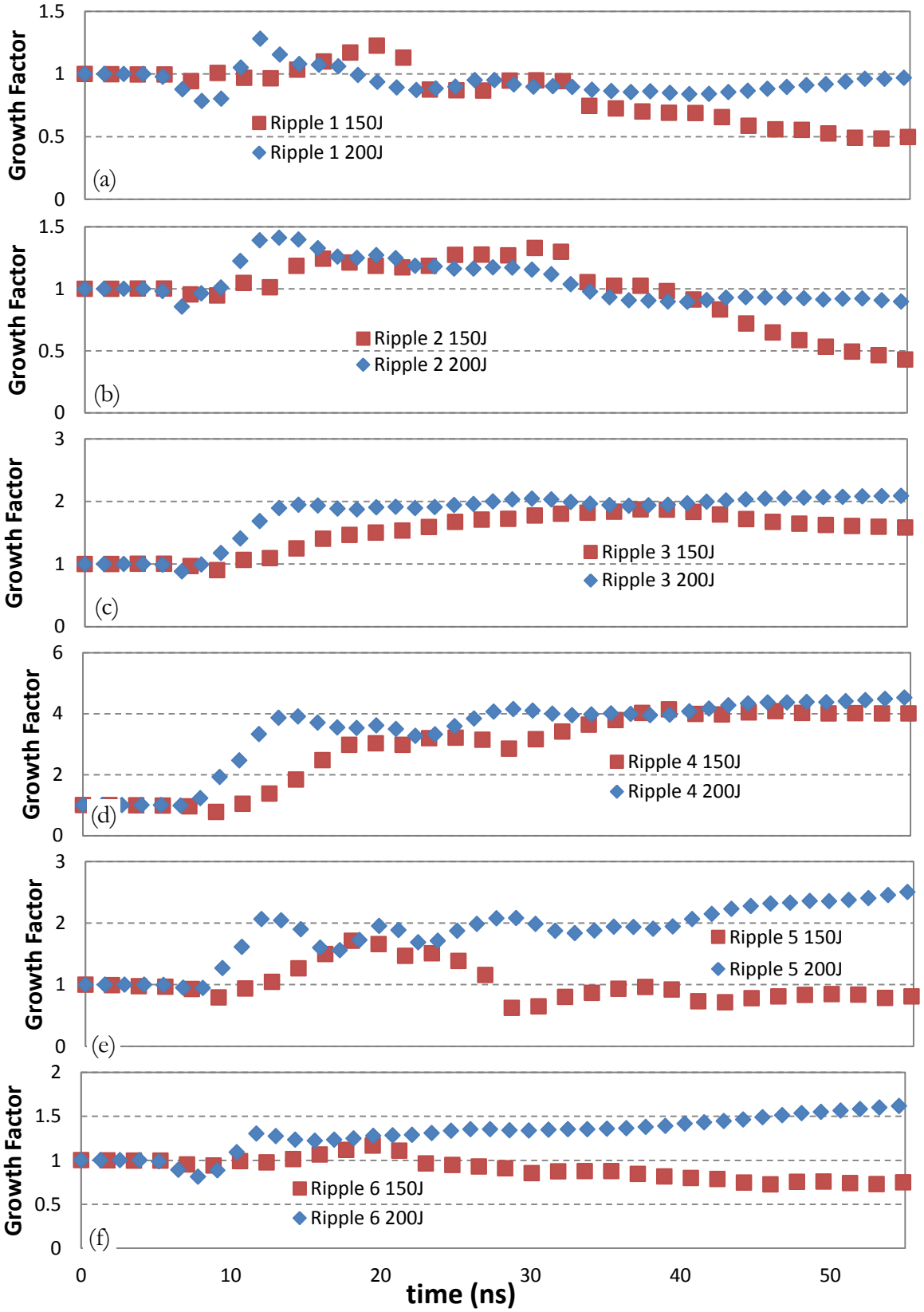

Figure 5.51: Comparison of Growth Factor vs. time for three-mode Pattern # 4 subjected to two different energies, 150 and 200 J for (a)-(f) corresponding to Ripple #s 1-6.

For each of the ripples, the 200 J energy drive shows more growth than the 150 J energy drive, which is exactly what is expected. Also, most of the growth factors are in the expected range for these energies (between 1 and 2). Ripple #s 4 and 5 have slightly higher growth factors than the other ripples, but these are also the two ripples with the smallest initial heights, which means they are harder to measure and have more error associated with the nodal displacement analysis. For the 200 J drive, the peak growth factor occurs at an earlier time, as expected. All the ripples follow the same trend of staying at a growth factor of 1 and then peaking at some point (Figure 5.51). For the 150 J drive, following the peak in the growth factor, it steadily decreases for 5 of the 6 ripples. However, for the 200 J drive, the growth factors slowly increase. This is a likely phenomena expected in multimode growth, where at some point the ripples merge and begin to grow as a whole.

Following the consistent and expected trends for the three-mode Pattern # 4, it was chosen as the multimode configuration for tantalum to use in the Omega laser experiments. This is discussed further at the end of this Chapter. The benefit of running these simulations is to predict what energies to choose when performing the Omega experiments. These results can also be used to determine the threshold for melting, the minimum threshold for producing growth, and provide insight into interesting phenomena that might occur at certain energies. They can also provide the opportunity to make predictions of the range of growth factors that may occur at different energies. Following the experiments, more simulations can be performed if the energies produced at Omega are not the exact energies requested on the day of the experiment. The experimental results also help to validate the simulations, as well as the constitutive model and the material parameters that are being used.

5.3.2 Pattern # 5

Three-mode Pattern # 5 is represented by the following equation, where θ represents the angle-of-descent:

$$\eta_{P5}(x) = 3\sin\left(\frac{2\pi}{40}x + \frac{\pi}{3}\right) + 1.5\sin\left(\frac{2\pi}{60}x + \frac{\pi}{2}\right) + 2\sin\left(\frac{2\pi}{120}x\right) \quad (5.22)$$

$$\theta^{max} = 34° \quad (5.23)$$

5.3.2.1 Pattern # 5 – 150 J

A simulation was performed for the three-mode Pattern # 5 configuration with 150 J of energy for the drive. Figure 5.521 shows a selection of the images from the simulation with approximately 11 ns between successive images. In these images, the red region is the Ta sample and the grey region is the heat shield. In the Richtmyer-Meshkov configuration, the drive comes from the top down such that the heat shield is driven into the Ta sample.

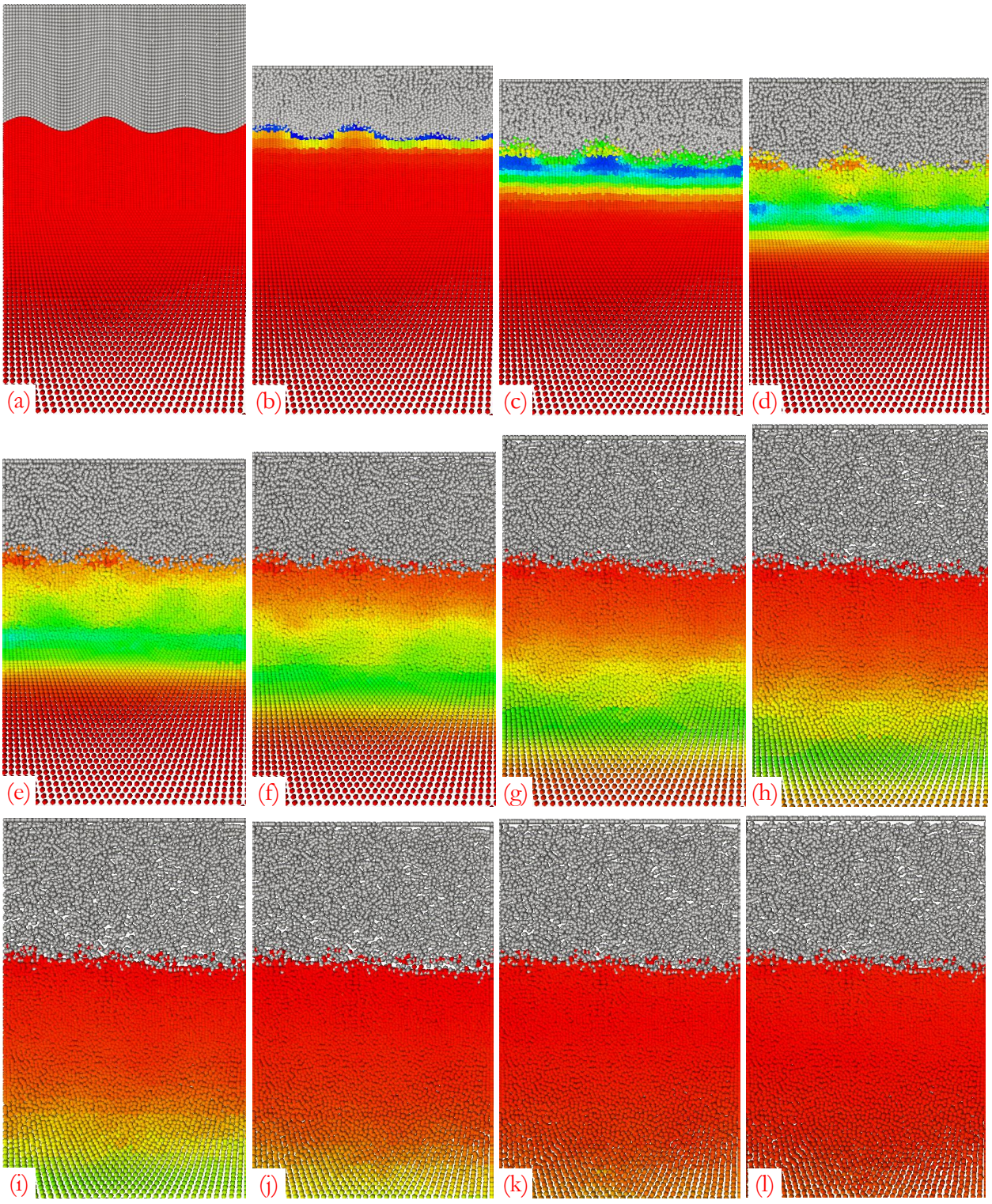

Figure 5.52: Three-mode Pattern # 5 subjected to a drive corresponding to a laser energy of 150 J – Evolution of the ripple and target in time. The images (a)-(l) are snapshots of the ripples starting from time t=0 to t= 122 ns, with 11 ns between the images.

Figure 5.52 shows the expected physics: the heat shield compressing initially, the heat shield expanding about halfway through the simulation, the wave reaching the interface and propagating through the Ta sample, compressing it and causing growth of the ripples. At about two thirds into the simulation, the interface becomes blurred and the ripples are hard to identify. It is possible that the ripples have merged and are growing as a whole. This is something that occurs in the multimode configuration.

The vertical axis in Figure 5.53 represents the distance along the direction of the loading. Each line represents the location of the ripple surface at a particular time during the simulation. In these plots, the drive is coming from the bottom up, i.e. the lowermost curve represents the three-mode ripple pattern before loading at t=0.

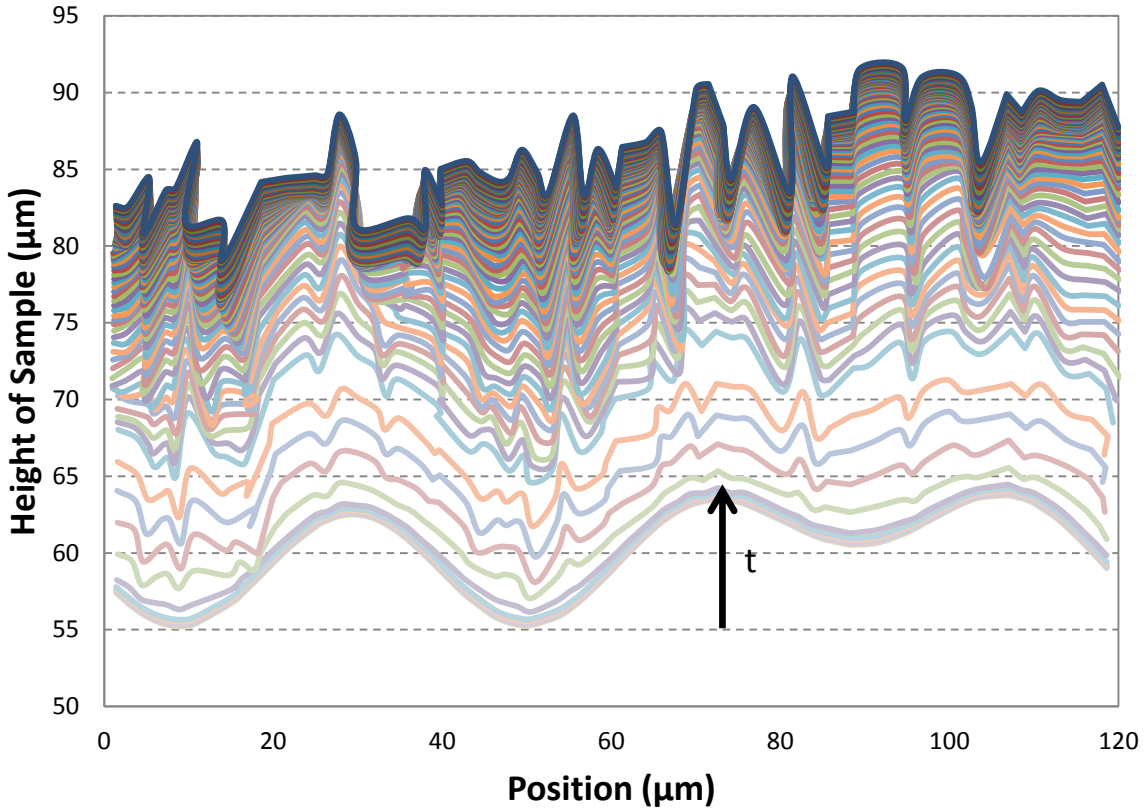

Figure 5.53: Three-mode Pattern # 5 subjected to a drive corresponding to a laser energy of 150 J – Evolution of the ripple surface as a function of time.

As time increases, the ripple surface moves further along the direction of loading, as expected. In the early stage of loading, the surface remains smooth. The plot in Figure 5.54 shows the same evolution of the ripple surface in Figure 5.53, but with only the 12 data points of interest.

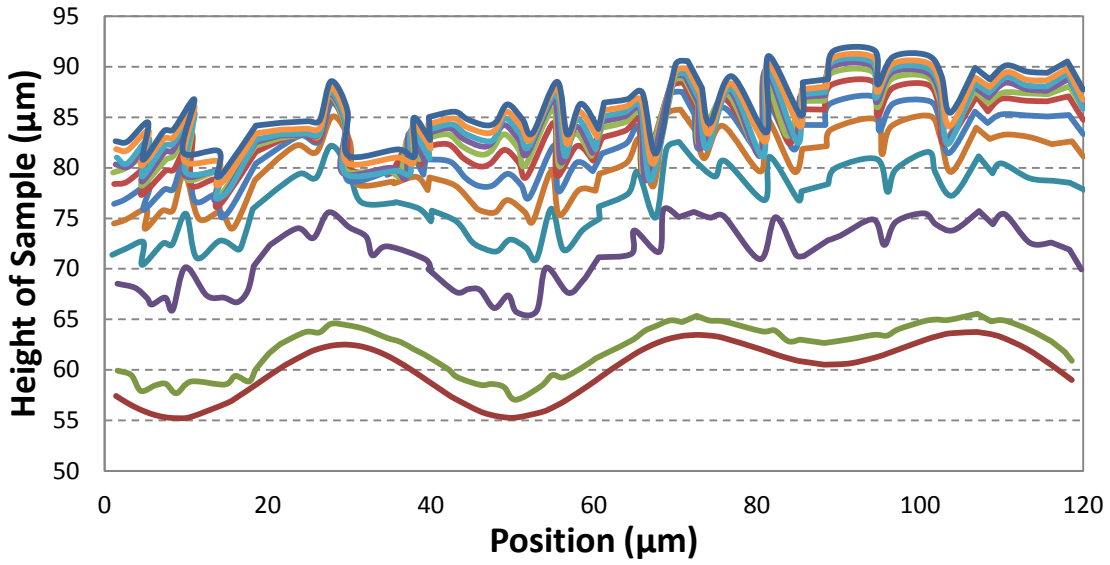

Figure 5.54: Three-mode Pattern # 5 subjected to a drive corresponding to a laser energy of 150 J – Evolution of the ripple surface as a function of time plotted with only 12 points of interest from Figure 5.53.

Figure 5.53 and 5.54 show similar behavior as seen in other simulations. In the early stage of loading, the surface remains smooth. As time progresses, the ripple surface begins to show wrinkles and is no longer smooth and continuous. The first two time steps show less growth because of the compression of the heat shield. Between the second and third time steps, the progression of the surface is at a maximum, and as time progresses the ripple surface continues to move up, but at a slower rate.

Figure 5.55 shows the growth factors computed using Equation 5.8 as a function of time for each of the six different ripples. This is followed by Figure 5.56, which shows the plots of the growth factors for a few of the selected ripples from Figure 5.55.

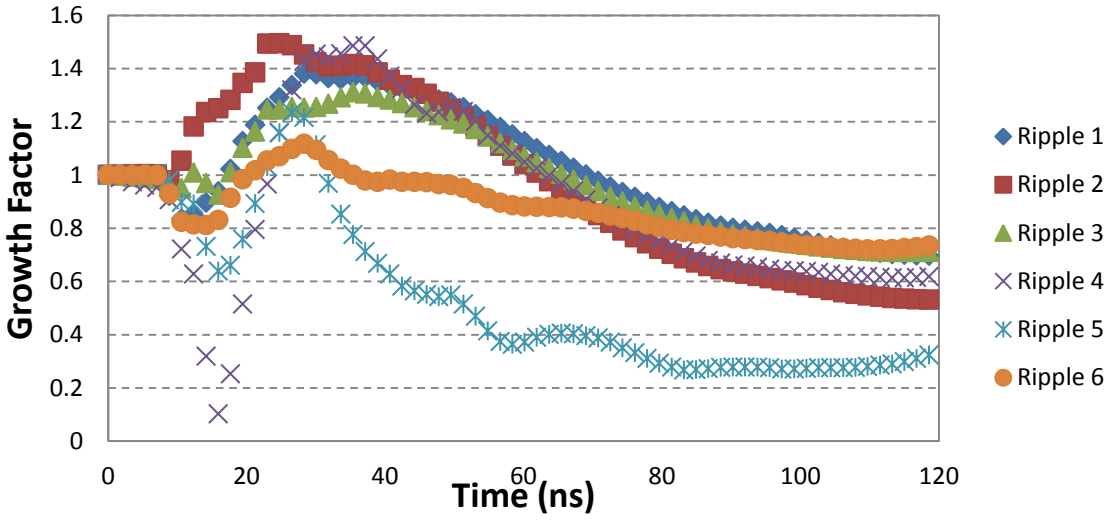

Figure 5.55: Growth Factor vs. time for three-mode Pattern # 5 subjected to a drive corresponding to a laser energy of 150 J.

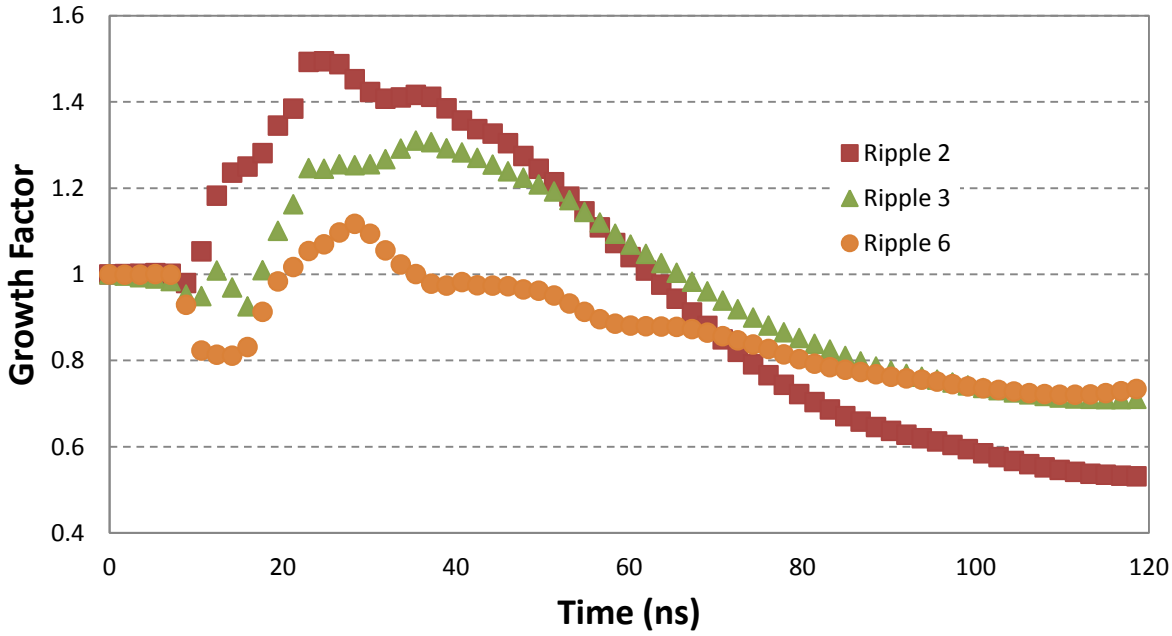

Figure 5.56: Growth Factor vs. time for selected ripples of interest for three-mode Pattern # 5 subjected to a drive corresponding to a laser energy of 150 J.

The growth factors for three-mode Pattern # 5, like in Pattern # 4, are what were expected for these energies based on experimental data from single-mode experiments. All six ripples follow the same trend where they start out at a growth factor of 1, peak at around 30 ns, then steadily decrease (Figures 5.55). In Figure 5.56, Ripple #s 2, 3, and 6 peak at growth factors of about 1.5, 1.3, and 1.1, respectively. This is on the same order of magnitude as the Pattern # 4 growth factors, which were in the range of 1.2 to 1.8 for 150 J. It is expected that the growth factors would be in the same range given two different patterns, assuming the energies stay the same as they did in the simulations.

5.4 Summary

Based on the results and analysis of the three-mode and four-mode patterns for the ripples in the laser driven Richtmyer-Meshkov instability experiments, the three-mode (Pattern # 4) was selected for the experiments. The three different four-mode patterns showed too much error in growth factors and were difficult to analyze due to the distortion of the interface. The ripples that started out very small initially (1-2 μm peak to valley height) showed large error in the growth factor. Additionally, trying to fit four peaks and valleys into the 120 μm width of the sample created issues predicting growth factor accurately in the simulations. It is likely it would also have been difficult to characterize ripple growth in the post-experiment characterization of the samples.

To overcome the problems associated with the four-mode patterns, the three-mode patterns were designed, modeled, and simulated with the intention of creating three distinguishable peaks, each with initial heights that were large enough (>3 μm) to avoid the issues with the four-mode patterns. Both three-mode patterns showed the type of growth anticipated at these energies. The interface and growth factors in the simulations were much more distinguishable, allowing for more accurate nodal displacement analysis and computation of growth factors.

Finally, the three-mode Pattern # 4 was selected over Pattern # 5 because the peaks in Pattern # 4 are slightly less steep ($\theta^{max} = 31°$ for Pattern # 4 as opposed to $\theta^{max} = 34°$ for Pattern # 5). The angle θ, referred to as the angle-of-descent boundary or the angle of the slope of the ripples, is a concern during the manufacturing process. The angle is limited due to diamond turning of the ripple die. A certain amount of clearance is needed so that the tool is able to fit into the bottom of the ripple without impinging on the sides.

Simulating the different patterns was useful for more than just determining which pattern to use in the laser experiments at Omega. This effort serves as validation for the constitutive model and the material parameters for tantalum that are used in the simulations. Analyzing the different patterns at different laser energies provided a method of observing if the simulations predicted more growth for higher energies. In most cases, but not all, this occurred. The simulations provided a means of understanding the trend of growth factor versus time. In the experiments, only final growth factor could be obtained by comparing the initial height to the height measured after the experiment. Simulating the various multimode configurations allowed for observation of the possible merging of ripples at high energies. By using simulations, certain trends and phenomena could be observed, such as where and when the growth factor peaked. Examining the different patterns provided insight into the effect of initial amplitude on growth factor. Although not presented here, these simulations have also provided insight into the thresholds for melting, the minimum energy level to achieve growth, and predictions of the range of growth factors expected at different energies. The results of the simulations for three-mode Pattern # 4 provide the only predictions that are used in the multimode experiments at Omega. The results can help determine which laser energies to use in Omega for the experiments. Following the experiments, more simulations can be performed in order to model the energies that were actually achieved at Omega. Overall, these multimode simulations have proven an extremely useful tool for designing the experiments and providing predictions of growth of Richtmyer-Meshkov instabilities.

Chapter 6

Summary and Future Work

6.1 Summary

Richtmyer-Meshkov (RM) instabilities in tantalum (Ta) at high pressures through laser compression experiments and simulations were used to determine and validate strength models. Two powerful tools made this research possible: a high energy laser (Omega) and simulations based on the Optimal Transportation Meshfree method. The goal was to understand the strength of tantalum at high pressures (>1Mbar) and high strain rates (10^6-10^8 s^{-1}).

To achieve this, the Omega Laser in Rochester, New York was used. Carefully designed tantalum samples with ripples were constructed, and observations were made before and after these samples were subjected to high energy laser beams. In these experiments, the observational parameter was the Richtmyer-Meshkov (RM) instability in the form of ripple growth. The experimental platform used was the laser compression recovery experiments, providing a method to perform research at Omega in a ride-along fashion alongside existing experiments. Six different "shots" or experiments were performed on the Omega laser using single-mode tantalum targets. The experimental effort was led by Dr. Aaron Stebner from Caltech and the experiments were conducted at the Omega laser facility by scientists from Lawrence Livermore National Laboratory, with Dr. Chris Wehrenberg as the experimental lead. The recovered samples were characterized at General Atomics in San Diego, California. For each of the six different experiments, the six targets were the same, but six different energies were used. The energy or drives indicate the amount of laser energy that impinged on the target. Additionally, these energies were correlated to measures of pressure using both the OTM simulations and the rad-hydro code Hyades. For each target, values for growth factor were obtained. For each successive increasing energy, the respective growth factor increased as expected. The energies ranged from 56.6 to 252.9 J and the corresponding growth factors ranged from 1.26 to 1.97. The predicted pressures ranged from 0.98 to 3.41 Mbar. Overall, the single-mode ripple experiments provided a reliable platform for studying the strength of tantalum at high pressures and high strain rates.

Constitutive models are needed to correlate the measurements of growth to a measure of strength. In order to validate the experiments and to aid in the design of future experiments, a series of simulations was performed. These simulations were performed using a simulation code, Eureka, based on the Optimal Transportation Meshfree (OTM) method and an engineering model designed

at Caltech by Michael Ortiz and his group over the past decade. The simulation of laser driven RM instability experiments were developed by Dr. Bo Li in Professor Michael Ortiz's group. Before using Eureka, a series of pre- and post-processing tools were employed, including SolidWorks for modeling the samples, Femap for creating the meshes, Hyades for creating the velocity profiles, and Paraview for visualization of the simulations. Once the ideal sample configuration and boundary conditions were applied, certain material parameters and configuration parameters were altered in a series of simulations. Two different configurations were studied in the simulations: RM instabilities in single-mode ripples, and RM instabilities in multimode ripples.

The results of the single-mode tests were compared to the Omega experiments for single-mode ripples at the six same laser energies. To simulate the different energies (70 J, 100 J, 120 J, 150 J, 200 J, and 250 J), each simulation was subjected to a different velocity profile, which was obtained from the rad-hydro code Hyades. The velocity profile was applied as a boundary condition to a heat shield that sits in front of the Ta sample. A wave travels through the heat shield, passing through the interface of the heat shield and Ta sample, and creating the Richtmyer-Meshkov instability. Following the simulations, growth factors were calculated through visualization and nodal displacement analysis. Each successive simulation was performed at higher drive energy, and it was expected that with increasing energy the growth factor would increase. The results are summarized in Chapter 4 and the data shows that the values for peak growth factor do increase with increasing laser energy. The trends of growth factor versus time were also observed. For laser energies ranging from 70 to 150 J, the growth factor at the end increased. For laser energies 200 and 250 J, the growth factor at the end decreased, but the ripples were compressed substantially after the initial growth. Two different mesh sizes were used during these simulations. The finer mesh provided more accuracy, but it did not affect the values of the peak growth factor or the trends of growth factor over time. Predictions of peak pressure were also estimated in the simulations and agreed reasonably well with the predictions from the rad-hydro code Hyades.

Overall, there was favorable agreement between the data from the simulations and the experiments. The peak growth factors from the simulations and the experiments are within 10% agreement, and four of the six data points are within 5%.

For the multimode simulations, the goal was to validate the code and to assist in the design of Omega experiments. By testing various multimode configurations, the objective was to determine which configuration to use for the multimode campaign at Omega, and to determine which laser energies to use for the drives. The manufacturing of the targets occurs months in advance, and therefore it was necessary to determine which multimode configuration to use. The decision was based on which multimode ripple pattern would exhibit growth while also being able to evaluate this growth throughout the simulation and, most importantly, be able to characterize it post-experiment. Additionally, by simulating various energies and predicting the growth associated with each one, the decision could be made as to which energies to use for the experiments. The goal was to find a

range of energies that were each large enough to cause growth in the sample, but not so large that melting occurs.

Both four-mode and three-mode ripple patterns were examined. For the four-mode scenario, three different patterns were selected. Each pattern was simulated twice – once at an energy of 100 J and another at 150 J. In each simulation, the evolution of the ripple surface was tracked over time. Through visualization and nodal displacement analysis, observations were made on the interactions of the waves with the heat shield and sample, as well as the interface between the heat shield and sample. As expected, the heat shield was compressed in the beginning and eventually the waves reached the interface of the heat shield and Ta sample, causing the Ta sample to compress. At some point in the simulation, the heat shield expanded due to reflections, but the interface continued to compress. With time, the evolution of the ripple surface started out smooth but became non-smooth over time. The rate of the progression of the surface was observed, demonstrating that in the beginning, less growth occurs because of the compression of the heat shield, then the progression of the surface is at a maximum, and as time progresses, the ripple surface continues to deform but at a slower rate. Because of the four modes in the sample, eight different peak-to-valley height combinations existed for each experiment, referred to as Ripple #s 1 – 8. Therefore, growth factors over time were plotted for each of the eight ripples. For each of these, observations were made on whether the ripples grew or were compressed, what the values were for peak growth factor, when in the simulation the peak in growth factor occurred, and what the general trend of growth factor looked like over time. For each pattern, a comparison of the two energies was made to evaluate what happened when the energy was increased, with the expectation that a higher energy would result in more growth. In some cases, but not all, the higher energy drive resulted in a higher peak growth factor. For the eight ripples that were quantified in each simulation, the ones with a larger initial peak-to-valley height more often showed the expected trend of increased growth with increased energy. Overall, the analysis suggested that the four-mode patterns were not ideal for the experiments and the interface became less well-defined for accurate analysis. Ripples with initially small peak-to-valley heights were too difficult to characterize and resulted in too much error.

Therefore, the decision was made to perform simulations on patterns with only three modes. Two different three-mode patterns were designed, modeled, and simulated with the intention of creating three distinguishable peaks, each with initial peak-to-valley amplitudes large enough (>3 μm) to avoid the issues dealt with in the four-mode patterns. The interface and growth factors in the simulations were much more distinct, allowing for more accurate nodal displacement analysis. Both patterns were similar in design but one pattern had slightly larger peak-to-valley amplitudes, resulting in steeper slopes. The growth factors for both patterns fit with the trends for experimental data from single-mode experiments at equivalent energies. All six ripples followed similar trends over time, where they remained at a growth factor of 1, peaked at around 30 ns, then steadily decrease.d Comparing the two patterns, the values for peak growth factor were similar, as expected

for two different patterns of the same mode, assuming the energies stay the same as they did in the simulations. With the exception of one of the six ripples (which was an outlier for both patterns), the values for growth factor were reasonable and agreeable to single-mode RM experiments. The first pattern was simulated at both 150 J and 200 J, and the results indicated that with increased energy the growth factor increases, as expected. The trends of growth factor over time indicated that for 150 J, following a peak in the growth factor, the growth factor steadily decreases. However, for the 200 J case, the growth factor slowly increases. This is likely a phenomena expected in multimode growth, where at some point the ripples merge and begin to grow as a whole. The pattern selected (referred to as "Pattern # 4" in Chapter 5) was selected as the multimode configuration to use in the Omega experiments. Since both three-mode patterns showed the type of growth anticipated at these energies, the decision was made based on the fact that the slope of the ripples was slightly smaller for Pattern # 4 ($\theta^{max} = 31°$ as opposed to $\theta^{max} = 34°$), making it easier to manufacture.

Simulating the various patterns helped determine which configuration to use for the experiments, but also serve as validation for the constitutive model and the material parameters for tantalum that are used in the simulations. Comparing different energies allowed for observation of the expected trend of increased growth with increased energy. The simulations also provided a means of understanding the trend of growth factor versus time. In the experiments only final growth factor can be obtained, so the simulations provide observations of trends that otherwise would be overlooked. By studying the multimode configurations, observation of the possible merging of ripples at higher energies was observed. The simulations also provided insight into the effect of initial peak-to-valley height on growth factor. Additionally, the results of the multimode simulations for Pattern # 4 (see Chapter 5) provided guidelines for the Omega multimode experiments. These results were used to determine which energies to use on Omega for the experiments. Overall, the simulations performed on the multimode configuration proved to be a valuable tool for designing laser experiments and providing predictions of growth. Likewise, for the single-mode configuration, the simulations proved to be a useful tool for comparison of experimental values of growth factors.

Through experiments and simulations, the necessary tools to examine strength of tantalum at high pressures using RM instabilities were made feasible. By using Omega's high energy capabilities to perform laser compression recovery experiments in a ride-along capacity, the necessary experimental data was obtained. The simulations developed at Caltech by Dr. Bo Li provided comparisons to this experimental data and made predictions for future experiments. This effort also validated the simulations and the phenomenological constitutive model for tantalum discussed in Chapter 3. By designing samples with initial perturbations in the form of single-mode and multimode ripples and subjecting these samples to high pressures, the Richtmyer-Meshkov instability was investigated. By correlating the growth of these ripples to measures of strength, a

better understanding of the strength of Ta at high pressures has been achieved. As a result, both the models and experiments have been improved, and have pushed the limits of characterizing material strength at extreme pressures. The platform created by using the simulations in coordination with the ride-along laser experiments will serve as a useful tool for future investigations of studying the dynamic behavior of metals at high pressures and high strain rates.

6.2 Future Work

The experimental platform developed here can be applied in a variety of ways. The following sections discuss the future work involved in the multimode experiment predictions and analysis, as well as possible extensions of this research to include future laser driven experiments, Rayleigh-Taylor instabilities, different materials, the National Ignition Facility, the multiscale model, and other compression facilities such as gas guns.

6.2.1 Multimode Predictions

The results of the multimode simulations for three-mode Pattern # 4 in Chapter 5 provide the predictions that are used for the design of the Omega experiments on multimode ripples for RM studies in Ta. These results are used to determine which laser energies to use in Omega experiments. Following the multimode experiments, if necessary, more simulations can be performed in order to model the energies that were actually achieved at Omega. Comparison of simulations with experimental data for the multimode case will provide additional data concerning the interaction of modes and the RM instabilities at high pressures (>1 Mbar).

6.2.2 Extension to Future Laser Experiments

The results presented in this thesis suggest that the simulations provide valuable information that can be used as predictions for growth factors for future experiments. Furthermore, simulations can be performed prior to experiments at various laser energies to guide the decision of what energy drives to use for the experiments. Although not covered here, these simulations have also provided insight into the thresholds for melting, the minimum energy level to achieve growth, and predictions of the range of growth factors expected at different energies. These simulations can also provide insight into interesting phenomena that might occur at certain energies. Following the experiments, more simulations can be performed if the energies produced in the laser experiments are not the energies used in the simulations towards the design of experiments.

6.2.3 Extension to Rayleigh-Taylor Instability

The instability studied in this thesis was the Richtmyer-Meshkov (RM) instability. However, simulations using the same code and constitutive model have been performed for the Rayleigh-

Taylor (RT) instability discussed in Chapter 1. Some of the simulations already performed in the RT instability configuration have studied the effect on growth factor of changing various parameters such as initial yield stress, pressure, velocity, strain, von mises stress, and different drive profiles. The isentropic compression experiments described in Chapter 2 utilize the RT configuration. The laser compression recovery platform in ride-along mode can be used for either RM or RT as discussed in Chapter 2. Only the target package is altered. As discussed in Chapter 1, the Rayleigh-Taylor instability is critical for the success of creating ignition in inertial confinement fusion. RT instabilities are also used in the same way as RM instabilities to measure growth and correlate it to measures of strength, and to validate constitutive models either phenomenological or multiscale in nature.

6.2.4 Extension to Iron and Other Materials

The methodology discussed here can also be extended to a number of different metals. In the past, vanadium has been studied in experiments [32, 33], and plans for beryllium exist for future Omega experiments [35]. Provided the EOS data is available, then simulations could potentially be performed using either of these metals, or any metal where the EOS and strength model is available. A material of great interest is iron (Fe) since it is known to undergo the α to ε phase transition at 13 GPa (0.13 Mbar). Because of the phase transition that occurs in Fe at high pressures, there is interest in seeing what happens to the instabilities when subjected to the extreme conditions provided by Omega and other laser facilities [70]. Additionally, astrophysicists are interested in studying Earth core conditions, which can be done by subjecting Fe to pressures of 3.6 Mbar [71]. With facilities like Omega and NIF, this is now possible. Experiments have already taken place for Fe at Omega and more are to occur in the future. A multiscale model for Fe is being developed by Professor Michael Ortiz's group at Caltech. Advancing the Caltech simulations to include Fe is creating a means to compare the current and future experimental results to simulations.

6.2.5 Extension to NIF and Other Laser Facilities

The experiments in this research were performed on the Omega laser. Other high energy facilities are also available to provide similar or extreme pressure conditions. Lasers such as Nova, Janus, and Jupiter are available at LLNL [38], and through calls for proposals to Universities, it is possible to obtain laser time. LLNL is also home to the most powerful laser, the National Ignition Facility (NIF), which can achieve laser energies of 2 MJ and pressures in the tens of Mbars [72, 73].

6.2.6 Extension to Multiscale Model

The simulations performed in this thesis utilize a phenomenological engineering constitutive model for Ta. The multiscale models for Ta and Fe developed by Professor Michael Ortiz's group are based on a hierarchy of length scales and unit mechanisms shown in Figure 6.1 [50, 61, 74]. At

the quantum-mechanical scale, the model accounts for properties such as EOS of materials, elastic moduli, and heat capacity. At the nano-scale, properties of individual lattice defects, such as kink mobilities and grain-boundary energies, are included. At the sub-micron scale, dislocation dynamics govern the physics. At the sub-grain scale, dislocation patterns and martensitic structures (for metals that undergo phase transitions) are accounted for. At the micro-scale, properties such as ductile fracture and plastic void are accounted for. At the macro-scale, large grain ensembles and grain boundary sliding affect the response of polycrystalline metals.

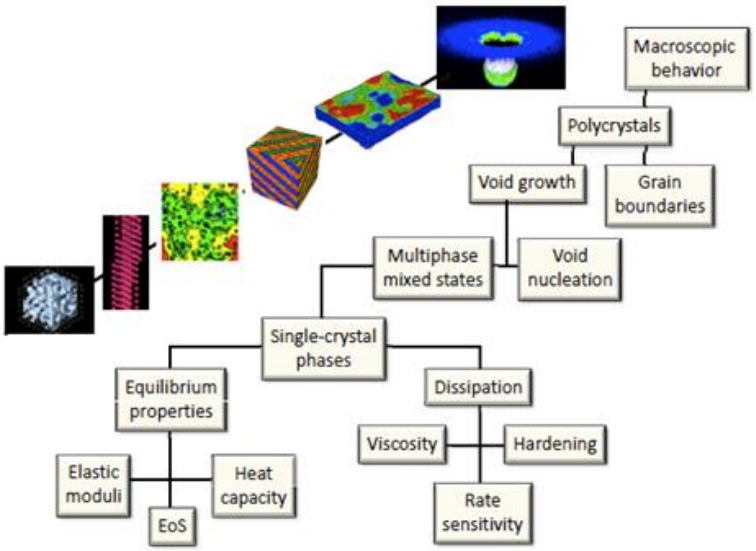

Figure 6.1: Hierarchy of the Caltech multiscale model with examples of some of the different unit mechanisms [50].

The same experimental platform and simulation configurations used in this thesis could be examined using the multiscale model simulations. The experimental data obtained from the laser experiments could be used for validation, and the results of the multiscale simulations could be compared to the results from the phenomenological engineering models for strength.

6.2.7 Extension to Gas Guns and Other Compression Facilities

Access to large laser facilities is not always simple and takes the coordination of several groups of scientists. At Caltech, a number of high pressure and high-strain rate facilities are available for characterizing material strength and other material properties, including split Hopkinson (Kolsky) pressure bars, gas guns, powder guns, and two-stage guns. Part of this research involved creating the RM experimental platform using Caltech's gas gun. A series of experiments was performed using ballistic gelatin as a model material. Although no measure of strength was obtained from these experiments, the results did demonstrate the correlation between strength and ripple growth [75]. This setup could be extended to other materials of interest, such as tin. Tin would be ideal

because it is a soft metal with low strength, so it should flow at relatively low pressures. If tin or another material where the EOS exists were used in these experiments, then the experimental data from the gas gun experiments could be compared to simulations. Performing such experiments at Caltech would offer a more independent means of studying strength of materials using the Richtmyer-Meshkov or Rayleigh-Taylor instability platform, while providing experimental data at the other end of the compression facilities spectrum.

References

[1] M.A. Meyers. *Dynamic Behavior of Materials*. John Wiley & Sons, Inc., 1994.

[2] T.Z. Blazynski. *Materials at High Strain Rates*. Elsevier Applied Science, 1987.

[3] B. Remington, H.S. Park, et al. *Progress towards materials science above 1000 GPa (10 Mbar) on the NIF laser*. DYMAT 2009 3-9, 2009.

[4] K.T. Lorenz, et al. *Accessing ultrahigh-pressure, quasi-isentropic states of matter*, Lawrence Livermore National Laboratory, Physics of Plasmas, 2005.

[5] G. Collins. *Physics of Dense Matter*, Presentation at the High Energy Density Physics Summer School, San Diego, CA, July 10-16, 2011.

[6] D. Steinberg. *Equation of State and Strength Properties of Selected Materials*, UCRL-MA-106439, 1996.

[7] D.L. Preston, D.L. Tonks, and D.C. Wallace. *Model of plastic deformation for extreme loading conditions*, Journal of Applied Physics 93: 211, 2003.

[8] R.W. Hertzberg. *Deformation and Fracture Mechanics of Engineering Materials.* 3d ed. John Wiley & Sons, Inc., 1989.

[9] N.R. Barton, N.R. Bernier, et al. *A multi-scale strength model for extreme loading conditions*, LLNL-JRNL-448591, 2010.

[10] R. Becker, A. Arsenlis, et al. *A tantalum strength model using a multiscale approach: version 2*, LLNL-TR-417075, 2009.

[11] M.Z. Hossain, G. Ravichandran, and K. Bhattacharya. *Coupling Materials Strength to Rayleigh-Taylor Instability in Solids*, California Institute of Technology, 2011.

[12] D. Youngs. *Turbulent mixing due to Rayleigh-Taylor instability*. American Physical Society Division of Fluid Dynamics Meeting, San Antonio, TX, Nov 23-25, 2008.

[13] S. Li and H. Li. *Parallel AMR Code for Compressible MHD or HD Equations*, Los Alamos National Laboratory, 2006.

[14] P.G. Drazin and W.H. Reid. *Hydrodynamic Stability*. 2d Ed. Cambridge University Press, 2004.

[15] R.D. Richtmyer. *Taylor instability in a shock acceleration of compressible fluids*, Communications on Pure and Applied Mathematics 13, 297-319 (1960).

[16] E.E. Meshkov. *Instability of the Interface of Two Gases Accelerated by a Shock Wave*, Soviet Fluid Dynamics 4,101-104 (1969).

[17] P.A. Thompson. *Compressible-Fluid Dynamics*. McGraw-Hill, 1988.

[18] R. Betti. *Hot Spot Dynamics and Hydrodynamic Instabilities*. Presentation at the High Energy Density Physics Summer School, San Diego, CA, July 10-16, 2011.

[19] K. Mikaelian. *Shock-induced interface instability in viscous fluids and metals*, Lawrence Livermore National Laboratory, American Physical Society, 2013.

[20] U. Alon, J. Hecht, D. Ofer, and D. Shvarts. *Power Laws and Similarity of Rayleigh-Taylor and Richtmyer-Meshkov Mixing Fronts at All Density Ratios*. Physical Review Letters, Vol 74, No 4, 534-537, 1995.

[21] G. Yonas. *High-Output Sandia Accelerator Able to Predict Nuclear Blast Physics*, Sandia National Laboratories, 1996.

[22] R. McBride. *Magnetized Liner Inertial Fusion and Cylindrical Dynamic Materials Properties Experiments on the Z Pulsed-Power Accelerator*, Presentation at the DOE NNSA SSGF Annual Program Review, Santa Fe, NM, June 25-27 2013.

[23] K. Schoenberg and P. Lisowski. *LANSCE – A Key Facility for National Science and Defense*, Los Alamos National Laboratories, 2006.

[24] J. Belof, R. Cavallo, et al. *Rayleigh-Taylor Strength Experiments of the Pressure-Induced a⟶ε Phase Transition in Iron*, Presentation at the APS SCCM Conference, Chicago, IL, June 26 - 30, 2011.

[25] R.P. Drake. *Introduction to High Energy Density Physics*, Presentation at the High Energy Density Physics Summer School, San Diego, CA, July 10-16, 2011.

[26] E. Moses. *The National Ignition Facility: the Path to Ignition, High Energy Density Science and Inertial Fusion Energy*, LLNL-PRES-468311, 2011.

[27] D.E. Hinkel. *Laser-plasma interactions and the National Ignition Campaign*. Presentation at the High Energy Density Physics Summer School, San Diego, CA, July 10-16, 2011.

[28] J. Soures. *National Laser Users' Facility (NLUF) Users' Guide*, University of Rochester – Laboratory for Laser Energetics, May 2007.

[29] D. Meyerhofer. *Diagnostics for High-Energy-Density Physics*. Presentation at the High Energy Density Physics Summer School, San Diego, CA, July 10-16, 2011.

[30] H.S. Park, N. Barton, et al. *Experimental results of tantalum material strength at high pressure and high strain rate*, AIP Conf. Proc. 1426, 1371, 2012.

[31] H.S. Park, B. Maddox, et al. *FY12 LLNL Omega Experimental Programs*, LLNL-TR-607997, 2012.

[32] H.S. Park, B. Remington, et al. *Strong stabilization of the Rayleigh-Taylor instability by material strength at megabar pressures*, Physics of Plasmas 17, 056314, 2010.

[33] H.S. Park, K.T. Lorenz, et al. *Viscous Raleigh-Taylor Instability Experiments at High Pressure and Strain Rate*, Physical Review Letters, 104, 135504, 2010.

[34] K. Lorenz, M. Edwards, et al. *High pressure, quasi-isentropic compression experiments on the Omega laser*, High Energy Density Physics 2, 113-125, 2006.

[35] K. Mikaelian. *Design of a Rayleigh-Taylor experiment to measure strength at high pressures*. Physics of Plasmas 17, 092701, 2010.

[36] R. Rudd, et al. *Metal deformation and phase transitions at extremely high strain rates*, MRS Bulletin, Vol 35, 999-1006, 2010.

[37] R. Betti. *Implosion Hydrodynamics for High Energy Density Physics and Inertial Confinement Fusion*. Presentation at the High Energy Density Physics Summer School, San Diego, CA, July 10-16, 2011.

[38] B. Remington, et al. *Materials Science Under Extreme Conditions of Pressure and Strain Rate*, Metallurgical and Materials Transactions A, Vol 35A – 2587-2607, 2004.

[39] J. Edwards, K.T. Lorenz, B. Remington, et al. *Laser-Driven Plasma Loader for Shockless Compression and Acceleration of Samples in the Solid State*. Physical Review Letters, Vol 92, No 7, 2004.

[40] R.F. Heeter, O.L. Landen, W.W. Hsing, and K.B. Fournier. *LLNL Contribution to LLE FY09 Annual Report: NIC and HED Results*. LLNL-TR-418046, 2009.

[41] B.A. Remington, S.V. Weber, et al. *Single-mode and multimode Rayleigh-Taylor experiments on Nova*, Phys. of Plasmas 2 (1), 241-255, 1995.

[42] R. Tilley. *Understanding Solids: The Science of Materials*. John Wiley & Sons, Inc., 2004.

[43] Y.C. Fung and P. Tong. *Classical and Computational Solid Mechanics*. World Scientific, 2001.

[44] P.M. Bellan. *Fundamentals of Plasma Physics*. Cambridge University Press, 2006.

[45] G. Randall, J. Vecchio, J. Knipping, et al. *Fabrication of Rippled Metals for Viscous Plastic Flow Studies*, Presentation at the NNSA Stewardship Science Academic Programs Annual Review Meeting, Albuquerque, NM, June 27-28, 2013.

[46] A. Stebner, K. John, G. Ravichandran, et al. *Laser Compression Recovery Experiments for Measuring Strength of Metals at High Pressures*, Presentation at the NNSA Stewardship Science Academic Programs Annual Review Meeting, Albuquerque, NM, June 27-28, 2013.

[47] H.W. Haslach and R.W. Armstrong. *Deformable bodies and their material behavior*. John Wiley & Sons, Inc., 2004.

[48] N. Huffington. *Behavior of Materials under Dynamic Loading*. The American Society of Mechnical Engineers, 1965.

[49] S. Govindjee. *Engineering Mechanics of Deformable Solids*. Oxford University Press, 2013.

[50] M.A. Meyers and K.K. Chawla. *Mechanical Behavior of Materials*. 2d Ed. Cambridge University Press, 2009.

[51] B. Li and M. Ortiz. *The Optimal Transportation Meshfree (OTM) Method for Hypervelocity Impact Simulation*, California Institute of Technology, 2010.

[52] B. Li, F. Habbal, and M. Ortiz. *The Optimal Transportation Meshfree (OTM) method*, California Institute of Technology, International Journal for Numerical Methods in Engineering, 2010.

[53] B. Li, et al. *Parallel Optimal Transportation Meshfree (OTM) method*, California Institute of Technology, PSAAP Meeting, Pasadena, CA. 2012.

[54] M. Ortiz. *Optimal Transportation Meshfree Approximation Schemes*, 8th European Solid Mechanics Conference (ESMC2012), Graz, Austria, 2012.

[55] B. Li, A. Kidane, G. Ravichandran, and M. Ortiz. *Verification and validation of the Optimal Transportation Meshfree (OTM) simulation of terminal ballistics*. International Journal of Impact Engineering 42, 25-36, 2012.

[56] B. Li. *OTM simulations of RTI tests using the variational thermomechanical coupling material model*, California Institute of Technology, International Journal for Impact Engineering, 2013.

[57] Q. Lang, L. Stainier, and M. Ortiz. *A variational formulation of the coupled thermo-mechanical boundary-value problem for general dissipative solids*. Journal of the Mechanics and Physics of Solids 54, 401-424, 2006.

[58] M. Ortiz and L. Stainier. *The variational formulation of viscoplastic constitutive updates*. Comput. Methods Appl. Mech. Engrg. 171, 419-444, 1999.

[59] B. Li. *Notes on the implementation of the variational thermalmechanical coupling constitutive model*, California Institute of Technology, 2013.

[60] K. John. *Notes on the constitutive model*, California Institute of Technology, 2013.

[61] K. Bhattacharya. *Multiscale Modeling*, California Institute of Technology, PSAAP Site Visit Meeting, Pasadena, CA, 2011.

[62] J. Kaeser. *FEMAP –Powering today's most advanced engineering analysis envirnoment*, Siemens PLM Software, 2012.

[63] U. Ayachit. *ParaView – Open Source Scientific Visualization*, Creative Commons Attribution, 2013.

[64] S. Brunett and M. Bartelt. *Caltech Center for Advanced Computing Research at the forefront of computational science and engineering*, California Institute of Technology, 2013.

[65] D. Rittel, A. Bhattacharyya, B. Poon, J. Zhao, and G. Ravichandran. *Thermomechanical characterization of pure polycrystalline tantalum*, Materials Science and Engineering, 447, 465-470, 2007.

[66] J. Larsen. *Hyades--A plasma hydrodynamics code for dense plasma studies*, Journal of Quantitative Spectroscopy & Radiative Transfer, ISSN 0022-4073, 1994.

[67] C. Plechaty. *Isentropic Compression Experiments for Tantalum, 12B – Readiness Review*, Lawrence Livermore National Laboratory, 2012.

[68] C. Plechaty. *Isentropic Compression Experiments for Tantalum, 12B – Update – LowT* Group Meeting, Lawrence Livermore National Laboratory, 2012.

[69] C. Plechaty. *Isentropic Compression Experiments for Tantalum, 12B and Iron, 12A: A Quick Look (HERIE)*, Lawrence Livermore National Laboratory, 2012.

[70] J. Belof, R. Cavallo, et al. *Rayleigh-Taylor strength experiments of the pressure-induced a→ ε→ a' phase transition in iron*, LLNL-PROC-492911, 2011.

[71] S. Tateno, et al. *The Structure of Iron in Earth's Inner Core*, Science 330, 359-361, 2010.

[72] B. Remington, et al. *High Pressure, Solid State Experiments for NIF*, UCRL-ID-142676, 2001.

[73] B. Remington. *An Introduction to High Energy Density Science*. Presentation to the 1st Workshop on High Energy Density Physics, San Diego, CA, June 28-30, 2010.

[74] G. Ravichandran. *Dynamic Behavior of Materials*, Presentation at the PSAAP TST Meeting, Pasadena, CA, May 20, 2011.

[75] K. John. *Strength of Materials through RT Experiments & Multiscale Model Validation*. Presentation at the DOE NNSA SSGF Annual Program Review, Santa Fe, NM, June 25-27 2013.